Synthesis of Nanostructured Block Copolymer in Supercritical Carbon Dioxide



Mohammad Alauhdin

Thesis submitted to the University of Nottingham

for the degree of Doctor of Philosophy

August 2017

Disclaimer

All work presented in this Thesis is the original work of the author, with the exception of results referenced to other sources. It has not been submitted as part of any other degree or professional qualification.

Signed : 

Date : 06/09/2017

Mohammad Alauhdin

Acknowledgment

I would like to first thank my supervisor, Prof. Steven M. Howdle for giving me the opportunity of doing this PhD and for all his advice and guidance throughout the course of my research. I would also like to acknowledge and thank Prof. Wim Bras, Dr. Daniel Hermida-Merino, and everyone from DUBBLE at the ESRF for offering their time and considerable expertise in X-ray scattering and all things related.

Thank you to Helen Carson who has organised a vast amount for me and the group. People in the clean energy workshop, in particular Martin Dellar, Pete Fields, and Rich Wilson for their technical help and keeping all the equipment running. NMRC staff, especially Nikki Weston and Denise Mclean in taking time to introduce me to the microscopic techniques which have been critical to my PhD.

Thanks also to past and present members of the Howdle group, for valued advice and discussions. In particular for Dr. Simon Bassett who helped me out right at the start and has always been there for valuable guidance. Dr. Guping He and Dr. Thomas Bennett for their time and scientific advice.

I must thank my family and all Indonesian fellows in Nottingham for their continuous support and encouragement. Finally, this doctoral thesis would not have been possible without the generous support of the Unnes-IDB scholarship.

Abstract

This thesis aims to expand our knowledge of block copolymer synthesis, particularly in supercritical CO_2 ($scCO_2$) and to study the microphase separation behaviour occurring within block copolymer microparticles during the synthesis. For these purposes, a new synthesis strategy was proposed and a high pressure X-ray autoclave was built and tested to facilitate the *in situ* microphase separation investigation by X-ray scattering. The success of this project has significantly broaden our understanding of the block copolymer synthesis and its phase separation mechanism in $scCO_2$ dispersion, which are highly important to generate self-organised nanostructures.

For the synthesis of block copolymers, a two-stage method has been successfully applied to add flexibility to the existing synthesis method, by allowing each block to be synthesised in independent steps. The results indicated that this method can be used for synthesising a variety of poly(methyl methacrylate)-based block copolymers. Importantly, these block copolymers can be prepared in a much shorter timeframe, since the polymerisation of the second block can be decoupled from the first. Different internal morphologies of the block copolymers were observed, including body centred cubic packing of spheres (SPH), hexagonally packed cylinders (CYL), bicontinuous gyroid (GYR), and lamellae (LAM). These morphologies were obtained by changing either the block copolymer pairs or the block volume fractions.

A new design of high pressure X-ray autoclave has been constructed and successfully applied in the monitoring of time-resolved Small-Angle X-ray Scattering (SAXS) during the Reversible Addition-Fragmentation Chain

Transfer (RAFT) dispersion polymerisation in $scCO_2$ using synchrotron radiation. During polymerisation of styrene using PMMA macro-RAFT agent, the microphase separation of PMMA-*b*-PS block copolymers developed with reaction time resulted in more distinct domains and an increase in the domain spacing. The investigation revealed that the nanostructured morphologies remain invariant from the initial formation. However, the ordering of the nanostructures was found as the polymerisation proceed.

We then sought to expand the potential of the two-stage synthesis method for preparing polymer/metal nanoparticle hybrid materials. Nanostructured PMMA-*b*-PDMAEMA block copolymer was selected as the host polymer. In this approach, the second block, PDMAEMA, can be synthesised while generating silver nanoparticles (AgNPs) in one-pot process. Importantly, the AgNPs can be located in the PDMAEMA domain selectively since the tertiary amine groups of the growing PDMAEMA chains anchored the AgNPs. This synthesis method produces a clean material as the solvent is readily removed on depressurisation and there was no additional reducing agent.

List of Abbreviations and Acronyms

$[M]_0$	: Concentration of monomer at time zero
$[M]_t$	: Concentration of monomer at time t
4VP	: 4-Vinyl Pyridine
Ag(hfac)(COD)	: (1,5-cyclooctadiene)(hexafluoroacetylacetonate)silver(I)
AGET	: Activator Generated by Electron Transfer
AgNP	: Silver nanoparticle
AIBN	: 2,2'-Azobis(isobutyronitrile)
ATRP	: Atom Transfer Radical Polymerisation
AuNP	: Gold nanoparticle
BCC	: Body Centered Cubic
BTSP	: Benzylsulfanylthiocarbonylsulfanylpropionic
BzMA	: Benzyl Methacrylate
CLRP	: Controlled/Living Radical Polymerisation
CO_2	: Carbon Dioxide
CSIRO	: Commonwealth Scientific and Industrial Research Organisation
CTA	: Chain Transfer Agent
C_v	: Coefficient of Variation
CYL	: Hexagonally Packed Cylindrical Morphology
D	: Domain Size
Đ	: Dispersity
DATC	: S-Dodecyl-S'-(α, α'-dimethyl-α''-acetic acid) trithiocarbonate
DEA	: *N,N*'-Diethylacrylamide
DEGMA	: Di(ethylene glycol) Methyl Ether Methacrylate
DMA	: *N,N*-Dimethyl Acrylamide
DMAEMA	: *N,N*-Dimethylaminoethyl Methacrylate
DNA	: Deoxyribonucleic Acid
DP	: Degree of Polymerisation
dRI	: Differential Refractive Index
DSC	: Differential Scanning Calorimetry
DUBBLE	: Dutch-Belgian Beamline
EPDM	: Ethylene Propylene Diene Monomer
ESRF	: European Synchrotron Radiation Facility

f	: Initiator efficiency
f_A	: Volume fraction (of block A)
FRP	: Free Radical Polymerisation
GI-SAXS	: Grazing Incidence Small Angle X-ray Scattering
GPC	: Gel Permeation Chromatography
GYR	: Gyroidal Morphology
HEMA	: 2-Hydroxyethyl Methacrylate
HPLC	: High Performance Liquid Chromatography
HPMA	: 2-Hydroxypropyl Methacrylate
J_{crit}	: Critical Molecular Weight
LAM	: Lamellar Morphology
MAA	: Methacrylic Acid
MADIX	: Macromolecular Design *via* the Interchange of Xanthates
MEA	: 2-Methoxyethyl Acrylate
MMA	: Methyl Methacrylate
M_n	: Number Average Molecular Weight
M_n^{GPC}	: GPC measured number average molecular weight
M_n^{th}	: Calculated number average molecular weight
M_n^{target}	: Targeted number average molecular weight
$NaBH_4$	: Sodium borohydride
NIPAM	: *N*-isopropylacrylamide
NMP	: Nitroxide Mediated Radical Polymerisation
NMR	: Nuclear Magnetic Resonance
ODT	: Order-disorder Transition
OOT	: Order-order Transition
OPAP	: 4-(4'-octylphenyl)azophenol
P2VP	: Poly(2-vinylpridine)
P4VP	: Poly(4-vinylpyridine)
PAA	: Poly(acrylic acid)
PDMS-MA	: Polydimethylsiloxane monomethyl methacrylate
PDP	: 3-*n*-pentadecylphenol
PE	: Polyethylene
PEG	: Poly(ethylene glycol)
PFMA	: Poly(2,2,2-trifluoroethyl methacrylate)
PFMA	: Poly(2,2,2-trifluoroethyl methacrylate)
PFOMA	: Poly(1H,1H,2H,2H-Perfluorooctyl Methacrylate)

PFPO	: Poly(hexafluoropropylene oxide)
PGMA	: Poly(glycerol mono methacrylate)
PI	: Polyisoprene
P*i*BMA	: Poly(iso-butyl methacrylate)
PISA	: Polymerisation-Induced Self-Assembly
PMPC	: Poly(2-(methacryloyloxy)ethyl phosphorylcholine)
P*n*HMA	: Poly(*n*-hexyl methacrylate)
POEGMA	: Poly[oligo(ethylene glycol) methacrylate]
PP	: Polypropylene
PPA	: Poly(acrylic acid)
PPO	: Poly(propylene oxide)
PS	: Polystyrene
PsfMA	: Poly(perfluoroalkyl methacrylate)
$PtMe_2(COD)$	: Dimethyl (1,5-cyclooctadiene)platinum
PVC	: Poly(vinyl chloride)
Q	: Scattering intensity
RAFT	: Reversible Addition-Fragmentation Chain Transfer
RTCP	: Reversible Chain Transfer Catalysed Polymerisation
SAXS	: Small Angle X-ray Scattering
$scCO_2$	: Supercritical Carbon Dioxide
SCF	: Supercritical Fluid
SEM	: Scanning Electron Microscopy
SG1	: *N*-tert-butyl-*N*-(1-diethylphosphono-2, 2-dimethylpropyl) nitroxide
SMA	: Stearyl Methacrylate
SPH	: Spherical Morphology
TEA	: Triethylamine
TEM	: Transmission Electron Microscopy
T_g	: Glass Transition Temperature
THF	: Tetrahydrofuran
WAXS	: Wide Angle X-ray Scattering
χ	: Flory-Huggins Interaction Parameter

Table of Contents

Chapter 1 Introduction 1
1.1 Overview 1
1.2 Polymer Chemistry 2
1.2.1 Synthesis of polymer 2
1.2.2 Polymer architecture 4
1.3 Polymerisation Techniques 5
1.3.1 Free radical polymerisation 5
1.3.2 Controlled/Living Radical Polymerisation (CLRP) 8
1.3.3 Reversible Addition-Fragmentation Chain Transfer (RAFT) 9
1.4 Polymerisation Processes 14
1.4.1 Homogeneous polymerisation 14
1.4.2 Heterogeneous polymerisation 15
1.4.3 Dispersion polymerisation 16
1.5 Block Copolymers 18
1.5.1 Synthesis of block copolymer 18
1.5.2 Phase separation behaviour 20
1.5.3 Application 23
1.6 Supercritical Fluids 27
1.6.1 Supercritical carbon dioxide 27
1.6.2 Polymer properties in $scCO_2$ 28
1.6.3 Polymerisation in $scCO_2$ 29
1.6.4 Dispersion CLRP in $scCO_2$ 30
1.7 Summary and Research Aims 32
1.8 References 33
Chapter 2 Experimental Technique 38
2.1 Overview 38
2.2 High Pressure Equipment 38
2.2.1 General Set Up 38
2.2.2 60 mL High Pressure Autoclave 39
2.2.3 60 mL High Pressure Autoclave with Additional Valves 42
2.2.4 High Pressure X-ray Autoclave (MKII) 45
2.3 Analytical Techniques 51
2.3.1 Gel Permeation Chromatography 51
2.3.2 Nuclear Magnetic Resonance Spectroscopy 53
2.3.3 Scanning Electron Microscopy 54

2.3.4 Transmission Electron Microscopy 54
2.3.5 Differential Scanning Calorimetry 55
2.3.6 Thermal Gravimetric Analysis 55
2.3.7 Small Angle X-ray Scattering 56
2.4 References 57
Chapter 3 Synthesis of Nanostructured Block Copolymers in Supercritical CO_2 58
3.1 Overview 58
3.2 Introduction 59
3.2.1 Synthesis and Self-assembly of Block Copolymer *via* RAFT Dispersion Polymerisation 59
3.2.2 Nanostructured Block Copolymer Particles 64
3.3 Objectives 68
3.4 Experimental 69
3.4.1 Material 69
3.4.2 Two-stage Polymerisation 69
3.5 Results and Discussion 73
3.5.1 Synthesis of Block Copolymer *via* Two-stage Method 73
3.5.2 Morphological Improvement of The Microparticles 83
3.5.3 Kinetic Studies of The Two-stage Synthesis 93
3.5.4 Internal Structure of Block Copolymer Microparticles 95
3.5.5 Particle Morphologies at Low PMMA Content 102
3.6 Conclusions 106
3.7 References 107
Chapter 4 Study of The Internal Nanostructure Development of Block Copolymer Microparticles 110
4.1 Overview 110
4.2 Introduction 111
4.2.1 SAXS Studies of Block Copolymer Phase Behaviour 111
4.2.2 Block Copolymer Phase Behaviour in $scCO_2$ 114
4.2.3 SAXS Studies in High Pressure System 116
4.3 Objectives 117
4.4 Experimental 118
4.4.1 Materials 118
4.4.2 Block Copolymer Synthesis 118
4.4.3 *In situ* SAXS Measurement 119
4.5 Results and Discussion 120

4.5.1 Block Copolymer Synthesis in the New High Pressure X-ray Autoclave 123
4.5.2 *In situ* SAXS Monitoring 129
4.5.3 Structural Evolution 137
4.5.4 The Invariant Plot 143
4.6 Conclusions 145
4.7 References 146
Chapter 5 One-pot Synthesis of Block Copolymer/Silver Nanoparticles Hybrid Materials 151
5.1 Overview 151
5.2 Introduction 152
5.2.1 Synthesis of Metal Nanoparticles in $scCO_2$ 152
5.2.2 Synthesis of Polymer/Metal Nanoparticles 154
5.2.3 Spatial Control of Nanoparticle Location in Phase Separated Block Copolymer 159
5.3 Objectives 165
5.4 Experimental 165
5.4.1 Material 165
5.4.2 Synthesis of PMMA-*b*-PDMAEMA 166
5.4.3 Synthesis of PMMA-AgNPs 166
5.4.4 Synthesis of PMMA-*b*-PDMAEMA/AgNPs 167
5.5 Results and Discussion 168
5.5.1 Initial Studies 168
5.5.2 Synthesis of PMMA-*b*-PDMAEMA/AgNPs 176
5.5.3 Selectivity of AgNPs within the polymer particles 178
5.5.4 The effect of precursor concentration 180
5.6 Conclusions 187
5.7 References 188
Chapter 6 Conclusion and Future Work 191
6.1 Overview 191
6.2 Conclusion 191
6.3 Future work 193
6.4 References 195

Chapter 1 Introduction

1.1 Overview

Polymers are found in many aspects of our lives, from personal care products and household appliances to biomedical and electronic devices.[1–3] Indeed, application of polymer-based materials has continuously expanded along with research and development in the field. Progress to date in polymer science and engineering has focussed on modifying existing polymers and fabricating novel polymeric materials with greater functionality. Both of these kinds of materials are expensive, yet have particular properties that can deliver high value, such as artificial heart valves, tissue adhesives, sensors, or semiconductor devices.[4,5] Although these specialty markets are still growing, their future in research and commercial application is obviously promising.

A class of polymer that has fascinating properties for advanced applications is block copolymers. The unique properties of block copolymers in many cases originate from their ability to self-assemble into well-defined nanostructure morphologies, such as spheres, cylinders, bicontinuous gyroids, and lamellae. Currently, there are some well-established methods to fabricate nanostructured block copolymers, but the routes normally require multiple steps from pre-synthesised block copolymers.[6,7] On the other hand, the development of versatile synthesis techniques such as controlled/living radical polymerisations (CLRP) has established and played a significant role in modern polymer science. In particular, CLRP in a dispersed system offers a more simplified and potentially more commercialisable approach since synthesis and self-assembly of block copolymers can be achieved in one-pot.[8]

A synthesis route *via* $scCO_2$ dispersion polymerisation has allowed fabrication of unique nanostructured block copolymer microparticles that are

difficult or even impossible to achieve *via* existing routes.[9] The low viscosity and high diffusivity of $scCO_2$ aids the mobility and rearrangement of the block copolymer chains to allow phase separation and to facilitate construction of a particular nanostructure. Moreover, the use of $scCO_2$ as a polymerisation medium is not only beneficial as an alternative 'green' solvent, but also provides additional advantages such as simplified product recovery, lower processing temperature, and elimination of solvent residues. Although still in the early stages, applications of such nanostructured block copolymer microparticles as functional materials are now being studied in depth, including as nanotemplates, drug delivery vehicles and protein separation matrices.[10,11]

The work in this thesis will explore CLRP to fabricate nanostructured-block copolymer microparticles *via* dispersion polymerisation in $scCO_2$. The investigation of how and when the internal nanostructure morphologies are formed during the polymerisation will be probed using *in situ* X-ray scattering in combination with electron microscopy. Finally, we will make the first step towards application to investigate if the phase-separated block copolymer can be used to direct loading of inorganic nanoparticles, which could lead to exciting new opportunities in sensors, catalysts, and nanophotonics.[11–13]

This chapter will introduce the fundamental concepts applicable to this thesis including CLRPs, heterogeneous polymerisations, phase separation behaviour and application of block copolymers, and finally the use of (and properties associated with) $scCO_2$.

1.2 Polymer Chemistry

1.2.1 Synthesis of polymer

There are two main mechanisms for producing synthetic polymers, namely step-growth and chain-growth polymerisation. A step-growth

polymerisation usually proceeds by reactions between two different functional groups and is often accompanied by the loss of small molecules such as water. The two different functional groups may come from a single monomer or two different bifunctional monomers where each monomer possesses only one type of functional group. Low molecular weight oligomeric products are generated at the beginning of the reactions which subsequently join together to form the high molecular weight polymer. This route makes polymerisation proceed with a relatively slow increase in the molecular weight of the polymer (Figure 1.1).

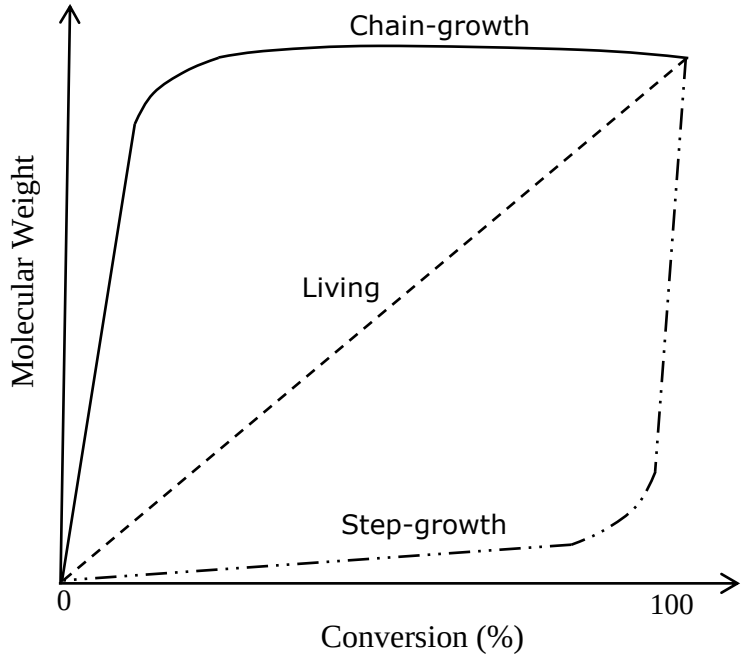


Figure 1.1. The relationship between molecular weight and monomer conversion for chain-growth, step-growth, and living polymerisation.

In chain-growth polymerisation, chain length increases with the consecutive addition of monomer units to the end of the growing chain involving some sort of active centre. The active centre is terminated at the end of the reaction to prevent further growth. However, this termination can be prevented through living polymerisation techniques, allowing further chain growth upon addition of monomer. In Figure 1.1, the relationship between

molecular weight and monomer conversion for the different types of polymerisations is presented. In chain-growth polymerisation, a high molecular weight polymer can be produced easily compared to step-growth, even at low conversion. Living polymerisations will be discussed further in Section 1.3.2.

1.2.2 Polymer architecture

Polymers can display a number of different architecture. The simplest ones are linear polymers, where monomers are linked to each other in a linear chain. Alternatives to such linear polymers are branched and cross-linked architecture (Figure 1.2). These different architecture affect the properties of the polymer. For example, linear polymers are usually more crystalline and denser than branched analogues of similar molecular weight.

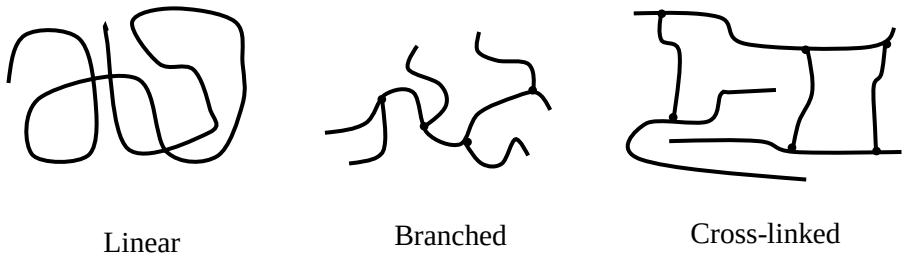


Figure 1.2. Schematic diagram of polymer architectures.

If a polymer comprises only one monomer, it is called a homopolymer. When more than one monomer unit is incorporated into a chain, it forms a copolymer; for example, a block copolymer, an alternating copolymer, a statistical copolymer, or a graft polymer (Figure 1.3).

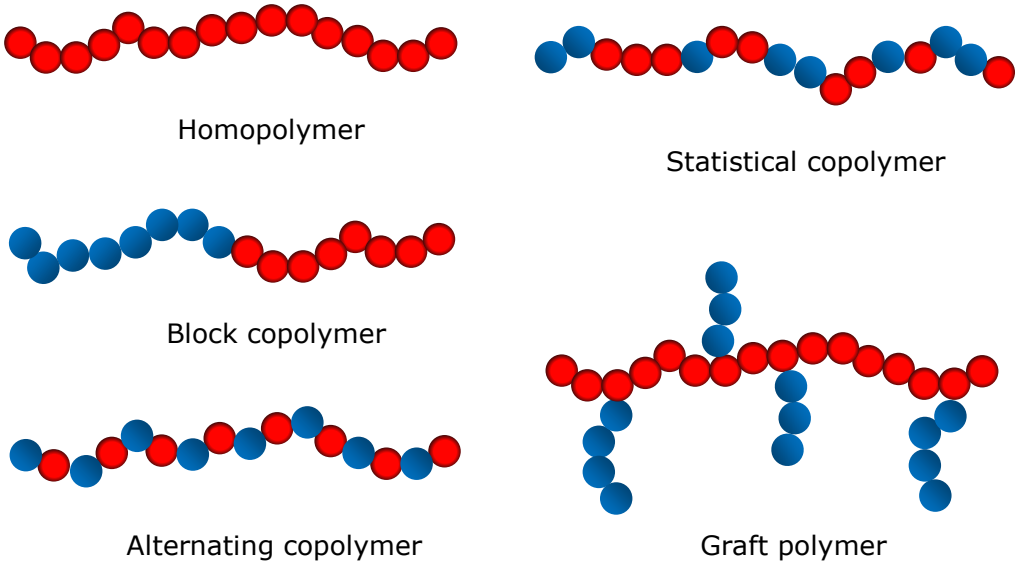


Figure 1.3 Schematic representation of homopolymer and copolymers.

1.3 Polymerisation Techniques

1.3.1 Free radical polymerisation

Free radical polymerisation (FRP) is a kind of chain-growth polymerisation. In this polymerisation, a polymer grows by successive addition of the monomer molecules. It takes place by breaking of a double bond of the monomer unit and converting it into an active propagating radical.[14] The advantages of FRP, with respect to other techniques, are that it is relatively tolerant to impurities[15] and suitable for nearly all vinyl monomers. It can also be performed under a variety of reaction conditions e.g. bulk, emulsion, or precipitation polymerisation, and in various solvents, including supercritical CO_2.[16–20] In spite of many advantages, the rapid chain growth and fast irreversible termination lead to some limitations towards the degree of control that can affect the molecular weight distribution and polymer structure.[15] Furthermore, block copolymers and polymers with complex architectures are not accessible directly *via* FRP.

A free radical polymerisation consists of initiation, propagation, and termination steps. The initiation takes place by decomposition of an initiator to form free radical species. These radicals then initiate the polymerisation. The radicals are generated usually by homolytic dissociation of a molecule, known as an initiator, by heating, electromagnetic radiation or chemical reaction.[21] The thermal decomposition of an azo compound is one of the most common ways to generate a free radical. The dissociation of an azo compound generates relatively stable carbon-centred tertiary radicals along with a highly stable nitrogen molecule. For example, an azo compound, 2,2'-azobis (isobutyronitrile) (AIBN) decomposes thermally and then forms two cyanopropyl radicals and a nitrogen molecule (Figure 1.4a).[14] Initiation of methyl methacrylate (MMA) by a cyanopropyl radical is shown in Figure 1.4b.

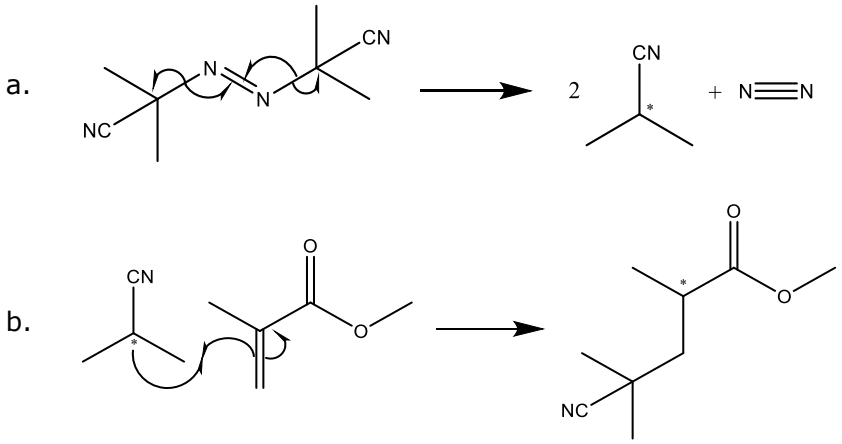


Figure 1.4. (a) Radical generation by homolytic dissociation of 2,2'-azobis (isobutyronitrile) (AIBN) into 2-cyano-2-propyl radicals and dinitrogen, (b) initiation of MMA by the 2-cyano-2-propyl radical.

Propagation involves successive addition of monomer to the active chain end, increasing the polymer chain length. The reactive site is retained after each addition of monomer until bimolecular chain termination occurs. An example of propagation is shown in Figure 1.5, again using MMA.

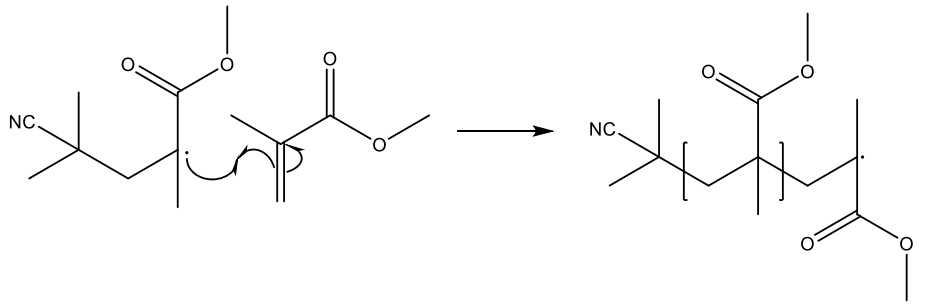


Figure 1.5. Mechanism of propagation of MMA.

The termination step forms unreactive (dead) polymer chains. It can occur by two mechanisms: combination or disproportionation (Figure 1.6). Combination involves coupling of two active centres to form a high molecular weight polymer. In contrast, disproportionation occurs *via* hydrogen transfer between active polymer radicals and forms two separate polymer chains; one with a double bond at the end of the chain and the other with a terminal hydrogen.

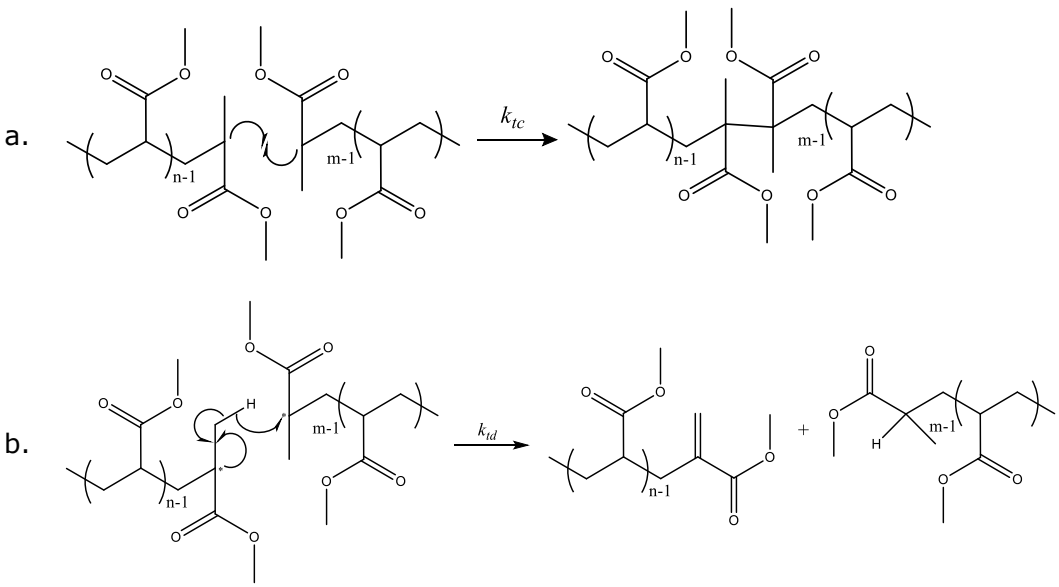


Figure 1.6. (a) Termination reactions in the polymerisation of MMA; combination and (b) disproportionation.

1.3.2 Controlled/Living Radical Polymerisation (CLRP)

It has been mentioned that conventional FRP has some limitations. To overcome such drawbacks, new techniques are needed to produce materials which can meet the demand for controlled polymer products for advanced technological applications such as electronic storage, tissue engineering, drug delivery, and membrane technology.[22–24] Living anionic polymerisation[25] can provide a well-defined polymer and precise molecular architecture, but it is rather limited due to being intolerant to functionality and impurities. Thus, the development of a process that combines the robustness of radical polymerisation with well-controlled molecular weight distributions and precise architecture of living anionic polymerisation is highly desirable. Therefore, Controlled/Living Radical Polymerisation (CLRP) methods have been introduced in order to fulfil this demand. CLRP can control polymerisation of vinyl monomers to dictate the molecular weight of the polymer, molecular weight distribution, and architecture.[26]

CLRP works by controlling the rate of propagation of the growing polymer chains in the presence of species that lead to reversible termination of the active centre to generate a dormant species. A rapid equilibrium between the propagating polymer radicals and the dormant chains leads to a significant difference between conventional radical polymerisations and the CLRP techniques. The typical features of a CLRP can be summarised as follows:

1. Initiation is very fast with respect to the propagation step. The growing polymers with active radical ends will grow at approximately the same rate. This means that the polymers formed have approximately the same molecular weight and exhibit narrow molecular weight distributions.
2. The polymerisation proceeds until all monomers are consumed and may continue growing by adding more monomer(s). If the additional

monomer(s) are different from the first monomer, a block copolymer will be formed.

3. The molecular weight increases linearly with the conversion. It is caused by rapid equilibration between the active propagating radical and the dormant polymer chains that ensures all of the chains have an equal opportunity for growth.

Typical examples of CLRP include Nitroxide-Mediated Polymerisation (NMP),[18, 19] Atom Transfer Radical Polymerisation (ATRP),[20, 21] Reversible Addition-Fragmentation Chain Transfer (RAFT) polymerisation,[2, 22-25] and Macromolecular Design *via* the Interchange of Xanthate (MADIX)[22, 24, 26] polymerisation. The mechanisms of ATRP and NMP work *via* reversible deactivation, with the capping of radicals by a halogen or a nitroxide fragment, respectively.[20, 27] NMP uses alkoxyamines as capping agents. In ATRP, the atom transfer step is important: it is responsible for producing uniform polymer chain growth. Meanwhile, RAFT and MADIX involve the same mechanism and differ only by the polymerisation mediator used. The work in this project focuses on using the RAFT technique for the synthesis of homopolymers and block copolymers. The RAFT process will be described in detail in the following section.

1.3.3 Reversible Addition-Fragmentation Chain Transfer (RAFT)

RAFT polymerisation was reported in 1998, at the Commonwealth Scientific and Industrial Research Organisation (CSIRO).[28] This technique is growing rapidly because it has proven tolerant to a very wide range of functionalities in both the monomer and solvent. As a controlled polymerisation, it produces polymers with defined molecular weights and architectures. It also has the advantage of easy application and metal-free

reactions. This process involves a RAFT agent, which is a compound that can act as a reversible chain transfer agent. RAFT agents are thiocarbonylthio compounds which are composed of two key parts, a stabilising group (Z) and a leaving group (R) (Figure 1.7).

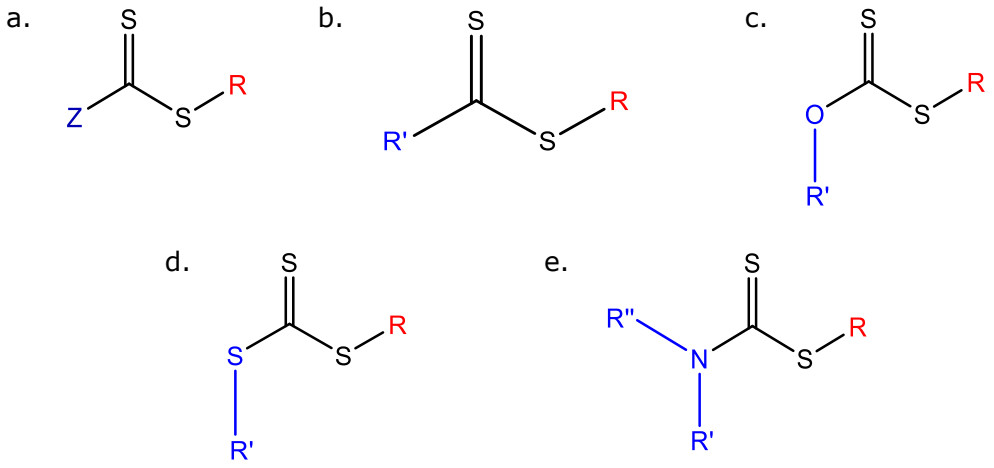


Figure 1.7. (a) General chemical structure of RAFT agents, (b) dithioesters, (c) xanthates, (d) trithiocarbonates, (e) dithiocarbamates; Z: stabilising group, R: leaving group

The RAFT process can be described as the insertion of monomer units into the S-R bond of the RAFT agent to yield a polymer (Figure 1.8). A polymer chain with a conserved RAFT end-group can be applied as a macro-RAFT agent to prepare a block copolymer through subsequent polymerisation of the second monomer.

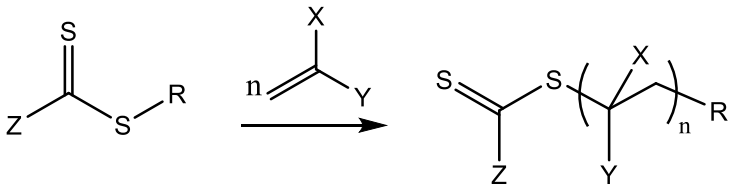
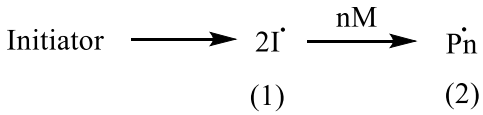


Figure 1.8. Simplified RAFT polymerisation

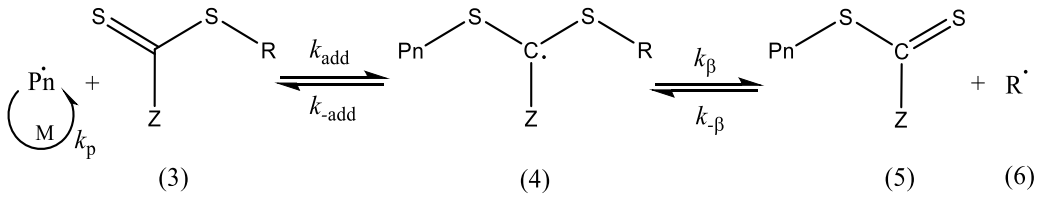
The proposed RAFT mechanism (Figure 1.9) shows that the process is initiated by free radicals (1), generated as in conventional free radical polymerisation. These radicals interact with the monomer (M) to produce propagating radicals (2). The reaction between the propagating radical and the highly reactive C=S bond of the thiocarbonylthio compound (3) produces a polymeric thiocarbonylthio compound (5), and a new radical (6) through an intermediate fragment (4). The newly formed radical can re-initiate polymerisation and produce propagating polymer chains (7). Then the propagating chains interact with the thiocarbonylthio-terminated polymer species and release another propagating radical. This process gives an opportunity for all polymer chains to grow at approximately the same rate and so produce polymers with low dispersity. Most of the polymer chains from the overall process retain the thiocarbonylthio end-group that can be re-initiated by additional radicals and monomers, or isolated as stable materials. The end-group also causes the final polymer of the RAFT process to be coloured.

The effectiveness of the RAFT agent is decided primarily by the characteristics of the leaving group, R, and the stabilising group, Z. The Z-group adjusts the reactivity of C=S double bond towards radical addition and the fragmentation rate of the RAFT intermediate radical with the most reactive Z has carbon (dithioesters) or sulfur (trithiocarbonates) next to the C=S double bond. Meanwhile, the RAFT agents with oxygen (xanthates) or nitrogen (dithiocarbamates) neighbouring to the C=S double bond are less reactive towards radical addition.[27]

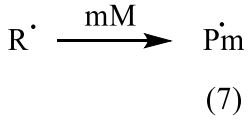
Initiation



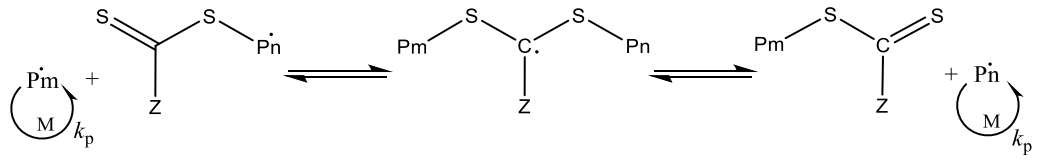
Reversible chain transfer/ propagation



Reinitiation



Main equilibrium



Termination

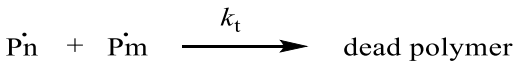


Figure 1.9. General mechanism for RAFT.

The theoretical molecular weight (M_n^{th}) of the synthesised polymer by RAFT polymerisation can be calculated using Equation 1.1.

$$M_n^{th} = \frac{([M]_0 - [M]_t)}{([RAFT]_0 + df([I]_0 - [I]_t)} \; x \; M_M + \; M_{RAFT} \qquad \text{(Equation 1.1)}$$

where $[M]_0-[M]_t$ is the concentration of the monomer consumed and M_M is molecular weight of the monomer. $[RAFT]_0$ is the initial concentration of the RAFT agent and M_{RAFT} is the molecular weight of the RAFT agent. *d* is the average number of chains formed from each radical–radical termination event, *f* is the initiator efficiency, and $[I]_0$ - $[I]_t$ is the concentration of initiator consumed. The theoretical molecular weight can also be predicted in a simpler equation (Equation 1.2) that is obtained by assuming the absence of chains initiated by the radical initiator. This could be applied when the molar ratio of RAFT agent to initiator concentration is relatively high and the RAFT agent has a large chain-transfer constant.

$$M_n^{th} = \frac{([M]_0-[M]_t)}{([RAFT]_0)} x M_M + M_{RAFT} \qquad \text{(Equation 1.2)}$$

A successful RAFT polymerisation must fulfil a number of conditions in which polymers of uniform molecular weight can be produced. Firstly, the rate of initiation should be much faster than that of propagation. This ensures that all chains grow at the same rate and results in polymers of low dispersity.[28] Secondly, it is important to minimise the lifetime of the active propagating radicals. This helps to reduce the probability of bimolecular termination reactions.[29] Additional termination reactions such as chain transfer should also be kept to a minimum.

Recent advances in RAFT attempt to solve some of the limitations of this technique. For example, exploring novel modes of activation of the RAFT agents to avoid the reliance on an additional initiator. These new modes include photolysis and a photoredox catalyst to activate the thiocarbonylthio compound rather than using a traditional free radical initiator.[29] As many other CLRP methods, RAFT requires oxygen-free condition to achieve a highly controlled

polymerisation. However, by using glucose oxidase (GO_x), an enzyme for deoxygenation by converting oxygen to hydrogen peroxide, RAFT polymerisations can be conducted in ambient oxygen.[30,31] Since only a low concentration of the enzyme is needed to fully consume oxygen in the system, hydrogen peroxide production can be negligible using this technique. Excellent controlled polymerisation of a wide range of monomers has been demonstrated, including both in solution polymerisation and dispersion polymerisation.

RAFT was also successfully applied to produce amphiphilic block copolymer nano-objects of controlled size and morphology through a robust and efficient route: Polymerisation-Induced Self-Assembly (PISA).[32] This route has gained considerable attention over recent years as an alternative strategy to produce block copolymer nanoparticles. In the meanwhile, RAFT dispersion polymerisation in $scCO_2$ can be exploited to produce a high blocking efficiency.[33] In addition, this technique resulted in block copolymers in microparticulate form with nanostructures such as lamellae, cylinders, and spheres.[9]

1.4 Polymerisation Processes

Polymerisation can be conducted in either a homogeneous or heterogeneous system. Homogeneous polymerisation involves a single phase of the reaction mixture for the entire polymerisation process. Meanwhile, two or more phases exist in a heterogeneous polymerisation.

1.4.1 Homogeneous polymerisation

Bulk and solution polymerisations are examples of a homogeneous polymerisation. In bulk polymerisation, initially only pure monomer and a monomer-soluble initiator (if required) exist in the system, while a

homogeneous solution of monomer, polymer, initiator and any controlling agent (if required) is involved in the solution polymerisation with an appropriate solvent.

Bulk polymerisation is a simple route for preparing polymers with minimum contamination of the polymer product. However, a few drawbacks have been encountered in its application. As the reaction goes to higher conversion, the viscosity of the medium increases and makes stirring and heat removal more difficult. The 'trapped' heat leads to auto-acceleration, sometimes known as the Trommsdorff-Norrish effect or gel effect[21] in which the propagation rate is much higher than that of the termination rate. This can lead to an uncontrolled reaction and a lack of control in CLRP mediated systems.

The use of a solvent in solution polymerisations allows lower viscosity, which is the main problem associated with bulk polymerisations. However, this method needs an additional step for product recovery that usually consumes large volumes of solvent. Additionally, the introduction of a solvent opens the possibility of chain transfer from the propagating radical to the solvent which can be unfavourable to the propagation process.

1.4.2 Heterogeneous polymerisation

Heterogeneous polymerisation can be either emulsion, suspension, precipitation, or dispersion polymerisation.[34] Emulsion polymerisation can be applied to produce polymer particles ranging from 0.05 – 1 μm depending on the components and conditions used. Basically, the system contains water (or another continuous phase), a water-insoluble monomer, a water-soluble initiator (but not soluble in monomer), and a surfactant/emulsifier. During the process, the monomer exists in surfactant-stabilised monomer droplets which become depleted as the polymerisation proceeds. Initiation occurs in the

continuous phase and leads to the formation of oligomers. When the critical degree of polymerisation (J_{crit}) is reached, the oligomers diffuse into monomer-swollen micelles and further propagation occurs therein until full conversion is achieved.

In suspension polymerisation, both monomer and initiator are insoluble in the continuous phase. They are mixed by mechanical agitation to form droplets. Polymerisation then takes place within the droplets, resulting in polymer particles of the order of 100s of microns. This method is commonly used in the production of commercial polymers including poly(vinyl chloride) (PVC) and polystyrene.[35]

Precipitation polymerisation involves the use of soluble monomer and initiator in a continuous phase. Therefore, polymerisation begins initially as a homogeneous system, but upon initiation, the formed polymer is insoluble and thus precipitates. Polymerisation then proceeds further within or at the surface of the precipitated polymer particles. This type of polymerisation typically produces polymer particles with poor control over their morphology. Another heterogeneous polymerisation that begins with a homogeneous system is dispersion polymerisation. This type of polymerisation will be discussed in detail in the next section.

1.4.3 Dispersion polymerisation

Dispersion polymerisation is a modified version of precipitation polymerisation, where precipitation of the growing polymers is prevented by the presence of a stabiliser (Figure 1.10). The polymerisation begins with a homogeneous phase of monomer, initiator, stabiliser, and possibly a transfer agent. Initially, initiation and propagation occur in the continuous phase to produce soluble polymers until the critical molecular weight (J_{crit}) is reached. At this point, the polymer chains are no longer soluble in the continuous phase.

A stabiliser adsorbs to or covalently bonds with the polymers and covers their surface such that they are stable in the continuous phase.

Normally, the stabilisers used in dispersion polymerisations are amphiphilic polymers which are composed of polymer-philic head groups and a component which is soluble in the continuous medium.[36] This confers a steric stabilisation which both solubilises the particles and helps to prevent aggregation. Dispersion polymerisation can yield polymer particles of 0.1–15 μm in diameter. This technique has been successfully applied in many solvents including aqueous, organics, and $scCO_2$.[16,37,38]

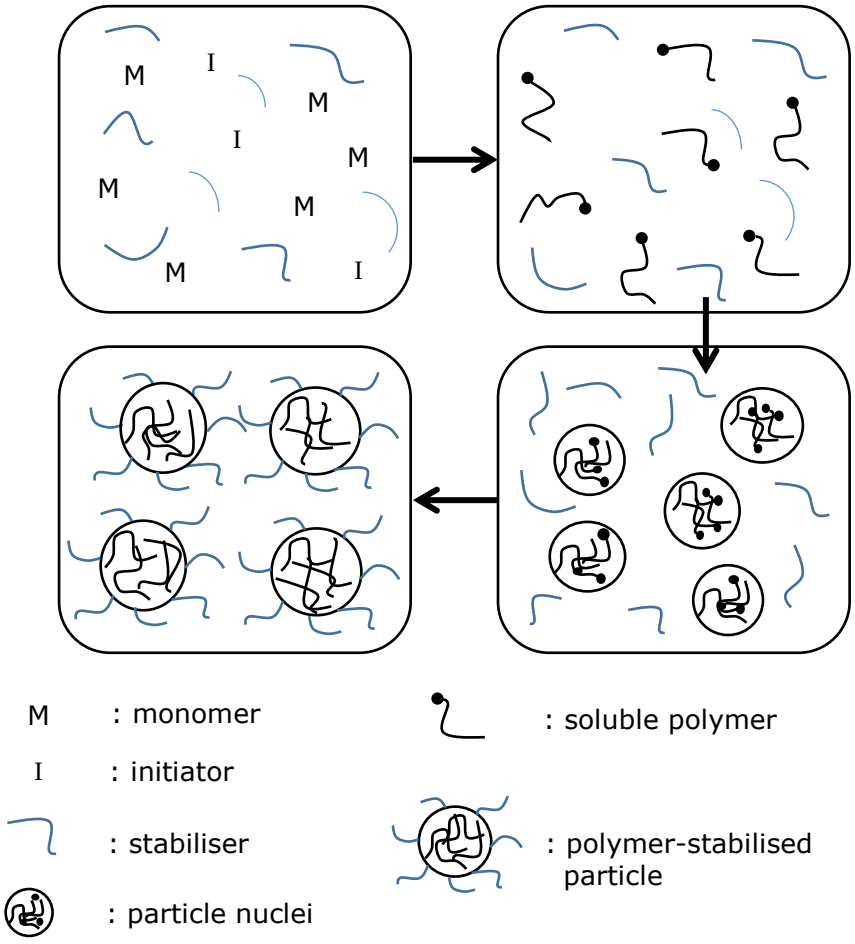


Figure 1.10. Schematic representation of dispersion polymerisation adapted from literature.[39]

Dispersion polymerisation in $scCO_2$ is a more or less generic technique since $scCO_2$ is a good solvent for most common vinyl monomers and a non-solvent for their polymers. DeSimone *et al*. reported the first synthesis of poly(methyl methacrylate) (PMMA) particles by dispersion in $scCO_2$ using poly(1,1-dihydrofluorooctyl acrylate) (PFOA) stabiliser.[16] Fluorinated and silicone-based polymers are common stabilisers that have been used in dispersion polymerisation in $scCO_2$. However, a series of poly(vinyl alkylate)-based copolymers with moderate CO_2 solubility has been synthesised and can be applied as stabilisers for the dispersion polymerisation of *N*-vinyl pyrrolidone (NVP) in $scCO_2$.[40–42] More recently, dispersion polymerisation in $scCO_2$ has been exploited for controlling the size and morphology of polymer particles using a single stabiliser, methacrylate-terminated poly(dimethylsiloxane) (PDMS-MA).[43]

1.5 Block Copolymers

Block copolymers consist of two or more homopolymers linked together by covalent bonds. Since their first synthesis in the 1950s, after the discovery of anionic polymerisation,[35] many block copolymer synthesis methods and techniques have been developed. In addition to the synthesis methods, properties, phase behaviour, and application of block copolymers have also been studied extensively in the last 50 years.

1.5.1 Synthesis of block copolymer

The concept of block copolymer synthesis started when Szwarc in 1956 discovered living anionic polymerisation.[25] The anionic active centre persisted even when all monomer had been consumed in the polymerisation. The active centre can continue the polymerisation to produce a block copolymer upon addition of a new batch of monomer. However, anionic polymerisation with a

carbon-centred anion is very sensitive to traces of protic impurities and needs very stringent reaction conditions. Therefore, anionic polymerisation is not frequently used on a commercial scale compare to FRP. Lately, Controlled/Living Radical Polymerisations (CLRP) have also been applied for the synthesis of block copolymers.

CLRP, including Atom Transfer Radical Polymerisation (ATRP), Nitroxide-Mediated Polymerisation (NMP), and Reversible Addition-Fragmentation Chain Transfer (RAFT) polymerisation, have been employed for the synthesis of numerous block copolymers from vinyl monomers. Compared to anionic polymerisation, CLRP results in a less pure block copolymer product due to the irreversible termination that could form non-functional or dead polymer chains. These chains are not extendable for block copolymer synthesis and remain as a homopolymer contaminant in the final product.[33] However, CLRP can be performed under mild conditions to produce well-defined functional polymers.

RAFT polymerisation as one of the CLRP methods is a versatile route to produce block copolymers.[27,44] In RAFT, a simple diblock copolymer can be prepared by successive polymerisation of two different monomers (Figure 1.11). A homopolymer formed from the first RAFT polymerisation will act as a macro-CTA for the second polymerisation. The RAFT agent must sufficiently control the polymerisation to maintain controlled properties of the block copolymer product.

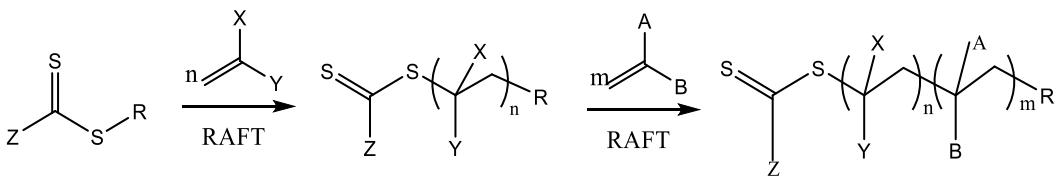


Figure 1.11. Diagram of block copolymer synthesis by sequential RAFT polymerisations.

The order of monomer addition in the RAFT block copolymer synthesis should be considered since the first polymer acts as a leaving group in the polymerisation of the second monomer. For instance, when preparing an MMA and styrene block copolymer, the MMA should be polymerised first,followed by styrene.[27] The MMA monomers produce tertiary propagating radicals which are better leaving groups than the secondary propagating radicals formed by styrene.

Using RAFT, a broad range of block copolymer architectures and functionalities can be prepared that are useful for many applications. A number of groups have synthesised block copolymers *via* RAFT polymerisation in various reaction media, including $scCO_2$.[8] A more detailed account specific to block copolymer synthesis *via* RAFT dispersion polymerisation is provided in Chapter 3.

1.5.2 Phase separation behaviour

Covalent bonds in block copolymers that link between the blocks lead to microphase separation of chemically dissimilar polymer blocks on length scales of around 5-100 nm. Figure 1.12a shows an example of such a microphase separation for a diblock copolymer. In contrast, two chemically distinct homopolymers undergo macrophase separation on a length scale of more than 1 μm, as shown in Figure 1.12b.

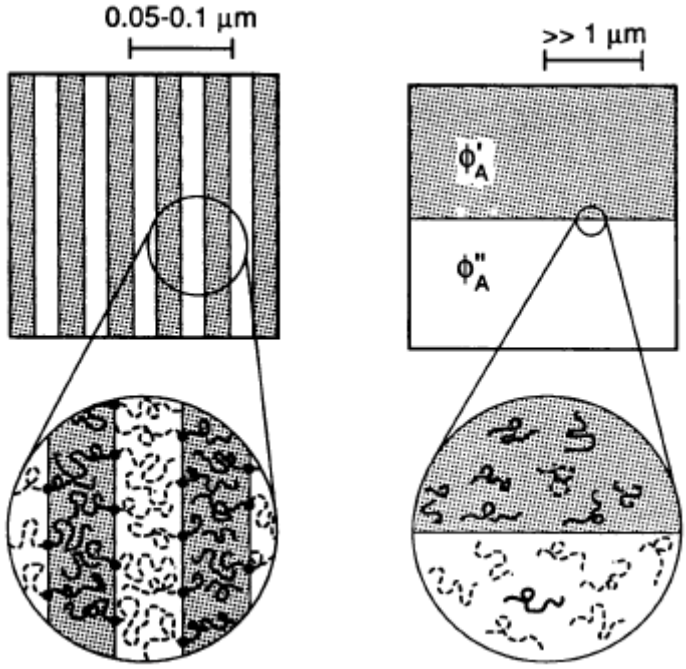


Figure 1.12. Schematic representation of polymer-polymer (dashed and solid curves) behaviours, (a) microphase separation of a symmetric diblock copolymer, (b) macrophase separation of a thermodynamically incompatible homopolymer blend.[45]

Three essential parameters that determine the microphase separation behaviour of block copolymers are (i) volume fraction (*f*), (ii) the degree of polymerisation (*N*), and (iii) the Flory-Huggins interaction parameter (χ).[46] The volume fraction represents the composition of one block relative to the others. The degree of polymerisation defines the number of repeating units (monomers) of the block copolymer. Meanwhile, the Flory-Huggins parameter refers to the degree of incompatibility of the polymer blocks which lead to the phase separation. The first two factors are adjusted through the stoichiometry of polymerisation, while the value of χ is determined by the choice of monomers and has a temperature dependence as given in Equation 1.3.[26]

$$\chi \approx \alpha T^{-1} + \beta \qquad \text{(Equation 1.3)}$$

α and β are constants which depend on the composition and architectural constraints of the block copolymer. A symmetric composition of the diblock copolymer will display phase separation if the product of χN is greater than a critical transition which is defined by χN= 10.5, but disorder is observed for smaller χN. At high temperatures, the block components mix randomly and form a disordered state. As the temperature decreases, which corresponds to an increase in the Flory-Huggins interaction parameter, the blocks self-assemble into one of the various possible ordered structures. Common morphologies include body-centred cubic of spheres, hexagonal-packed cylinders, and lamellae. A lamellar structure is observed when the volume fraction of the blocks is comparable. As the volume fraction of one block increases or decreases, the morphology will shift from hexagonal-packed cylinders to body-centred cubic spheres, with the smaller block distributed within a matrix of the majority block (Figure 1.13). The transition between these structures may appear with more complex morphologies, such as the bicontinuous gyriod phase.

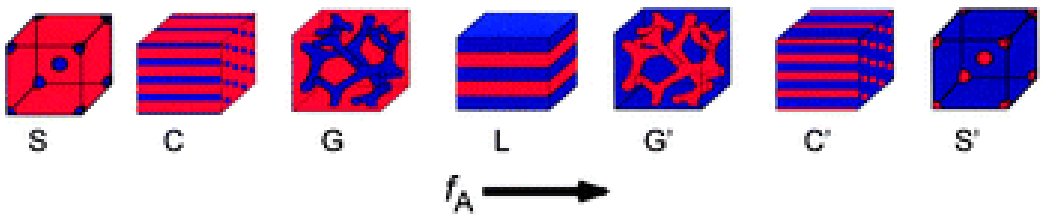


Figure 1.13. A schematic representation of the morphology of a AB diblock copolymer as f_A is increased for fixed χN, with type A and B monomers confined to the blue and red regions, respectively. S: body-center cubic (BCC) spheres, C: hexagonal arrangement of cylinders, G: Gyroid, L: Lamellae.[47]

The morphological development of a diblock copolymer can be presented in a phase diagram showing the relationship between the three parameters in the formation of a particular morphology. The phase diagram can be also constructed theoretically using self-consistent field theory.[48] For the experimental phase diagram, block copolymers need to be prepared with a wide range of volume fractions and then their morphology is characterised by neutron or X-ray scattering and electron microscopy.[49] The typical phase diagram for a linear diblock copolymer appears in Figure 1.14.

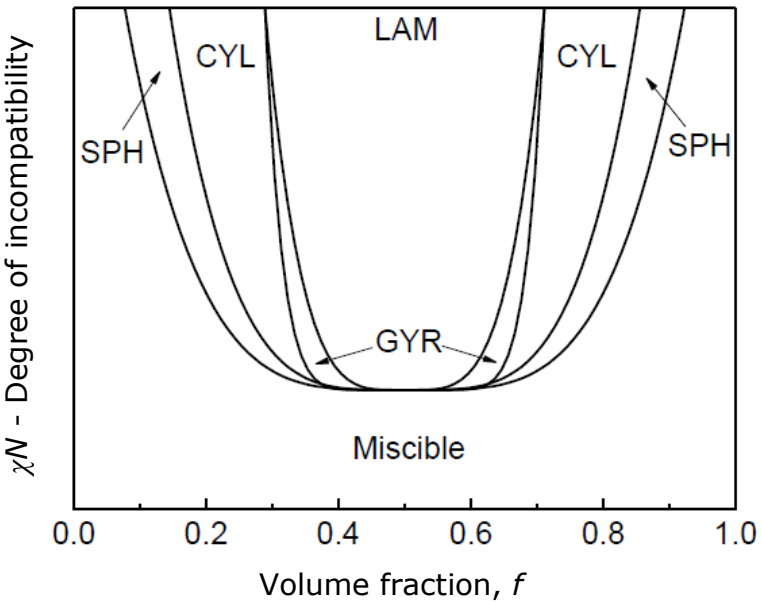


Figure 1.14. Theoretical phase diagram for linear AB diblock copolymer showing regions of spherical (SPH), cylindrical (CYL), gyroidal (GYR) and lamellar (LAM) morphology, along with a miscible region.[47]

1.5.3 Application

The first commercial block copolymer was used as a surfactant with the trade name Pluronic.[35] This is an ABA triblock copolymer composed of a hydrophobic segment, poly(propylene oxide), as the central block sided by two

hydrophilic segments of poly(ethylene oxide). Later, block copolymers became widely used in applications such as adhesives, automotive components, sporting goods, synthetic fibres, etc. Most of them are thermoplastic elastomers, which exploit the hard and soft components to provide the combined properties of a thermoplastic and an elastomer.

More recently, block copolymers have been explored to be used for more advanced applications. These mainly exploit the ability of block copolymers to self-assemble through their microphase separation behaviour. Drug delivery, protein separation, photovoltaic cells, electronic devices, and nanolithography are a few examples.

Microspheres of polystyrene-*b*-poly(acrylic acid) (PS-*b*-PAA) block copolymer with monodisperse continuous nanoporosity was applied for protein separation and drug delivery (Figure 1.15).[10] The carboxylic acid groups of PAA segments can be ionised to confer anionic charge. This charged and highly porous particle enables separation of similarly-sized proteins that cannot be separated efficiently *via* conventional dialysis membrane processes. The separation occurs based on size differences between the various proteins and an electrostatic interaction between the particles and the proteins. These offer highly selective protein separation. In addition, their porous structure and anionic charge also make the particles promising candidates as drug carriers. The highly porous structure ensures a high loading capacity, which is important to reduce the dose of the carrier in clinical practice.

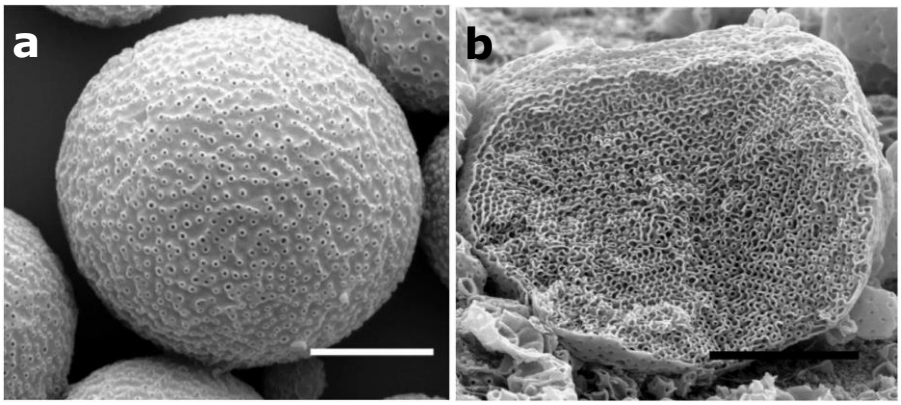


Figure 1.15. SEM images of PS-*b*-PAA (a) spherical particles with regular nanopores of high density, (b) cross-sectional image of the fractured porous particle. Scale bars represent 1 μm.[10]

The application of block copolymers as an active layer of photovoltaic cells appears in many reports.[50–54] This application uses a block copolymer that comprises electron donor and acceptor blocks. Using a block copolymer results in higher efficiency when compared to using its homopolymer blends.[51] This remarkable performance is due to the self-assembly of block copolymer into mesoscale lamellar morphologies primarily oriented perpendicular to the substrate.

Block copolymers have also been applied in nanolithography as an alternative to traditional lithography. In this application, a nanostructured block copolymer thin film is used as a template for preparing highly patterned nanostructures. Dense periodic hexagonally ordered arrays of $\sim 10^{11}$ holes can be obtained over 1 cm^2 area using this method.[55] In the microelectronics industry, IBM has applied such methods to produce semiconductor chips. These chips have remarkable performance (faster electrical signals) and consume 15% less energy than the most advanced chips produced by conventional techniques.[56,57]

Block copolymers have also been used as a template for preparing metal nanoparticle arrays. For example, PS-*b*-P2VP-*b*-PS triblock copolymer particles with tunable internal morphologies were used as a template to generate unique mesostructured silica and titania particles.[58] First, silica and titania precursors were attached to a particular domain of the block copolymer by using a structure-directing agent. The block copolymer template was then removed by calcination, resulting in a mesoporous structure with high fidelity of the original phase-separated block copolymer domains (Figure 1.16).

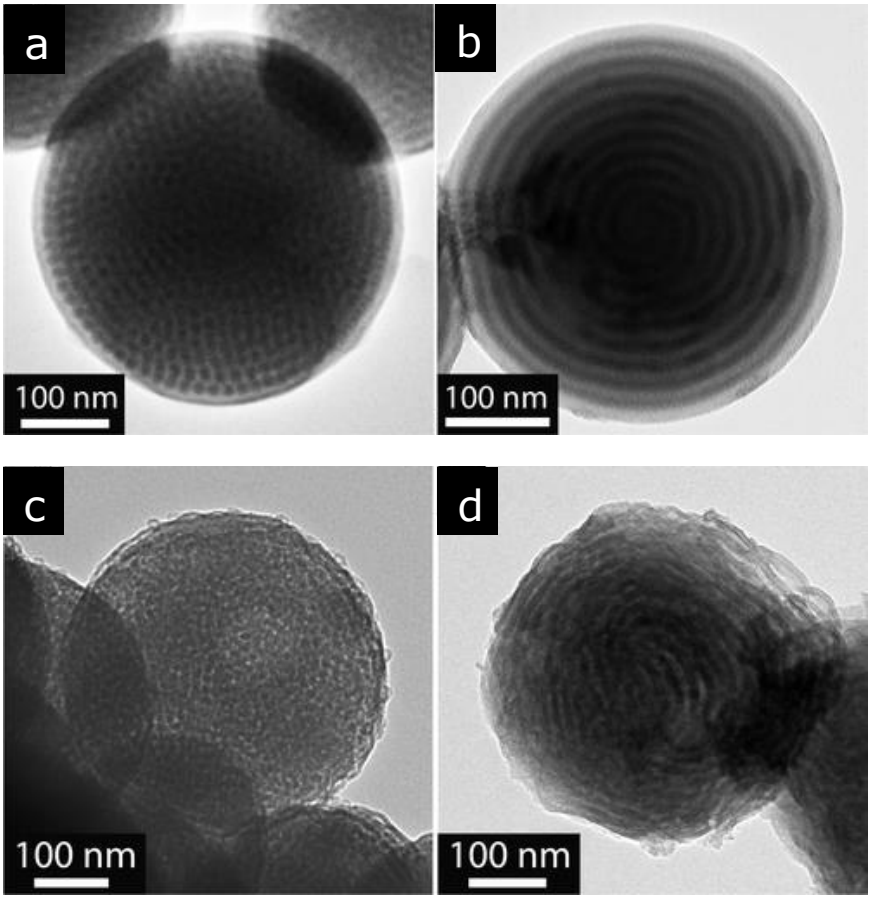


Figure 1.16. TEM images of (a) PS-*b*-P2VP-*b*-PS showing P2VP sphere in PS matrix, (b) lamellar structure of PS-*b*-P2VP-*b*-PS, (c) silica mesoporous nanoparticles obtained after removal of spherical PS-*b*-P2VP-*b*-PS block copolymer (image a) template, (d) titania nanoparticles in lamellar structure obtained after removal of lamellar PS-*b*-P2VP-*b*-PS block copolymer (image b) template.[58]

1.6 Supercritical Fluids

A fluid is stated to be in the supercritical state when its pressure and temperature exceed a certain critical state.[59] In this state, there is only a single phase existing, and neither a distinct liquid phase nor vapour phase occurs. The solvent power of a supercritical fluid (SCF) is strongly affected by the density, which can be adjusted by altering the temperature and pressure. A SCF exhibits liquid-like density, yet gas-like transport properties of diffusivity and viscosity.

1.6.1 Supercritical carbon dioxide

Supercritical CO_2 ($scCO_2$) is one kind of SCF that is non-toxic, non-flammable, and chemically inert. These properties allow $scCO_2$ to be used as a green material in chemical processes, especially as a promising alternative to noxious organic solvents. Critical conditions of CO_2 are relatively easy to obtain with a temperature of 31.1 °C and a pressure of 73.8 bars. The phase diagram for pure CO_2 is shown in Figure 1.17. CO_2 can exist either as a solid, liquid or gas. All there phases coexist at the triple point. By increasing the pressure and/or temperature from the triple point along the gas-liquid curve, the liquid becomes less dense due to thermal expansion. In contrast, the gas becomes denser at higher pressure. As a result, the density of the two phases becomes identical and there is no difference between the gas and the liquid. At the end of the coexistence curve, the critical point of CO_2 is reached. Since the density of a SCF depends on temperature and pressure variables, the SCF can be adjusted to have either gas- or liquid-like density by manipulating both variables.[60]

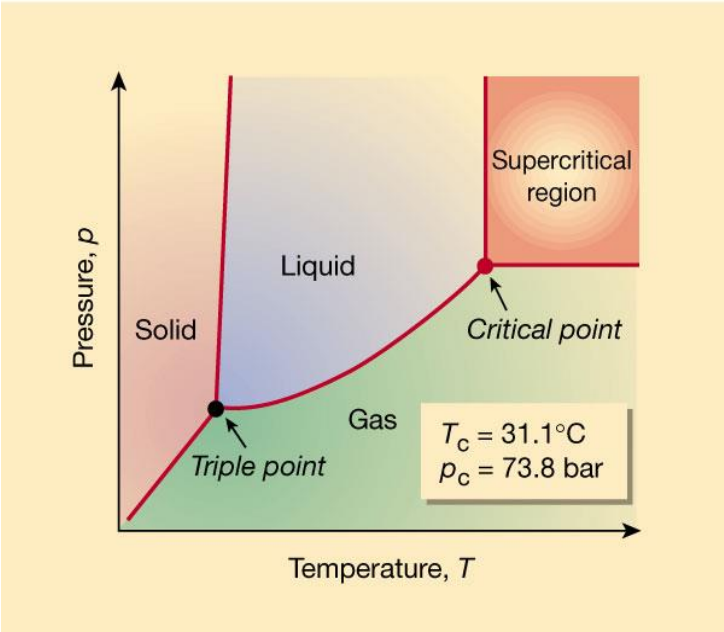


Figure 1.17 Phase diagram for pure carbon dioxide.[61]

$scCO_2$ has been used in various chemical processes such as extraction,[62] chromatography,[63] syntheses and processing of polymers,[17,64] as well as the synthesis of nanomaterials.[65,66] Chemical reactions using $scCO_2$ have been developed not only at the laboratory scale but also at the plant scale.[67] By using $scCO_2$, separation of the reaction products from the solvent can be achieved easily, simply by returning the system to room temperature and standard pressure. Under these conditions, gaseous CO_2 can easily be separated from the desired product.

1.6.2 Polymer properties in $scCO_2$

In general, CO_2 is a good solvent for small non-polar molecules, yet a very weak solvent for most polymers. Only a few polymers have shown good solubility in pure CO_2 under mild conditions; this includes fluoropolymers and polysiloxanes. Favourable interactions between CO_2 and the C-F bonds helps to solubilise fluoropolymers in CO_2.[60] Meanwhile, the solubility of polysiloxanes in CO_2 is likely due to the very flexible nature of these polymers that provides them with much larger free volumes as compared to other polymers.[68] The

solubility of polymers in CO_2 can be improved by altering their degree of polymerisation[68] or adding fluorinated groups[69,70]. For example, poly(propylene oxide) (PPO) is partially soluble in $scCO_2$,[71] but the solubility significantly increases upon fluorination to produce poly(hexafluoropropylene oxide) (PFPO).[69]

High viscosity is the main hindrance to processing a high molecular weight polymer. It may be overcome by processing at an elevated temperature since viscosity decreases with increasing temperature, but this may degrade the polymer. In addition, it consumes a large amount of energy. We can avoid this problem by using organic solvents to reduce the viscosity while the temperature remains low. Nevertheless, the solvent residue, product recovery, and the reactive nature of the solvents are major problems. The use of $scCO_2$ may be an alternative option since $scCO_2$ can lead to polymer plasticisation by lowering its glass transition temperature (T_g). In this way, the processing of polymers can be carried out at low temperatures, and hence degradation can be avoided.[72]

1.6.3 Polymerisation in $scCO_2$

Since the majority of polymers are not soluble in $scCO_2$ (at a modest temperature and pressure), most polymerisations in $scCO_2$ are carried out *via* heterogeneous polymerisations such as precipitation and dispersion polymerisation,[16,17,60,73,74] although examples of suspension and emulsion polymerisation have also been reported.[75,76]

Many polymerisation mechanisms have been employed, including radical, ring-opening, cationic and condensation polymerisations.[17] $scCO_2$ is unreactive to radicals[60], and hence the chain transfer to solvent that is often found with some commonly used organic solvents such as toluene can be negligible. Therefore, $scCO_2$ is an ideal solvent for radical polymerisation.

However, initiator decomposition[77] and polymerisation rates can be significantly altered in $scCO_2$. The versatility of free radical polymerisation in $scCO_2$ has been demonstrated by application to a range of monomers including MMA,[16] styrene,[78] *N*,*N*-dimethyl acrylamide,[79] *N*-vinyl pyrrolidone,[41] and a range of functional methacrylates.[80]

The difference in solubility between the monomer and polymers in $scCO_2$ is beneficial for purification after polymerisation. The unreacted monomer can be easily removed during depressurisation through a supercritical fluid extraction process, leaving the dry polymer product in the reactor. This can significantly reduce energy consumption and expensive work-up procedures.

1.6.4 Dispersion CLRP in $scCO_2$

RAFT,[9,74,81] NMP,[82–84] ATRP,[85,86] and other CLRP methods[87,88] now have been implemented in $scCO_2$ dispersion. RAFT dispersion polymerisation of MMA in $scCO_2$ was performed successfully for the first time by Howdle and coworkers.[81] PMMA was synthesised in the presence of a RAFT agent and stabiliser poly(dimethyl siloxane) monomethacrylate (PDMS-MA). The product was well-defined as spherical microparticles of PMMA with controlled molecular weight in high yields. This work was extended by a study on the effects of various RAFT agents to examine the effect of altering both the stabilising and leaving groups on molecular weight evolution and final polymer morphology.[74] Zong *et al* used a fluorinated polymer, poly(1H,1H,2H,2H-perfluorooctyl methacrylate) (PFOMA) as a macro RAFT agent and stabiliser for the dispersion polymerisation of MMA.[89] Polymerisation control was confirmed by low dispersity and good agreement between experimental and targeted molecular weight, while the formation of micron-size spherical particles indicated successful stabilisation of the dispersion. Jennings *et al* conducted one-pot

RAFT dispersion polymerizations in $scCO_2$ using a PDMS-MA stabiliser to prepare spherical diblock copolymer microparticles with various nanostructured morphologies.[9,33] A range of PMMA-based diblock copolymers were obtained with high blocking efficiencies. In some block copolymers, different degrees of CO_2 swelling between the blocks influence the formation of the internal nanostructure.

The first dispersion NMP in $scCO_2$ was performed to polymerise styrene using *N*-tert-butyl-*N*-(1-diethylphosphono-2, 2-dimethylpropyl) nitroxide (SG1) as a control agent at 100 °C and 420 bar.[82] A poly(dimethylsiloxane) (PDMS) based azo initiator was employed with dual function as an initiator and a stabiliser (inistab). The molecular weight increased linearly with conversion in reasonable agreement with the predicted values. The polymer chains' living character was demonstrated by successful chain extensions in bulk and solution. However, in many cases, the molecular weight distributions are rather broad. The product was obtained as non-spherical particles, possibly due to significant coagulation caused by imperfect stabilisation. Regarding the particle morphology, a better result was obtained when employing a different inistab.[83] The inistab comprised a PDMS and a PS block end capped with SG1 (PDMS-*b*-PS-SG1). In this attempt, sub-micron sized PS particles with narrow molecular weight distribution were obtained. Dispersion NMP in $scCO_2$ was also attempted for the synthesis of PMMA.[90] The synthesis was carried out at 70 °C and 300 bar in the presence of a small amount of styrene using BlocBuilder and PFDA-SG1 as an initiator and a stabiliser respectively. The latter species initiated MMA during the polymerisation to form PFDA-*b*-PMMA diblock copolymer stabiliser *in situ*. The formed particles varied in morphology depending on the targeted molecular weight. These included well-defined microspheres, quasi microspheres, and ones with an undefined morphology.

Dispersion ATRP of MMA in $scCO_2$ has been carried out using a fluorinated polymeric species which acted both as macroligands for the copper bromide and as steric stabilisers for the growing PMMA particles.[91] The same macroligand was also used in the ATRP synthesis of living PMMA chains.[85] These living PMMA chains could be extended by feeding more MMA after the first feed was consumed. A shift on GPC traces confirmed the chain extension, although a low molecular weight shoulder was also observed concerning the presence of some dead chains. The living PMMA could also be used to prepare poly(methyl methacrylate)-*b*-poly(2,2,2-trifluoroethyl methacrylate) (PMMA-*b*-PFMA) diblock copolymers. The formation of PMMA-*b*-PFMA block copolymers was confirmed by GPC, where the GPC trace of PMMA first block was shifted towards higher molecular weight as a result of the polymerisation of FMA. ATRP could also be combined with a click reaction to produce functional PMMA microspheres.[86] Functionalisation of PMMA by pyrene groups was successfully demonstrated, which resulted in fluorescent PMMA microspheres.

1.7 Summary and Research Aims

This chapter has introduced the key concepts applicable to this thesis including controlled/living radical polymerisations, heterogeneous polymerisations, phase separation behaviour and applications of block copolymers and finally the use of $scCO_2$ as a polymerisation medium. Chapter 2 provides a detailed description of the high pressure equipment, as well as the analytical techniques used throughout this thesis.

Chapter 3 aims to develop a new strategy to synthesise the nanostructured block copolymers in $scCO_2$ in a series of shorter independent steps, by exploiting the living character of RAFT polymer chains. The versatility of this approach is examined by application to a range of monomer classes.

The work is continued in Chapter 4, which investigates the block copolymer phase behaviour using the new high pressure X-ray autoclave, with *in situ* X-ray scattering experiments. This work aims to determine how and when the phase separation behaviour occurs in the $scCO_2$ dispersion. The new method developed in Chapter 3 will be used for this *in situ* experiment. Understanding this microphase separation behaviour offers a wider perspective for future application of block copolymers and for the first time allows this to be controlled in microparticles rather than in the usual thin films.

The success of controlled phase morphology in block copolymers prompted an investigation of introducing metal nanoparticles into a phase-separated block copolymer. This introduction might generate new properties and hence provide a wider application of the materials. Therefore, Chapter 5 aims to exploit the newly developed polymerisation method in the previous chapter to prepare such materials. The metal nanoparticle precursor is introduced during the polymerisation to generate phase-separated block copolymer microspheres which are internally decorated with metal nanoparticles.

1.8 References

1. Odian, G. *Principles of Polymerization*. 4th edition. John Wiley & Sons, Inc.: New Jersey, USA. (2004).
2. Schacher, F.H., Rupar, P.A. & Manners, I. *Angew. Chemie Int. Ed.* **51**, 7898–7921 (2012).
3. Mülhaupt, R. *Macromol. Chem. Phys.* **214**, 159–174 (2013).
4. Maitz, M.F. *Biosurface and Biotribology* **1**, 161–176 (2015).
5. Kim, H., Park, S. & Hinsberg, W.D. *Chem. Rev.* **110**, 146–177 (2010).
6. Jin, Z. & Fan, H. *Soft Matter* **10**, 9212–9219 (2014).
7. Yabu, H., Higuchi, T. & Jinnai, H. *Soft Matter* **10**, 2919–2931 (2014).
8. Jennings, J., He, G., Howdle, S.M. & Zetterlund, P.B. *Chem. Soc. Rev.*

45, 5055–5084 (2016).

9. Jennings, J. et al. *J. Am. Chem. Soc.* **134**, 4772–4781 (2012).

10. Yu, H., Qiu, X., Nunes, S.P. & Peinemann, K.V. *Nat. Commun.* **5**, 4110 (2014).

11. Choi, S.-J., Ku, K.H., Kim, B.J. & Kim, I.-D. *ACS Sensors* **1**, 1124–1131 (2016).

12. Jiang, K. et al. *ACS Appl. Mater. Interfaces* **8**, 25529–25534 (2016).

13. Stefik, M., Guldin, S., Vignolini, S., Wiesner, U. & Steiner, U. *Chem. Soc. Rev.* **44**, 5076–5091 (2015).

14. Moad, G. et al. *Macromol. Symp.* **182**, 65–80 (2002).

15. Moad, G. & Solomon, D.H. *The Chemistry of Radical Polymerization*. Elsevier: Oxford, UK (2006).

16. DeSimone, J.M. et al. *Science.* **265**, 4 (1994).

17. Kendall, J.L., Canelas, D.A., Young, J.L. & DeSimone, J.M. *Chem. Rev.* **99**, 22 (1999).

18. Wood, C.D., Cooper, A.I. & DeSimone, J.M. *Curr. Opin. Solid State Mater. Sci.* **8**, 325–331 (2004).

19. Song, J.S. & Winnik, M.A. *Macromolecules* **39**, 8318–8325 (2006).

20. Scorah, M.J., Cosentino, R., Dhib, R. & Penlidis, A. *Polym. Bull.* **57**, 157–167 (2006).

21. Cowie, J.M.G. & Arrighi, V. *Polymers: Chemistry and Physics of Modern Materials*. CRC Press: Boca Raton, Florida (2008).

22. Davies, O.R. et al. *Adv. Drug Deliv. Rev.* **60**, 373–387 (2008).

23. Wang, Y., Chen, K.S., Mishler, J., Cho, S.C. & Adroher, X.C. *Appl. Energy* **88**, 981–1007 (2011).

24. Ling, Q.D. et al. *Prog. Polym. Sci.* **33**, 917–978 (2008).

25. Szwarc, M. *Nature* **178**, 1168 (1956).

26. Chong, (Bill) Y K, Le, T.P.T., Moad, G., Rizzardo, E. & Thang, S.H. *Macromolecules* **32**, 2071–2074 (1999).

27. Keddie, D.J. *Chem. Soc. Rev.* **43**, 496–505 (2014).

28. Quirk, R.P. & Lee, B. *Polym. Int.* **27**, 359–367 (1992).

29. McKenzie, T.G. et al. *Adv. Sci.* **3**, 1–9 (2016).

30. Chapman, R., Gormley, A.J., Herpoldt, K.-L. & Stevens, M.M. *Macromolecules* **47**, 8541–8547 (2014).

31. Zhang, B. et al. *Macromolecules* **48**, 7792–7802 (2015).

32. Canning, S.L., Smith, G.N. & Armes, S.P. *Macromolecules* **49**, 1985–2001 (2016).

33. Jennings, J. et al. *Macromolecules* **46**, 6843–6851 (2013).

34. Herk, A.M. van & Monteiro, M. Heterogeneous Systems. *Handbook of Radical Polymerization.* Ed. Krzysztof Matyjaszewski, Ed. Thomas P. Davis. Wiley-Interscience: New York. 301-332. (2002).

35. Carraher, C.E. *Polymer Chemistry*. Marcel Dekker Inc.: New York (2003).

36. Woods, H.M., Nouvel, C., Licence, P., Irvine, D.J. & Howdle, S.M. *Macromolecules* **38**, 3271–3282 (2005).

37. Sugihara, S., Blanazs, A., Armes, S.P., Ryan, A.J. & Lewis, A.L. *J. Am. Chem. Soc.* **133**, 15707–15713 (2011).

38. Zehm, D., Ratcliffe, L.P.D., Armes, S.P., Ratcliffe, L.P.D. & Armes, S.P. *Macromolecules* **46**, 128−139 (2013).

39. Kawaguchi, S. & Ito, K. Dispersion Polymerization. *Advances in Polymer Science: Polymer Particles*. Ed. Masayoshi Okubo. Springer: Heidelberg, Germany. 299-328. (2005).

40. Park, E.J. et al. *Polymer.* **52**, 5403–5409 (2011).

41. Birkin, N.A., Arrowsmith, N.J., Park, E.J., Richez, A.P. & Howdle, S.M. *Polym. Chem.* **2**, 1293–1299 (2011).

42. Birkin, N.A., Wildig, O.J. & Howdle, S.M. *Polym. Chem.* **4**, 3791–3799 (2013).

43. McAllister, T.D., Farrand, L.D. & Howdle, S.M. *Macromol. Chem. Phys.* **217**, 2294–2301 (2016).

44. Gregory, A. & Stenzel, M.H. *Prog. Polym. Sci.* **37**, 68 (2012).

45. Bates, F.S. *Science.* **251**, 898–905 (1991).

46. Bates, F.S. & Fredrickson, G.H. *Annu. Rev. Phys. Chem.* **41**, 525–557 (1990).

47. Bates, F.S. & Fredrickson, G.H. *Phys. Today* **52**, 32–38 (1999).

48. Hadjichristidis, N., Pispas, S. & Floudas, G. *Block Copolymers: Synthetic Strategies, Physical Properties, and Application*. Wiley-VCH: New Jersey, USA (2003).

49. Khandpur, A.K. et al. *Macromolecules* **28**, 8796–8806 (1995).

50. Sary, N. et al. *Adv. Mater.* **22**, 763–8 (2010).

51. Guo, C. et al. *Nano Lett.* **13**, 2957−2963 (2013).

52. Lee, Y. & Gomez, E.D. *Macromolecules* **48**, 7385–7395 (2015).

53. Guo, C. et al. *Macromolecules* **49**, 4599–4608 (2016).

54. Grieco, C. et al. *J. Phys. Chem. C* **120**, 6978–6988 (2016).

55. Park, M. *Science.* **276**, 1401–1404 (1997).

56. Black, C.T. et al. *IBM J. Res. Dev.* **51**, 605–633 (2007).

57. http://www-03.ibm.com/press/us/en/pressrelease/21473.wss. 19/05/2016

58. Connal, L.A. et al. *Chem. Mater.* **24**, 4036–4042 (2012).

59. Darr, J.A. & Poliakoff, M. *Chem. Rev.* **99**, 495–541 (1999).

60. Cooper, A.I. *J. Mater. Chem.* **10**, 207–234 (2000).

61. Leitner, W. *Nature* **405**, 2 (2000).

62. Ruen-ngam, D., Shotipruk, A., Pavasant, P., Machmudah, S. & Goto, M. *Chem. Eng. Technol.* **35**, 255–260 (2012).

63. Taylor, L.T. *Anal. Chem.* **82**, 4925–4935 (2010).

64. Erdmenger, T., Guerrero-Sanchez, C., Vitz, J., Hoogenboom, R. & Schubert, U.S. *Chem. Soc. Rev.* **39**, 17 (2010).

65. Sanli, D., Bozbag, S.E., Erkey, C., Sanli, D. & Erkey, C. *J. Mater. Sci.* **47**, 3469–3492 (2012).

66. Hasell, T., Thurecht, K.J., Jones, R.D.W., Brown, P.D. & Howdle, S.M. *Chem. Commun.* **38**, 3933–3935 (2007).

67. Licence, P., Ke, J., Sokolova, M., Rossb, S.K. & Poliakoff, M. *Green Chem.* **5**, (2003).

68. Kirby, C.F. & McHugh, M.A. *Chem. Rev.* **99**, 565–602 (1999).

69. Hoefling, T., Stofesky, D., Reid, M., Beckman, E. & Enick, R.M. *J. Supercrit. Fluids* **5**, 237–241 (1992).

70. Girard, E. et al. *J. Am. Chem. Soc.* **134**, 11920–11923 (2012).

71. O'Neill, M.L. et al. *Ind. Eng. Chem. Res.* **37**, 3067–3079 (1998).

72. Curia, S., Focatiis, D.S.A. De & Howdle, S.M. *Polymer.* **69**, 17–24 (2015).

73. Romack, T.J., Maury, E.E. & DeSimone, J.M. *Macromolecules* **28**, 912–915 (1995).

74. Gregory, A.M., Thurecht, K.J. & Howdle, S.M. *Macromolecules* **41**, 1215–1222 (2008).

75. Adamsky, F.A. & Beckman, E.J. *Macromolecules* **27**, 312–314 (1994).

76. Bratton, D., Brown, M. & Howdle, S.M. *Macromolecules* **36**, 5908–5911 (2003).

77. Guan, Z., Combes, J.R., Menceloglu, Y.Z. & DeSimone, J.M. *Macromolecules* **26**, 2663–2669 (1993).

78. Canelas, D.A., Betts, D.E. & DeSimone, J.M. *Macromolecules* **29**, 2818–2821 (1996).

79. Galia, A., Muratore, A. & Filardo, G. *Ind. Eng. Chem. Res.* **42**, 448–455 (2003).

80. Giles, M.R., Griffiths, R.M.T., Irvine, D.J. & Howdle, S.M. *Eur. Polym. J.* **39**, 1785–1790 (2003).

81. Thurecht, K.J., Gregory, A.M., Wang, W. & Howdle, S.M. *Macromolecules* **40**, 2965–2967 (2007).

82. Ryan, J., Aldabbagh, F., Zetterlund, P.B. & Okubo, M. *Polymer.* **46**, 9769–9777 (2005).

83. McHale, R., Aldabbagh, F., Zetterlund, P.B. & Okubo, M. *Macromol. Rapid Commun.* **27**, 1465–1471 (2006).

84. Aldabbagh, F., Zetterlund, P.B. & Okubo, M. *Macromolecules* **41**, 2732–2734 (2008).

85. Grignard, B. et al. *Macromolecules* **41**, 8575–8583 (2008).

86. Grignard, B., Calberg, C., Jerome, C. & Detrembleur, C. *J. Supercrit. Fluids* **53**, 151–155 (2010).

87. Taniyama, T., Kuroda, T., Minami, H. & Okubo, M. *Polym J* **44**, 1082–1086 (2012).

88. Kuroda, T. et al. *Polymer.* **53**, 1212–1218 (2012).

89. Zong, M., Thurecht, K.J. & Howdle, S.M. *Chem. Commun.* **45**, 5942–5944 (2008).

90. Grignard, B. et al. *Polym. Chem.* **1**, 837–840 (2010).

91. Grignard, B. et al. *Chem. Commun.* **3**, 314–316 (2008).

Chapter 2 Experimental Technique

2.1 Overview

This chapter describes the experimental apparatus and analytical techniques used throughout this thesis. The high pressure equipment is outlined in the first half of this chapter. This details the general set-up of the equipment and the reactors used to conduct dispersion polymerisation in supercritical CO_2 ($scCO_2$). The standard operating procedure for all equipment is also presented in this section. The second half of this chapter presents the analytical techniques for the characterisation of all products synthesised in this thesis.

2.2 High Pressure Equipment

2.2.1 General Set Up

General set-up for all high pressure experiments consists of a CO_2 pump, a reaction vessel, associated pipe work, and electronics. The CO_2 pump, a PM-101 high pressure pump (New Ways of Analytics, Germany), was used to generate pressure and distribute CO_2 to individual fume hoods where the reaction vessel, a high pressure autoclave, was placed. A series of Swagelok pipes and fitting was used to connect the pump and the autoclave. The autoclave was equipped with pressure and temperature monitors and an electrical trip system.

In order to control the CO_2 flow, HIP (High Pressure Equipment Co.) valves were used. Non-return valves (NRV) were placed before each autoclave to allow only one direction of the CO_2 flow. This is not only prevented the risk of contamination of reagents transported from one autoclave to another

through a pressure differential but also avoided reagents flowing back into the main line. Figure 2.1 is a simplified schematic set-up where the CO_2 cylinder and CO_2 pump are linked to the autoclave.

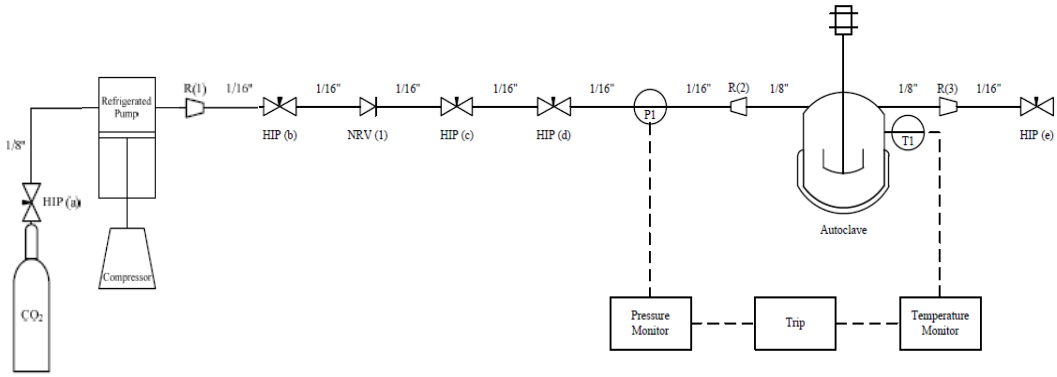


Figure 2.1. Schematic diagram for high pressure equipment set-up, showing how the CO_2 cylinder and CO_2 pump connected to the autoclave.

2.2.2 60 mL High Pressure Autoclave

A high pressure autoclave, made from stainless steel 316, was designed in-house for polymerisations in supercritical CO_2 ($scCO_2$) with maximum working pressure is 300 bar and 300 °C. A schematic representation and a digital image of the autoclave are shown in Figure 2.2.

The autoclave consists of two main parts, the head and the body. The head with magnetically-coupled stirrer column (1) contains the required port for CO_2 inlet and outlet, reagents addition, and monitoring purposes (2). The body with the detachable heating band is the bulk volume of the reactor. These two parts were sealed by a polymeric O-ring (EPDM, Ethylene Propylene Diene Monomer) (3) and then clamped (4) together and tightened with a screw mechanism which was turned with a unique key (5) until hand tight. This key was then screwed into the autoclave head to create a final seal before pressurising the autoclave. This assembly provides two safety features; firstly

that the clamp cannot be undone whilst the autoclave is under pressure. Secondly, in the event of outlet valve blockage during venting process the key can be loosened slowly with the residual pressure being released *via* the vent hole (6).

The temperature within the autoclave was monitored by a thermocouple (K-type, RS Components) (10) which was connected to the external heating band (Watlow) (11) and controlled using a Cal 3200 digital heating controller (RS, UK), allowing the temperature to be changed as required. The pressure was monitored by a quartz piezoelectric transducer (345 bars, RDP Electronics) and connected to an in-house digital read-out. In the event of the pressure exceeding the maximum limit (300 bars), an electrical trip was incorporated which disconnects power to the heating band, reducing the temperature and subsequently the pressure. The shaft of the stirrer (8) extends down into the main body of the autoclave where it was attached to a stirrer blade (9) allowing for the efficient mixing of the reaction contents. The stirrer was driven by a stirring motor (IKA Eurostar Digital) with stirring rates of between 50 and 2000 rpm.

A standard procedure was applied for all the reactions in the autoclave with some modifications to the methods depending on the type of reaction required. The procedure below is referred to Figure 2.1. Before a reaction was conducted the HIP d and HIP e were initially closed. HIP 1 and HIP 2 were always open and only closed when the CO_2 cylinder needed to be exchanged. The procedure for the polymerisation is as follows:

1. The autoclave was set up carefully and leak-tested prior to use with CO_2 (*ca* 183 bar) to check all the fittings were secured correctly.

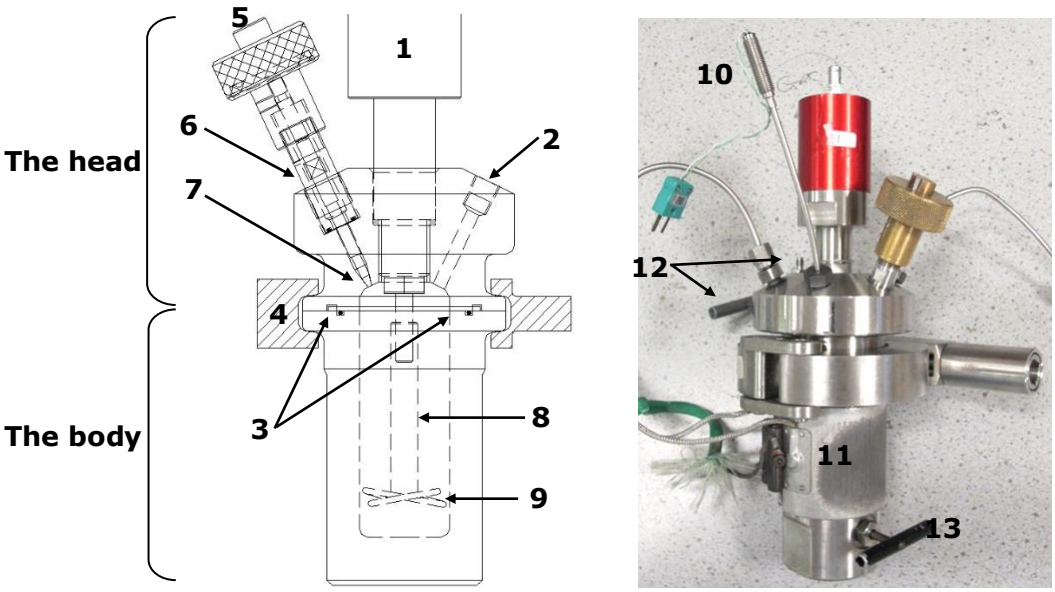


Figure 2.2. Schematic representation (left) and image (right) of a 60 mL high pressure autoclave. (1) overhead stirrer, (2) inlet/outlet/monitoring port, (3) O-ring, (4) Clamp, (5) key and torque thumbwheel, (6) vent hole, (7) safety needle, (8) stirrer shaft, (9) stirrer blade, (10) thermocouple, (11) heating band, (12) built-in HIP valve and Swagelok port to connect to HPLC set-up, (13) built-in HIP valve for sample collection.

2. In the event of a leak, the autoclave was depressurised by opening HIP e to atmospheric pressure, any leaking fittings adjusted and then step 1 was repeated. Fittings were never tightened while the autoclave was under pressure. Then any remaining gas was vented through HIP e until the vessel was at atmospheric pressure.
3. HIP e was closed. The safety key was unscrewed and the autoclave was purged with CO_2 (*ca* 2.0 bars) for 30 minutes by opening HIP d to remove the residual oxygen.
4. The required reagents i.e. monomer, initiator etc. were added into the autoclave through the open key hole under positive pressure of CO_2 to ensure no oxygen entered the vessel.

5. The safety key was added into the head unit to seal the system. HIP d was opened to add CO_2 to the autoclave to *ca* 55 bar. HIP d was then closed. The stirrer was turned on and set to the desired speed, 300 rpm.
6. The internal thermocouple and heating band were connected to the control box and set to the desired temperature with the pressure monitored throughout.
7. HIP d was opened slowly to add CO_2 if necessary, to reach the final reaction pressure (typically 275 bar). The HIP d was then closed and the reaction was allowed to run for as long as required.
8. Once the reaction time had elapsed, the autoclave was allowed to cool to room temperature by switching off the heater. HIP e was then opened to allow the CO_2 to escape. Once atmospheric pressure was reached (1.0 bar) the clamp was removed, the autoclave was opened and the product was collected.

2.2.3 60 mL High Pressure Autoclave with Additional Valves

A modified autoclave has also been developed to allow additional functions to be carried out whilst still under pressure. Two built-in HIP valves were added. The HIP valve in the head, to which a reducing union could be added (12), allows attachment of additional piping through which monomer or other liquid reagents could be added. The HIP valve in the body (13) allowed attachment of a small sample tube (~0.1 mL volume) so that samples could be taken during the reaction.

2.2.3.1 In-situ Monomer Addition via HPLC Pump

In order to allow addition of the second monomer during a block copolymer synthesis, an HPLC pump (Jasco PU980) was connected to the

system through the reducing union and the additional HIP valve attached in the head. A pipe schematic is shown in Figure 2.3.

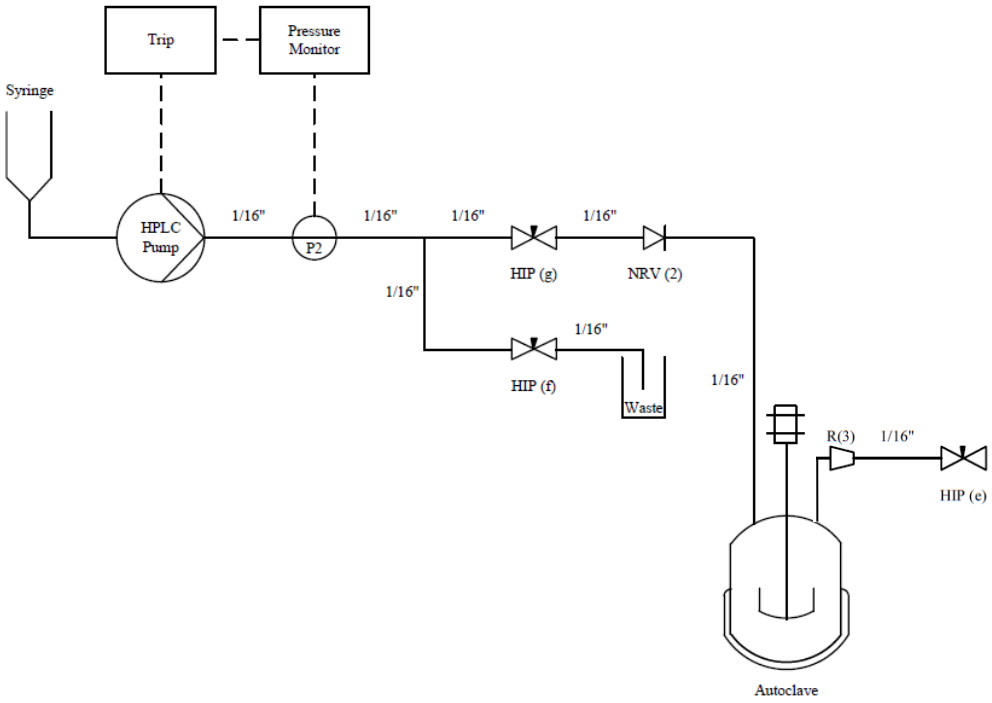


Figure 2.3. HPLC set up diagram

The following is standard operating procedure for monomer addition *via* an HPLC pump, referred to Figure 2.3.

1. The system was left at 275 bar and 65 °C for the desired time, following the procedure in section 2.2.2.
2. The autoclave was depressurised (if necessary) to ~200 bar, depending on the amount of reagents to be added, by opening HIP e. This enables space to be created for the addition of the second monomer which would have increased the pressure above the safety limit (300 bar).
3. HPLC pump outlet was connected to the addition port in the autoclave head.
4. The monomer-initiator solution was transferred to syringe attached to HPLC inlet.

5. The pump was primed by opening HIP f, ensuring valve leading to the autoclave (HIP g) were closed. Monomer solution was then flowed through the line for a few second.
6. Pump was stopped, HIP f was closed and the additional valve in the autoclave head was opened. A pressure drop should be observed on the autoclave transducer.
7. HIP g was opened while monitoring back pressure on the HPLC pump display.
8. The monomer solution was pumped at 1 ml min^{-1} until the HPLC pressure approximately equals the pressure inside the autoclave.
9. The monomer level in the syringe was noted and the desired amount of the monomer solution was added, taking into account the dead volume between the entry pipe and the autoclave head (usually 1 mL). The autoclave pressure was monitored throughout.
10. The pump was stopped when the desired volume reached and addition valve on the autoclave head was closed. HIP 6 was opened to release residual pressure from pump.
11. The HPLC set-up was detached from the autoclave. Some monomer solution was still in the pipe, so the fitting was opened in a fume hood slowly to release residual pressure.
12. The pressure inside autoclave was monitored and no more CO_2 was added at this point as a pressure increase lag may occur.
13. The HPLC pipes were flushed with solvent, typically acetone, to prevent residual monomer solution polymerising in the pipes. HPLC pipes were flushed with air to remove solvent before next use.
14. If necessary, more CO_2 was added into the autoclave to increase the reaction pressure.

2.2.3.2 Sampling under pressure

In order to allow sampling under pressure, a sampling tube was inserted into the cavity at the bottom of the autoclave and secured in place by an autoclave engineer nut. The sampling valve (13, Figure 2.2) was then opened for ~10 s, before being closed again and the sampling tube removed. Normally, three to five aliquots were taken at each time interval. The first was discarded, and the following four samples were collected for analysis.

2.2.4 High Pressure X-ray Autoclave (MKII)

A high pressure X-ray autoclave was developed from the standard 60 mL autoclave presented in section 2.2.2. The main difference is the addition of an optical part for X-ray measurement i.e. two diamond windows housed in the body of the autoclave. Figure 2.4 showed the scaled engineering drawing of the X-ray autoclave.

This autoclave was assembled from AISI 316/316L EN1.4401/4404 certified stainless steel. Like the standard autoclave, this autoclave also comprised two main parts, the head and the body. The head is basically similar to the head of the standard autoclave. Therefore, the main modification was made in the body. Two diamond windows, made of a synthetic single crystal diamond (Element 6), were housed in this section. The windows were of 6 mm diameter where 2 mm of its external diameter was coated with AU/Sn (80/20). Thus, the clear optical aperture of the windows was 4 mm.

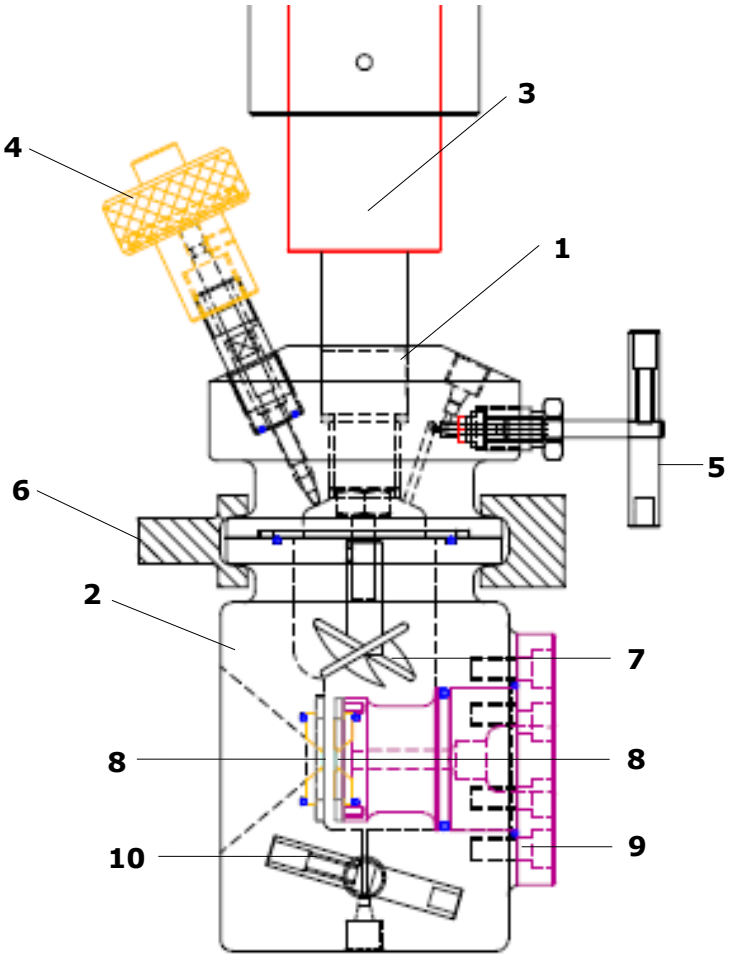


Figure 2.4. The scaled engineering drawing of the X-ray autoclave. (1) head, (2) body, (3) overhead magnetic stirrer, (4) torque thumbwheel with safety needle assembly, (5) built-in valve for the second monomer addition, (6) clamp, (7) stirrer blade, (8) diamond windows, (9) screwed window holder, (10) built-in valve for sample collection.

One window was sealed by an EPDM O-ring and screwed on the body (1, Figure 2.5), whilst the other one was screwed in the detachable holder (2, Figure 2.5). This detachable holder provided easy collecting of product and cleaning after finishing a reaction. Moreover, it is interchangeable, enabling different experimental modes such as Grazing-Incident SAXS (GISAXS). The opening angle for the window is 40°, which allows simultaneous SAXS/WAXS measurements. The optical path length between the windows is 2.0 - 2.5 mm.

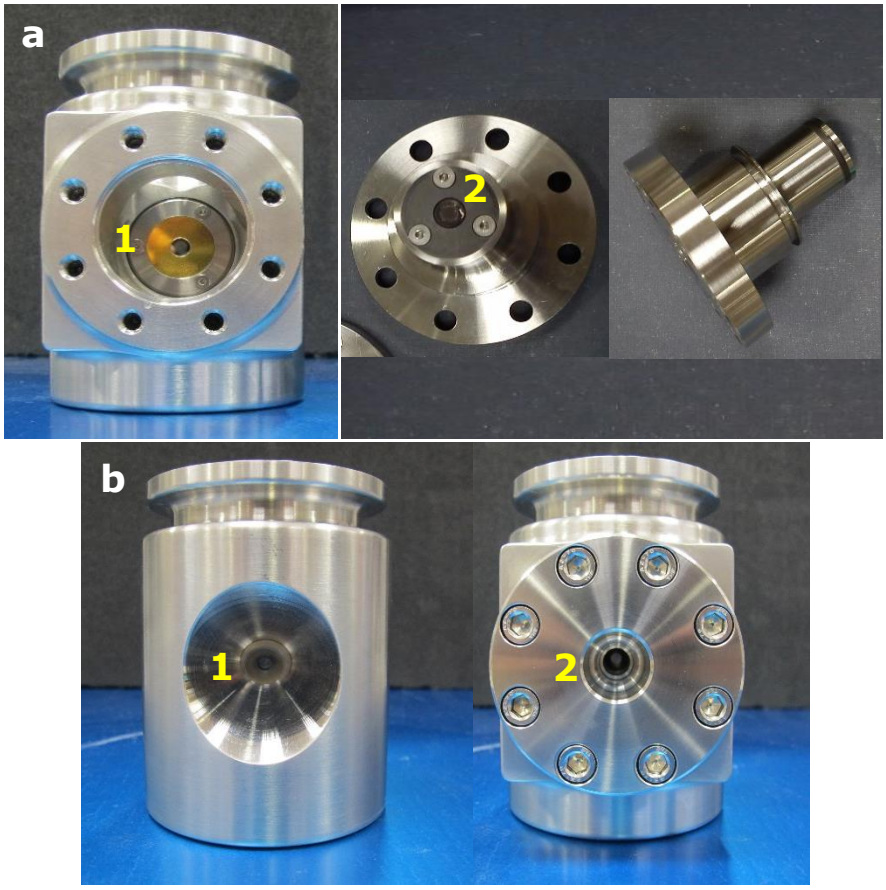


Figure 2.5. Images of (a) diamond windows, one is screwed on the body holder (1) and one is screwed on the detachable holder (2), (b) the holder screwed on the body.

The head and the body were joined using clamp mechanism as in the standard autoclave with EPDM O-ring to seal between them. The clamp was tightened using a safety key which was used as the final seal for preventing the vessel being opened whilst under pressure. The autoclave has a maximum working pressure equal to the standard autoclave (300 bar) with a maximum temperature of 120°C.

The internal temperature was regulated by means of an external heating box controlled to ± 1 °C using a Cal 3200 digital heating controller (RS, UK). The reaction conditions were monitored *via* an internal thermocouple (K-type, RS Components) and external pressure transducers (type A-105

transducer, 690 bars maximum, RDP Electronics). An HIP valve was also be housed at the base of the body to allow samples to be taken during reaction. HIP high pressure valves and Swagelok tubing and fittings were adopted to connect the system to the CO_2 pump, which was a high pressure PM101 pump (New Ways of Analytics, Germany).

For experiments in the x-ray beamline, two set of autoclaves were prepared so that two measurements can be ran in parallel. The autoclaves were placed on the stage equipped with robotic motor to assist the alignment process and move between the two autoclaves during the measurement (Figure 2.6b). An HPLC pump (JASCO PU-980) was connected for the addition of the second monomer. The pumps and controllers were placed on a trolley for mobility between laboratories.

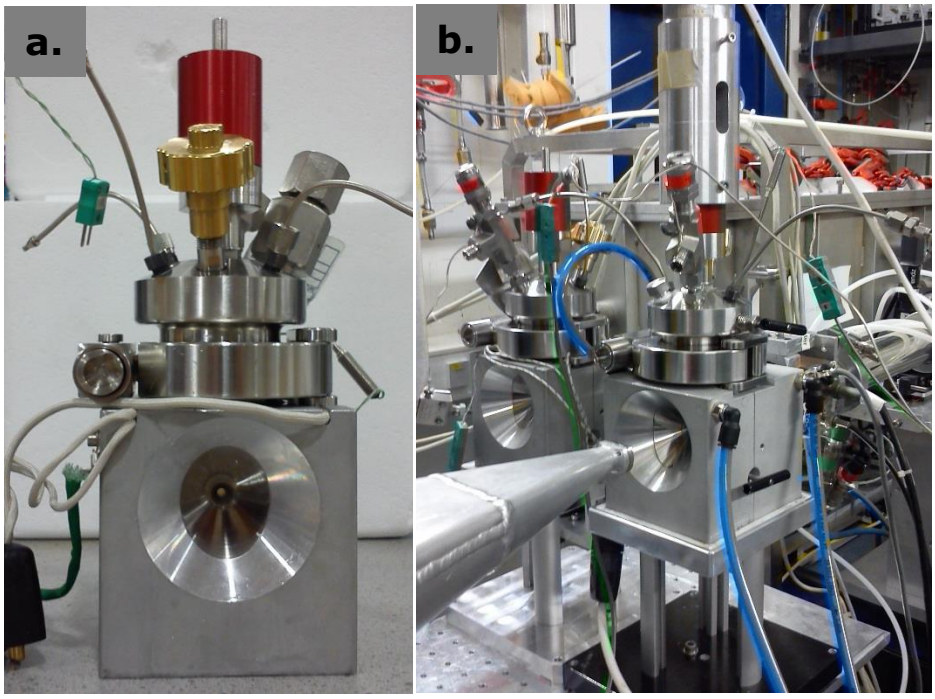


Figure 2.6. (a) Images of the X-ray autoclave with heating box and (b) the autoclaves aligned in the beamline.

The operational integrity of the vessel was protected by two safety devices. The first one is a pre-set spring-loaded relief valve, set to 320 bar to protect the working integrity of the autoclave. The second is a 350 bar rupture disc to protect the structural integrity of the cell.

The reactions performed in the X-ray autoclave follow the same SOP as for the standard autoclave, although differences in the heating must be noted. The temperature control is based on the external heating box, therefore this must be set higher than the desired temperature to ensure that the internal temperature reaches this value. The heating step took longer than that for the normal autoclave owing to the increased wall thickness. The following is the SOP for the X-ray autoclave, referred to Figure 2.7.

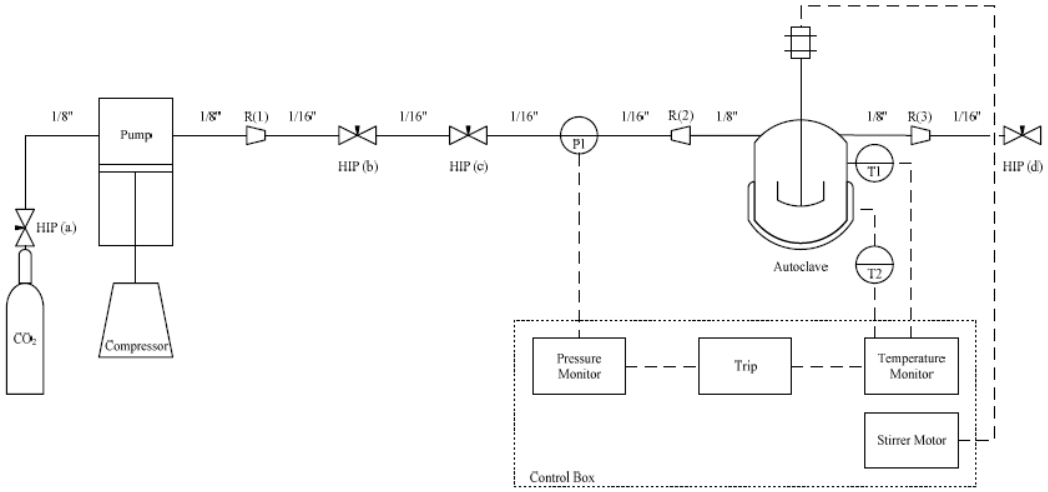


Figure 2.7. Schematic diagram of the pipelines for the X-ray scattering autoclave.

1. The autoclave was assembled carefully and all the fittings were tightened, ensuring an EPDM O-ring was in the autoclave body.
2. All pipe work was secured to avoid whipping of the pipes.

3. The setup was pressurised to ~55 bars in order to leak-test the set-up by opening HIP 2 and HIP 3 slowly to add CO_2 and then increased gradually to ~180 bars. All the taps were fully closed then all fittings were checked for leaks with 'Snoop' from Swagelok.
4. In the event of a leak, the cell was vented through the outlet valve (HIP 4) and any leaking fittings were adjusted and step 3 is repeated. Fittings were never tightened while the autoclave was under pressure. Then any remaining gas was vented through HIP 4 until the cell was at atmospheric pressure.
5. The HIP 4 was closed. The safety needle was removed and the autoclave was purged with CO_2 (ca 2.0 bar) for ~30 minutes to remove the residual oxygen.
6. The required reagents i.e. monomer, initiator etc. were added into the autoclave through the key hole under positive pressure of CO_2 to ensure no oxygen entered the vessel
7. The safety key was inserted and sealed by turning clockwise. The vessel was charged with around 48 bar of CO_2 by opening HIP 3. The stirrer was turned on to achieve the desired speed.
8. The heating box was turned on to the desired temperature. The pressure in the vessel was monitored constantly throughout this process (T2).
9. The autoclave was allowed to reach its final temperature, adjusting the set temperature so the internal thermocouple (T1) was at the desired reaction temperature. The pressure in the vessel was monitored constantly throughout this process (T2).
10. Once the temperature had been reached, the pressure was topped up to its final pressure. This process caused the autoclave to cool slightly, so the temperature was allowed to stabilise after each addition of CO_2. HIP 3 was then closed and the reaction was left to run as long as required.

11. Once the reaction time had elapsed, the autoclave was allowed to cool to room temperature by turning off the heater. HIP 4 was then opened to vent the autoclave. Once ambient temperature and pressure were reached, the key was unscrewed, the clamp was removed and the autoclave was opened.

For HPLC addition of the second monomer, the SOP was similar to the standard autoclave (subsection 2.2.3.1). The only difference was that the monomer was not added through the top but through the exit line (HIP 5 in Figure 2.3).

2.3 Analytical Techniques

2.3.1 Gel Permeation Chromatography

One of the vital instruments in the characterisation of polymer is Gel Permeation Chromatography (GPC), also known as Size Exclusion Chromatography (SEC). This instrument is used to determine the molecular weight and the molecular weight distribution of polymers, parameters which influence the polymer properties.

In this thesis, the GPC analysis is carried out on either an Agilent GPC with Wyatt modules for Multi-Angle Light Scattering (MALS) detection (DAWN 8^+) or another Agilent GPC with Wyatt module for Refractive Index (RI) detection (Optilab rEX). The former GPC uses THF (HPLC grade, Fisher) as the eluent. The elution was carried out at a flow rate of 1 mL min^{-1} through a guard column and two PL PolarGel-M columns in series. The latter uses chloroform (HPLC grade, Aldrich) as the eluent and eluted through a guard column (Shodex K-G) and two separation columns (Shodex K-805L and Shodex HT-803) in series. Samples were dissolved in the solvent at approximately 10 – 20 mg mL^{-1} and filtered prior to injection through 0.2 μm PTFE syringe filters

(Whatman). Responses from the detector were analysed using Astra 6.1 software.

The response of a light scattering detector is very dependent on the refractive index increment (dn/dc) i.e. the degree by which the refractive index of a solution varies as the concentration of the solute changes. Therefore, a dn/dc value for each sample is required to calculate the absolute molecular weight. In this work, dn/dc values were obtained from either the literature or by measurement. The dn/dc measurement was conducted using a Wyatt Optilab rEX differential refractometer. A series of solutions was prepared in THF at copolymer concentrations of 1, 2, 3, 4, and 5 mg ml^{-1} and one blank solution. The solution was injected consecutively into the instrument started with blank solution and followed by the copolymer solution from the lowest concentration. Figure 2.8 illustrates a typical data set obtained for PMMA-*b*-PS block copolymer sample. Plotting a calibration graph of dRI against copolymer concentration allows the dn/dc to be calculated directly from the linear gradient.

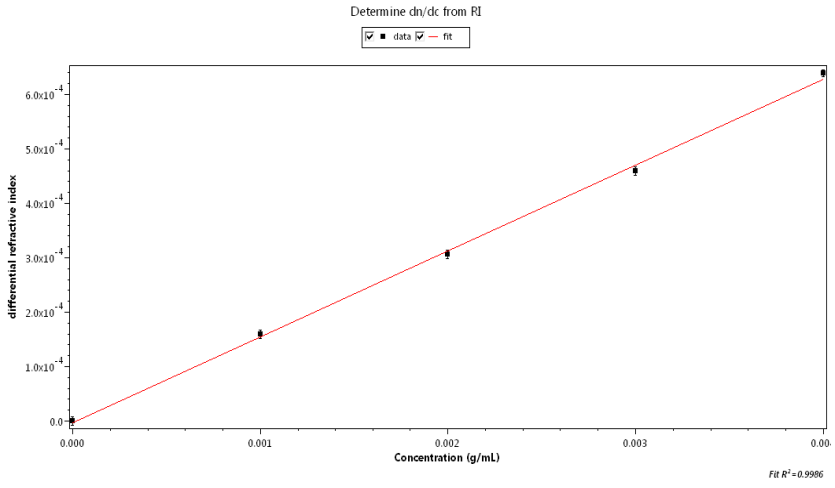


Figure 2.8. Plot of dRI vs PMMA-*b*-PS concentration, which is subsequently used to calculate the dn/dc value for the block copolymer.

2.3.2 Nuclear Magnetic Resonance Spectroscopy

Proton Nuclear Magnetic Resonance (^{1}H NMR) was used in this thesis to verify the presence of polymer and monomer and determine the composition of block copolymers. The composition is presented as a weight fraction of PMMA block (w_{PMMA}) relative to the second block. Spectra were obtained on a Bruker DPX 300 MHz spectrometer. Samples were dissolved in deuterated chloroform ($CDCl_3$) at a concentration of 1 mg mL^{-1}. Characteristic signals for the monomer and polymer (Table 2.1) were integrated and applied in the calculation.

Table 2.1. List of ^{1}H NMR chemical shift regions for monomers and polymers used in this thesis

Polymer	Monomer chemical shift in $CDCl_3$ (ppm)	*n*H	Polymer chemical shift in $CDCl_3$ (ppm)	*n*H
PMMA	3.8	3	3.6	3
PBzMA	5.2	2	4.8–5.1	2
PS	5.2-5.3	1	6.2-7.2	5
PDEA	5.6	1	2.8-3.2	5
PDMAEMA	4.2-4.4	2	3.9-4.2	2

The weight ratio of PMMA (w_{PMMA}) within a block copolymer was calculated by first integrating polymer peaks of each block (Table 2.1). Peak intensities (I_{block}) were then normalised with respect to the number of protons (nH_{block}) to give the PMMA mol fraction (nf_{PMMA}) (Equation 2.1).

$$nf_{PMMA} = \frac{I_{PMMA}/nH_{PMMA}}{I_{PMMA}/nH_{PMMA}+I_{block2}/nH_{block2}} \qquad \text{(Equation 2.1)}$$

From DPf_{PMMA}, PMMA weight ratio (w_{PMMA}) was then calculated by taking into account the monomer molar masses (Mr_{PMMA} and $Mr_{monomer2}$) (Equation 2.2).

$$w_{PMMA} = \frac{nf_{PMMA}xMr_{MMA}}{nf_{PMMA}xMr_{MMA}+nf_{block}xMr_{monomer2}} \qquad \text{(Equation 2.2)}$$

2.3.3 Scanning Electron Microscopy

Scanning Electron Microscopy (SEM) analysis was carried out to look at the external morphology and to determine the particle size of the polymer microparticles synthesised in $scCO_2$ dispersion. The particle size distribution was measured from at least 100 particles and presented as Coefficient of variation (C_v).

$$C_v = \left(\frac{\sigma}{D_n}\right) x100\% \qquad \text{(Equation 2.3)}$$

Polymer samples were mounted on aluminium stubs (Agar Scientific, UK) with sticky carbon tabs (Agar Scientific, UK). The samples were then sputter-coated with gold using Leica EM SCD005 prior to analysis. Exposing an uncoated polymer sample to the electron beam would result in charging the sample and distorting the final image. Imaging was performed either on a JEOL JSM-6060LV or Philips XL30 ESEM FEG instrument over a range of magnification.

2.3.4 Transmission Electron Microscopy

The nanoscale internal morphology of block copolymer particles was imaged using TEM. For this purpose, samples were embedded in epoxy resin (Agar 100) and cured at 45 °C for 72 hrs. Thin sections (~80-100 nm) of the embedded samples were microtomed using an RMC MT-X ultramicrotome with a diamond knife (Leica Diatome Ultra 45°) at room temperature. Thin sectioning enabled examination of cross-sections through samples to view their internal structure.

The microtomed sections were floated on water and subsequently placed on copper TEM grids (Sigma Aldrich). The sections of PMMA-*b*-PBzMA and PMMA-*b*-PS were stained with RuO_4 (Acros, 0.5% solution in water or prepared following the literature[1]) for ~2 hrs. The RuO_4 was adsorbed

selectively to either PBzMA or PS domains of related block copolymers. Meanwhile, the sections of PMMA-*b*-PDMA, PMMA-*b*-PDEA, and PMMA-*b*-PDMAEMA were stained with I_2 vapour, which selectively adsorbed to non-PMMA domains, for ~2 hrs. The staining provides additional contrast in the TEM images.[2]

Imaging of the samples involved using a FEI Tecnai 12 Biotwin microscope in bright field mode. The accelerating voltage was 100 kV. The images were acquired using Gatan SIS Megaview IV digital camera. The beam intensity, magnification and image focus were adjusted during imaging to obtain the best image of the analysed samples.

2.3.5 Differential Scanning Calorimetry

Glass transition temperatures (T_g) were measured using Differential Scanning Calorimetry (DSC). The glass transition temperature is the temperature region where the polymer transitions from a hard, glassy material to a soft, rubbery material. It is different for each polymer, so it can be used to characterise the polymer.

The specific DSC used in this work is a TA Instruments Q2000, equipped with an auto-sampler, suitable for use from -90 to 300 °C using indium standards. Tzero aluminium pans (TA instruments) were used for all samples and pressed prior to use. Samples were run at a heating/cooling rate of 10 °C min^{-1} in a nitrogen atmosphere. Data were analysed by Universal Analysis software.

2.3.6 Thermal Gravimetric Analysis

Thermogravimetric Analysis (TGA) measures the weight change of a sample as a function of increasing temperature at a constant heating rate or as a function of time at constant temperature. The weight changes are determined using a highly precise balance situated inside a programmable

furnace. A sample is placed on a previously weighed platinum pan. The pan is placed in the furnace under a nitrogen atmosphere to prevent combustion. Decomposition profiles can be used to analyse the characteristics of the sample, such as chemical composition, water content, and sample purity.

In this work, TGA was used mainly to determine the amount of silver incorporated within block copolymer samples produced by the $scCO_2$ polymerisation. The remaining weight is assumed as silver content since it is the only substance that does not decompose at the final observed temperature (800 °C). All the TGA analysis performed in this thesis was carried out using a TA-Q500 instrument (TA Instruments).

2.3.7 Small Angle X-ray Scattering

Small Angle X-ray Scattering (SAXS) is an analytical method to determine the structure of a particle system in term of average particle size and shape. The particle or structure size that can be resolved ranges from few nm to hundreds nm in a typical set-up. Normally, X-rays are sent through the sample and every particle that happens to be inside the beam will contribute to the signal. Thus, the average structure of all illuminated particles is measured. In the polymer field, small angle X-ray scattering (SAXS) is a vital tool for investigating phase separation of block copolymers on the 1-100 nanometre scale.[3] Unlike microscopy, SAXS results are representative of the entire sample, so are ideal to complement electron microscopy methods that provide unique but local information. Moreover, SAXS allows *in situ* measurements, thus it is possible to follow the reaction and observe the onset of block copolymer phase separation. A high-intensity X-ray beam allows probing of block copolymers if there is an electron density difference between the respective blocks. The development of synchrotron X-ray sources has enabled time-resolved measurements to be performed.

In general, a monochromatic X-ray beam is fired at the sample, with the majority of the X-rays passing through the sample; the X-rays that do interact are scattered dependent on the sample structure. The scattering pattern generated can then be analysed to determine morphologies, presented as a function of the scattering vector (q). Further details of the specific analyses are given in Chapter 4.

SAXS experiments were conducted using a high pressure X-ray autoclave in beamline BM26-B at the European Synchrotron Radiation Facility (ESRF) in Grenoble, France. The beamline was the by Dutch-Belgian Beamline (DUBBLE).

2.4 References

1. Haubruge, H.G., Jonas, A.M. & Legras, R. *Polymer.* **44**, 3229–3234 (2003).
2. Huong, D. M., Drechsler, M., Cantow, H. J., and Moller, M. *Macromolecules* **26**, 864–866 (1993).
3. Hamley, I.W. *Block Copolymer Physics*. Oxford Science Publications: Oxford, UK. (1998).

Chapter 3 Synthesis of Nanostructured Block Copolymers in Supercritical CO_2

3.1 Overview

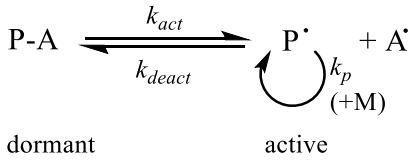
This chapter focuses on the synthesis of nanostructured block copolymer microparticles using Reversible Addition-Fragmentation Chain Transfer (RAFT) dispersion polymerisation in $scCO_2$. The Howdle group has reported the preparation of these materials in one-pot through the sequential addition of monomers using an HPLC pump.[1] This is a versatile route to produce nanostructured microparticles, but it requires a considerable time investment spanning several days because two consecutive polymerisations are conducted in series. To overcome this issue, it is necessary to speed up the process. This will be attempted by trying to devise a two-stage polymerisation to add flexibility of the synthesis process, by allowing each block to be synthesised in shorter independent steps. The method employs a pre-synthesised batch of poly(methyl methacrylate) (PMMA) particles as seeds, which act as a macro-Chain Transfer Agent (CTA) to control polymerisation of the second block in a $scCO_2$ dispersion. Using PMMA particles as macro-CTAs in a $scCO_2$ dispersion has been previously reported to polymerise MMA resulting a PMMA chain extension.[2] Critically, it must be shown that the spherical particle structure of the original PMMA particle is retained during the chain extension process. The goal of this chapter is therefore to assess the possibility of developing this new method for the synthesis of PMMA-based block copolymers by chain extending pre-synthesised PMMA particles. Moreover, it will be vital to understand whether this proposed method could produce nanostructured PMMA-based block copolymers in a much shorter timeframe, since the polymerisation of the second block can be decoupled from the first.

In order to assess the proposed method, the chemical structure of the block copolymer products synthesised in this way will be analysed using proton Nuclear Magnetic Resonance (^{1}H NMR), Gel Permeation Chromatography (GPC), and Differential Scanning Calorimetry (DSC). Furthermore, confirmation that a successful dispersion has been maintained during the syntheses will be obtained through morphological analysis using Scanning Electron Microscopy (SEM). Finally, the internal nanostructure of the particle products will be assessed by Transmission Electron Microscopy (TEM).

3.2 Introduction

3.2.1 Synthesis and Self-assembly of Block Copolymer *via* RAFT Dispersion Polymerisation

RAFT polymerisation is one of the three major controlled/living radical polymerisations (CLRP) techniques, together with Nitroxide Mediated Radical Polymerisation (NMP) and Atom Transfer Radical Polymerisation (ATRP).[3] CLRP relies upon the existence of a reversible activation/deactivation equilibrium that alternates between dormant and active states (Scheme 3.1).[3] In RAFT, the dormant state is a polymer chain with a RAFT functional end-group. If monomer is available, these dormant chains can be extended leading to chain extension or a block copolymer. The RAFT polymerisation is tolerant to a range of monomer types and hence numerous block copolymers with a wider range of block compositions are accessible.



Scheme 3.1. General dormant-active equilibrium

Many research groups have examined the use of RAFT in dispersed systems to produce amphiphilic block copolymer particles with various morphologies *via* Polymerisation-Induced Self-Assembly (PISA).[4–6] PISA occurs during the synthesis of a block copolymer with both a solvophobic and solvophilic component, either in an emulsion or a dispersion system. The formed block copolymer will aggregate spontaneously with the solvophobic block forming a core surrounded by the solvophilic block which extends into the solvent phase.[6] These aggregates then self-assemble into nano-objects including spherical micelles, worm/cylindrical micelles, and vesicles (polymersomes) (Figure 3.1). This range of morphologies depends on several parameters such as degree of polymerisation of the blocks, solvent character, and monomer concentration. PISA has been developed not only in aqueous systems but also in non-polar organic solvents such as lower alcohols and *n*-alkanes.

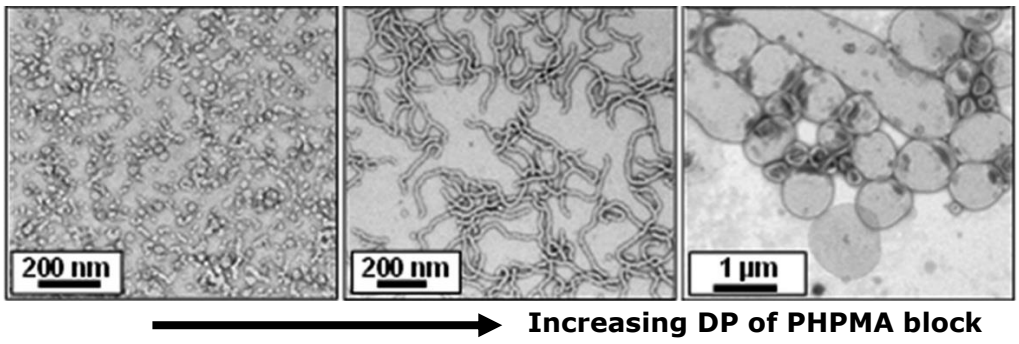


Figure 3.1. TEM images of poly(ethylene glycol)-*b*-poly(hydroxypropyl methacrylate (PEG-*b*-PHPMA) block copolymer, showing (a) spherical micelles, (b) worm/cylindrical micelles, and (c) vesicular morphology obtained by increasing the degree of polymerisation of the solvophilic block (PHPMA).[7]

PISA in aqueous dispersion systems requires the use of water-soluble monomers, that when polymerised form a water-insoluble polymer. These

monomers include *N*-isopropylacrylamide (NIPAM),[8] *N,N'*-diethylacrylamide (DEA),[9] 2-hydroxypropyl methacrylate (HPMA),[10,11] di(ethylene glycol) methyl ether methacrylate (DEGMA),[12] and 2-methoxyethyl acrylate (MEA)[13,14]. Controlled polymerisations of HPMA have been conducted using hydrophilic macro-CTAs such as poly(glycerol monomethacrylate) (PGMA),[10] poly(2-(methacryloyloxyl)ethylphosphorylcholine (PMPC)[15] or poly(ethylene glycol) (PEG)[7] with RAFT functionality, leading to block copolymers with spherical, worm and vesicular morphologies formed through the PISA process. A high monomer conversion (≥ 95% within 2 hours at 70 °C) and high blocking efficiency (90%) can be obtained through this approach. The first phase diagram for the PISA process was constructed by careful assessment of the polymerisation of HPMA using PMPC-based CTA in an aqueous system (Figure 3.2).[15]

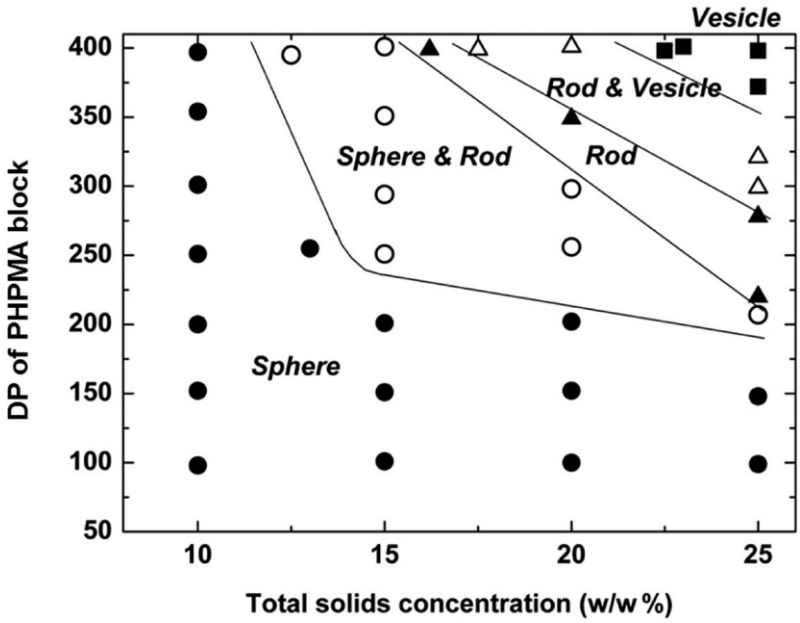


Figure 3.2. Phase diagram constructed for PMPC-*b*-PHPMA block copolymer by variation of the total solid concentration (w/w%) and the target degree of polymerisation of PHPMA block.[15]

The phase diagram enables prediction of morphological changes associated with precise block compositions. It was found that the type of

particle formed was determined by the total solids concentration and the degree of polymerisation of the hydrophobic PHPMA block. A spherical morphology was obtained at low total solids concentration (10 w/w%) for all targeted degree of polymerisations, with the sphere sizes progressively increasing as the degree of polymerisation increased. At higher total solids concentration (25 w/w%), all morphologies (sphere, rod/worm, and vesicle) can be achieved by increasing the targeted degree of polymerisation from 100 to 400.

Further monitoring of the morphological changes were conducted by TEM analysis on the polymerisation products of HPMA with water-soluble PGMA as a macro-CTA in the aqueous phase. During these morphological transitions, intermediate nanostructured morphologies were observed (Figure 3.3).[10] Initially, spheres grow to short worms before linear long worms are achieved. As the polymerisation proceeds, the linear worms form branched worms which then partially coalesce and form jellyfish intermediates before enclosing to form vesicles.

In addition to the aqueous system, organic solvents such as lower alcohols were also used for PISA. The process was demonstrated for of methacrylate monomers.[16–20] Benzyl methacrylate (BzMA) was polymerised in methanol, ethanol or isopropanol using either poly(2-hydroxyethyl methacrylate) (PHEMA) or poly(2-hydroxypropyl methacrylate) (PHPMA) macro-CTAs to make amphiphilic block copolymers.[18] The block copolymers self-assembled into spherical, worm, and vesicle nano-objects, which was driven by the growing solvophobic PBzMA chains. These nano-objects can be accessed with relatively low DP macro-CTAs. In contrast, when using macro-CTAs with a higher DP only spherical morphology was observed.

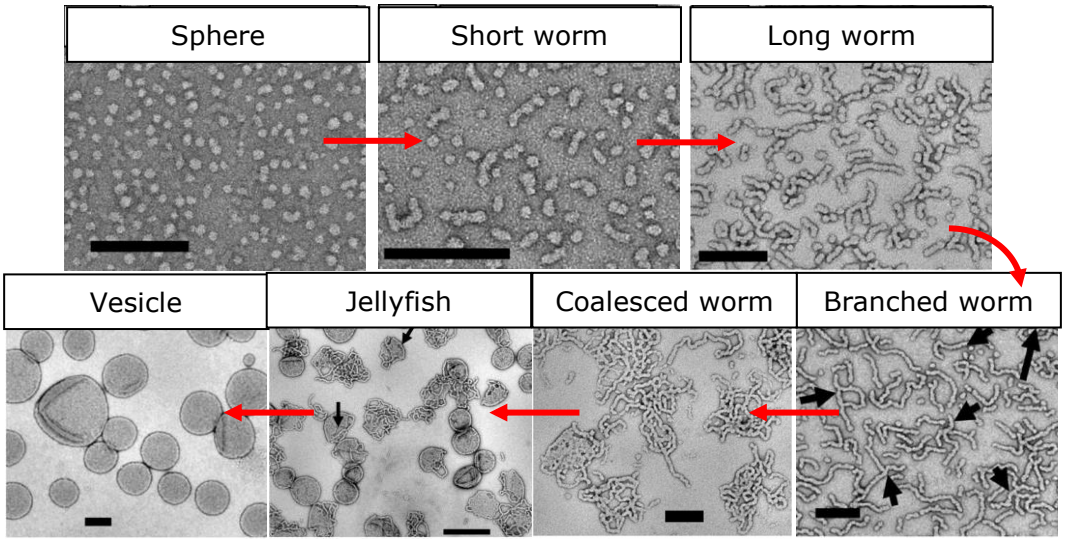


Figure 3.3. TEM images showing the morphological evolution during the PISA synthesis of PGMA-*b*-PHPMA in aqueous system. Intermediate nanostructures (short worms, branched worms, coalesced worms, jellyfish) are observed during transformation from spheres to worms to vesicles. Scale bars = 200 nm.[10]

An investigation of the growth of the spherical morphology during the PISA process was conducted in the dispersion polymerisation of BzMA using a PDMAEMA macro-CTA in ethanol.[21] The results suggested that both the increase of DP of the core-forming PBzMA block and exchange of individual copolymer chains between micelles and/or the fusing of spheres dictated the increasing diameter of the spherical micelles. Furthermore, synchrotron SAXS was used for the first time to investigate the block copolymer morphological transitions that occur *in situ* during non-aqueous PISA process of poly(stearyl methacrylate)-*b*-poly(benzyl methacrylate) (PSMA-*b*-PBzMA) diblock copolymers. This powerful technique was able to monitor the morphological evolution, as a function of monomer conversion.[22]

3.2.2 Nanostructured Block Copolymer Particles

The block copolymer self-assembly through PISA presented in the previous section results in colloidal nano-objects. In addition to that self-assembly, block copolymers can also self-assemble into nanostructured thin film,[23–25] or nanostructured microparticles[1,26,27]. In thin films, the self-assembly of block copolymers is generated through a post-polymerisation process. Typically, a thin film of the block copolymer with well-defined thickness is prepared by spin coating, and then thermally annealed to induce nanostructure formation and improve ordering of the domains.[25,28] Alternatively, solvent vapour annealing has been applied, especially for thermally unstable materials.[24,25,29] This approach has been applied to obtain a range of morphologies including lamellar, gyroidal, hexagonal, and spherical from a single block copolymer.[24]

In the case of nanostructured block copolymer particles, the Okubo group reported the preparation of PiBMA-*b*-PS block copolymers by a two-step Activators Generated by Electron Transfer Atom-Transfer Radical Polymerisation (AGET ATRP) in an aqueous dispersed system.[26] The first step was a microsuspension AGET ATRP to prepare PiBMA-Br. This was then used both as macroinitiator and seed particles for preparing PiBMA-*b*-PS in the second step. An onion-like multilayer structure was obtained through this method, with high blocking efficiency as a critical requirement to obtain that morphology. At high temperature (110 °C), rapid propagation occurred which resulted in low blocking efficiency, and hence the particles appeared disordered (Figure 3.4).

The group also reported preparation of PMMA-*b*-PBzMA particles by a two-step Reversible Chain Transfer Catalysed Polymerisation (RTCP) in a miniemulsion system.[30] An emulsion of PMMA prepared by miniemulsion RTCP in the first step was then employed as macroinitiator and seed particles for

the targeted block copolymer in the second step. Successful controlled polymerisations were demonstrated by a linear increase of M_n with conversion and narrow dispersities. Approximately 88% of the PMMA was chain-extended into PMMA-*b*-PBzMA within 12 hours, and the particle size increased from 160 nm (PMMA-I) to 184 nm (PMMA-*b*-PBzMA). However, no internal structure formed due to both chain lengths of PMMA and PBzMA blocks being below the critical molecular weight required for phase separation to occur.

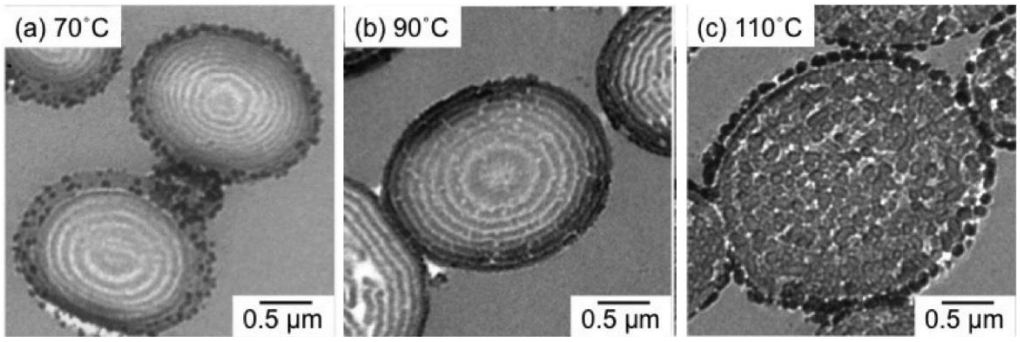


Figure 3.4. TEM images of ultrathin cross-sectional PiBMA-*b*-PS particles prepared by seeded AGET ATRP of styrene with PiBMA seed particles at various temperatures showing lamellar (a and b) and disorder structure (c).[26]

The Howdle group has exploited the unique properties of $scCO_2$ to prepare nanostructured block copolymers microsphere by RAFT dispersion polymerisation.[22,23] Their first attempt was an *in situ* copolymerisation,[31] in which two polymerisations were conducted in series at 65°C by introducing a second monomer following the initial polymerisation under supercritical conditions (~200 bar). Various length of pipes with a valve were attached to a high pressure reactor permitting a range of different monomer volumes to be introduced. A series of block copolymers were synthesised in which a PMMA first block was used to grow styrene or various other functionalised methacrylate monomers but none of these had internal nanostructures.

Another attempt from the group was the application of macro-CTAs for controlling MMA polymerisations in $scCO_2$ dispersions. Firstly, spherical PMMA particles having RAFT-end functional groups were used as macro-CTAs for the polymerisation of MMA. This technique not only achieved PMMA chain extension but also maintained the spherical structure of the initial PMMA particles. Secondly, a RAFT-terminated CO_2-philic polymer, poly(1H,1H,2H,2H-perfluorooctyl methacrylate (PFOMA), was used as both a macro-CTA and stabiliser for the dispersion polymerisation of MMA, yielding a series of PFOMA-*b*-PMMA block copolymers.[32] A kinetics study showed that the macro-CTA resulted in a shorter inhibition period compared to a small molecule CTA *i.e.* 1 hr vs ~10 hrs.[2] This was suggested to be due to the different stabilities of the radical intermediates formed by the macro-CTA and the small molecule CTA.[33] This difference is likely caused by the leaving group (R group) of the macro-CTA already being a polymeric species. However, the PFOMA-*b*-PMMA block copolymer showed no phase separation because $scCO_2$ acts as a compatibiliser that enhances the miscibility between the two blocks. Thus, selection of an appropriate block pair is important. The absence of phase separation may also be caused by the short chain lengths of PFOMA relative to PMMA, which will also influence the incompatibility between the two blocks.

The group further developed an *in situ* method by utilising an HPLC pump to add monomer under high pressure.[1] This method, referred to as the one-pot method, overcame many of the issues relating to unsuccessful monomer addition which had hampered the previous method. A range of block copolymers including methacrylates, styrenics, and acrylamides were obtained as dry spherical microparticles. High blocking efficiencies were also confirmed for many of these products.[1,34] The block copolymers were also able to undergo *in situ* self-assembly into a range of internal nanostructures

including lamellar, cylindrical, and spherical (Figure 3.5) that could be controlled by varying the block pair and the volume fraction of the blocks. The self-assembly in this $scCO_2$ dispersion route is driven by polymer–polymer microphase separation, which contrasts with the PISA process, where the self-assembly is driven by the different solubilities of each block in a continuous phase.[6]

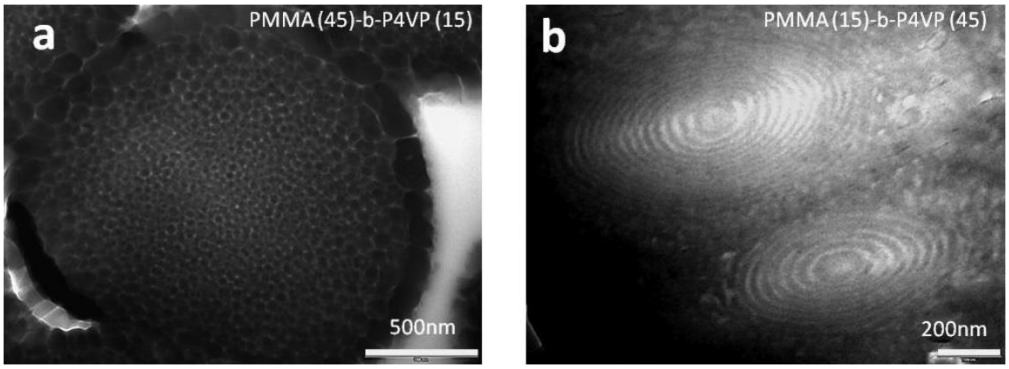


Figure 3.5. TEM images of PMMA-*b*-P4VP, prepared by the one-pot method of RAFT dispersion polymerisation in $scCO_2$, showing different morphologies, (a) spherical and (b) lamellar obtained by changing the block ratio.[1]

Further investigation found that the internal nanostructures in the diblock copolymers synthesised by the $scCO_2$ dispersion route were also influenced by differences in the CO_2-philicity of one block relative to another.[27] When blocks had a similar CO_2-philicity, the morphology obtained followed the expected diblock copolymer phase diagram.[35] A phase diagram, as detailed in Chapter 1, is a plot of the essential parameters that determine the block copolymer phase separation. In contrast, a large difference in the CO_2-philicity of the blocks induced a morphological shift from the expected phase diagram and resulted in unexpected morphologies. A block with higher CO_2-philicity will absorb more CO_2 than the less CO_2-philic one so that the

former block has higher effective mass and volume than expected. As a result, there is a shift in the block copolymer phase diagram.

To summarise, it is now understood how to synthese a variety of nanostructured block copolymer microparticles in $scCO_2$. The exploitation of the RAFT process in these syntheses highlights the usefulness of living polymer chains with pre-determined end-groups. The chains can be re-initiated to continue propagation and enable chain extension or block copolymer formation. Importantly, the use of $scCO_2$ as a polymerisation medium results in dry spherical block copolymer microparticles with a range of internal nanostructures. These would not normally be obtained in conventional media due to the high glass transition temperature of the blocks under investigation,[36,37] which are suppressed in the presence of $scCO_2$. Moreover, the low viscosity and high diffusivity of $scCO_2$ aids mobility and arrangement of the copolymer chains to phase separate and construct a particular nanostructure. However, rather long reaction times are required to create such nanostructured particles, since the minimum polymerisation time required for each block under such conditions is at least 18 hours.

3.3 Objectives

The key aim of this chapter is to develop a new method for the synthesis of nanostructured block copolymer microparticles; a two-stage dispersion polymerisation in $scCO_2$ to stagger the reaction time. The process will utilise pre-synthesised particles of RAFT-terminated PMMA which will simultaneously act as a seed particles and macro-CTAs. The initial target is to develop block copolymers with moderate molecular weights ranging between 50 to 100 kg mol^{-1}.

The versatility of this approach will be tested by application to a range of monomer classes, including methacrylates, styrenics, and acrylamides.

Multiple analytical techniques including ^{1}H NMR, GPC, and DSC will be employed to assess the chemical structure of the block copolymers formed. Furthermore, SEM and TEM will then be used to study the morphology and internal nanostructure of the particles formed.

3.4 Experimental

3.4.1 Material

Methyl methacrylate (MMA, 99%, Fisher), benzyl methacrylate (BzMA, 98%, Alfa Aesar), *N,N*-dimethylacrylamide (DMA, 99%, Sigma Aldrich), and *N,N*-diethylacrylamide (DEA, >98%, TCI) were purified by passing through a neutral aluminium oxide column prior to use. RAFT agent, S-Dodecyl-S'-(α, α'-dimethyl-α''-acetic acid)-trithiocarbonate (DATC) was synthesised following a literature procedure.[38] Poly(dimethylsiloxane monomethyl methacrylate) (PDMS-MA, 10kDa, ABCR Gmbh), initiator 2,2'-azobis(isobutyronitrile) (AIBN, Sigma Aldrich), aluminium oxide (Across Organic), HPLC grade chloroform (Sigma Aldrich), HPLC grade THF (Sigma Aldrich), ruthenium tetroxide (RuO_4, 0.5% solution in water, Acros), iodine (Fisher), and Agar 100 resin (Agar Scientific) were used as received. Dry CO_2 (99.99%) was purchased from BOC. EPDM O-rings were acquired from Brammer. All of the monomers were degassed by bubbling with argon for 30 minutes prior to use.

3.4.2 Two-stage Polymerisation

3.4.2.1 Synthesis of RAFT-terminated PMMA (PMMA-DATC, seed particle)

The synthesis is a RAFT-controlled dispersion polymerisation of MMA (Figure 3.6, A). In order to synthesis PMMA of 50 kg mol^{-1}, the reaction vessel, a 60 mL autoclave, was purged with CO_2 (*ca* 2.0 bar) for 15 minutes to remove oxygen that may inhibit the polymerisation. The vessel then was charged with the degassed solution of MMA (18 mL, 168 mmol), DATC (122.7

mg, 0.336 mmol), PDMS-MA (842 mg, 5 wt% w.r.t. MMA), and AIBN (55.2 mg, 0.336 mmol). The ratio of [MMA]:[DATC]:[AIBN] was 500:1:1. Once the solution was injected, the autoclave was sealed and CO_2 was introduced to 50 bar. The stirrer and the heater were then switched on and set to 300 rpm and 65 °C, respectively. When 65 °C was reached, additional CO_2 was added to reach a pressure of 275 bar. The reaction was then left for 18 hours to reach completion, after which time the heater and the stirrer were switched off and the autoclave was left to cool to room temperature. Once this temperature had been reached the CO_2 was slowly released. At atmospheric pressure (1.0 bar), the autoclave was opened and the product was collected. The polymer product was then characterised as required.

3.4.2.2 Chain Extension into Block Copolymers

3.4.2.2.1 Single addition of second monomer

The procedure is as follows for a reaction in which a symmetrical block copolymer PMMA-*b*-PBzMA of 100 kg mol^{-1} was targeted (Figure 3.6, B). The pre-synthesised PMMA (PMMA-DATC, sub-section 3.4.2.1) (5616 mg, 0.112 mmol, assumed M_n = 50 kg mol^{-1}) was placed in a 60 mL autoclave with BzMA (9.5 mL, 56 mmol), PDMS-MA (280 mg, 5 wt% w.r.t. BzMA) and AIBN (18.4 mg, 0.112 mmol). The autoclave was then clamped and purged with CO_2 (3 - 4 bar) for 15 minutes. The autoclave was sealed and pressurised to 55 bar by charging with CO_2. The stirrer was turned on and adjusted to 300 rpm. The heater was then set to 65 °C. Once 65 °C had been reached, additional CO_2 was added to reach a pressure of 275 bar and the reaction was run for 48 hrs. Once the allotted time had been reached, the heater and the stirrer were switched off and the autoclave was cooled to room temperature and then depressurised by releasing CO_2 through the outlet valve. At atmospheric pressure (1.0 bar), the autoclave was opened and the

product was collected. The product was then ready for analysis and characterisation.

3.4.2.2.2 High pressure addition of second monomer

To prepare a symmetrical block copolymer PMMA-*b*-PBzMA of 100 kg mol^{-1}, a 60 mL autoclave was charged with pre-synthesised PMMA (5616 mg, 0.112 mmol, assumed M_n = 50 kg mol^{-1}) and PDMS-MA (280 mg, 5 wt% w.r.t. BzMA) and was then clamped and purged with CO_2 (3 - 4 bar) for 15 minutes. The autoclave was sealed and pressurised with the addition of CO_2 to 55 bar. The stirrer was turned on and adjusted to 300 rpm. The heater was then set to 65 °C. Once 65 °C had been reached, additional CO_2 was added to reach a pressure of 205 bar for 1 – 2 hours. After that, degassed BzMA (9.5 mL, 56 mmol) and AIBN (18.4 mg, 0.112 mmol) were added *via* HPLC pump at 1 ml min^{-1}. Additional CO_2 was then added as required to reach a final reaction pressure of 275 bar. The reaction was then left for 16 h at 65 °C.

Once the allotted time had been reached, the heater and the stirrer were switched off and the autoclave was cooled to room temperature and then depressurised. At atmospheric pressure (1.0 bar), the autoclave was opened and the product was collected. The product was then ready for analysis and characterisation. The synthesis scheme is presented in Figure 3.6 C.

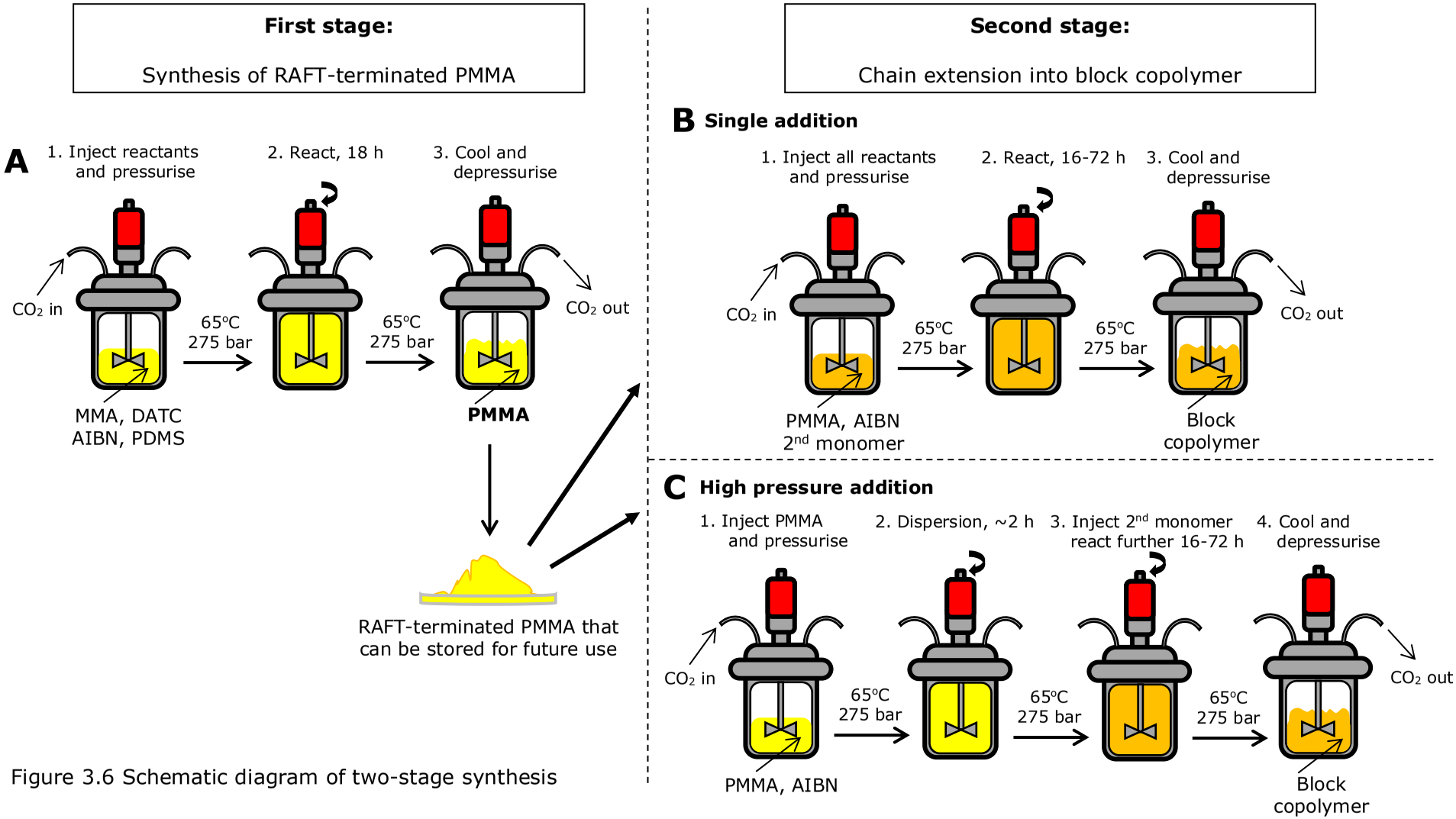


Figure 3.6 Schematic diagram of two-stage synthesis

3.5 Results and Discussion

3.5.1 Synthesis of Block Copolymer *via* Two-stage Method

This section presents a newly developed method for preparing block copolymer microparticles in successive steps, termed the two-stage method. The method consists of two sequential polymerisations which are conducted independently. The first polymerisation produces RAFT-terminated PMMA chains, which are isolated as a dry microparticulate polymer and can be stored for future use. The second polymerisation is the re-dispersion and chain extension of the PMMA to form a block copolymer.

3.5.1.1 The First Polymerisation (Synthesis of RAFT-terminated PMMA)

The first polymerisation is a RAFT-controlled dispersion polymerisation of MMA in $scCO_2$. All of the block copolymers prepared in this thesis were synthesised with PMMA as the first block. PMMA was chosen because it can serve as an effective macro-CTA.[39] One main requirement of a macro-CTA is that it can act as an effective homolytic leaving group which can serve as a good propagating radical. It must be able to initiate the polymerisation of the new block efficiently. PMMA generates stabilised-tertiary propagating radicals that act as a good leaving group and hence it is a versatile starting block (Figure 3.7).[39] Furthermore, PMMA has been successfully synthesised in $scCO_2$ through dispersion polymerisation and produced well-defined polymer microparticles.[2] Moreover, the ability of $scCO_2$ to plasticise and swell PMMA may promote diffusion of monomer into the polymer phase and facilitate chain extension. Successful block copolymer syntheses with PMMA as the first block has also been reported previously.[1,31,40]

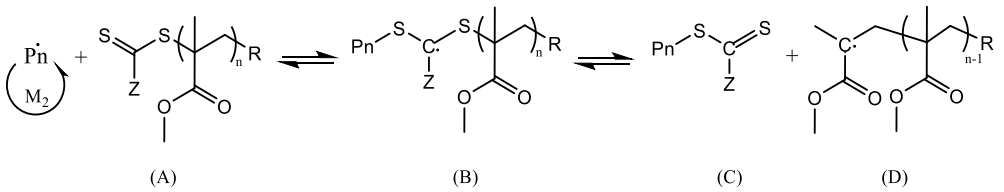


Figure 3.7 Reversible chain transfer step of the RAFT process showing the formation of PMMA leaving group radical (D) as a stabilised-tertiary propagating radical. $P_{n}\cdot$: propagating radical from initiation step, M_2: monomer, A: PMMA-macro RAFT agent, B: intermediate radical, C: polymeric RAFT agent.

DATC and AIBN were used as the chain transfer agent (CTA) and initiator respectively. AIBN decomposition in $scCO_2$ is slower compared to that in benzene for the same reaction condition,[41] therefore, we need a higher concentration of AIBN for reaction in $scCO_2$ relative to CTA to enable the reaction to proceed faster. Here, a 1:1 molar ratio of CTA to initiator was used, unless stated. DATC, a carboxyl-terminated trithiocarbonate, has a high chain transfer efficiency and provides good control over the radical polymerisation because the tertiary carbon attached to the labile sulfur atom provides a radical-stabilising carboxyl group (Figure 3.8).[38] This RAFT agent can be used effectively for controlled polymerisation in $scCO_2$,[31] and even appears to have better control compared to that in toluene[42].

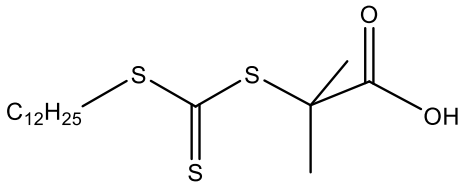


Figure 3.8 Structure of DATC, a carboxyl-terminated trithiocarbonate RAFT agent

Methacrylate-terminated polydimethylsiloxane (PDMS-MA) (Figure 3.9) was used as a grafting steric stabiliser in the dispersion process. This stabiliser has a CO_2-philic (siloxane chain) and CO_2-phobic segments and is

located at the polymer-solvent interface to prevent precipitation of particles by coating the surface of each particle. It allows polymer growth as discrete particles and proceeds to high conversion. The long CO_2-philic siloxane chain can effectively anchor to the nucleated particles and extend into the continuous phase.[43]

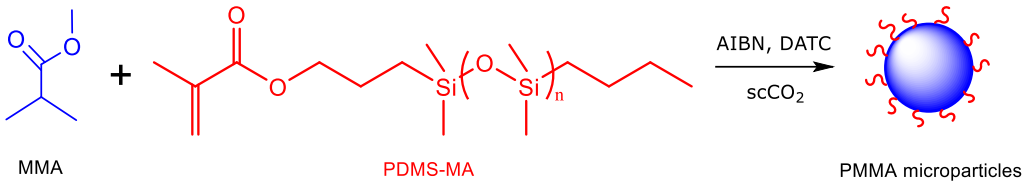


Figure 3.9 Synthetic route to PMMA microparticles. PDMS-MA (red) exists at the polymer-solvent interface and prevents precipitation of the polymer particles.

The synthesis was performed at a constant pressure and temperature of 275 bar and 65 °C, respectively. These have been previously determined to be effective conditions to decompose AIBN and achieved PDMS-MA solubility.[2,43] A series of samples were collected through a sampling tap at the bottom of the autoclave (Figure 2.2) to investigate the kinetics of the dispersion polymerisation of MMA. This enabled a series of samples at various time points to be collected without having to depressurise the reaction vessel.

A selection of GPC traces (Figure 3.10) show the growth of a PMMA homopolymer over time with unimodal molecular weight distribution. Low dispersity of the products indicates that the RAFT process is behaving as intended over the course of the reaction. The excellent mass-transfer properties of $scCO_2$ towards the reactants and high chain mobility in the polymer particles also ensure good control over the polymerisation.[44]

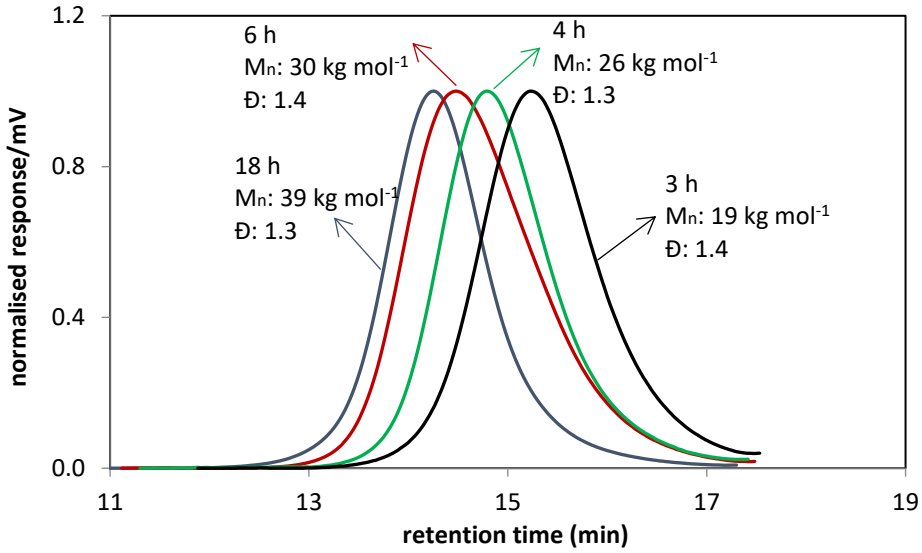


Figure 3.10 GPC traces of PMMA showing polymer growth over time with unimodal molecular weight distribution.

Molecular weight (M_n) can be readily controlled (Table 3.1) by altering the concentration of the RAFT agent (CTA) relative to the monomer concentration. The experimental M_n (M_n^{th} and M_n^{GPC}) values exhibit good agreement at all targeted molecular weight (M_n^{target}) values. The M_n^{th} was obtained by calculation from the monomer conversion (assuming linear growth of M_n with conversion) using Equation 3.1.[45] The M_n^{GPC} was measured by GPC using an RI detector with THF as the eluent and applying PMMA standards.

$$M_n^{th} = \frac{[M]_0 \, x \, conversion}{[CTA]_0} x MW_{monomer} + MW_{CTA} \qquad \text{(Equation 3.1)}$$

As anticipated, there is a gradual broadening of polymer dispersity when the targeted molecular weight is increased. This is a consequence of decreasing the initial concentration of CTA (relative to the monomer concentration) as controlling agent. Nevertheless, the results still indicate

good control over the polymerisations. Reactions were repeated (Table 3.1, entry 3, 4, and 5) using identical conditions and showed comparable and reproducible final polymer products.

Table 3.1 MMA polymerisation targeting different molecular weight by using different molar ratios of monomer (M) and RAFT agent (CTA)

Entry	[M]:[CTA]	M_n (kg mol^{-1})			Đ[b]	Conv.(%)[c]
		M_n^{target}	M_n^{th} [a]	M_n^{GPC} [b]		
1	750 : 3	25	24	27	1.17	96
2	750 : 1.75	30	28	31	1.16	96
3	750 : 1.5	50	49	49	1.18	98
4	750 : 1.5	50	49	48	1.21	98
5	750 : 1.5	50	48	47	1.22	95
6	750 : 1	75	69	66	1.50	92

The reactions were conducted at 65 °C and 275 bar for 18 hrs with molar ratio CTA : I = 1 : 1 and 5% stabiliser w.r.t. monomer

a. Calculated from Equation 3.1: ([MMA]/[CTA])* conv.*MW_{MMA} + MW_{CTA}
b. Measured using an RI GPC with THF as the eluent and applying PMMA standards
c. Determined gravimetrically

Polymerisations with different CTA to initiator molar ratio were also performed (Table 3.2). Less initiator results in lower dispersity/better control (Table 3.2, entry 3 and 4) because there are fewer termination reactions and this also increases the livingness of the RAFT process. Using less initiator also provides better agreement between experimental (M_n^{th} and M_n^{GPC}) and targeted (M_n^{target}) molecular weight.

Table 3.2 MMA polymerisation with different molar ratios of RAFT agent (CTA) and initiator (I)

Entry	[CTA]:[I]	M_n (kg mol^{-1})			Đ[b]	Conv.[c](%)
		M_n^{target}	M_n^{th} [a]	M_n^{GPC} [b]		
1	1:1	50	48	41	1.57	95%
2	1:1	50	46	42	1.40	92%
3	1:0.5	50	48	51	1.21	96%
4	1:0.5	50	47	49	1.23	94%

The reactions were conducted at 65 °C and 275 bar for 18 hrs with molar ratio M : CTA = 500 : 1 and 5% stabiliser w.r.t. monomer

a. Calculated from Equation 3.1: ([MMA]/[CTA])* conv.*MW_{MMA} + MW_{CTA}
b. Measured using an RI GPC with THF as the eluent and applying PMMA standards
c. Determined gravimetrically

A dry and solvent-free polymer powder can be isolated directly upon opening the autoclave. The product was then analysed using SEM to determine the particle morphology. The discrete spherical morphology (Figure 3.11) indicates that the stabiliser functioned well and prevented aggregation of the polymer particles during the reaction. The particle sizes (D_n=1 – 2 μm) and their distribution (C_v ~20%, refer to Eq. 2.3) are similar to previous reports of PMMA particles synthesised by RAFT dispersion polymerisation in $scCO_2$.[2]

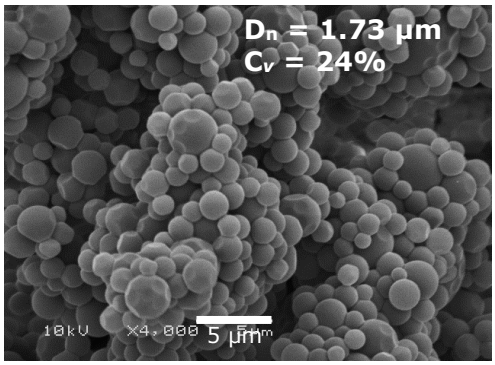


Figure 3.11. Representative of PMMA particle morphology (Table 3.2 entry 3), showing spherical morphology with measurements of particle diameter (D_n) and particle size distribution (C_v).

3.5.1.2 The Second Polymerisation (PMMA Chain Extension into Block Copolymers)

PMMA chains obtained from RAFT polymerisation were extendable through redispersion in $scCO_2$ and addition of fresh MMA monomer.[2] This chain extension was conducted by further reacting the chains with fresh initiator and monomer (MMA) through a second-stage dispersion polymerisation. In this process, RAFT-terminated PMMA acts as a macro-CTA that is insoluble in the reaction medium. The chain extension can be achieved since the PMMA chains remain in a dormant state with RAFT functional end-groups. However, to the best of the author's knowledge this

process has not yet been undertaken in the presence of monomers other than MMA to produce PMMA-based block copolymers.

Here, we investigate the chain extension of PMMA into block copolymers by reactivating DATC-terminated PMMA chains (Figure 3.12a), obtained from the first polymerisation (section 3.5.1.1), and reacting them further with a second monomer. A range of monomer classes (Figure 3.12) were examined as the second monomer to determine the versatility of these techniques. Two monomers have already been reported for RAFT polymerisation in $scCO_2$ dispersion, *i.e.* benzyl methacrylate (BzMA), styrene (S), and *N,N'*-dimethyl acrylamide (DMA).[42] A new dialkyl acrylamide monomer, *N,N'*-diethyl acrylamide (DEA), was also introduced to achieve a wider class of monomer.

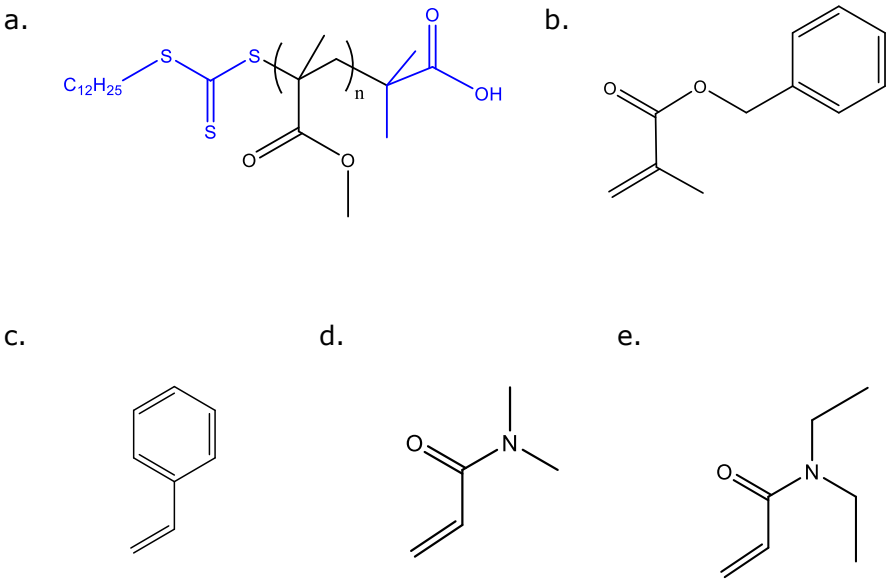


Figure 3.12. Structure of (a) DATC-terminated PMMA and the second monomers introduced in this chapter, *i.e.* (b) BzMA, (c) styrene, (d) DMA, and (e) DEA.

The polymerisation was conducted by introducing PMMA microparticles, monomer, and initiator all together into the reactor from the beginning of the reaction, termed the single addition. The technique

was employed to prepare PMMA-*b*-PBzMA block copolymers (Figure 3.13). Pre-synthesised PMMA particles and BzMA monomer were charged into a high pressure autoclave along with initiator and reacted for 48 hours at constant temperature and pressure (65 °C and 275 bar). These reaction conditions (time, temperature, and pressure) are based on the procedure for polymerising BzMA using the one-pot method reported elsewhere for PMMA-*b*-PBzMA block copolymer.[1]

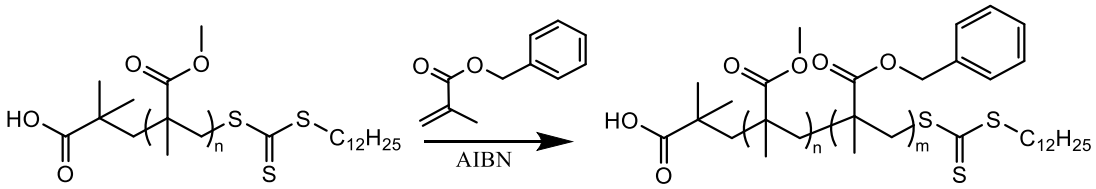


Figure 3.13. Chain extension of PMMA-DATC with BzMA leading to PMMA-*b*-PBzMA block copolymer.

The molecular weight of the original PMMA approximately doubled after polymerisation of BzMA (Table 3.3) indicating successful chain extension of the original PMMA homopolymer (Figure 3.14). The dispersity values of the block copolymers were slightly broader than that for the pre-synthesised PMMA. This is well known due to loss of some control with the second block. However, the dispersity obtained was fairly similar to the result obtained for the RAFT polymerisation of BzMA using DATC.[42]

Table 3.3 PMMA-*b*-PBzMA block copolymer properties prepared through single addition of the second monomer (BzMA)

Entry	PMMA		PMMA-*b*-PBzMA		Morphology[b]	Conv (%)[c]
	M_n^{GPC} (kg mol^{-1})[a]	Đ [a]	M_n^{GPC} (kg mol^{-1}) [a]	Đ [a]		
1	45	1.30	88	1.37	tacky solid	99
2	45	1.30	95	1.42	tacky solid	99

The reactions were conducted using pre-synthesised PMMA with given M_n values at 65 °C and 275 bar for 48 hrs with molar ratio CTA : I = 1 : 1 and 5% stabiliser w.r.t. BzMA. The targeted M_n of the PBzMA block is 50 kg mol^{-1}.
a. Measured using an RI GPC with THF as the eluent and applying PMMA standards
b. Initial appearance upon opening the vessel
c. Calculated from ^{1}H NMR spectrum

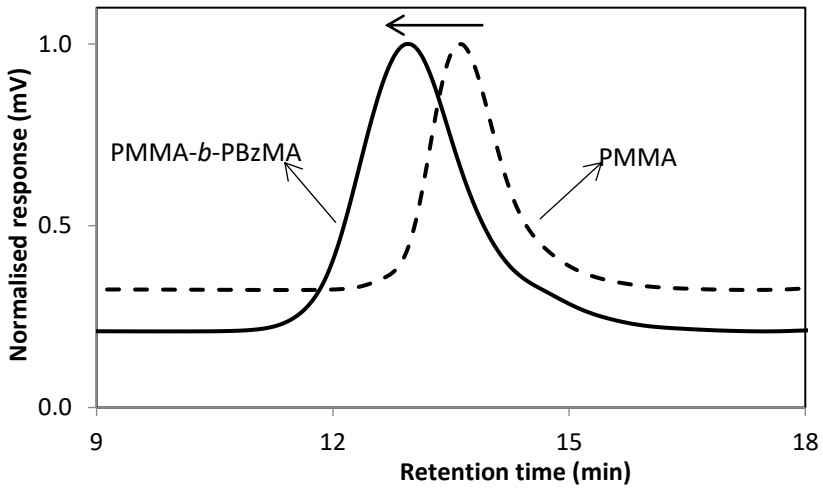


Figure 3.14 Example of GPC traces showing the increase in molecular weight (chain extension) of PMMA with BzMA, forming a PMMA-*b*-PBzMA block copolymer.

The ^{1}H NMR spectrum (Figure 3.15) confirmed that the monomer (BzMA, 5.2 ppm) has polymerised to PBzMA (4.7-5.0 ppm) leading to PMMA-*b*-PBzMA block copolymer. Unfortunately, an ill-defined morphology was observed by SEM rather than the spherical particles that were desired (Figure 3.16). This could be caused by softening or even dissolution of PMMA particles in BzMA prior to the reaction, which might destroy the spherical morphology of the particles. Here, the second monomer acted as cosolvent for the PMMA microparticles. This also produced a tacky solid product instead of the powder that was expected upon opening the reactor.

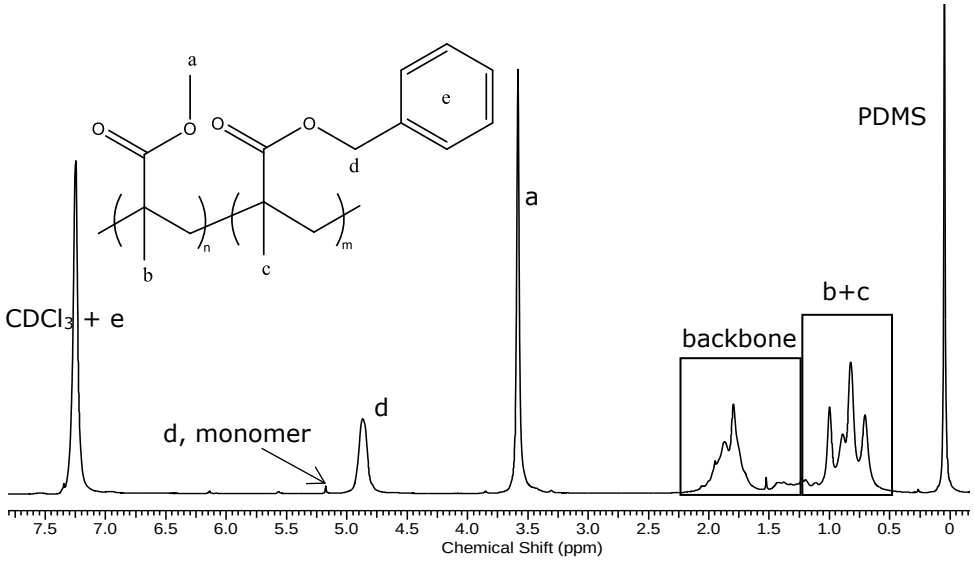


Figure 3.15. ^{1}H NMR spectrum of PMMA-*b*-PBzMA from Table 3.3. BzMA monomer (peak δ=5.2 ppm) has polymerised to PBzMA (peak δ=4.7-5.0 ppm).

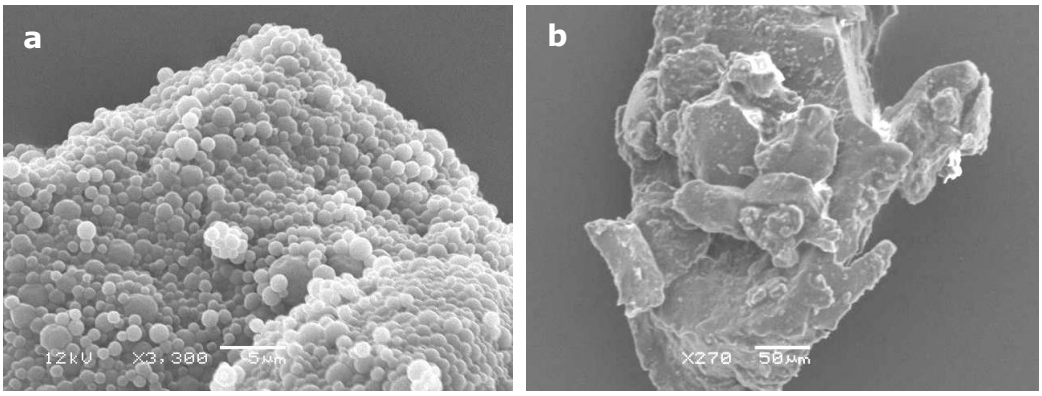


Figure 3.16 SEM images of (a) initial PMMA microparticles, and (b) PMMA-*b*-PBzMA (Table 3.3, entry 2) prepared through single addition of the second monomer, showing an ill-defined morphology

Regardless of the morphology, the PMMA chains were successfully extended to block copolymer chains as demonstrated by GPC and ^{1}H NMR. The living nature of the PMMA-RAFT polymer chains is also clear. However, the loss of the particle morphology during the reaction means that this

process is not suitable for the dispersion synthesis of nanostructured block copolymer microparticles in $scCO_2$ as intended in this Chapter.

3.5.2 Morphological Improvement of The Microparticles

3.5.2.1 High pressure addition of the second monomer

In order to obtain high-quality microparticles, it is essential that the initial PMMA materials are not softened or dissolved by the addition of the second monomer. This will be a particular problem for those second monomers in which PMMA is itself soluble, as occurring when BzMA was added above. To overcome this, we devised a strategy to avoid direct exposure of the PMMA microparticles with the second monomer and keep the concentration of the second monomer low during the addition. To avoid direct exposure, the PMMA microparticles were dispersed in $scCO_2$ prior to the injection and the second monomer addition was therefore conducted at high pressure (Figure 3.17). An HPLC pump was used to aid injection of the monomer into the autoclave at the required pressure (~200 bar).

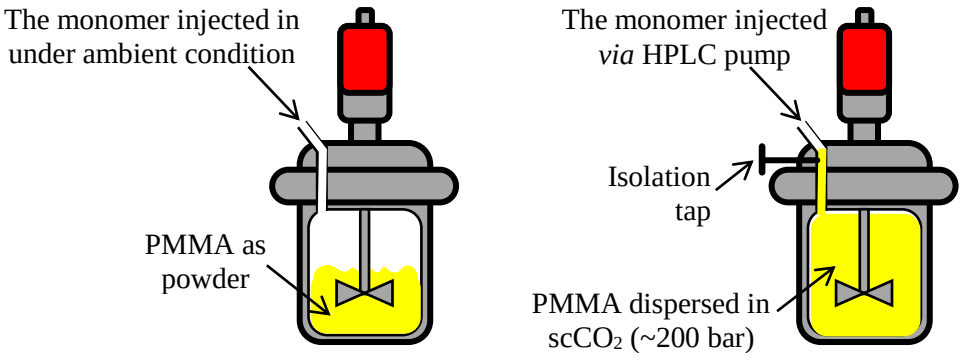


Figure 3.17. Diagram of the second monomer addition for (a) single addition, in which the second monomer added under ambient conditions results in PMMA particles directly mixing with the monomer, and (b) high pressure addition. The latter technique allows for the PMMA particles to be dispersed in $scCO_2$ prior to injection of the second monomer.

Injection at high pressure allows the second monomer to dissolve instantly in $scCO_2$ once injected into the autoclave in which the PMMA particles have already been dispersed. This approach should impede direct exposure of the PMMA particles to the BzMA monomer and hence prevent dissolution of the particles.

The synthesis of PMMA-*b*-PBzMA was used to evaluate these techniques. Initially, the pre-synthesised PMMA microparticles were charged into the autoclave and then pressurised with CO_2 and heated to reach 200 bar and 65 °C, respectively. The first synthesis was attempted by injecting the BzMA immediately once the required temperature and pressure achieved. This attempt produced a glassy solid rather than a free-flowing powder (Table 3.4, entry 1).

The second attempt was carried out using the same procedure with a higher concentration of the second monomer (Table 3.4, entry 2). This was expected to produce free-flowing powder since availability of monomer in higher concentration enables stabilisation of the dispersion.[43] It was also conducted to achieve a higher target molecular weight by altering the molar ratio of monomer and CTA. As expected, a free-flowing powder and higher molecular weight polymer were achieved. In addition, it also yielded a higher monomer conversion since the higher BzMA concentration enabled the reaction to proceed faster. However, the SEM image (Figure 3.18) shows a mixture of small (~1.0 μm) and large particles (~5.4 μm). These sizes are larger than the original PMMA seed particles (0.8 μm). Thus, the smaller size is not the product of unreacted or dead PMMA chains. This is in agreement with the GPC analysis that shows a unimodal distribution (Figure 3.19). The large particles might instead be ascribed to incomplete dispersion of the original PMMA seed particles, leading perhaps to localised dissolution of PMMA and subsequent agglomeration and larger particles.

Table 3.4. Characteristics of PMMA-*b*-PBzMA block copolymer obtained by addition of the second monomer immediately once the required temperature and pressure achieved.

Entry	PMMA		PMMA-*b*-PBzMA			Morphology[c]	Conv (%)[d]
	M_n^{GPC} (kg mol^{-1})[a]	Đ[a]	M_n^{th} (kg mol^{-1})[b]	M_n^{GPC} (kg mol^{-1})[a]	Đ[a]		
1	41	1.5	71[e]	51	1.4	Glassy powder	71
2	43	1.4	145[f]	90	1.5	Fine powder	97

The reactions were conducted at 65 °C and 275 bar for 48 hrs with molar ratio CTA : I = 1 : 1. The second monomer, BzMA, was added *via* an HPLC pump at ~200 bar.

a. Measured using an RI GPC with THF as the eluent and applying PMMA standards
b. Calculated from M_n^{PMMA} + ([BzMA]/[CTA])*MW_{BzMA}*conv)
c. Initial appearance upon opening the vessel
d. Determined gravimetrically
e. [BzMA] : [CTA] = 500 : 1
f. [BzMA] : [CTA] = 750 : 1

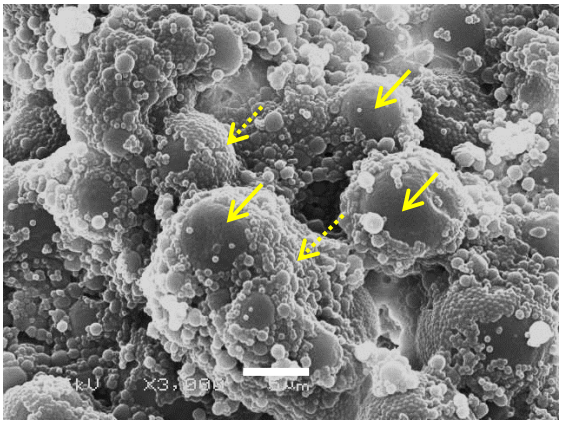


Figure 3.18. SEM image of PMMA-*b*-PBzMA particles prepared by injecting the BzMA immediately once the required temperature and pressure were achieved. The image shows small (dotted arrows) and large (solid arrows) particles of the block copolymer. Scale bar is 5 μm.

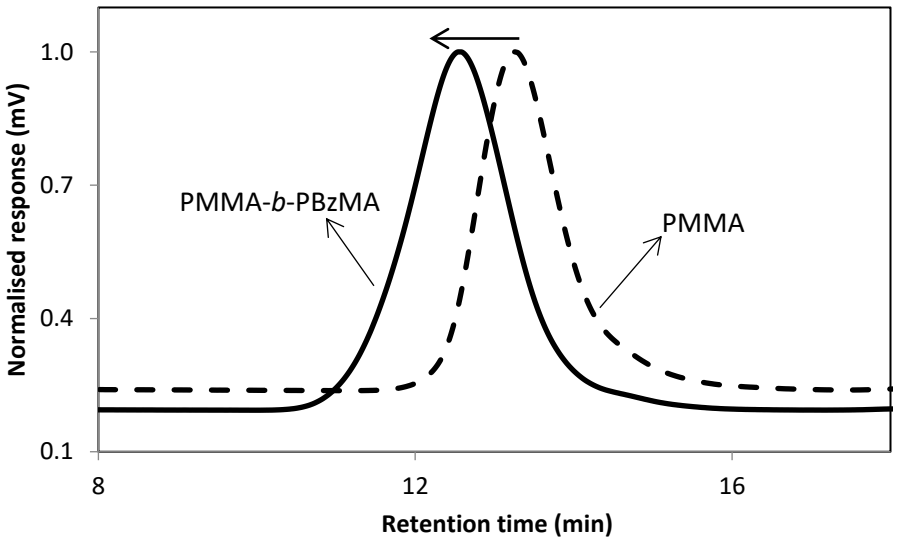


Figure 3.19 GPC traces showing the increase in molecular weight (chain extension) of PMMA, forming PMMA-*b*-PBzMA block copolymer with a unimodal distribution.

In order to minimise aggregation and further improve the particle morphology, longer dispersion times (delayed injection) were attempted

and additional PDMS-MA stabiliser was also added to the reaction along with the second monomer. The longer dispersion time was intended to ensure that all the PMMA microparticles are thoroughly dispersed. The PMMA dispersion was left for 1-2 hours prior to the injection. Adding fresh PDMS-MA stabiliser (5 wt%, w.r.t. the second monomer) should facilitate the redispersion of PMMA microparticles due to the increased surface area of the larger particles following chain extension. Using this combination, the same formulation for entry 1 of Table 3.4 was reproduced. A free-flowing polymer powder with a spherical morphology was obtained (Figure 3.20). Thus, it is clear that a longer dispersion time and additional stabiliser improves the particle morphology. The particle size (D_n=1.8 μm) and particle size distribution (C_v=28%, see Eq. 2.3) are comparable to previous reports of RAFT polymerisation in $scCO_2$.[2]

Table 3.5 Characteristics of PMMA-*b*-PBzMA block copolymer obtained by delayed injection of the second monomer

PMMA		PMMA-*b*-PBzMA				
M_n^{GPC} (kg mol^{-1})[a]	Đ[a]	M_n^{th} (kg mol^{-1})[b]	M_n^{GPC} (kg mol^{-1})[a]	Đ[a]	Morphology[c]	Conv (%)[d]
45	1.5	80	56	1.6	Powder	80

The reaction was conducted at 65 °C and 275 bar for 48 hrs with molar ratio CTA : I = 1 : 1. The second monomer, BzMA, along with additional 5 % stabiliser w.r.t. monomer were added *via* an HPLC pump at ~200 bar after PMMA being dispersed in $scCO_2$ for 2 hrs.

a. Measured using an RI GPC with THF as the eluent and applying PMMA standards
b. Calculated from M_n^{PMMA} + ([BzMA]/[CTA])*MW_{BzMA}*conv)
c. Initial appearance upon opening the vessel
d. Determined gravimetrically

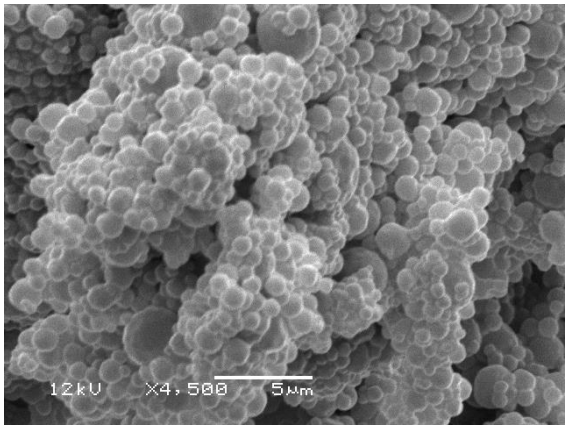


Figure 3.20. SEM image of PMMA-*b*-PBzMA synthesised by delayed injection. The second monomer, BzMA, was injected after the PMMA particles were dispersed in $scCO_2$ for 1-2 hours.

3.5.2.2 High Pressure Addition with Reducing Monomer Exposure

Meanwhile, the concentration of the second monomer was kept low by addition over a certain time interval throughout the reaction (Figure 3.21a) and by lowering the injection flow rate (Figure 3.21b). These approaches were expected to reduce the instantaneous concentration of the second monomer, and hence minimise PMMA dissolution. In addition, the delayed injection that was previously demonstrated was also implemented.

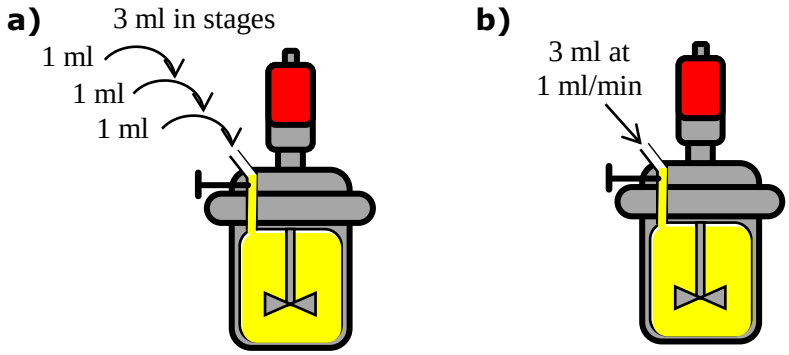


Figure 3.21. Diagram showing the injection protocol required to keep the concentration of the second monomer low, (a) the monomer injected in stages at certain time intervals, (b) the monomer injected at a low constant flow rate (1 ml min^{-1}).

The synthesis of PMMA-*b*-PDMA particles was used to demonstrate these approaches. These two approaches resulted in comparable morphologies. Spherical polymer particles were obtained (Figure 3.22) with particle size ~2.5 μm. However, the former approach is less desirable because it is rather complicated and it takes more time to manage the injection in stages to reach the desired final volume of the second monomer throughout the reaction.

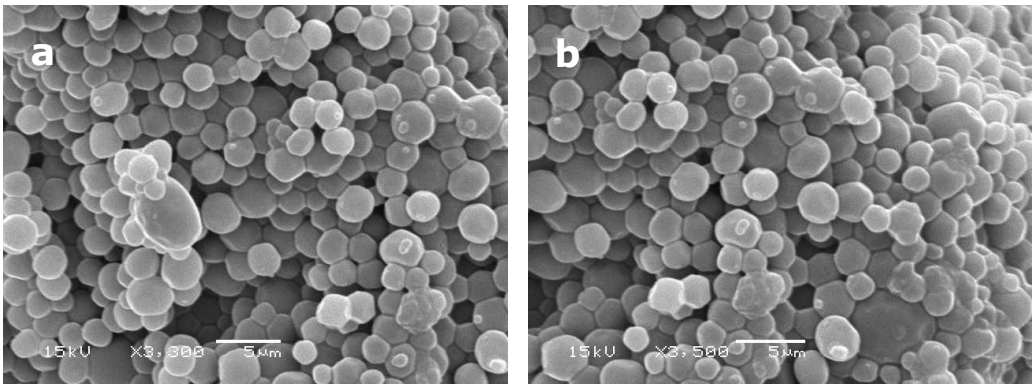


Figure 3.22. SEM images of PMMA-*b*-PDMA particles synthesised by (a) staged addition with D_n = 2.4±0.03 μm and C_v = 17%, and (b) low flow rate injection of the second monomer with D_n = 2.3±0.04 μm and C_v = 18%. Scale bars are 5 μm.

Being performed in such a way that the PMMA microparticles are not exposed to high concentrations of the second monomer resulted in a well-defined morphology. Considering these results, all further syntheses of block copolymer microparticles were performed using the delayed injection protocol with low injection flow rate.

Characteristics of block copolymers obtained *via* the chosen technique are presented in Table 3.6. A series of well-defined block copolymers were obtained with good control over the M_n and dispersity. The products were collected as dry powders, although considerable agglomeration was observed for some samples (entries 3 and 4). Overall,

the M_n values of the block copolymers increased relative to those measured for the original PMMA homopolymers. This is a clear indication that chain extension has been successful. The difference between M_n^{th} and M_n^{GPC} can be ascribed to deviations in the solution behaviour of the different polymers relative to the PMMA standards used in GPC. There is also a slight increase in dispersity between the block copolymers and the original PMMA precursor. This is proposed to be due to the different control afforded by the PMMA macro-CTA compared to the original CTA.

SEM analysis of each sample shows a spherical morphology with a size range between 1.4 - 2.5 μm (Table 3.6). The formation of spherical particles along with the high conversions suggests that the dispersion process is working well during the reaction. The coefficient of variation (C_v), ranged between 20% and 30%, which is similar to previous reports of the RAFT dispersion polymerisation in $scCO_2$.[2] Broad size distributions have been widely reported to result from heterogeneous CRP and can be related to a delay in the onset of particle nucleation.[46,47]

Table 3.6 Characteristics of block copolymer synthesised by delayed low injection flow rate of the second monomer at high pressure.

Entry	PMMA		Block copolymer						Morphology[f]	Conv (%)[g]	T_g (°C)[h]	
	M_n^{GPC} (kg mol^{-1})[a]	Đ[a]	Block copolymer	M_n^{th} (kg mol^{-1})[b]	M_n^{GPC} (kg mol^{-1})[c]	Đ[c]	D_n (μm)[d]	C_v[e] (%)			PMMA	2nd block
1	45	1.3	PMMA-*b*-PBzMA	80	74	1.4	1.77±0.04	22	Powder	76	112	61
2	45	1.3	PMMA-*b*-PBzMA	90	64	1.5	1.60±0.04	29	Powder	70	114	55
3	35	1.5	PMMA-*b*-PDEA	79	57	1.7	1.72±0.03	20	Powder and agglomerate	97	118	96
4	25	1.2	PMMA-*b*-PDEA	58	40	1.6	1.75±0.03	24	Powder and agglomerate	79	120	99
5	32	1.8	PMMA-b-PDMA	60	42	1.6	1.42±0.04	26	Powder	86	107	
6	47	1.2	PMMA-b-PS	92	81	1.6	2.20±0.06	28	Powder	95	124	104
7	27	1.2	PMMA-b-PS	77	73	1.7	2.45±0.08	32	Powder	84	119	104

The reactions were conducted at 65 °C and 275 bar for 16-72 hrs (depending on the second monomers) with molar ratio R : I = 1 : 1 and 5% stabiliser w.r.t. monomer. The second monomer was added *via* an HPLC pump at ~200 bar after PMMA being dispersed in $scCO_2$ for 2 hrs.

a. Measured using an RI GPC with THF as the eluent and applying PMMA standards
b. Calculated from: $M_n^{PMMA}+([M2]/[CTA])*MW_{M2}*conversion$
c. Measured using an RI GPC with either THF (entry 1 and 2) or $CHCl_3$ (entry 3, 4, and 5) as the eluent and applying PMMA standards. Entry 6 and 7 were measured using GPC with LS detector and THF as the eluent
d. Particle size determined from SEM images, with at least 100 particles measured.
e. Calculated using Eq. 3.2: $C_v=(\sigma/D_n)*100\%$
f. Initial appearance upon opening the vessel
g. Determined gravimetrically
h. Determined by DSC

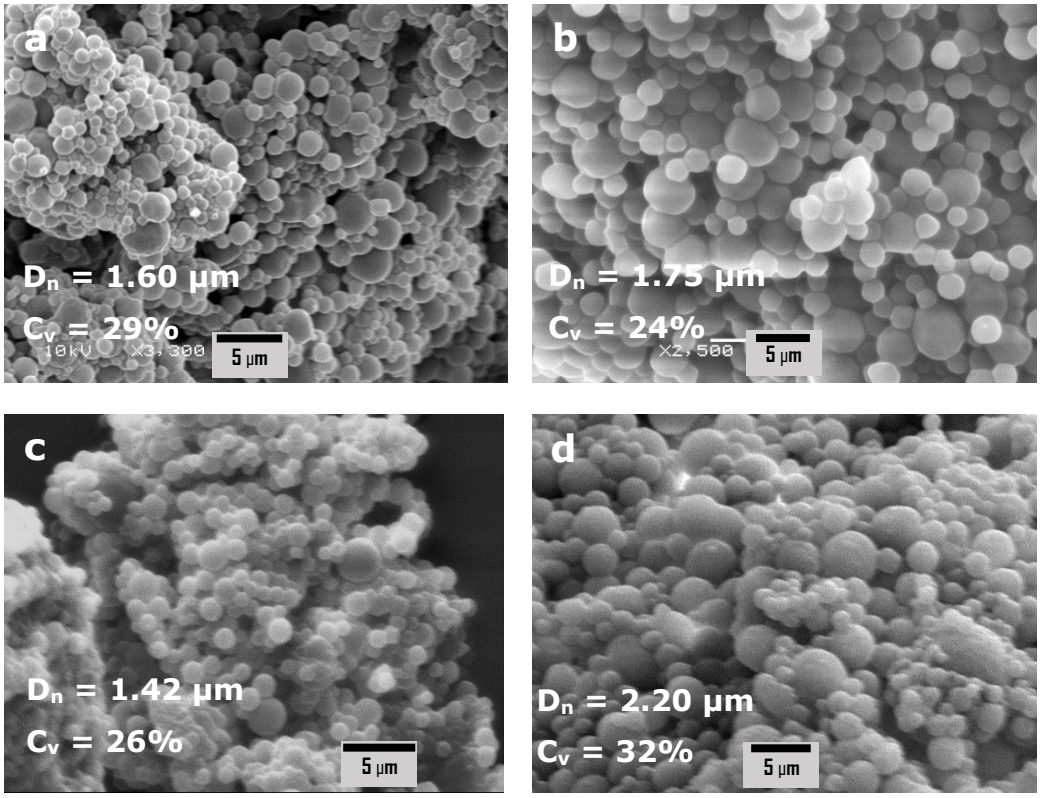


Figure 3.23. SEM images for various block copolymers from Table 3.6 (a) PMMA-*b*-PBzMA (entry 2), (b) PMMA-*b*-PDEA (entry 4), (c) PMMA-*b*-PDMA (entry 5), and (d) PMMA-*b*-PS (entry 6). All show a spherical morphology with measurements of particle diameter (D_n) and coefficient of variation (C_v). Scale bar is 5 µm.

DSC analysis shows the block copolymers have two T_gs, with the exception being PMMA-*b*-PDMA (Figure 3.24). Only minimum chain extension occurs in PMMA-*b*-PDMA as revealed by GPC (Table 3.6, entry 5). The T_gs between 112-124 °C are attributed to the PMMA block, while the lower transitions occur at values expected for the respective extended blocks, as summarised in Table 3.6. This provides evidence of the existence of the second polymer block and also indicates that the block copolymers exhibit microphase separation behaviour.

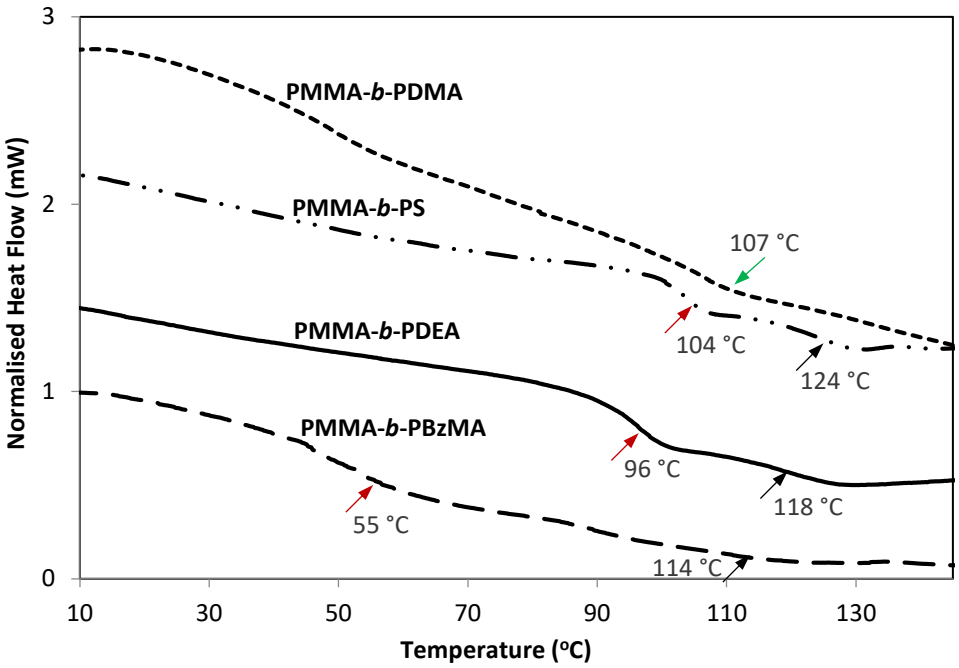


Figure 3.24. Representative DSC traces of block copolymers presented in Table 3.6. PMMA-*b*-PBzMA (entry 2), PMMA-*b*-PDEA (entry 3), PMMA-*b*-PS (entry 6), and PMMA-*b*-PDMA (entry 5). Green arrow shows T_g of PMMA-*b*-PDMA copolymer. Black and red arrows show the T_g of the PMMA block and the second block, respectively.

3.5.3 Kinetic Studies of The Two-stage Synthesis

Kinetics of the first polymerisation stage, which is a RAFT-controlled polymerisation of MMA in $scCO_2$ have been reported elsewhere and indicated good control.[2,48] Meanwhile, a kinetic study needs to be carried out to investigate the extent of control over the second-stage polymerisation. For this study, the polymerisation was performed in a 60 mL autoclave with a sampling tap at the bottom of the autoclave, enabling collection of the intermediate block copolymer products at certain time intervals during the reaction without depressurising the reaction vessel (Figure 2.2). Kinetic studies of both the PMMA-*b*-PBzMA and PMMA-*b*-PS block copolymer reactions were investigated. A series of samples were collected at various times after addition of the second monomer, from

which a plot of M_n^{GPC} and dispersity vs. time were constructed (Figure 3.25).

The plots show the growth of the polymer chains over the course of the reaction. A linear correlation between the molecular weight and the reaction time was obtained, indicating steady growth of the polymer both for PMMA-*b*-PBzMA and PMMA-*b*-PS. Dispersities of the samples collected during the polymerisation of BzMA are relatively constant (1.4) over the reaction with the final dispersity of 1.5. On the other hand, polymerisation of styrene initially exhibited low dispersity (~1.2) but this then increase up to 1.3 at high conversion.

In general, the dispersity values for all samples were well below 1.6. These confirm the PMMA-DATC macro RAFT agent controlled the dispersion polymerisation of both BzMA and styrene in $scCO_2$. The plots also show that the PMMA chains are living and can be extended to obtain a block copolymer. Regarding the reaction time, the polymerisation of styrene takes longer than BzMA. Polymerisation of styrene is often very slow, especially for controlled polymerisations since styrene has low reactivity.[36]

A plot of M_n vs. conversion was not created, because some volatilisation of monomer always occurs during sampling from the vessel. Even in absence of this plot, the controlled mechanism of the polymerisation seemed to be maintained, which explains the efficient control over molecular weight and dispersity observed in this Chapter.

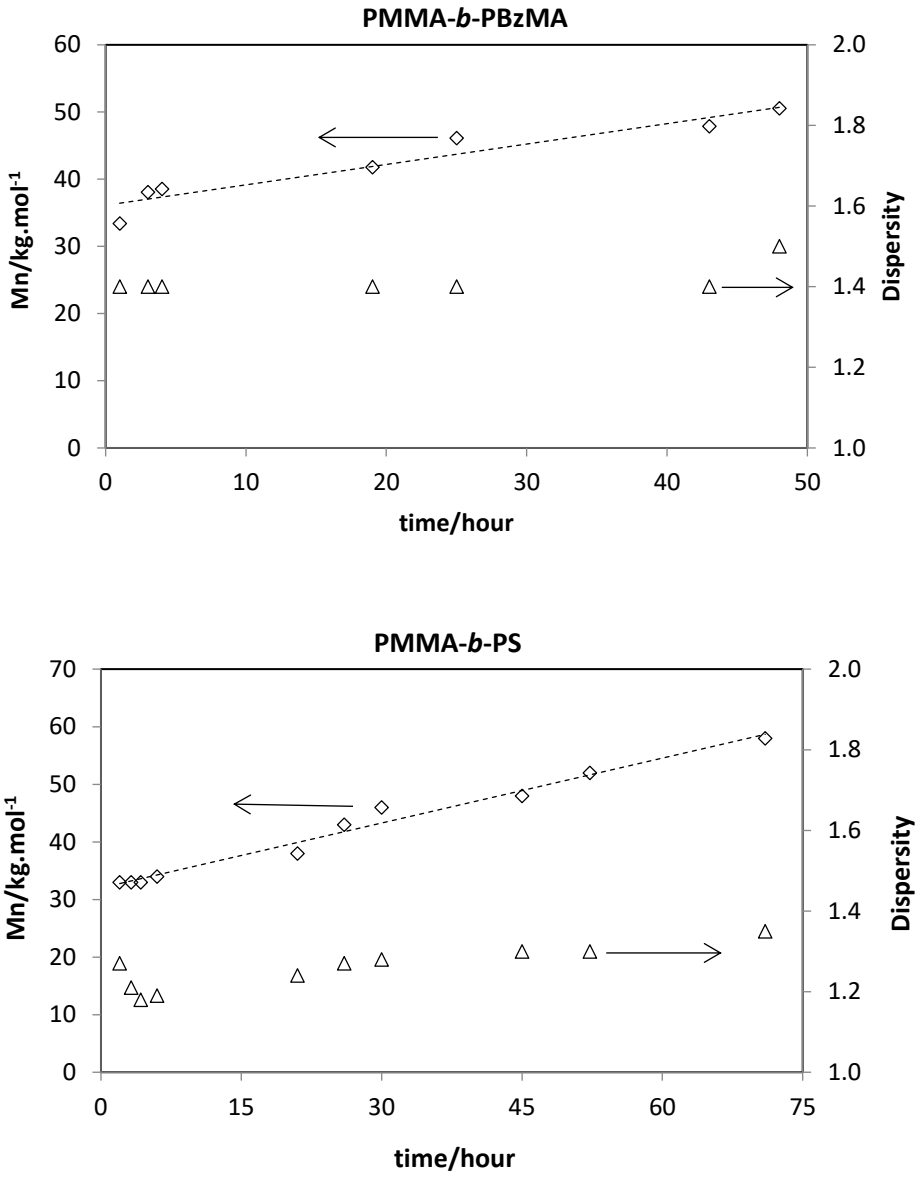


Figure 3.25. Plot of M_n^{GPC} and dispersity vs. time for the polymerisation of BzMA (top) and styrene (bottom) using the PMMA macro-RAFT agent, showing a linear increase between the molecular weight and the reaction time with low dispersity for all samples. The dashed line is a linear fit to the data in both cases.

3.5.4 Internal Structure of Block Copolymer Microparticles

A block copolymer that comprises two polymer blocks which are thermodynamically incompatible should undergo microphase separation under certain conditions. As discussed in Chapter 1, this process depends

upon the interaction parameter of the blocks (χ), volume fraction (f), and the overall degree of polymerisation (N). Microphase separation results in the formation of nanostructured morphologies, such as body centered cubic (BCC) packing of spheres (SPH), hexagonally packed cylinders (CYL), the bicontinuous gyroid phase (GYR), and lamellae (LAM).[35,49] The copolymer morphology is an important characteristic which can exert a strong influence on the bulk physical properties and is therefore of great importance with regard to applications.[50]

A range of block copolymer microparticles synthesised in $scCO_2$ were imaged by TEM (cross-sectional view) to investigate their internal morphology.[1] Varying either the block volume fraction or block pair resulted in a wide range of controlled internal nanostructure morphologies, including LAM, CYL, and SPH.

In this section, the internal nanostructure of the block copolymers obtained using the two-stage method was investigated by TEM. Dry powders of the synthesised products were embedded in epoxy resin and then ultramicrotomed to make ultra-thin cross-sectional slices (80–100 nm) through the spherical block copolymer microparticles. The sections were treated with an appropriate staining compound prior to TEM imaging to increase the contrast between the block domains so that the image can clearly show the phase separation of the block copolymers.

Three different block copolymer systems, PMMA-*b*-PBzMA, PMMA-*b*-PS, and PMMA-*b*-PDEA, were analysed over a range of volume fractions. The volume fraction of the two blocks within a diblock copolymer is a key factor in determining the morphology.[35] In this study, the volume fraction was adjusted by varying the amount of PMMA-macro CTA and the second block to control their molar ratios and relative chain lenghts. The volume fraction with respect to PMMA was calculated using Equation 3.2.

$$f_{PMMA} = \frac{w_{PMMA}/D_{PMMA}}{w_{PMMA}/D_{PMMA} + w_{block\,2}/D_{block\,2}} \qquad \text{(Equation 3.2)}$$

The weight ratio of PMMA (w_{PMMA}) within a block copolymer was obtained from Equation 2.2. Densities (D) of PMMA, PBzMA, and PS are 1.17 g cm^{-3}, 1.179 g cm^{-3}, and 1.05 g cm^{-3}, respectively.[36] The density for PDEA was not available, hence weight fraction was measured and used as a proxy instead of the volume fraction.

The first system studied for its phase separation was PMMA-*b*-PBzMA (Table 3.7). Samples were stained with RuO_4 vapour prior to TEM imaging to increase the contrast between the PMMA and PBzMA domains. RuO_4 was adsorbed selectively by the PBzMA domains, thus the PMMA and PBzMA domains appear as bright and dark regions, respectively. The staining process has been demonstrated previously and it had no effect on the nanostructure.[1]

Table 3.7 Characteristics of PMMA-*b*-PBzMA microparticles investigated for phase separation behaviour

Entry	M_n^{GPC} (kg.mol^{-1})	$Đ$	W_{PMMA}	f_{PMMA}	Internal Structure
1	64	1.5	0.46	0.46	LAM
2	90	1.5	0.31	0.31	LAM

PMMA-*b*-PBzMA block copolymer microparticles with a PMMA volume fraction of 0.46 showed a LAM morphology (Figure 3.26 a and b). This morphology could be anticipated based on the volume fraction when compared to the expected diblock copolymer phase diagrams in the literature.[35] The LAM structure was also observed for a volume fraction of 0.31 (Figure 3.26 c and d). This finding was similar to previously reported[42] since this system has a wide window/range for LAM structure. Well-ordered PMMA and PBzMA domains can be clearly seen in high magnification images (Figure 3.26 b and d) with long range/double layer domain size is

~40 nm. Both domains of this block copolymer are methacrylates and have a similar degree of swelling in $scCO_2$. Thus, the solvent ($scCO_2$) does not induce any significant effect on the phase separation anticipated by the traditional phase diagram of diblock copolymer.

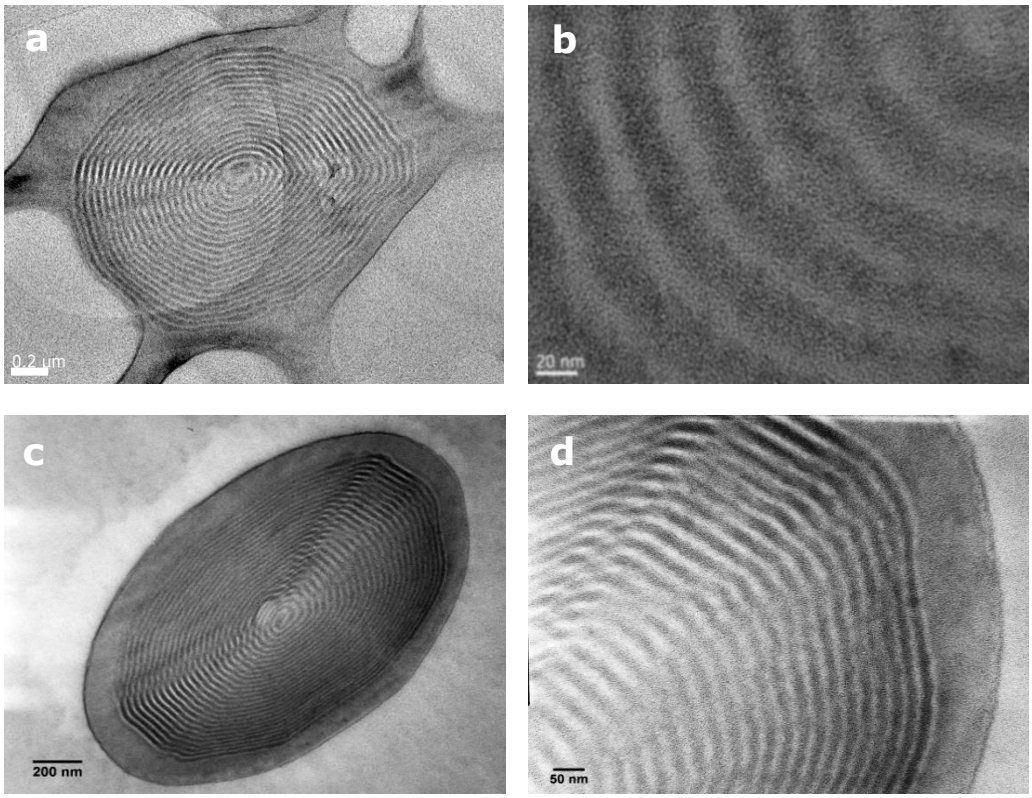


Figure 3.26 TEM images of cross-sectional PMMA-*b*-PBzMA microparticles from Table 3.7, (a) and (b) showing LAM structure correspond to entry 1, and (c) and (d) showing LAM structure correspond to entry 2. High magnification images (b and d) clearly show well-ordered domains.

The second block copolymer is PMMA-*b*-PS (Table 3.8). The phase separation of this block copolymer has been reported in bulk films,[51,52] thin films[24,53,54] as well as in spherical particles[1,26,55]. Most reports have targeted the onion-like multilayer (lamellar) structure. Here, block copolymers with a range of volume fractions were prepared in order to observe the change in copolymer morphology.

Table 3.8 Characteristics of PMMA-*b*-PS microparticles investigated for internal nanostructure

Entry	M_n^{GPC} (kg.mol^{-1})	*Đ*	W_{PMMA}	f_{PMMA}	Internal Structure
1	65	1.4	0.85	0.83	SPH
2	71	1.5	0.56	0.53	CYL
3	73	1.7	0.51	0.49	CYL
4	70	1.4	0.33	0.31	LAM
5	53	1.8	0.27	0.25	LAM/CYL*

*the first mentioned is the majority

When the volume fraction of PMMA is much higher than PS (0.83), a SPH structure was obtained (Table 3.8 entry 1; Figure 3.27a). Decreasing the PMMA volume fraction to 0.25 relative to the PS domains resulted in mixed structures which contained regions of both LAM and CYL morphologies (Table 3.8 entry 5; Figure 3.27e). The presence of mixed structures will be discussed in the next section.

A CYL structure was observed for the symmetrical PMMA-*b*-PS copolymer (Table 3.8 entry 2 and 3; Figure 3.27 b and c). This deviates from the expected LAM structure theoretically predicted for a symmetrical diblock copolymer. Meanwhile, the LAM structure was obtained at a lower PMMA volume fraction of 0.31 (Table 3.8 entry 4; Figure 3.27e). Previous reports indicate that the deviation in this block copolymer system is due to differences in the CO_2-philicity of PMMA relative to PS.[1,27] The solubility of CO_2 in PMMA is higher than in PS, and hence PMMA absorbs more CO_2 than PS.[56] This results in a higher effective volume fraction of PMMA than expected.

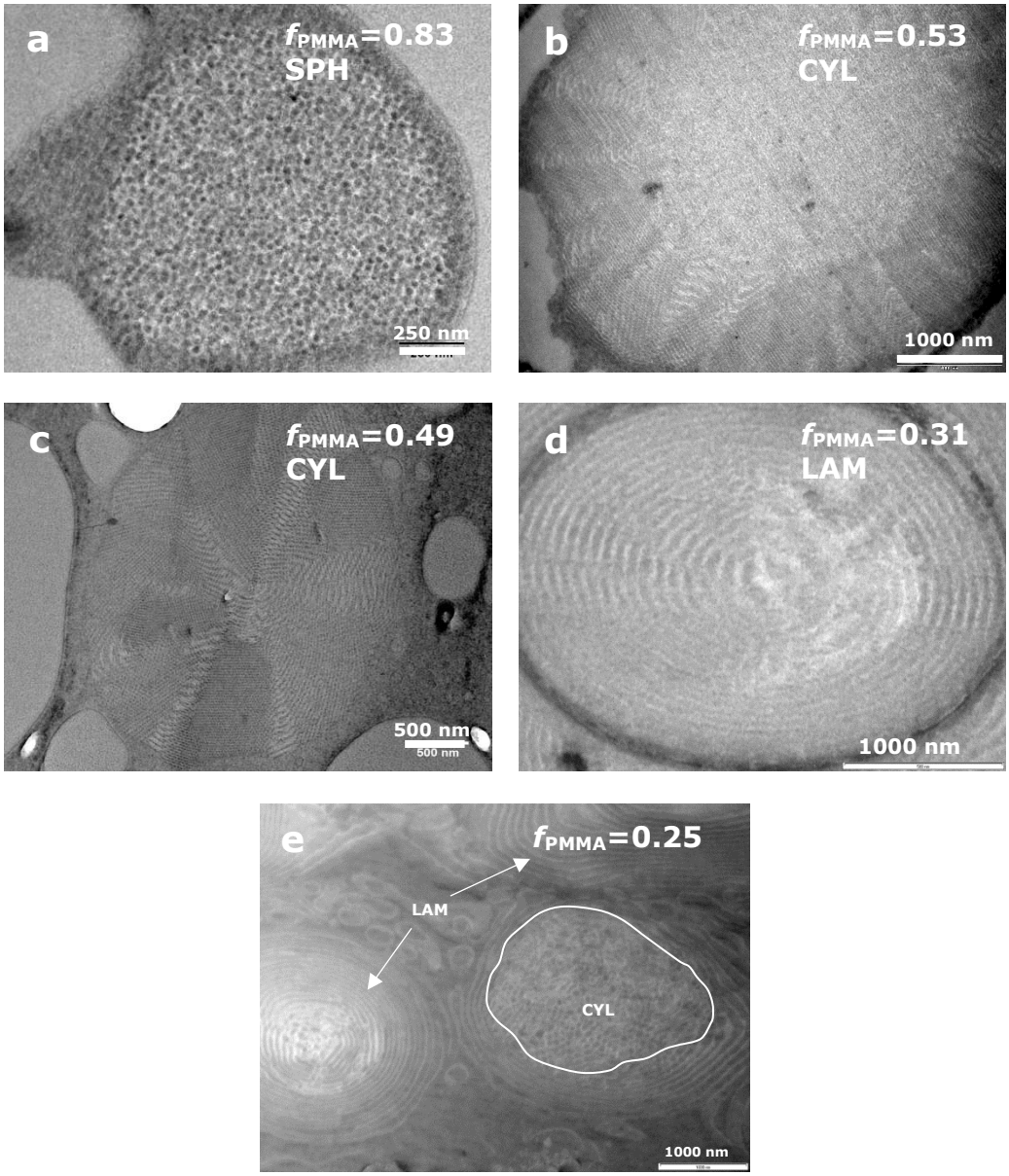


Figure 3.27 TEM images showing internal nanostructures of PMMA-*b*-PS microparticles from Table 3.8. (a) SPH structure corresponds to entry 1, (b) CYL structure corresponds to entry 2, (c) CYL structure corresponds to entry 3, (d) LAM structure corresponds to entry 4, (e) LAM/CYL mixed structure corresponds to entry 5.

PMMA-*b*-PDEA block copolymers were also synthesised targeting different molecular weights and weight fractions to produce two different structures (Table 3.9). A morphological shift was also observed for this system as the blocks have different CO_2-philicity. Nearly symmetrical PMMA-*b*-PDEA copolymer (Table 3.9 entry 1) showed a GYR structure along

with some LAM (Figure 3.28, a and b). When w_{PMMA} increased to 0.85, SPH of PDEA in a PMMA matrix with a considerable quantity of disordered particles were instead observed (Figure 3.28, c and d). The appearance of the disordered particles is probably due to proximity to the order-disorder transition (ODT).

Table 3.9 Characteristics of PMMA-*b*-PDEA microparticles investigated for phase behaviour

Entry	M_n^{GPC} (kg.mol^{-1})	*Đ*	W_{PMMA}	Internal Structure
1	57	1.7	0.43	GYR/LAM
2	109	1.9	0.85	SPH/DIS

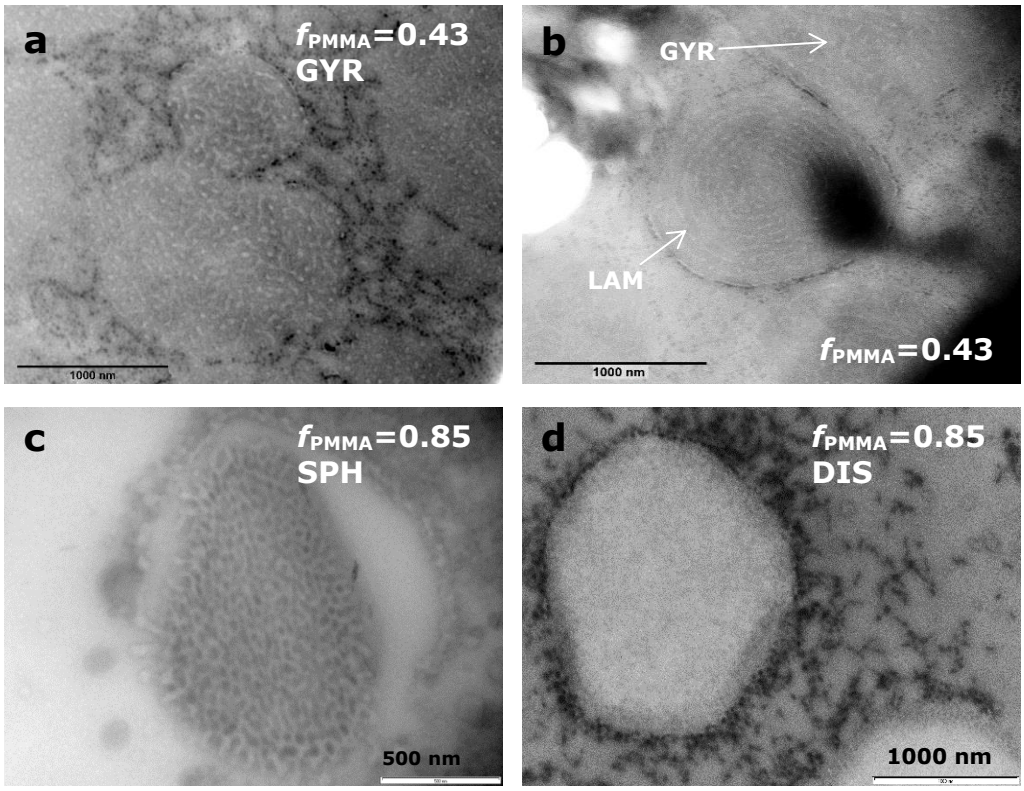


Figure 3.28 TEM images showing internal nanostructures of PMMA-*b*-PDEA microparticles from Table 3.9. (a) GYR and (b) LAM/GYR structure correspond to entry 1, (c) SPH and (d) disordered morphologies correspond to entry 2.

In summary, these block copolymer microparticles have internal nanostructures due to polymer-polymer microphase separation. The

nanostructures can be controlled by changing the volume fraction or block pair. Additionally, the different CO_2-philicities of the block pair alters the phase separation behaviour from the traditional phase diagram. All of these results show that the developed method produces a comparable product to the one-pot method previously reported.[1] More importantly, the nanostructured PMMA-based block copolymers can be prepared within a much shorter timeframe, as intended.

3.5.5 Particle Morphologies at Low PMMA Content

Some block copolymers showed the presence of two or more structures within a single particle (Table 3.10). Different nanostructures appear between the interior and the exterior of the particles. An interior structure indicates lower volume fraction of the second block (SPH, CYL) compared to the exterior (LAM) (Figure 3.29). Here, the second block, either PS or PBzMA, appears as the dark region due to selective staining by RuO_4.

Table 3.10 Characteristics of block copolymers with low PMMA content

Entry	Block copolymer	M_n^{GPC} (kg/mol)	Đ	f_{PMMA}	Morphology
1	PMMA-*b*-PS	53	1.9	0.25	SPH/CYL/LAM
2	PMMA-*b*-PS	40	1.5	0.31	CYL/LAM
3	PMMA-*b*-PBzMA	90	1.5	0.31	LAM
4	PMMA-*b*-PBzMA	117	1.7	0.30	LAM

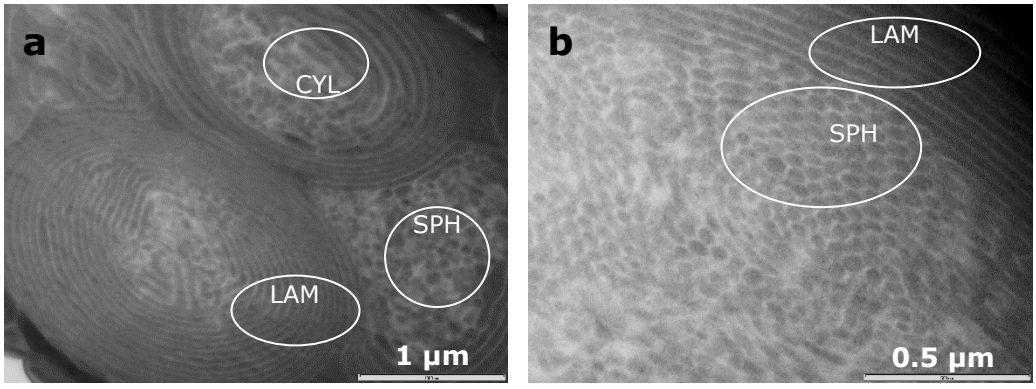


Figure 3.29 TEM images of PMMA-*b*-PS (entry 1, Table 3.10) showing mixed structures within a single particle.

These mixed structures could be a consequence of the high dispersity of the diblock copolymers. Similar mixed morphologies have been reported by Matsushita *et al*.[57,58] Heterogeneity of the block chain length appears to affect the arrangement of polymer segments for the domain formation. There is also a well-established dependence of chain length and domain size.[59] Figure 3.30 shows a schematic comparison of chain conformation between monodisperse and polydisperse block chain length.

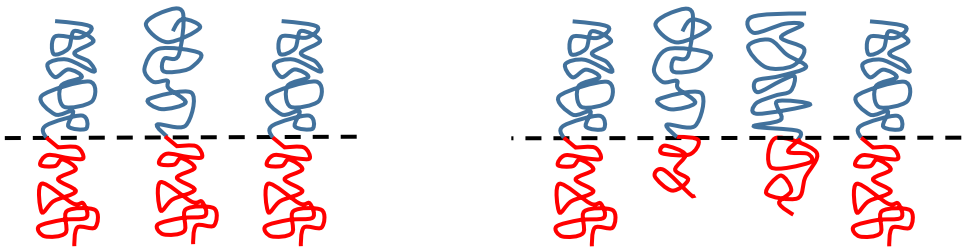


Figure 3.30 Schematic comparison of chain conformation between monodisperse (left) and polydisperse (right) block chain length in a diblock copolymer. Adapted from literature.[57]

Domain size of the second block (PS) gradually increased when moving from the core (~3 nm) towards the surface (~7 nm) regions of the particles (Figure 3.31a). These features were only found in block copolymers with a low PMMA content, especially PMMA-*b*-PS. At lower PMMA contents, a high concentration of the second monomer was added, thus the propagation occurred even more rapidly. However, in PMMA-*b*-PBzMA, mixed structures appear to be avoided (Figure 3.31b). This might be because the miscibilities of all-methacrylate blocks in CO_2 are relatively similar. For this reason, we can speculate there is a much more uniform diffusion of monomer across the particle and hence more uniform propagation to block copolymer.

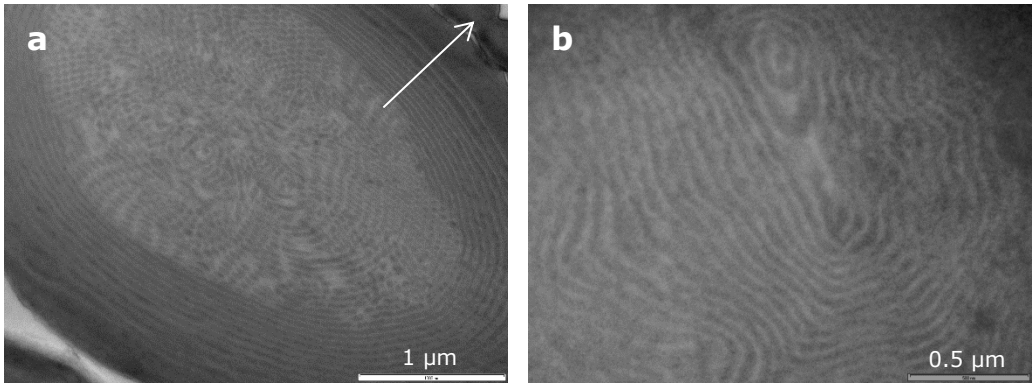


Figure 3.31 TEM images of cross-sectional (a) PMMA-*b*-PS particles with SPH/CYL/LAM structures (entry 1 in Table 3.10) and (b) PMMA-*b*-PBzMA particles with LAM structure (entry 4 in Table 3.10). The arrow shows an increase in domain size from the inner into the outer layer of the particles.

Introducing a high concentration of the second monomer also appears to affect the block copolymer particle size and their surface morphology. The particles have a large size (> 5 µm) and a rough surface. TEM images of cross-sectional particles indicate that the large particles are covered by a layer of smaller particles (~0.4 µm) (Figure 3.32a). The smaller particles are believed to be PS homopolymer due to their dark appearance as a result of RuO_4 staining (Figure 3.32b). In addition, GPC analysis showed the appearance of a low molecular weight shoulder that indicates the presence of PS homopolymer (Figure 3.33). However, this is rather speculative since the shoulder could also refer to the polymeric stabiliser used in the synthesis.

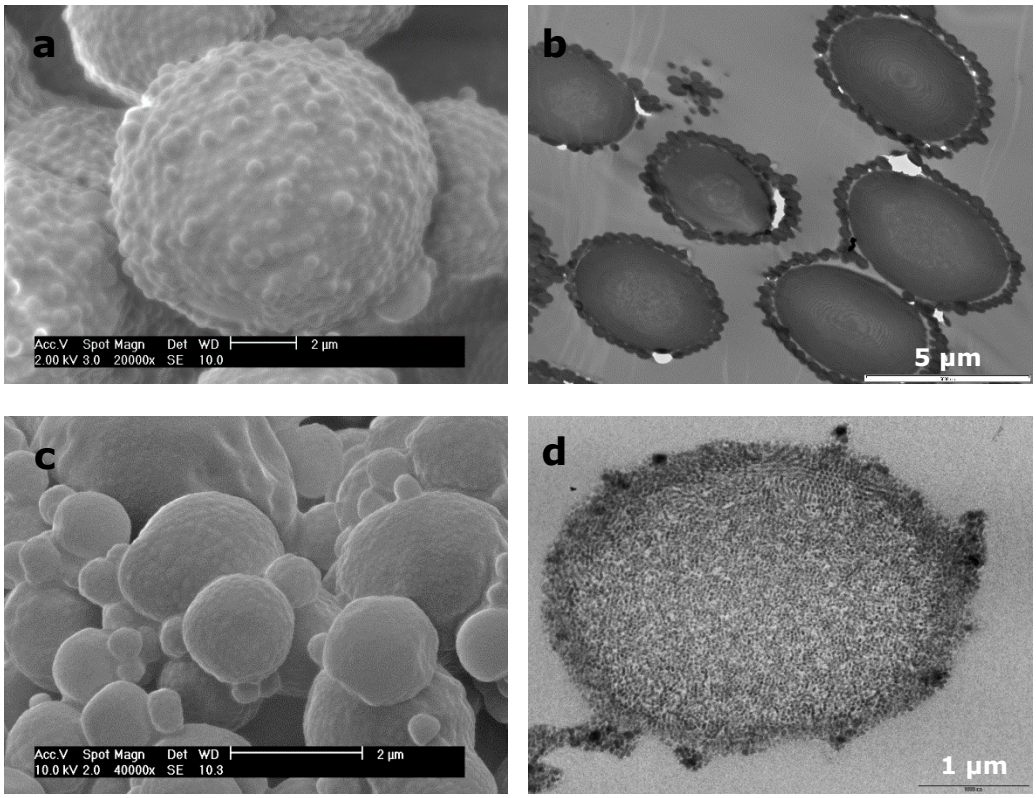


Figure 3.32 (a) SEM, and (b) TEM images of PMMA-*b*-PS (Table 3.10, entry 1) with a low PMMA content showing large particles with rough surface, the large particles are covered by smaller particles. (c) SEM and (d) TEM images of symmetrical PMMA-*b*-PS particles as comparison, showing a smooth morphology surface,

These observations can be explained by considering the case when a high concentration of the second monomer is added. In this case, the monomer concentration in the particles increases, which corresponds to more monomer being polymerised in the PMMA seed particles and thus larger particles are formed. The more monomer that is added, the larger the particles that will be formed. Furthermore, the amount of monomer in the continuous phase will also increase, which can increase the likelihood of secondary nucleation. This secondary nucleation leads to a new population of smaller particles from the second monomer being added (in this case styrene).

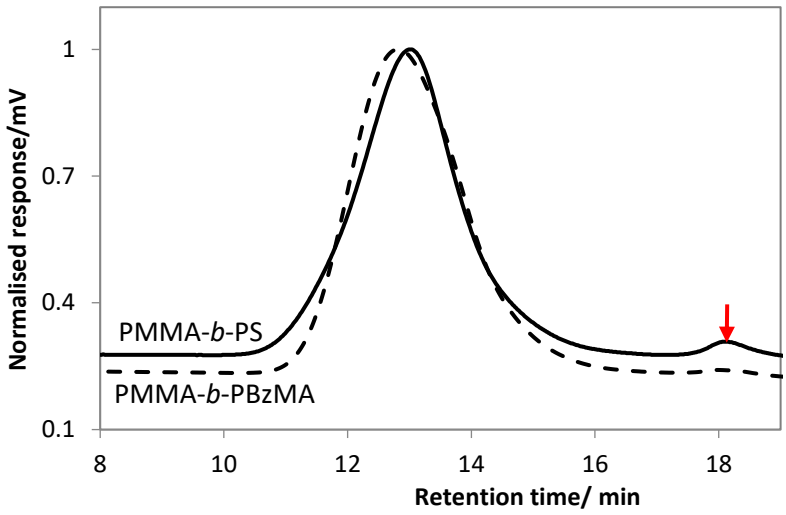


Figure 3.33. GPC traces of PMMA-*b*-PS (Table 3.10, entry 1) showing the appearance of a low molecular weight shoulder (arrow) and PMMA-*b*-PBzMA (Table 3.10, entry 4) without a low molecular weight shoulder.

3.6 Conclusions

This chapter has presented a new and versatile method to prepare nanostructured block copolymer microparticles *via* a two-stage method. The method exploited the living character of pre-synthesised RAFT functional polymer chains. The first stage involved RAFT polymerisation of MMA in $scCO_2$ dispersion, which produced well-controlled PMMA microparticles at high conversion. Moreover, the PMMA chain-ends remained reactive/living, even after storage for months. Therefore, it is possible to create large batches of PMMA living microparticles that can be stored for further processing on demand.

The chain extension to form block copolymers was also easily performed by using the living PMMA microparticles as macro-CTAs to control polymerisation of the second monomer. In order to maintain the morphology of the PMMA microparticles, care needed to be exercised when adding the second monomer. This addition needed to be delayed until the PMMA particles were already well-dispersed in $scCO_2$ to prevent softening or even dissolution of the PMMA particles by the monomer. Once this

process was understood, the technique was successfully applied to a broad range of monomers including styrene and dialkyl acrylamides.

The block copolymers undergo microphase separation to form nanostructures inside the spherical particles due to incompatibility between the two polymer blocks. Different internal morphologies were observed, including body centered cubic packing of spheres, hexagonally packed cylinders, the bicontinuous gyroid, and lamellae. These morphologies were obtained by changing either the block copolymer pairs or the block volume fractions. For the PMMA-*b*-PBzMA block copolymers, the phase-separated morphologies followed the theoretical phase diagram, while deviations were observed for PMMA-*b*-PS and PMMA-*b*-PDEA. These deviations are due to differences in the CO_2-philicity of PMMA relative to the second block. This interpretation is consistent with previous reports that CO_2 acts as a block selective solvent during the synthesis.[1,27]

The two-stage synthesis method also appears to affect the particle morphology when a high concentration of second monomer was added in the second stage. This led to the formation of large particles (>5 μm) with a rough surface. In addition, large particles with high dispersity exhibit more than one internal nanostructure.

3.7 References

1. Jennings, J. et al. *J. Am. Chem. Soc.* **134**, 4772–4781 (2012).
2. Gregory, A.M., Thurecht, K.J. & Howdle, S.M. *Macromolecules* **41**, 1215–1222 (2008).
3. Zetterlund, P.B., Kagawa, Y. & Okubo, M. *Chem. Rev.* **108**, 3747–3794 (2008).
4. Warren, N.J. & Armes, S.P. *Prog. Polym. Sci.* **136**, 10174–10185 (2014).
5. Charleux, B., Delaittre, G., Rieger, J. & D'Agosto, F. *Macromolecules* **45**, 6753–6765 (2012).
6. Derry, M.J., Fielding, L.A. & Armes, S.P. *Prog. Polym. Sci.* **52**, 1–18 (2016).

7. Warren, N.J., Mykhaylyk, O.O., Mahmood, D., Ryan, A.J. & Armes, S.P. *J. Am. Chem. Soc.* **136**, 1023–1033 (2014).

8. An, Z. et al. *J. Am. Chem. Soc.* **129**, 14493–14499 (2007).

9. Rieger, J. & Charleux, B. *Soft Matter* **7**, 3482–3490 (2011).

10. Blanazs, A., Madsen, J., Battaglia, G., Ryan, A.J. & Armes, S.P. *J. Am. Chem. Soc.* **133**, 16581–16587 (2011).

11. Chambon, P., Blanazs, A., Battaglia, G. & Armes, S.P. *Macromolecules* **45**, 5081–5090 (2012).

12. Shen, W. et al. *Macromolecules* **44**, 2524–2530 (2011).

13. Liu, G., Qiu, Q., Shen, W. & An, Z. *Macromolecules* **44**, 5237–5245 (2011).

14. Liu, G., Qiu, Q. & An, Z. *Polym. Chem.* **3**, 504–513 (2012).

15. Sugihara, S., Blanazs, A., Armes, S.P., Ryan, A.J. & Lewis, A.L. *J. Am. Chem. Soc.* **133**, 15707–15713 (2011).

16. Semsarilar, M., Jones, E.R., Blanazs, A. & Armes, S.P. *Adv. Mater.* **24**, 3378–3382 (2012).

17. Jones, E.R., Semsarilar, M., Blanazs, A. & Armes, S.P. *Macromolecules* **45**, 5091–5098 (2012).

18. Zehm, D., Ratcliffe, L.P.D., Armes, S.P., Ratcliffe, L.P.D. & Armes, S.P. *Macromolecules* **46**, 128−139 (2013).

19. Semsarilar, M., Penfold, N.J.W., Jones, E.R. & Armes, S.P. *Polym. Chem.* **6**, 1751–1757 (2015).

20. Semsarilar, M., Jones, E.R. & Armes, S.P. *Polym. Chem.* **5**, 195–203 (2014).

21. Jones, E.R. et al. *Macromolecules* **49**, 172–181 (2016).

22. Derry, M.J. et al. *Chem. Sci.* **7**, 5078–5090 (2016).

23. Magerle, R. & Krausch, G. *Adv. Mater.* **14**, 1579–1583 (2002).

24. Chavis, M.A., Smilgies, D.-M., Wiesner, U.B. & Ober, C.K. *Adv. Funct. Mater.* **25**, 3057–3065 (2015).

25. Gu, X., Gunkel, I., Hexemer, A. & Russell, T.P. *Macromolecules* **49**, 3373–3381 (2016).

26. Kitayama, Y., Kagawa, Y., Minami, H. & Okubo, M. *Langmuir* **26**, 7029–7034 (2010).

27. Jennings, J. et al. *Polym. Chem.* **7**, 905–916 (2016).

28. Lupi, F.F. et al. *Nanotechnology* **24**, 315601 (2013).

29. Paradiso, S.P., Delaney, K.T., García-Cervera, C.J., Ceniceros, H.D. & Fredrickson, G.H. *Macromolecules* **49**, 1743–1751 (2016).

30. Kitayama, Y., Yorizane, M., Minami, H. & Okubo, M. *Polym. Chem.* **3**, 1394–1398 (2012).

31. Gregory, A.M. Controlled polymerisations in Supercritical Carbon Dioxide. *Thesis*. The University of Nottingham (2007).

32. Zong, M., Thurecht, K.J. & Howdle, S.M. *Chem. Commun.* **45**, 5942–5944 (2008).

33. Perrier, S., Barner-Kowollik, C., Quinn, J.F., Vana, P. & Davis, T.P.

Macromolecules **35**, 8300–8306 (2002).

34. Jennings, J. et al. *Macromolecules* **46**, 6843–6851 (2013).
35. Bates, F.S. & Fredrickson, G.H. *Annu. Rev. Phys. Chem.* **41**, 525–557 (1990).
36. J. Brandrup E. A. Grulke, A. Abe and D. R. Bloch, E.H.I. *Polymer Handbook*. 4th Edition. John Wiley & Sons: New Jersey, USA, (1999).
37. Hamley, I.W. *Block Copolymer Physics*. Oxford Science Publications: Oxford, UK (1998).
38. Lai, J.T., Filla, D. & Shea, R.Y. *Macromolecules* **35**, 6754–6756 (2002).
39. Keddie, D.J. *Chem. Soc. Rev.* **43**, 496–505 (2014).
40. Grignard, B. et al. *Macromolecules* **41**, 8575–8583 (2008).
41. Guan, Z., Combes, J.R., Menceloglu, Y.Z. & DeSimone, J.M. *Macromolecules* **26**, 2663–2669 (1993).
42. Jennings, J. Synthesis and Self-Assembly of Block copolymers in Supercritical CO_2. *Thesis.* The University of Nottingham (2013).
43. O'Neill M. L. et al. *Macromolecules* **31**, 2838–2847 (1998).
44. Cooper, A.I. *J. Mater. Chem.* **10**, 207–234 (2000).
45. Benaglia, M., Rizzardo, E., Alberti, A. & Guerra, M. *Macromolecules* **38**, 3129–3140 (2005).
46. Saikia, P.J., Lee, J.M., Lee, B.H. & Choe, S. *J. Polym. Sci. Part A Polym. Chem.* **45**, 348–360 (2007).
47. Song, J.S. & Winnik, M.A. *Macromolecules* **39**, 8318–8325 (2006).
48. Thurecht, K.J., Gregory, A.M., Wang, W. & Howdle, S.M. *Macromolecules* **40**, 2965–2967 (2007).
49. Bates, F.S. & Fredrickson, G.H. *Phys. Today* **52**, 32–38 (1999).
50. Darling, S.B. *Prog. Polym. Sci.* **32**, 1152–1204 (2007).
51. Widin, J.M. et al. *Macromolecules* **46**, 4472–4480 (2013).
52. Liu, C.C. et al. *Macromolecules* **46**, 1415–1424 (2013).
53. Kim, K. et al. *Macromolecules* **49**, 1722–1730 (2016).
54. Xuan, Y. et al. *Macromolecules* **37**, 7301–7307 (2004).
55. Tanaka, T., Saito, N. & Okubo, M. *Macromolecules* **42**, 7423–7429 (2009).
56. Aubert, J.H. *J. Supercrit. Fluids* **11**, 163–172 (1998).
57. Matsushita, Y. et al. *Macromolecules* **36**, 8074–8077 (2003).
58. Noro, A., Iinuma, M., Suzuki, J., Takano, A. & Matsushita, Y. *Macromolecules* **37**, 3804–3808 (2004).
59. Black, C.T. et al. *IBM J. Res. Dev.* **51**, 605–633 (2007).

Chapter 4 Study of The Internal Nanostructure Development of Block Copolymer Microparticles

4.1 Overview

Block copolymers can form ordered morphologies, such as lamellae, hexagonally packed cylinders, spheres, and more complex structures.[1] These morphologies are organised through the microphase separation behaviour of individual blocks and influence to the physical properties of the block copolymers. Therefore, understanding the mechanism of microphase separation and how the morphology develops is vital to ensure reproducibility of a particular morphology with the desired properties. This chapter will focus on the development of the internal nanostructure of block copolymer microparticles which are produced by Reversible Addition Fragmentation Chain Transfer (RAFT) dispersion polymerisation in supercritical CO_2 ($scCO_2$).

The internal nanostructure will be monitored by *in situ* Small Angle X-ray Scattering (SAXS) in combination with off-line Transmission Electron Microscopy (TEM), which are often used to observe structural features at the nano-scale. Importantly, *in situ* SAXS measurements enable morphological changes to be monitored as well as the understanding of the growth mechanism online. A new high pressure X-ray autoclave was designed to achieve more efficient mixing during the structural investigation by *in situ* SAXS experiments under high pressure. Reproducibility tests will be conducted to ensure that the new vessel produces comparable products to the standard vessel that is normally used in routine syntheses.

These *in situ* SAXS studies together with Nuclear Magnetic Resonance (^{1}H NMR) and electron microscopy techniques should provide detailed insights

regarding block copolymer morphological transition during the dispersion polymerisation in $scCO_2$, thus a mechanism of the microphase separation development can be envisaged.

4.2 Introduction

4.2.1 SAXS Studies of Block Copolymer Phase Behaviour

Small-Angle X-ray Scattering (SAXS) is used to analyse structural features of systems at the supramolecular dimension, typically ranging from few nm to hundreds nm.[2] Since X-rays are primarily scattered by electrons, SAXS reveals electron density inhomogeneities within a sample.

A diblock copolymer can be treated as a two-phase system. The scattering intensity of diblock copolymers can be correlated with the electron density difference between the two blocks (ρ_i), and the volume fraction of both blocks (ϕ_i) (Equation 4.1). The total scattering intensity (Q) or Porod invariant reaches a maximum value when the relative volume fractions of the two phases are equal. It is particularly useful to follow the composition changes in a reacting system because the invariant is independent of morphological features.[2,3]

$$Q = \int_0^\infty I(q)q^2dq \approx (\rho_1 - \rho_2)^2 \emptyset_1 \emptyset_2 \qquad \text{(Equation 4.1)}$$

The periodic distance (d) of microphase-separated domains of the block copolymer can be obtained from Bragg's law. Using the peak maxima (q^*) of the SAXS profile, the domain sizes can be calculated using Equation 4.2.[4]

$$d = \frac{2\pi}{q^*} \qquad \text{(Equation 4.2)}$$

Multiple scattering peaks can be attributed to a block copolymer with long-range order of its periodic microdomain structure. The relative position of

the peaks has a characteristic spatial relationship depending on the shape of the microdomain structure. Therefore, this can be used to determine the microdomain morphology of the block copolymer. For example, the microdomain with lamellae morphology should exhibit higher order reflections with a ratio to the *q* values at the scattering maxima of 1, 2, 3, 4, …, n. Cylinders in a hexagonal array and spheres in a body-centred cubic array should have characteristic *q* ratios of 1, √3, 2, √7, 3,... and 1, √2, √3, 2, √5,..., respectively.[5]

SAXS analysis is commonly used together with electron microscopy techniques,[6–8] as SAXS is an indirect technique but probes a larger sample volume without detrimental sample preparation steps; thus, it provides a more representative information of the whole sample. For example, SAXS analysis was used to confirm the formation of double gyroid morphology in diblock copolymer complexes of polystyrene-*b*-poly(4-vinylpyridine) (3-pentadecylphenol) (PS-*b*-P4VP(PDP)$_x$) together with TEM studies.[6] The presence of the double gyroid phase was confirmed by a *q* ratio of √6:√8 for the first two reflections and also some higher order gyroid peaks of relatively low intensity. The systematic change in the PDP and PS contents produced a range of morphologies, including lamellae, gyroid, hexagonally-packed cylinders, and biphasic (mixed) morphologies. The biphasic morphologies were confirmed by TEM. However, SAXS patterns typically exhibited typically poorly-defined reflections as the peaks of both phases generally coincide but also one of the phases could be dominant or the phases might have a low degree of ordering. In this case, the combination of TEM and SAXS is crucial to elucidate the structure precisely.

A combination of TEM and SAXS analysis has also been utilised to fully characterise the microphase separation within block copolymer microparticles

prepared in $scCO_2$.[7,8] In particular, SAXS was used to confirm the persistence of the morphology across samples, as shown by the appearance of the Bragg reflection peak(s). However, the discrete nature of the microparticles provided a complex SAXS profile. In addition, broad reflection maxima were observed, suggesting some variation in domain sizes within a sample, which was in agreement with TEM images.

Moreover, synchrotron SAXS studies of the *in situ* morphological evolution during polymerisation-induced self-assembly (PISA) has been conducted.[9] These studies provided a mechanism for vesicle growth and time scales for the nanoparticle growth transitions (sphere-worm-vesicle) during PISA in non-aqueous media. It should be noted that faster reaction rate compared to the standard laboratory reaction was observed. The effect on the kinetics was suggested to be the result of generation of additional radical species by the intense X-ray flux. SAXS profiles were recorded during the PISA synthesis of PSMA-*b*-PBzMA in mineral oil with a targeted degree of polymerisation (*N*) of PBzMA of 150. The system was initially soluble until the copolymer chains reached a critical *N* value (30) of PBzMA (approximately 20% BzMA conversion) and induced nucleation. Spherical nanoparticles were formed just after nucleation, as indicated by the approximately zero gradient observed at low *q*. Then, the spheres transformed into worms within the next 10 min, as indicated by the slope of approximately -1 at low *q*. A mixed phase of worms and vesicles were observed after 46 to 56 min which corresponded to *N* (PBzMA) = 76 to 104. Finally, a gradient of -2 at low *q* confirmed the presence of well-defined vesicles in the final stage of polymerisation (~58-120 min).

Time-resolved SAXS studies have also been reported previously during the synthesis of PMMA-*b*-PBzMA block copolymer microparticles *via* RAFT

dispersion polymerisation in $scCO_2$.[3] However, the main focus in this earlier study was the technical design of the reaction vessel.

4.2.2 Block Copolymer Phase Behaviour in $scCO_2$

It is well-known that block copolymers can phase-separate to form a particular morphology.[10,11] As detailed in Chapter 1, this phase separation is determined by the polymer-polymer interactions (χ), relative volume fractions of block components (f) and the degree of polymerisation (N). In addition to these three parameters, the phase separation can also be influenced by additional factors including polymer dispersity,[12–14] selective solvents,[15–17] and additives such as homopolymers,[16] and ionic liquids[18]. One of the selective solvents that attracts great interest is $scCO_2$, as its solvent quality can be manipulated easily by altering its pressure and temperature. Moreover, CO_2 is also an inexpensive, chemically and environmentally-benign agent for polymer synthesis and processing under moderate critical conditions (31.1 $^{\circ}$C and 73.8 bar).[19]

$scCO_2$ swells various polymers and induces plasticisation to lower the glass transition temperature (T_g) of amorphous polymers.[19] Chemically-different polymers will have a different degree of swelling in $scCO_2$ which depends on their CO_2-affinity. Two different polymer blocks with dissimilar CO_2-philicity will preferentially swell relative to the other. Consequently, in a $scCO_2$ environment the apparent volume fraction of the segments would significantly change and could induce a morphological transition.[16,17] Such a CO_2-induced transition has been observed for PS-*b*-PFMA block copolymers.[16] Order-Order Transition (OOT) occurred upon increasing the pressure of CO_2. Initially, hexagonal cylinders transformed to lamellae at 100 bar and, as the pressure was further increased, the lamellae structure was transformed to a foam structure. Further investigation was conducted by employing PMMA as the first block because it is more CO_2-philic than PS, but much less CO_2-philic than

PFMA.[17] Therefore, the PMMA-*b*-PFMA block copolymer has lower swelling selectivity compared to the previously reported PS-*b*-PFMA. In the PMMA-*b*-PFMA system, an indirect effect of temperature was observed. The disordered phase appeared at a lower temperature than generally found and is denoted as a retrograde Order-Disorder Transition (ODT). Lowering the temperature leads to denser CO_2 that increases block copolymer swelling and so favours disorder. This preferential swelling behaviour could be utilised for the preparation of nanoporous structures by removing CO_2 from the swollen block copolymers.[20,21] Moreover, CO_2 can also depress the ODT temperature as CO_2 can enhance the miscibility between the block copolymer segments. The ODT of polystyrene-*b*-poly(*n*-hexyl methacrylate) (PS-*b*-P*n*HMA) was found to be depressed by around 7 °C in the presence of 0.25 g cm^{-3} CO_2.[22] The same effect was also found in polystyrene-*b*-polyisoprene (PS-*b*-PI) block copolymers.[23]

Furthermore, the CO_2-selective swelling effect on the phase separation in block copolymer microparticles synthesised in $scCO_2$ dispersion has been investigated.[7,8] A series of phase-separated block copolymer microparticles with different CO_2-philicities were prepared. PMMA was systematically employed as the first block, followed by a series of second blocks such as poly(benzyl methacrylate) (PBzMA), poly(*N*,*N*-dimethylaminoethyl methacrylate) (PDMAEMA), polystyrene (PS) or poly(4-vinylpyridine) (P4VP). PBzMA and PDMAEMA have relatively similar CO_2-philicity with the first block (PMMA), while the PS and P4VP possess a relatively large difference in CO_2-philicity compared to PMMA. Polymer morphologies generally predicted by the phase behaviour for PMMA-*b*-PBzMA and PMMA-*b*-PDMAEMA were observed. In contrast, a large difference in the degree of CO_2 swelling produced unexpected phase-separated morphologies for PMMA-*b*-PS and PMMA-*b*-P4VP systems. The CO_2 effect on the polymeric structure was clearly evident after dissolving

and solvent casting the as-synthesised block copolymer microparticles to form bulk films. The morphology of the PMMA-*b*-PBzMA film was consistent with the as-synthesised microparticles whilst the morphology of the PMMA-*b*-PS and PMMA-*b*-P4VP films returned to the predicted equilibrium morphology. These morphological differences strongly indicate that the contrast in CO_2-philicity influenced phase behaviour for these block copolymer systems.

4.2.3 SAXS Studies in High Pressure System

High pressure experiments require special equipment to ensure safe operation. In addition, a vessel for conducting X-ray scattering experiments under high pressure requires windows as optical features for attaining small angle and wide angle scattering (SAXS and WAXS). The windows must be able to transmit the X-ray beam as well as mechanically resist the extreme conditions required for the experiments. The development and application of high pressure X-ray vessels has been reported in the literature previously.[3,24–26] The majority of the previous vessels employed either diamond or beryllium windows as these materials have low X-ray absorption, good mechanical properties, and are chemically inert. Sapphire windows could also be used,[24,27] but the transmission of X-rays is greatly decreased for this material. For example, a 0.15 mm thickness of sapphire window only transmits around 50% of the X-ray beam.[27]

A vessel that used stainless steel as the building material and featured beryllium windows has been developed for conducting X-ray absorption and scattering experiments under extreme conditions of pressure and temperature.[24] This X-ray vessel was designed to work over a temperature and pressure range of 30-1700 °C and 1-2000 bars, for geochemical analysis of iron under hydrothermal conditions. Similarly, a stainless steel vessel containing two diamond windows and a single sapphire window as a view port

has been built for SAXS studies at synchrotron facilities.[28] The X-ray vessel had a maximum working pressure of 500 bar and a sample volume of 10 ml.

The development of high-intensity synchrotron radiation and fast detectors has allowed time-resolved SAXS measurements to monitor structural developments *in situ*.[27,29,30] Such measurements afford detailed kinetic information which potentially reveals the mechanisms involved. A high pressure X-ray autoclave with diamond windows has been built for conducting *in situ* time-resolved X-ray scattering experiments during polymerisation. The X-ray autoclave has a relatively large volume (60 ml) that permits the reaction to be probed directly the reaction avoiding detrimental sampling effects that occur in modular view ports. The X-ray autoclave possesses a maximum working pressure and temperature of 210 bar and 120 °C, respectively for conducting SAXS measurements during dispersion polymerisation in $scCO_2$.

4.3 Objectives

The main aim of this chapter is to understand the mechanism of the internal nanostructure organisation within block copolymer microparticles during RAFT dispersion polymerisation in $scCO_2$. To achieve this aim, *in situ* time-resolved SAXS studies will be conducted using synchrotron radiation to monitor the structural changes that occur during the polymerisation. The studies will use a new high pressure X-ray autoclave as the main apparatus. Therefore, details of this new autoclave and comparative studies with the standard autoclave will be discussed.

The combination of SAXS experiments with NMR spectroscopy and electron microscopy analyses should provide detailed information regarding the development of the internal nanostructure of the block as well as the

mechanism of formation. Importantly, understanding the key parameters of the mechanism of formation will enable us to target morphologies for specific applications.

4.4 Experimental

4.4.1 Materials

PMMA-DATC was synthesised by RAFT dispersion polymerisation in $scCO_2$ as presented in Chapter 3. Methyl methacrylate (MMA, 99%) and styrene (St, 99%) were obtained from Sigma-Aldrich. Inhibitors were removed from both monomers prior to use by passing through a column of neutral aluminium oxide. Monomers were then degassed by bubbling with argon for 30 minutes and stored in the freezer. 2,2'-Azobis(2-isobutyronitrile) (AIBN, 98%) was purchased from Sigma-Aldrich and purified by recrystallising twice in methanol. 2-(Dodecylthiocarbonothioylthio)-2-methylpropionic acid (DATC) was synthesised following a literature procedure[31] or purchased from Sigma-Aldrich (97% purity) and used as received. Poly(dimethylsiloxane monomethyl methacrylate) (PDMS-MA, M_n = 10 kDa) was purchased from ABCR Gmbh. Dry CO_2 (SFC grade, 99.99%) was purchased from BOC or Air Liquid.

4.4.2 Block Copolymer Synthesis

In order to synthesise a symmetrical PMMA-*b*-PS block copolymer of 100 kg mol^{-1}, the pre-synthesised PMMA (PMMA-DATC) (5,616 mg, 0.112 mmol, assumed M_n PMMA = 50 kg mol^{-1}) was placed in an X-ray autoclave with PDMS-MA (280 mg, 5wt% w.r.t. styrene). The autoclave was then clamped and purged with CO_2 (3 - 4 bar) for 15 minutes. After sealing, the autoclave was pressurised with the addition of CO_2 to 55 bar. The stirrer was turned on and adjusted to ~600 rpm. The heater was then set to 65 °C. Once 65 °C had been reached, additional CO_2 was added to reach a pressure of 205 bar and

allow equilibration of the system for 1 – 2 hours. Afterwards, degassed styrene (6.4 ml, 56.1 mmol) and AIBN (18.4 mg, 0.112 mmol) were added *via* HPLC pump. Additional CO_2 was then added as required to reach a final reaction pressure of 275 bar. The stirred reaction solution was then left for an allotted time (72 hours) at 65 ^oC.

Once the allotted time had been reached, the heater and the stirrer were switched off and the autoclave was cooled to room temperature and then depressurised by releasing CO_2 through the outlet valve. At atmospheric pressure (1.0 bar), the autoclave was opened and the product was collected. The product was then ready for analysis and characterisation.

4.4.3 *In situ* SAXS Measurement

Time-resolved SAXS experiments were conducted at the Dutch-Belgian Beamline (DUBBLE) station BM26-B of the European Synchrotron Radiation Facility (ESRF) in Grenoble (France). The X-ray autoclave was mounted on a motorised stage and the windows were aligned to the X-ray beam incident and detector.

Data were collected at a sample-to-detector distance of either 3 m or 6.15 m with a wavelength of 1.033 or 0.8266 Å respectively. The scattering vector q is defined as $q = 4\pi/\lambda \sin\theta$, with 2θ being the scattering angle. A Dectris-Pilatus 1M detector with a resolution of 981 × 1043 pixels and a pixel size of 172 × 172 μm has been employed to record the 2D SAXS scattering patterns. The data were normalised to the incident beam intensity and were corrected for absorption and background scattering from the diamond windows and $scCO_2$. Silver behenate patterns were used for the wave-vector calibration. The vessel allows simultaneous SAXS-WAXS experiments to be conducted and the maximum recordable diffraction angle is about $2\theta = 40°$ with a pixel size of 172 × 172 μm.

The autoclave was mounted on the stage with the optical path (windows) aligned to the incident beam and the detector. The setup enabled experiments using two autoclaves simultaneously and hence two experiments can be run in parallel. The experiments were synchronised to conduct alternate measurements in both X-ray autoclaves by moving each autoclave at scheduled time intervals using a linear stage.

4.5 Results and Discussion

4.5.1 Block Copolymer Synthesis in the New High Pressure X-ray Autoclave

4.5.1.1 High Pressure X-ray Autoclave (MKII)

This new autoclave was produced in The School of Chemistry Workshop, The University of Nottingham. This new design was developed from the first generation X-ray autoclave (MKI).[3] The main modification was carried out on the autoclave body in order to optimise stirring and mixing as well as providing easier assembly-disassembly and post-reaction cleaning. The details of the new vessel have been described in Chapter 2, along with the rig diagrams and standard operating procedures.

Figure 4.1 shows a representation of the vessel, illustrating the main technical components. The vessel was constructed from a certified stainless-steel bar. It consists of two main sections: the head and the body. The head contains a stirrer, thermocouple, over-pressure safety devices, and CO_2 inlet and outlet pipes. The head is clamped to the bottom section (the body), which is equipped with a cleavable heating box. Two diamond windows are housed in the body and they are mounted on the screwable removable holder. The windows holder design allows easy cleaning after reaction. The windows have a mean thickness of 0.4 mm ± 0.05 mm and are made from a synthetic single crystal diamond type III supplied by Element 6. The optical path length

between them is 2.0 - 2.5 mm. In contrast with the previous vessel (MKI), the MKII has a higher maximum working pressure (300 bar) with a maximum temperature of 120 °C. These values are equal to the standard autoclave used for routine syntheses. The over-pressure devices and electrical trips protect the integrity of the vessel. The vessel was pressure-tested to ensure its safe operation prior to use, and that all of the new features associated with the diamond windows were suitable.

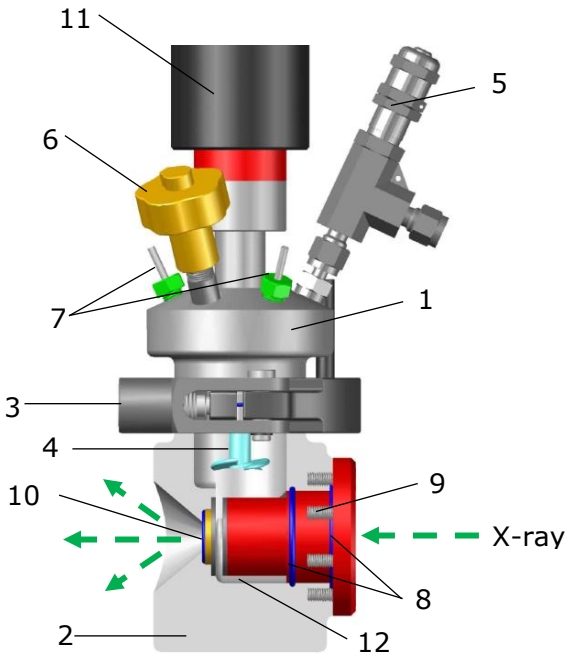


Figure 4.1. Representation of the new high pressure *X*-ray autoclave (MKII). (1) Head, (2) Body, (3) Clamp, (4) Stirrer Blade, (5) Spring Loaded Pressure Relief Valve, (6) Torque Thumbwheel, (7) Inlet and outlet pipes, (8) O-rings, (9) Screws to secure new window holder into the cell body, (10) Diamond windows, (11) Magnetically Coupled Overhead Stirrer.

The window holder is secured into the body using screws which are not open to the internal reactor volume (Figure 4.1, (9)). This design avoids the possibility of monomer polymerising around the screws, which should enable far easier removal of the insert and facilitate product collection and post-

reaction cleaning. Figure 4.2 presents the internal design of the vessels. In order to ensure representative sampling across the whole volume of the reactor, a curved interior and smooth surface was designed to prevent the polymer particles building up at the edge where the mixing is least efficient, thus avoiding a detrimental dead volume.

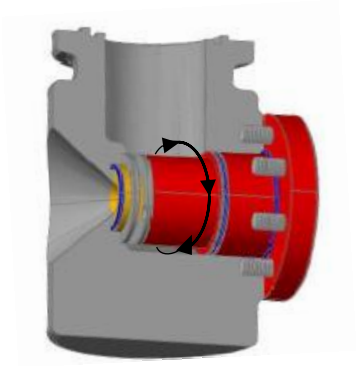


Figure 4.2. A cut-out view of the internal design of the vessel, showing the window holder (red) and the main reactor volume. The arrows show how the CO_2/reactants can flow around the window holder.

4.5.1.2 Reproducibility test

Initial experiments were performed in order to determine whether comparable polymerisation products could be obtained in both a standard 60 mL autoclave and the new X-ray vessel. The first test was the synthesis of PMMA microparticles in a RAFT-controlled $scCO_2$ dispersion polymerisation. PDMS-MA was used as the stabiliser at 5 wt% relative to monomer, DATC as the RAFT agent, and AIBN as the initiator at a [RAFT]:[I] molar ratio of 2:1.[7,32] The same procedure, 18 hr reaction time at 65°C and 275 bar with 300 rpm of stirring rate, was applied to both syntheses.

In a standard autoclave, the reaction proceeds in a controlled manner (Table 4.1, Entry 1), affording a narrow dispersity with good agreement between M_n^{th} and M_n^{GPC}. Similarly, the first polymerisation in the X-ray

autoclave gave a similar dispersity (Table 4.1, Entry 2) to that obtained from the standard autoclave. In addition, the experimentally-derived molecular weight (M_n^{GPC}) is close to the M_n^{th}. The polymer characterisation confirmed that the RAFT mechanism was working effectively in the new vessel. The conversion was lower than that obtained with the standard autoclave but still in the range typically obtained from our system. Upon opening the autoclave, the polymer product was a free-flowing powder, proving that a stable dispersion was achieved and maintained during the reaction.

Table 4.1. RAFT controlled $scCO_2$ dispersion polymerisation of MMA in standard autoclave and MKII for reproducibility test

Vessel	M_n^{target} ($kg.mol^{-1}$)	M_n^{th} ($kg.mol^{-1}$)[a]	M_n^{GPC} ($kg.mol^{-1}$)[b]	Đ[b]	Conv. (%)[c]	Initial appearance
Standard	50	47	47	1.2	95	Powder
MKII	50	41	43	1.2	83	Powder

The reactions were conducted at 65 °C and 275 bar for 18 h with molar ratio R : I = 1 : 1 and 5% stabiliser wrt. monomer. Stirring rate 300 rpm.

a. *Calculated* from ([MMA]/[R]*conv.)*$Mr_{monomer}$ + Mr_{RAFT}

b. *Measured by GPC in THF with LS detector*

c. *Determined gravimetrically*

Figure 4.3 presents SEM images of the obtained PMMA microparticles from both the standard and the X-ray autoclave. Discrete and relatively uniform spherical microparticles were obtained. Importantly, the powder texture indicates that the new design autoclave has better mixing compared to the previous vessel (MKI), which produced an agglomerated product.[33]

The autoclave was further tested for conducting the synthesis of block copolymer particles in a two-stage procedure. This protocol uses a solid reactant (PMMA powder) as the main starting material rather than liquid compared to the MMA polymerisation. Thus, the mixing process may be more challenging, and hence the homogeneity of the dispersion could be more difficult to be achieved.

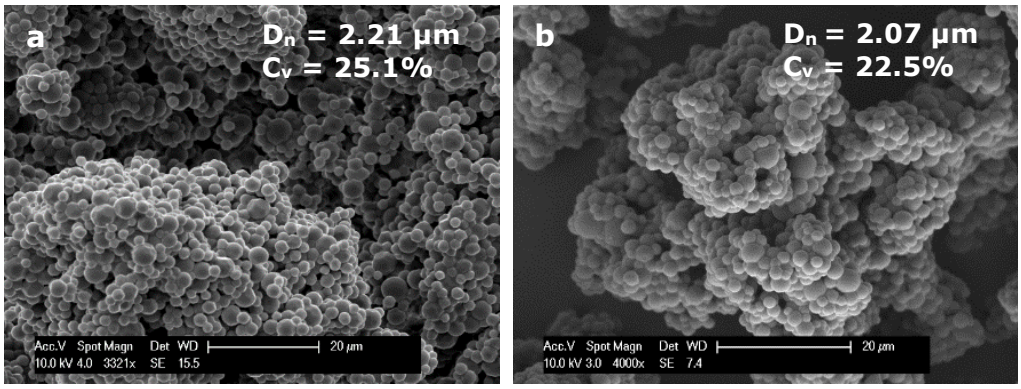


Figure 4.3. SEM images of the PMMA microparticles synthesised in (a) standard autoclave and (b) MKII, showing a comparable morphology produced from two different vessels.

Synthesis of PMMA-*b*-PDEA block copolymer was selected for the second reproducibility test as this synthesis has the shortest reaction time compared to other second blocks. The first reaction was conducted following the same procedure as in the standard vessel (Table 4.2, entry 1). As one might predict, a good dispersion was more difficult to achieve and resulted in agglomerated particles rather than a free flowing powder. In order to improve the mixing, a new synthetic approach with less reactants and a faster stirring rate was applied to achieve better homogeneity and a stable dispersion. Dispersion homogeneity of the reaction medium in the new vessel is crucial to monitor *in situ* the morphological development during the polymerisation. In a homogeneous system, the fluid was expected to have the same properties in the whole vessel even within the narrower optical path channel (2.0 - 2.5 mm) between the two windows. Thus, the analysed fluid in the optical path must be representative of the whole system.

Table 4.2. Trial of two-stage synthesis of block copolymers in MKII

Entry	Block copolymer	PMMA loading (%)[a]	Stirring rate (rpm)	M_n^{GPC} (kg mol^{-1})[b]	Đ[b]	Conv. (%)[c]	Initial appearance
1	PMMA-b-PDEA	10	300	33	1.5	78	Monolith
2	PMMA-b-PDEA	5.0	300	37	1.5	67	Monolith
3	PMMA-b-PDEA	5.0	400	41	1.4	63	Monolith
4	PMMA-b-PDEA	7.5	600	35	1.5	80	Powder, Monolith

The reactions were conducted at 65 °C and 275 bar for 16 hrs with molar ratio R : I = 1 : 1 and 5% stabiliser wrt. monomer. The second monomer was added after PMMA dispersed in $scCO_2$ for 2 hrs.

a. Relative to the vessel volume

b. Measured by GPC in $CHCl_3$ with RI detector and calibrated against PMMA standards

c. Calculated gravimetrically

For low PMMA loading (Table 4.2, entry 2 and 3), lower conversion was obtained as the kinetics were slower. However, faster stirring rate produced higher conversions (Table 4.2, entry 4), as it allowed the monomer to propagate faster. Faster stirring also resulted in a mixture of powder and monolith, showing that better mixing and hence a more homogeneous dispersion was formed. Moreover, as the stirring rate was increased, an improvement in the product morphologies was also found (see Figure 4.4), and more defined particles were obtained at faster stirring rates. However, some agglomerate was found as a consequence of altering the stirring rate. A higher stirring rate increases the degree of agitation in the reaction medium and affects the particle morphology.[34]

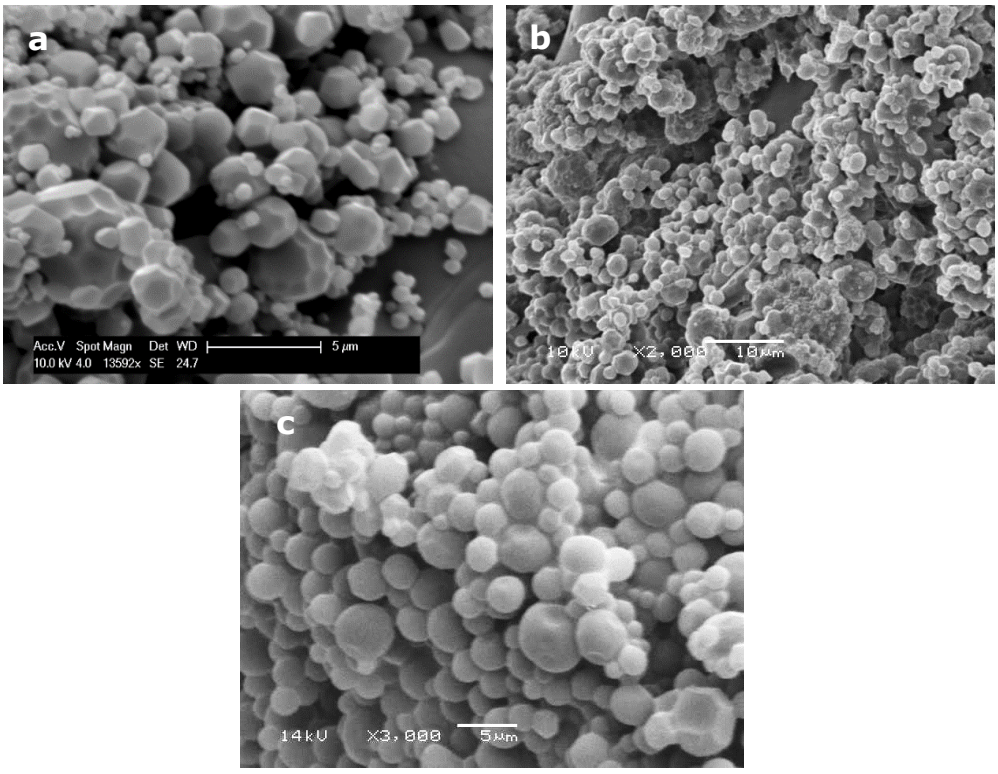


Figure 4.4. SEM images from the trial synthesis of PMMA-*b*-PDEA using the new X-ray autoclave presented in Table 4.2 (a) entry 1, (b) entry 3, (c) entry 4.

In order to further improve the stirring efficiency, the diameter of the window holder was reduced whilst preserving the window size. In the previous design, the window holder diameter was 30 mm and was reduced to 24 mm. The diameter reduction promotes efficient mixing within the narrow area under the window holder (Figure 4.2), and hence increases the homogeneity of the dispersion.

In summary, comparable polymer products can be obtained using the new X-ray autoclave by increasing the stirring rate up to 600 rpm, whilst maintaining parameters such as reaction time, temperature, and pressure similar to those used for the standard autoclave. The reaction parameters found offline in the new X-ray autoclave were then applied during the *in situ* SAXS measurements.

4.5.2 *In situ* SAXS Monitoring

The block copolymer selected for performing the *in situ* SAXS experiment was PMMA-*b*-PS. Although this block copolymer requires a long reaction time (72 hr, detailed in Chapter 3), PMMA-*b*-PS possesses high electron contrast and thus, it is an ideal candidate to consider the effect of CO_2 while monitoring the phase separation behaviour.[7,8] Synchrotron X-ray radiation was used to acquire SAXS patterns during the RAFT dispersion polymerisation in scCO_2. Polymerisations were conducted using the high pressure X-ray cell presented in the previous section. Various morphological transitions that occur during the polymerisation were followed *in situ* by time-resolved SAXS patterns. All the SAXS data were generated and analysed with the assistance of Dr. Daniel Hermida-Merino at DUBBLE, BM-26 at the ESRF.

A series of polymerisations were conducted *via* the two-stage procedure (see Chapter 3) to minimise the reaction time during the online

SAXS measurements. The envisaged block copolymers were designed to target different internal structures by varying the volume fraction of PMMA relative to PS (f_{PMMA}) as presented in Table 4.3. In general, the polymerisation resulted in relatively low dispersity, which suggested good polymerisation control (Figure 4.5). The block copolymers generated in the new X-ray vessel also presented two T_g values, except for the block copolymer with the higher PMMA content (see table 4.3, entry 3). The existence of two T_g values in a block copolymer similar to those for the single blocks confirms the microphase separation behaviour of the block copolymer.

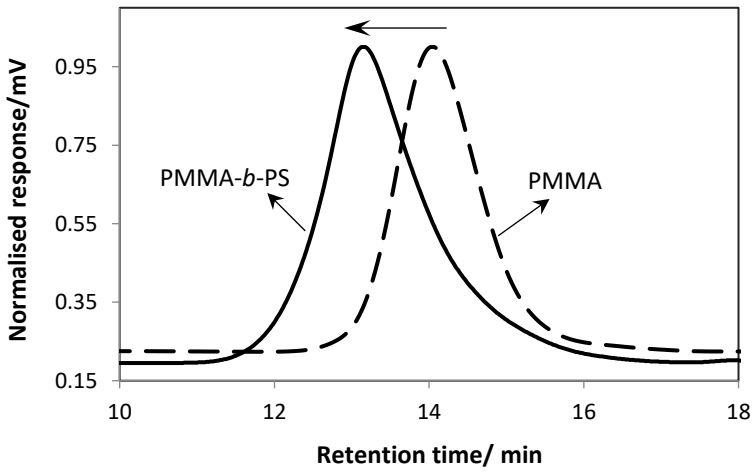


Figure 4.5 GPC traces of exp09 (Table 4.2 entry 2) and its initial PMMA-RAFT, showing the increase in molecular weight (chain extension) of PMMA, forming PMMA-*b*-PS block copolymer with a unimodal peak.

Table 4.3. The characteristics of PMMA-*b*-PS copolymer synthesised during *in situ* SAXS analysis

Entry	Sample	M_n^{target} (kg.mol^{-1})	PMMA		PMMA-*b*-PS			T_g (°C)[c]		Internal structure[d]
			M_n^{GPC} (kg.mol^{-1})[a]	Đ[a]	M_n^{GPC} (kg.mol^{-1})[a]	Đ[a]	f_{PMMA}[b]	PMMA	PS	
1	Exp02	60	31	1.2	52	1.5	0.53	121	103	CYL
2	Exp09	100	24	1.2	70	1.4	0.31	114	92	LAM/CYL
3	Exp11	100	58	1.4	71	1.5	0.81	123		DIS

The reactions were conducted at 65 °C and 275 bar, stirring rate ~600 rpm for ~65 hrs with molar ratio R : I = 1 : 1 and 5% stabiliser w.r.t. monomer. The second monomer was added after PMMA dispersed in $scCO_2$ for ~2 hrs.

a. *Measured by GPC in THF with LS detector*
b. *Calculated by Equation 3.2*
c. *Determined by DSC*
d. *Observed from TEM images of the final product, the first mentioned is the majority phase. CYL: hexagonal packed cylinder, LAM: lamellae, SPH: body centred cubic packing of sphere, DIS: disorder*

The first system investigated for the *in situ* SAXS monitoring was PMMA-*b*-PS with f_{PMMA}=0.53 (exp02, Table 4.3 entry 1). The time-resolved SAXS profiles were recorded during the second stage of the two-stage polymerisation. Polymerisation of styrene using RAFT-terminated PMMA occurs and produces PMMA-*b*-PS block copolymer. The growth of the second block induces the microphase separation of the obtained block copolymer at a critical degree of polymerisation. The reaction was conducted at 65 °C and 275 bar for 64 hrs. Ideally, the polymerisation requires 72 hrs to achieve high conversion (>90%). However, the reaction was performed for 64 hrs due to the limited beamtime and a final conversion of 80% was achieved. The lower final polymerisation conversion has a negligible effect on the copolymer morphology. The 2D scattering data were collected and subsequently data reduction was conducted to generate the SAXS profiles, where the scattered intensity is plotted with respect to the scattering vector *q* (Figure 4.6), as defined by Equation 4.3.

$$q = \frac{4\pi}{\lambda}\sin\theta \qquad \text{(Equation 4.3)}$$

Where θ is half of the scattering angle and λ is the X-ray wavelength.

Initially, the SAXS profile shows a monotonic reduction in intensity related to the PMMA homopolymer and the absence of scattering reflections confirms no microphase separation. A broad peak centred at q=0.220 nm^{-1} appeared after ~6 hrs reaction, indicating the onset of microphase separation. This suggests that microphase separation has an induction period in which the polymerisation proceeds but the molecular weight has not achieved the critical value required to trigger the microphase separation.[35] The peak becomes more resolved as the phases become increasingly ordered.

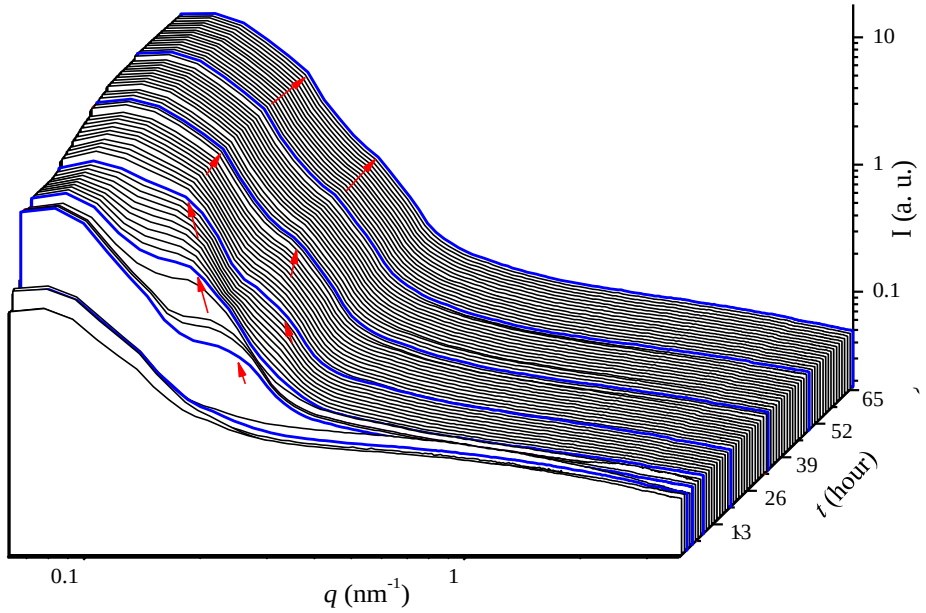


Figure 4.6. Time-resolved SAXS patterns for exp02, a PMMA-*b*-PS block copolymer with f_{PMMA}=0.53 (see Table 4.3, entry 1). The arrows indicate the scattering peaks.

The previous kinetic studies (see Chapter 3; section 3.5.3) shown that the degree of polymerisation (N) of styrene was ~10 at this reaction stage. As the polymerisation proceeds, the molecular weight and N of the product increase and hence the interaction parameter (χ) can also change. At a critical χN value, the segregation of the different blocks is triggered and thus a transition from the initial homogeneous state into a microphase-separated morphology occurs.

As the reaction proceeds, the scattering peak becomes sharper and shifts to lower q values, indicating an increase in domain spacing for the microphase-separated block copolymer chains. While the first reflection shifts to lower q as the styrene polymerises, a second order reflection appears at q = 0.234 nm^{-1} after ~21 hrs. This second reflection is positioned at a q ratio of 1:$\sqrt{3}$ with respect to the first reflection (q^*) and is attributed to the

hexagonally-packed cylinder structure.[4,5] These two reflections are displaced to lower q until the reaction time reaches ~50 hrs. At this polymerisation stage, the reflections remained in the same positions until the end of the reaction.

To confirm the final morphology of the block copolymer, a TEM investigation was conducted on ultrathin sections of the produced microparticles stained with RuO_4 to enhance the phase contrast. The observed morphology is cylindrical (CYL, Figure 4.7) which is in good agreement with the result indicated by the final SAXS pattern. The cylinder-to-cylinder distance (a) measured from the TEM images was found to be 28.7±1.5 nm. The cylinder dimension obtained by TEM is far smaller than the obtained from the final SAXS profile ($a=2d/\sqrt{3}$)[4]; 54.13 nm (q^*=0.134 nm^{-1}). However, it is well documented in the literature that there can be differences of up to 30% between the sizes reported by SAXS and TEM. Moreover, the thicker cylinders observed by SAXS could be a result of domain swelling by CO_2, as SAXS data were acquired *in situ* in the presence of CO_2. It is well-known that $scCO_2$ swells most polymers, including PMMA and PS.[36] On releasing CO_2, the domain size shrinks without changing the final structure as the morphology becomes frozen on cooling the reaction (below T_gs of the block). In addition, sample preparation such as resin embedding and statistical error (measured from ~5 particles) could result in considerable error for the measurements from TEM images.

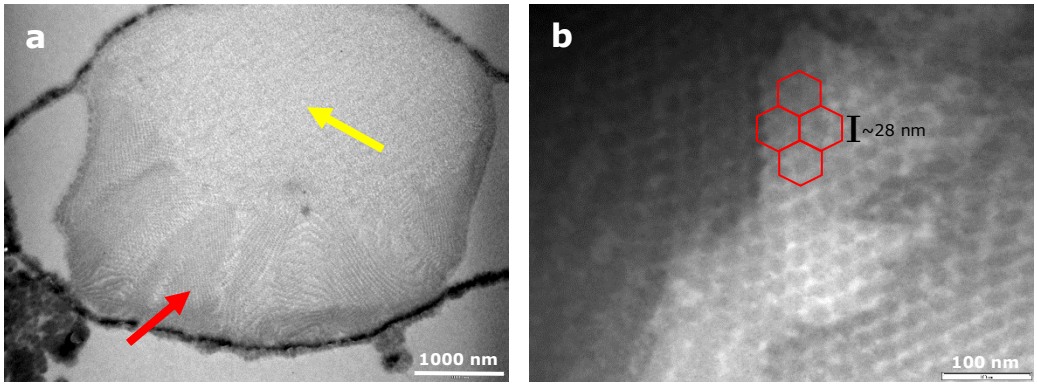


Figure 4.7. Cross-sectional TEM images of the final product of PMMA-*b*-PS (exp02) produced during *in situ* SAXS monitoring. (a) The CYL structure is found in different orientations in a single microparticle; horizontal or line/stripe patterns (red arrow) and vertical or dot patterns (yellow arrow), (b) high magnification image showing cylinders in a hexagonal array.

A series of *in situ* SAXS patterns were also acquired during the synthesis of PMMA-*b*-PS at a lower PMMA volume fraction, f_{PMMA}=0.31 (see exp09, Table 4.3 entry 2). A formulation with a significantly different PMMA volume fraction was used to study the effect of CO_2–philicity in the final morphology. A longer reaction time was required for the onset of microphase separation for the PMMA-*b*-PS block copolymer of exp09.

The SAXS profiles (Figure 4.8) illustrate that a PMMA homopolymer was present in the early stages of the reaction, similar to the previous reaction. The first scattering peak (q= 0.235 nm^{-1}) appears at ~16 hrs, indicating the onset of microphase separation. The induction period of the microphase separation for exp09 is significantly longer than exp02 and thus is achieved at higher N. The critical N for exp02 was approximately 10 while the critical N for exp09 was ~20. The latter value is based on the kinetic data presented in the following section. As the microphase separation is related to χN, the longer induction time prior to the onset of the microphase separation is suggested to result from the lower N of the starting material (PMMA-RAFT) of exp09

compared to exp02; 240 versus 310. It is known that the degree of polymerisation may determine the extent of the chemical incompatibility and hence the degree of segregation.[10] Additionally, the microphase separation morphology of exp09 is more complex as shown by SAXS measurements. The final morphology might arise from the appearance of a biphasic morphology, as confirmed by TEM images of the final product. This biphasic morphology is quite difficult to confirm by SAXS as one of the phases might be too dominant or the phase(s) may have a low degree of ordering.

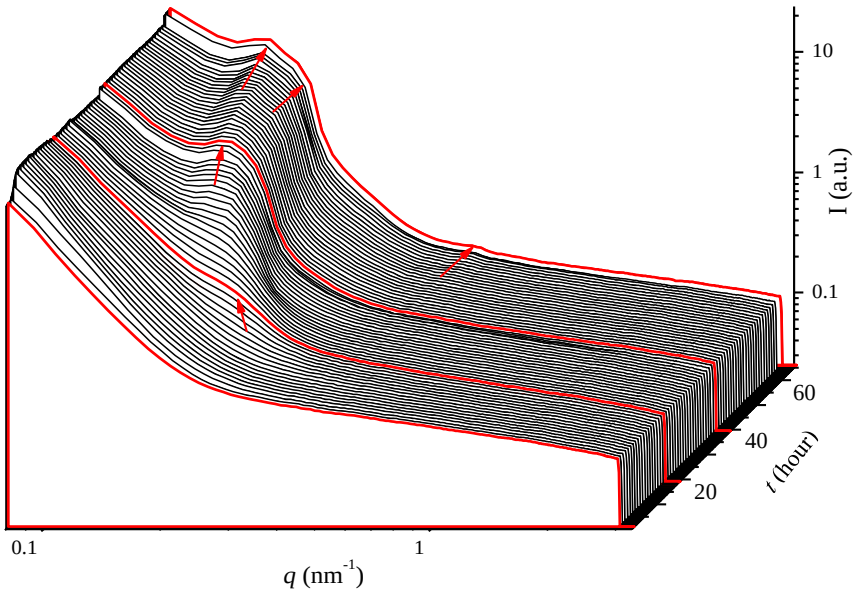


Figure 4.8. Time-resolved SAXS patterns I (q,t) as a function of the scattering vector, q, and the time, t, of exp09 (see Table 4.3, entry 2). The arrows show the scattering peaks.

The scattered intensity of the first peak continuously increases as the polymerisation progresses prior to a shift to lower q (0.170 nm^{-1}) at ~29 hours. At this reaction stage, the appearance of the second reflection was observed at q = 0.196 nm^{-1}. The higher order reflection suggests the appearance of a different morphology. The two peaks developed further as the polymerisation

proceeded and the mean degree of polymerisation increased. The morphological development results also in a gradual increase in the domain spacing, and thus q^* shifts to smaller values. Additionally, a higher order reflection centred at q = 0.183 nm^{-1} was observed after ~53 hrs of reaction. Finally, the main features of the SAXS profiles remain practically constant until the final scattering pattern (65 hrs).

The evolution of the domain spacing was observed from the primary peak using Equation 4.2. The morphological evolution was revealed by shifting the primary peak (q^*) to lower q. Selected SAXS profiles were highlighted from Figure 4.8 in order to better illustrate the evolution (Figure 4.9). The last scattering pattern has a primary peak centred at q=0.144 nm^{-1}, implying the domain spacing of the structure to be 43.6 nm. Broader peaks suggested short-range order arising from the size disparity of the microspheres.

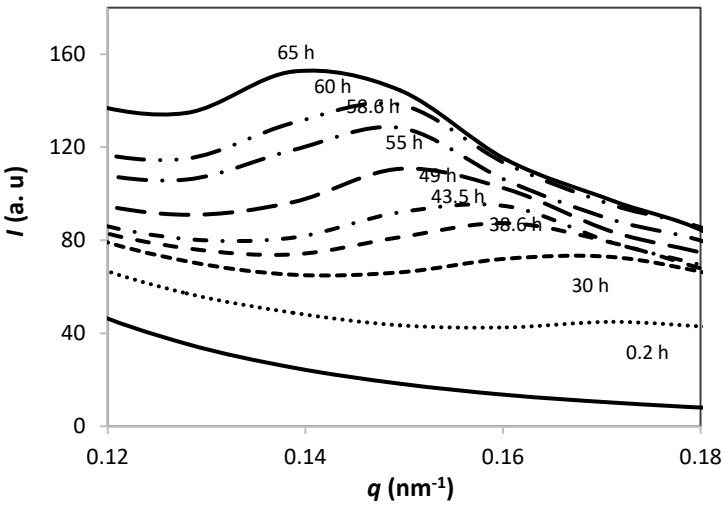


Figure 4.9. Plot of scattered intensity versus scattering vector at selected times showing the shifting of the primary peak to lower q depicted from Figure 4.8, the *in situ* SAXS monitoring of exp09 (Table 1 entry 2).

The cross-sectional TEM images of the final product confirms the appearance of LAM (Figure 4.10a) and SPH (Figure 4.10b) structure, and considerable mixed structures comprising LAM and SPH/CYL (Figure 4.10c, d) within single microparticles. Such mixed structures have been observed before when a high concentration of second monomer was applied in the synthesis, as discussed in Chapter 3.

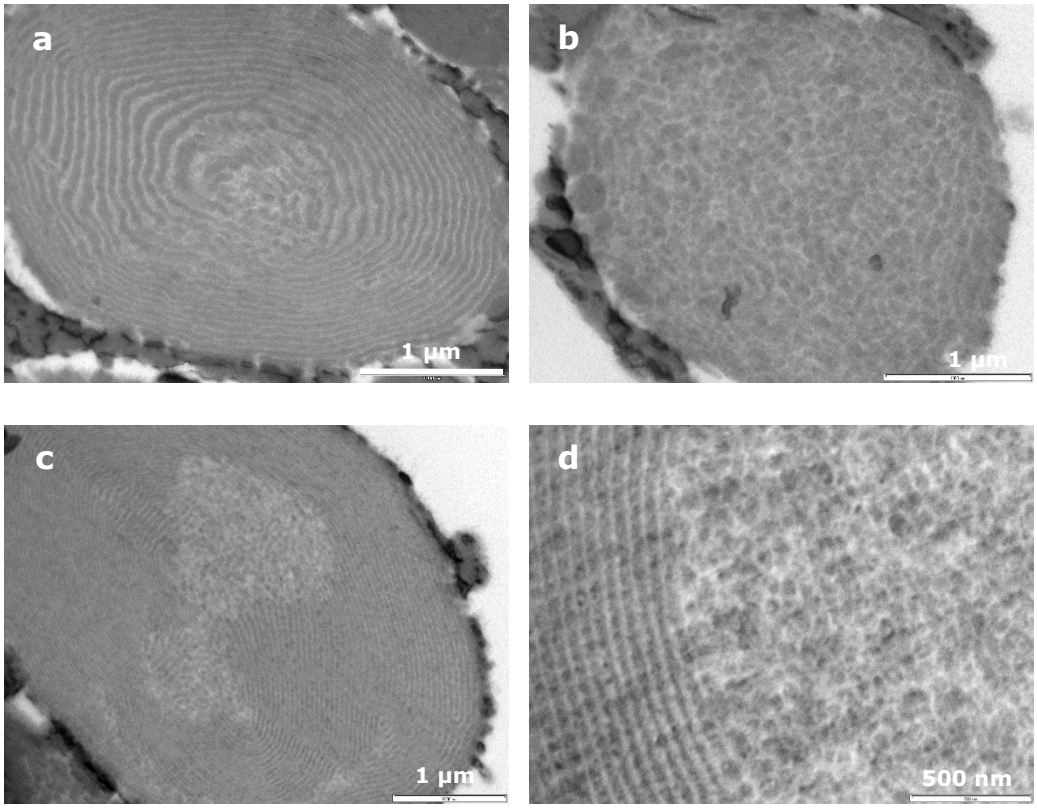
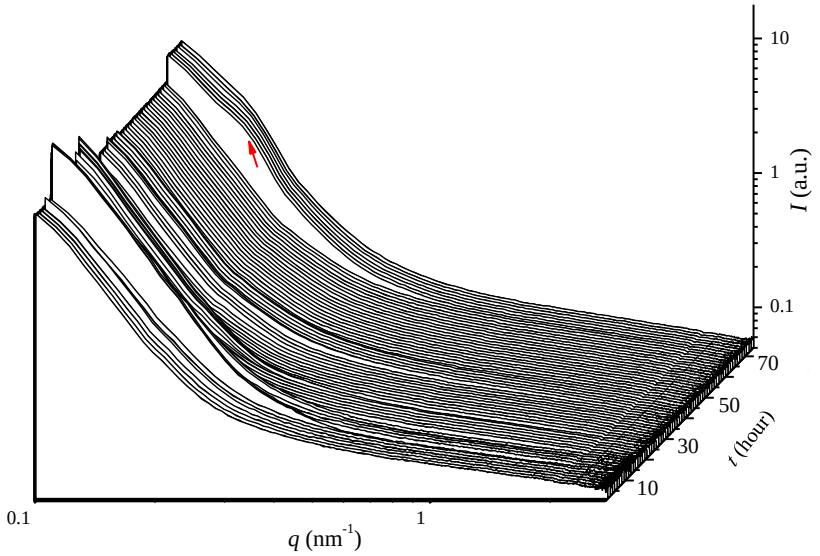


Figure 4.10. TEM images of the final product of exp09, showing (a) LAM, (b) SPH, (c and d) the mixed-structure of LAM – SPH/CYL.

Finally, the synthesis of a PMMA-*b*-PS block copolymer with a target high f_{PMMA} (see exp11, Table 4.3 entry 3) was studied by *in situ* SAXS experiment. However, only a small shoulder centred at q=0.152 nm^{-1} appeared when the reaction was about to finish (t=~65 hrs) (Figure 4.11a). This can be attributed to the initial microphase separation. However, the shoulder did not develop further until the last scattering peak (71 hrs), suggesting a lack of

internally nanostructured microparticles. TEM images of the final product (Figure 4.11b) showed disordered microparticles. The low microphase separation was expected as a high f_{PMMA} (0.81) content facilitates the miscibility of the PS block with the PMMA matrix. Intensity fluctuations in the SAXS plot is related to the instability of the pressure. At certain time intervals, more CO_2 was added into the system to maintain the required pressure.

a.



b.

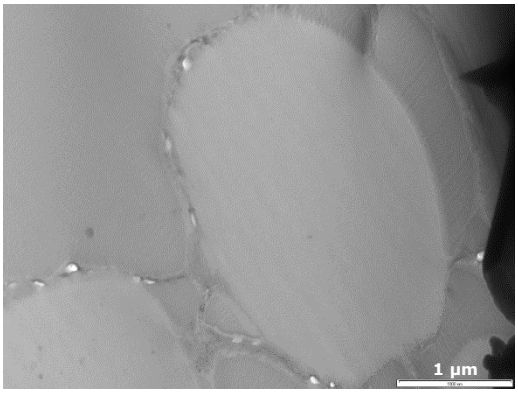


Figure 4.11. a) SAXS patterns from the time-resolved SAXS measurement of exp11 (Table 4.3, entry 3), showing the lack of microphase separation. b) TEM image of exp11, showing unstructured microparticles.

4.5.3 Structural Evolution

In order to confirm the structural evolution, the synthesis of exp09 was reproduced in our lab using the standard autoclave equipped with a sampling tap (Figure 2.2). Our aim was to use the block copolymer sampling at time intervals during the synthesis to permit characterisation of the polymer at various monomer conversions and thus correlate such data with the *in situ* SAXS experiments. A series of samples were collected and their internal nanostructures were investigated using TEM. As rapid cooling to room temperature occurs during sampling, the particle morphology is frozen and hence the observed copolymer morphologies from the TEM images are expected to be comparable to the actual morphology at the corresponding sampling period. The mean degree of polymerisation (N) and volume fraction of PMMA (f_{PMMA}) relative to PS were also measured for each sample using GPC and NMR spectroscopy (Equation 3.2). These experiments were conducted with the assistance of Dr Guping He.

The first sample studied by TEM was collected after 21 hrs of reaction (Figure 4.12a, b). The sample was partially contaminated with unreacted monomer as the conversion was low (~18%). However, microphase-separated morphologies were observed, such as CYL structure. A combination of homogeneous and heterogeneous phases was also found within a single microparticle (Figure 4.12a). The phase mixing indicates that the phase separation was not yet developed throughout the whole particle. The single-shot SAXS profile that corresponds to the same material investigated by TEM confirms the lack of microphase separation (Figure 4.14a). At this point, the mean degree of polymerisation (N) of styrene is 14 (Figure 4.13).

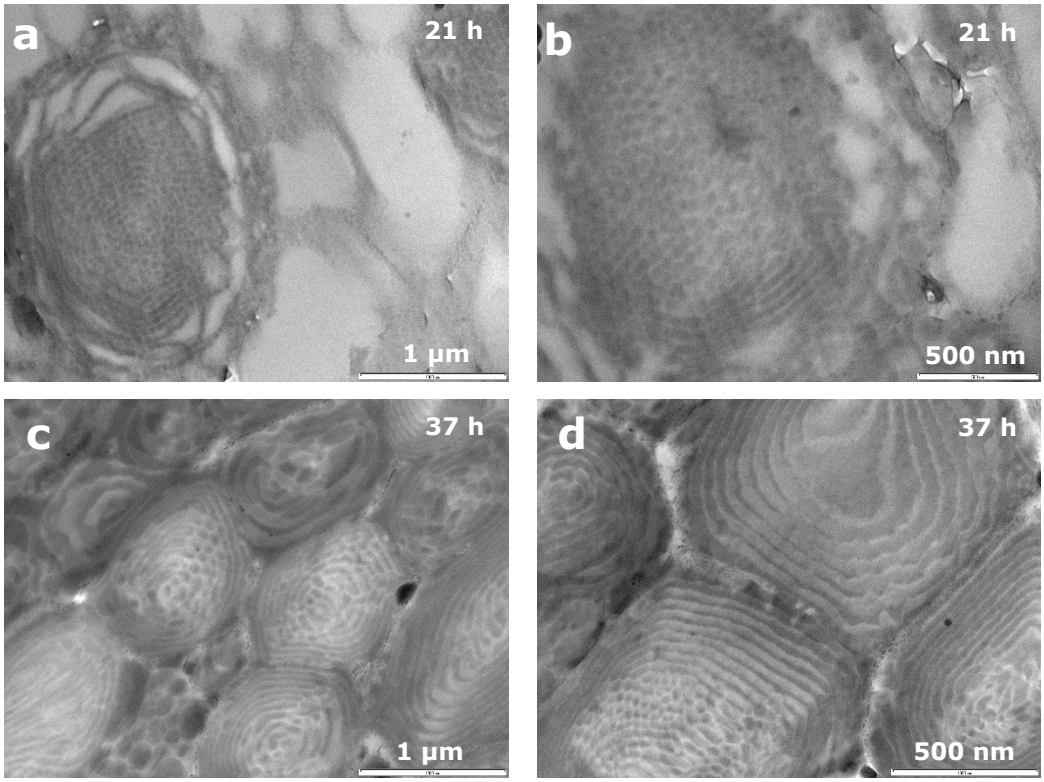


Figure 4.12. TEM images of the internal nanostructure of exp09 duplicate at different time intervals of reaction, (a) 21 hrs, showing a combination of homogeneous and heterogeneous phases, (b) 21 hrs, showing CYL structures, (c) and (d) 37 hrs, showing mixed structures of CYL and LAM. The experiment was conducted under typical laboratory conditions using a standard autoclave.

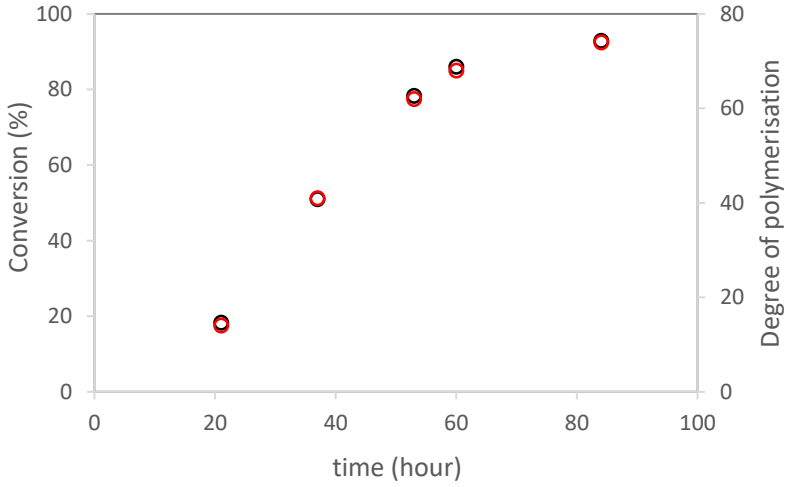
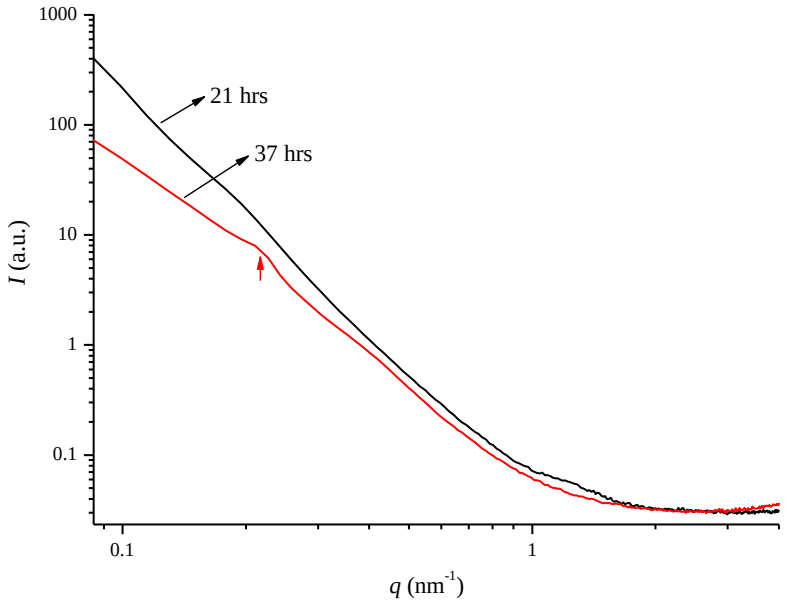


Figure 4.13. Kinetic plot of styrene polymerisation using the PMMA-macro RAFT agent, showing conversion and degree of polymerisation (*N*) of styrene as a function of reaction time.

a.



b.

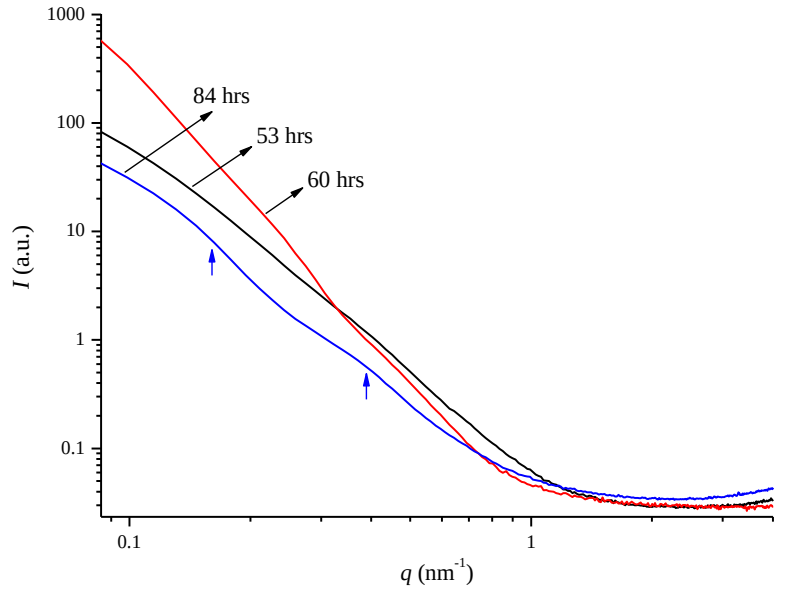


Figure 4.14 Single-shot SAXS patterns recorded for exp09 duplicate. The samples were collected at different reaction times: (a) 21 and 37 hrs, (b) 53, 60 and 84 hrs.

The second sample at 37 hrs (N=41) shown a mixed morphology of CYL and LAM with a relatively similar composition (Figure 4.12c, d). Interestingly, the whole particle area shows microphase separation and well-defined

nanostructures. Moreover, SAXS (Figure 4.14a) showed a well-defined reflection that indicates an increase in ordering and confirmed that the microphase separation had developed across the whole particle as observed by TEM.

At longer reaction times (53 and 60 hrs), the mixed morphology remained. However, the CYL phase seems to diminish and the LAM phase becomes more pronounced (Figure 4.15a-d). The reaction was allowed to run further until 84 hrs (93% conversion) and the morphology maintained the same LAM/CYL ratio, with LAM as the major structure (Figure 4.15e-f). Overall, this mixed morphology was observed in all investigated samples in the range of f_{PMMA} 0.60 – 0.23. This thermodynamically unfavourable morphology could be attributed by many factors, such as CO_2,[8,37] dispersity,[14] and homopolymer.[38]

For samples collected at 54, 60, and 84 hrs, the single-shot SAXS profiles (Figure 4.14b) are quite difficult to be observed, even though the TEM images showed an ordered nanostructure. This might be due to the existence of a mixed morphology that obscures the scattering peaks where the peaks for different structures may overlap.[6] The *in situ* SAXS patterns showed clearer scattering peaks than these offline measurements. Since the *in situ* measurement was conducted in a CO_2 environment, the different absorption level of CO_2 between the PMMA and PS blocks might result in an increase in polymer-polymer interaction parameter and hence a larger discrepancy.

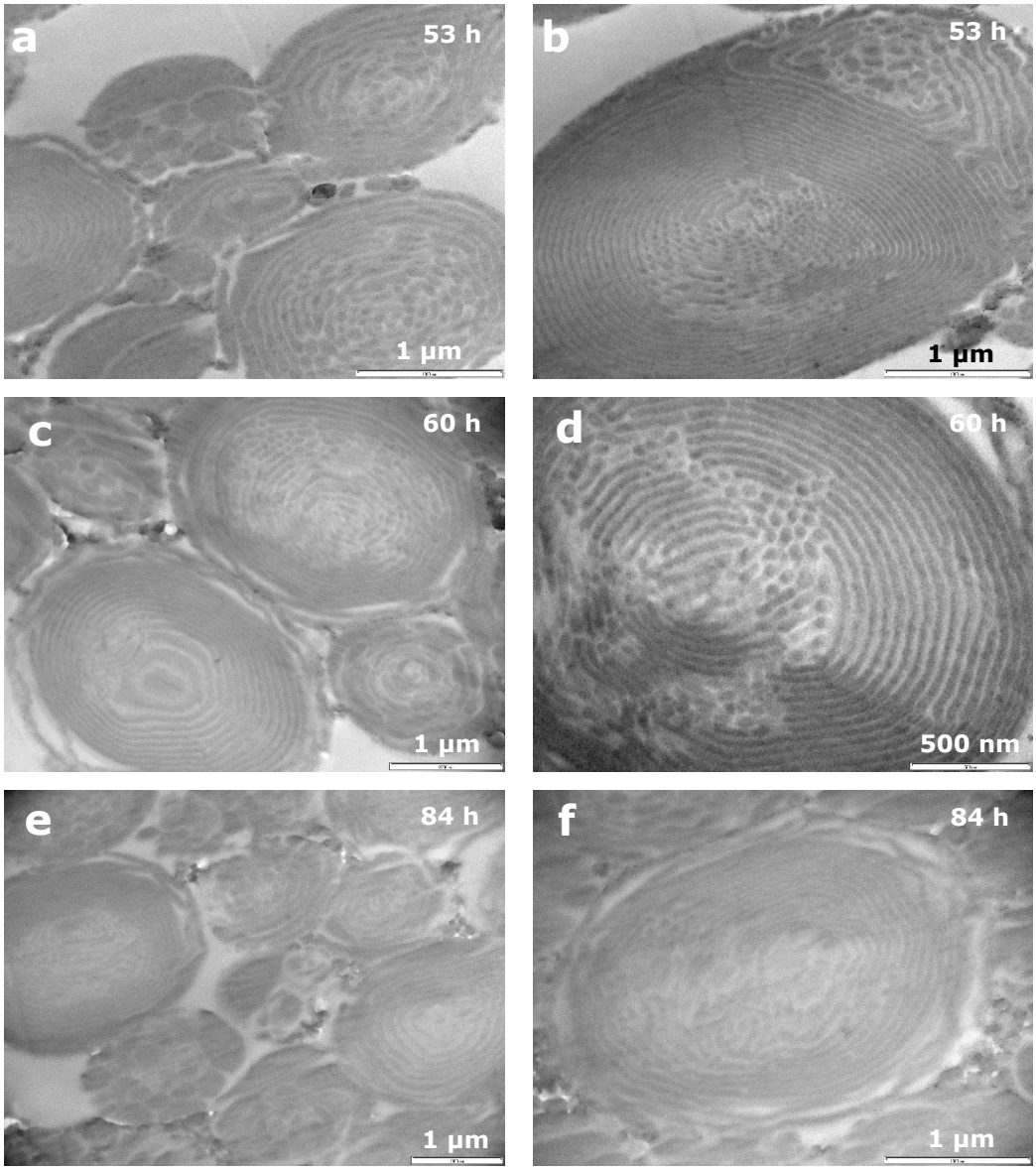


Figure 4.15. TEM images of the internal nanostructure of exp09 duplicate at different time intervals of reaction, (a), (b) 53 hrs, (c), (d) 60 hrs, and (e), (f) 84 hrs. All images show mixed phases of CYL and LAM. The experiment was conducted using a standard autoclave.

The TEM images confirm morphological development during the polymerisation. However, the general microphase-separated morphology remains constant from the initial formation. The mixed phases of exp09 that developed during the initial stages of microphase separation were also found in the final product. Similarly, SAXS profiles of exp02 show that the domain

spacing developed after ~20 hrs of reaction were practically constant until the end of the reaction. The structural information obtained by both SAXS and TEM studies suggest that the morphology of the microphase-separated domains formed in the microparticles does not change from the onset of the microphase separation. However, the internal nanostructure of the microparticles evolves as the PS block grows. Thus the volume of the internal microparticles (PMMA matrix) is occupied by higher ordered structures, as confirmed by both SAXS and TEM. The SAXS profiles show better resolved reflections while TEM images exhibit the disappearance of disordered regions as the reaction proceeds.

As revealed by SAXS and TEM, the microphase-separated morphology presents initially a low order structure. The initial structure of exp09 shows cylindrical domains of PS in PMMA matrix. As the reaction proceeded, PS segments grow to higher molecular weight and hence the CYL domains expand within the PMMA matrix (Figure 4.16). The selected expansion of the block domains seems to be facilitated by CO_2, which promotes the mobility and rearrangement of the copolymer chains. High chain mobility is normally achieved by heating. However, the CO_2 molecules can interact with the polymer chains, mainly due to their quadrupole moment,[19] and as a result, high sorption levels of CO_2 can lead to a reduction in the intermolecular forces between the chains.[39] The disruption of the intermolecular chains induces an increase in the free volume and thus higher mobility of the polymer chains.

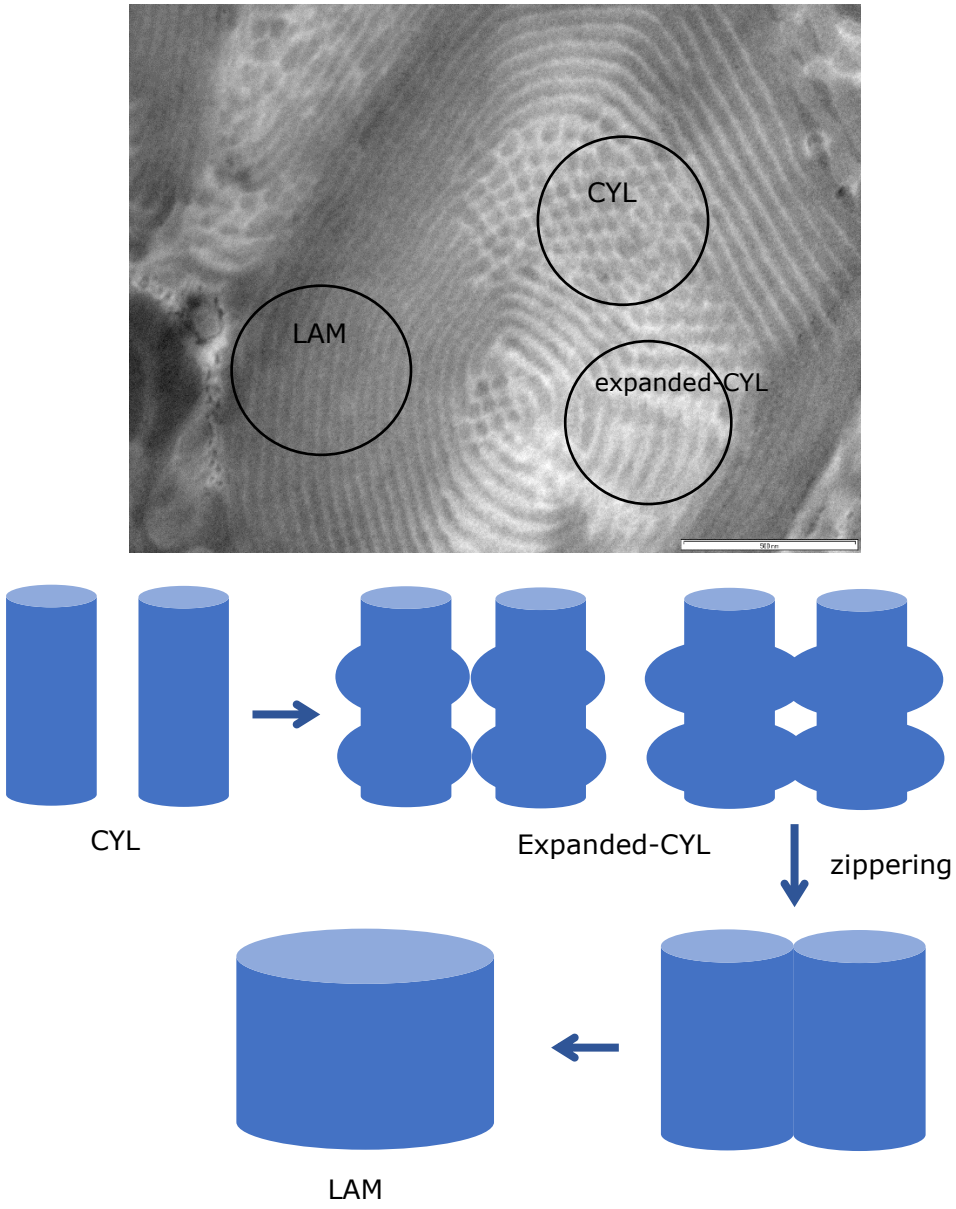


Figure 4.16. (Top) Representative TEM images showing different structural level development and (Bottom) a scheme illustrating a transformation of CYL into LAM structure (adopted from literature).[40]

Moreover, it has been observed in the thermally induced microphase transition that the neighbouring expanded-CYLs approach each other until there is interconnection of the CYLs, which results in a LAM structure (Figure 4.16).[40] Similarly, the transition from high order to lower order structure has also been investigated by others. The CYL structure of polystyrene-*b*-

polyethylene-*co*-polybutylene-*b*-polystyrene (PS-*b*-PE-*co*-PB-*b*-PS) block copolymer collapses and forms subsequently a rippled CYL as an intermediate prior to the transformation into a SPH structure in a selective solvent.[41]

4.5.4 The Invariant Plot

The kinetics of microphase separation can be studied by the invariant (*Q*). Importantly, the invariant is independent of the size or spatial arrangement of structural heterogeneities. The invariant is a linear function of the electron density variance and a quadratic function of the volume fraction (Equation 4.1). Assuming a two-phase system, an increase in the invariant corresponds to an increase in the different electron densities between the separated phases and indicates an increase in the degree of phase separation. Therefore, the development of the invariant can be related to the microphase separation kinetics.

For both samples, exp02 and exp09, the invariant increases with time during the reaction (Figure 4.17). This indicates the enhancement of the electron density difference between the PMMA and PS domains as the PS chains grow during the polymerisation, generating incompatibility between the dissimilar block copolymer domains. The discontinuities in the experimental invariant curves are related to pressure fluctuations of the system. This shows that the structure of the scattering plot is sensitive to the pressure which can alter the scattering background; i.e. associated with pressure-dependent density fluctuations.[3]

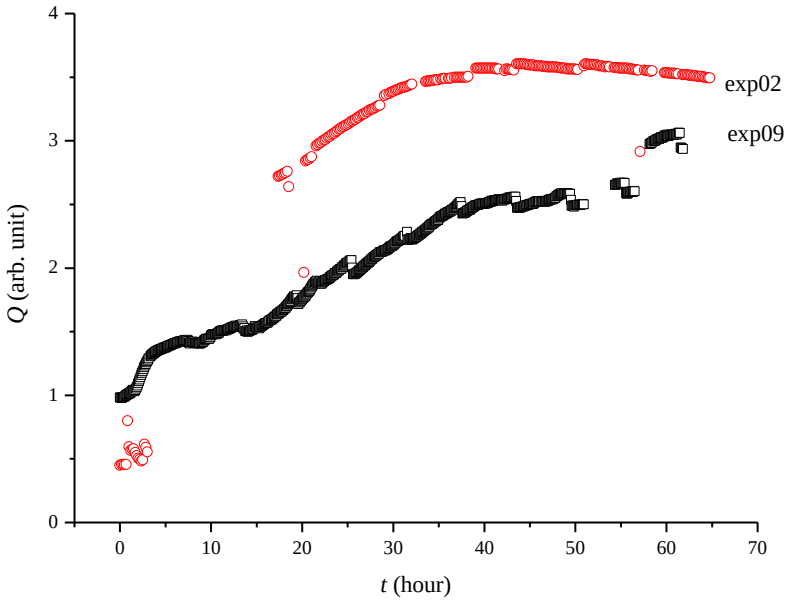


Figure 4.17. The invariant (Q) as a function of time, showing an increase of total scattering with time during the reactions. For clarity, the invariant of exp02 is shifted vertically by an arbitrary scaling factor.

In exp02, a sharp increase in the invariant between 5 and 16 hrs confirmed a transition from the homogeneous state to the microphase-separated state. This structural transition is also observed in the SAXS profiles that correspond to development of pronounced intensity of the first scattering reflection (q^*) (Figure 4.18). The dramatic increase in the invariant is then followed by a gradual increase up to ~40 hrs as the PS chains grow during the polymerisation. The increase in the total scattered intensity reaches a maximum when the relative volume fraction of the PS block approaches ~0.5[3] which is approximately the final composition of the exp02 block copolymer (f_{PMMA}=0.53 by NMR). From the maximum value, the invariant is then more or less constant until the reaction is complete.

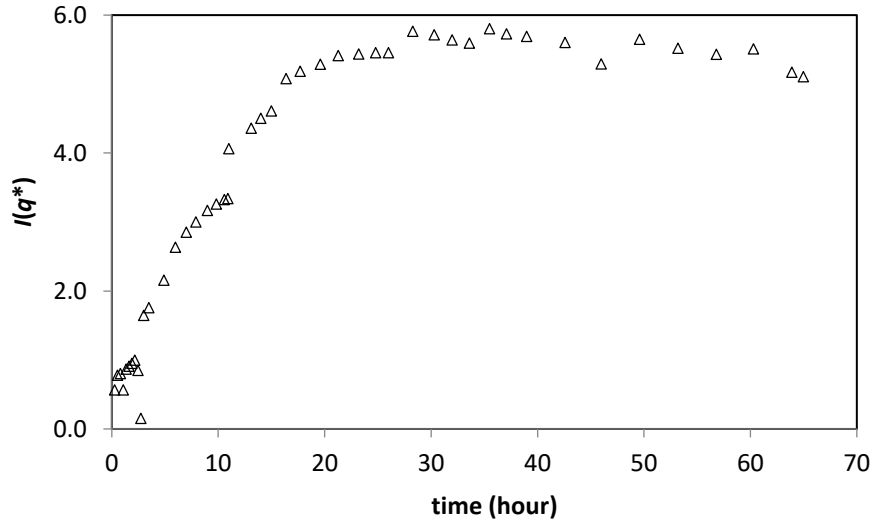


Figure 4.18. Scattering intensity of the primary peak, $I(q^*)$ of exp02, extracted from Figure 4.6, showing the sharp increase in the intensity between 5 and 16 hrs.

The invariant plot of exp09 confirmed that microphase separation is slow and occurs over a long time period. A structural transition during the growth mechanism either as the formation of intermediate structure(s) or the appearance of a second structure can be envisaged. The presence of a second structure has been observed by TEM (Figure 4.15) during periodic sampling of the polymerisation. In the invariant plot, the transitions were shown by a gradual increase in the total invariant with time as PS chains grow, and hence an increase in the electron density difference between the blocks.

In summary, monitoring the styrene polymerisation by time-resolved SAXS in combination with TEM analysis allows the microphase separation mechanism to be probed, including the onset of phase separation and the morphological development. Further investigation will be required to gain more details about the kinetics and mechanism of the microphase separation. In future experiments, a broader range of f_{PMMA} should be investigated to explore the microphase separation phase behaviour.

4.6 Conclusions

The current chapter has described the design of a new high pressure X-ray autoclave and its use in performing time-resolved SAXS experiments during RAFT dispersion polymerisation in $scCO_2$. The acquired scattering data were then used to observe the mechanism and kinetics of microphase separation during the polymerisation at different f_{PMMA} contents.

The new autoclave was developed from the standard 60 mL autoclave that is generally employed for the RAFT dispersion polymerisation in $scCO_2$. The main difference is the insertion of an optical part for X-ray measurement that featured two diamond windows housed in the body of the autoclave. The design provides ease of assembly-disassembly and post-reaction cleaning. Importantly, the new design produces comparable polymer products with the standard autoclave. However, a higher stirring rate was required while other synthetic parameters were maintained similar to the reaction conditions employed for the standard autoclave.

Using synchrotron radiation, the new autoclave was successfully applied to monitor *in situ* SAXS measurement during dispersion polymerisation in $scCO_2$. A series of polymerisations with different f_{PMMA} contents were conducted *via* the two-stage method to target different internal structures for PMMA-*b*-PS block copolymers and study their phase separation behaviour. The structural development that was monitored by *in situ* SAXS showed an enhancement of the Bragg reflections as well as a shift to lower q values as the reaction progressed. These indicate the development of the microphase separation and an increase in block copolymer domain spacing. SAXS and TEM analyses revealed that the copolymer morphology do not develop significantly from the initial microphase-separated morphology. However, the ordering of the nanostructures was found as the polymerisation proceeded.

4.7 References

1. Bates, F.S. & Fredrickson, G.H. *Phys. Today* **52**, 32–38 (1999).
2. Kratky, O. *Small Angle X-ray Scattering*. Academic Press: London, UK. (1982).
3. Hermida-Merino, D. et al. *Rev. Sci. Instrum.* **85**, 093905 (1-7) (2014).
4. Vukovic, I., ten Brinke, G. & Loos, K. *Macromolecules* **45**, 9409–9418 (2012).
5. Chu, B. & Hsiao, B.S. *Chem. Rev.* **101**, 1727–1762 (2001).
6. Vukovic, I. et al. *Macromolecules* **45**, 3503–3512 (2012).
7. Jennings, J. et al. *J. Am. Chem. Soc.* **134**, 4772–4781 (2012).
8. Jennings, J. et al. *Polym. Chem.* **7**, 905–916 (2016).
9. Derry, M.J. et al. *Chem. Sci.* **7**, 5078–5090 (2016).
10. Bates, F.S. & Fredrickson, G.H. *Annu. Rev. Phys. Chem.* **41**, 525–557 (1990).
11. Bates, F.S. *Science.* **251**, 898–905 (1991).
12. Lynd, N.A. & Hillmyer, M.A. *Macromolecules* **38**, 8803–8810 (2005).
13. Lynd, N.A., Meuler, A.J. & Hillmyer, M.A. *Prog. Polym. Sci.* **33**, 875–893 (2008).
14. Matsushita, Y. et al. *Macromolecules* **36**, 8074–8077 (2003).
15. Shi, L., Shen, Z. & Fan, X. *Macromolecules* **44**, 2900–2907 (2011).
16. Shinkai, T., Ito, M., Sugiyama, K., Ito, K. & Yokoyama, H. *Soft Matter* **8**, 5811–5817 (2012).
17. Shinkai, T., Ito, M., Sugiyama, K., Ito, K. & Yokoyama, H. *Soft Matter* **9**, 10689–10693 (2013).
18. Bennett, T.M., Jack, K.S., Thurecht, K.J. & Blakey, I. *Macromolecules* **49**, 205–214 (2016).
19. Cooper, A.I. *J. Mater. Chem.* **10**, 207–234 (2000).
20. Ghoshal, T., Biswas, S., O'Regan, C., Holmes, J.D. & Morris, M.A. *Nano Res.* **8**, 1279–1292 (2015).
21. Boyer, S.A.E., Iwamoto, C. & Yoshida, H. *J. Therm. Anal. Calorim.* **113**, 1565–1576 (2013).
22. Vogt, B.D. et al. *Macromolecules* **36**, 4029–4036 (2003).
23. Vogt, B.D., Brown, G.D., RamachandraRao, V.S. & Watkins, J.J. *Macromolecules* **32**, 7907–7912 (1999).
24. Testemale, D., Argoud, R., Geaymond, O. & Hazemann, J.L. *Rev. Sci. Instrum.* **76**, 043905 (1-5) (2005).
25. Krywka, C. et al. *ChemPhysChem* **9**, 2809–2815 (2008).
26. Gasc, F., Corso, B., Causse, J. & Lacroix-Desmazes, P. *J. Supercrit. Fluids* **114**, 26–31 (2016).
27. Bremholm, M., Jensen, H., Iversen, S.B. & Iversen, B.B. *J. Supercrit. Fluids* **44**, 385–390 (2008).

28. Carnahan, N.F. et al. *Langmuir* **9**, 2035–2044 (1993).

29. Jensen, H. et al. *Angew. Chemie Int. Ed.* **46**, 1113–1116 (2007).

30. Bremholm, M., Felicissimo, M. & Iversen, B.B. *Angew. Chemie Int. Ed.* **48**, 4788–4791 (2009).

31. Lai, J.T., Filla, D. & Shea, R.Y. *Macromolecules* **35**, 6754–6756 (2002).

32. Jennings, J. et al. *Macromolecules* **46**, 6843–6851 (2013).

33. Bassett, S.P. Polymerisation in Supercritical Carbon Dioxide. *Thesis*. The University of Nottingham (2015).

34. Rosell, A., Storti, G., Morbidelli, M., Bratton, D. & Howdle, S.M. *Macromolecules* **37**, 2996–3004 (2004).

35. Ryan, A.J., Willkommj, W.R., Bergstrom, T.B., Macosko, C.W. & Russell, T.P. *Macromolecules* **24**, 2883–2889 (1991).

36. Shinkai, T., Ito, K. & Yokoyama, H. *J. Supercrit. Fluids* **95**, 553–559 (2014).

37. Ito, M.M.M., Ito, K., Shibayama, M., Sugiyama, K. & Yokoyama, H. *Macromolecules* **48**, 3590–3597 (2015).

38. Chen, S.-C., Kuo, S.-W., Jeng, U.-S., Su, C.-J. & Chang, F.-C. *Macromolecules* **43**, 1083–1092 (2010).

39. Kelly, C.A., Howdle, S.M., Shakesheff, K.M., Jenkins, M.J. & Leeke, G.A. *J. Polym. Sci. Part B Polym. Phys.* **50**, 1383–1393 (2012).

40. Sakurai, S. et al. *Macromolecules* **26**, 485–491 (1993).

41. Li, M., Liu, Y., Nie, H., Bansil, R. & Steinhart, M. *Macromolecules* **40**, 9491–9502 (2007).

Chapter 5 One-pot Synthesis of Block Copolymer/Silver Nanoparticles Hybrid Materials

5.1 Overview

The success in controlling the phase morphology in block copolymer microparticles prompted an investigation of introducing metal nanoparticles into such phase-separated block copolymers. Our approach has been to determine whether it might be possible to introduce additional components into just one of the phases. This introduction might generate a hybrid material with new properties, and hence provide a wider application of the material. Moreover, incorporating metal nanoparticles within a particular domain of a phase-separated block copolymer could potentially produce metal nanostructures with controlled features, such as size or spacing. Others have obtained such phase separation in Pt-loaded poly(methyl methacrylate)-*b*-poly(perfluoroalkyl methacrylate) (PMMA-*b*-PsfMA) block copolymer micelles[1] and poly(3-(triethoxysilyl)propyl methacrylate)-*b*-poly(2-vinylpyridine)/Au-nanoparticles (PTEPMA-*b*-P2VP/AuNPs)[2], for example. However, these syntheses used pre-synthesised block copolymers that makes the process rather complex because they required several steps.

This chapter exploits a two-stage method developed in Chapter 3 for syntheses of a microparticulate block copolymer/metal nanoparticle hybrid material in supercritical CO_2 ($scCO_2$). Additionally, it is hypothesised that this approach might lead to a selective distribution of metal nanoparticles simultaneously during polymerisation in such a two-stage method. This would simplify a complex process that is normally applied for preparing metal loaded-polymers.[2–4]

For the intended purpose, silver metal is chosen because its soluble precursor is commercially available and has been shown to meet the suggested requirements when used in $scCO_2$, such as its solubility in $scCO_2$ and stability under high pressure conditions but readily degrading when required.[5] Moreover, silver nanoparticles (AgNPs) have a wide range of applications, such as for sensing materials, biomedical applications, and as a catalyst for various chemical reactions.[6–10] Loading such nanoparticles into a polymer provides stabilisation, prevents agglomeration and facilitates ease of application. PMMA-*b*-PDMAEMA block copolymer, which forms nanostructured morphologies,[11] is selected as the supporting polymer. In this approach, the second block, PDMAEMA, will be grown while generating the AgNPs in a one-pot protocol. The tertiary amine groups of the growing PDMAEMA chains should bind to the formed AgNPs. Therefore, the nanoparticles should be located in the PDMAEMA domains selectively.

The synthesis products will be characterised extensively by Scanning Electron Microscopy (SEM) to characterise the external morphology of the products. Meanwhile, Transmission Electron Microscopy (TEM) will be applied for inspecting the internal morphology, including the size and distribution of the metal nanoparticles in the copolymer microparticles.

5.2 Introduction

5.2.1 Synthesis of Metal Nanoparticles in $scCO_2$

Supercritical CO_2 is a fascinating medium for preparing metal nanoparticles since it has a high mass transfer rate and zero surface tension. In the syntheses of supported metal nanoparticles, these features may facilitate diffusion of the nanoparticles (or the soluble nanoparticle precursor) to achieve a homogeneous dispersion of the nanoparticles within the support.[12]

Such diffusion should be easier when a polymer is used as the supporting material since $scCO_2$ readily swells polymers and increases their chain mobility. Meanwhile, the zero surface tension could prevent the collapse of delicate support materials, such as aerogels, during the synthesis.[12] Additionally, the availability of many $scCO_2$-soluble metallic precursors has also prompted the use of $scCO_2$ as a reaction medium in this field.[13,14]

Metal nanoparticles can be deposited into both polymeric and inorganic porous supports using $scCO_2$. Watkins *et al*. reported the first preparation of polymer/metal nanocomposite materials in $scCO_2$.[15] In this work, an organoplatinum complex, dimethyl(1,5-cyclooctadiene)platinum(II) ($PtMe_2(COD)$) was impregnated into poly(4-methylpent-1-ene) (PMP) and poly(tetrafluoroethylene) (PTFE) assisted by $scCO_2$. The metallic Pt nanoparticles were obtained by reducing the complex precursor through either chemical or thermal reduction. The presence of metallic platinum in the composites was confirmed by TEM and WAXD (wide-angle X-ray diffraction). $scCO_2$-assisted impregnation of metallic precursor into fragile supports was demonstrated in the preparation of metal/aerogel composites.[16–18] Howdle and co-workers successfully produced AgNPs/silica aerogel nanocomposites using silver organocomplex precursors with different solubilities in $scCO_2$.[16] Precursors with lower solubilities resulted in lower metal loading, because it limited transfer into the aerogel. Similar results were also reported for the preparation of palladium nanoparticles/silica aerogel.[17] Another research group reported the use of carbon aerogels as supporting material for platinum nanoparticles (PtNPs).[18] The PtNPs were obtained by either thermal or chemical reduction (using H_2) after impregnating the precursor, $PtMe_2(COD)$, using $scCO_2$. In the chemical reduction, an autocatalytic mechanism occurred, forming a Pt film on the surface of the aerogel monolith and dispersing PtNPs

within its interior. Meanwhile, the thermal reduction produced monodisperse PtNPs with uniform spatial distribution.

Incorporating metal nanoparticles into support materials allows stabilisation to prevent agglomeration and facilitates ease of application. Preparing such supported metal nanoparticles in $scCO_2$ generally involves dissolution of a metallic precursor in $scCO_2$, incorporation of the precursor into the supporting material, and finally reduction of the precursor to its metallic form.[13,14] The dissolution of the precursor within $scCO_2$ is an essential parameter to ensure homogeneous distribution of the precursor within the fluid phase and allows high loading of the precursor on the support. After impregnating the precursor into the supporting material using $scCO_2$, the precursor must be reduced to its metallic form. The reduction of the precursor can be conducted by chemical or thermal reduction either in $scCO_2$ or at atmospheric pressure.[18,19] Chemical reduction is achieved by addition of reducing agents such as hydrogen (H_2) or alcohols.[12,20] Thermal reduction can be achieved by heating instead of using a reducing agent. It has been observed that in $scCO_2$ the reduction can be carried out at a lower temperature than at atmospheric pressure, although the mechanism is still unclear.[15,18] For example, the Pt precursor, $PtMe_2(COD)$, can be converted into metallic nanoparticles by a thermal reduction in $scCO_2$ at 135 °C and 310 bar. Meanwhile, a higher temperature (200 – 1000 °C) was required to obtain Pt nanoparticles at atmospheric pressure. Additionally, the use of $scCO_2$ resulted in a higher loading of nanoparticles on the support with larger particles, most probably as a result of the high mass transfer rate of $scCO_2$.[18]

5.2.2 Synthesis of Polymer/Metal Nanoparticles

Polymer/metal nanoparticle hybrid materials can be prepared by either an *ex situ* or *in situ* synthesis.[21] Most common is the *ex situ* synthesis, which

is conducted by introducing pre-formed functionalised metal nanoparticles into the polymer. For example, Yabu and co-workers prepared polymer/gold nanoparticles (AuNPs) *via* electrostatic interaction between amino-terminated polymers and citrate-stabilised AuNPs.[3,22] In other work, silanised magnetic Fe_3O_4 nanoparticles were placed selectively into PMMA domains of a PS-*b*-PMMA lamellar structure.[4,23] The silanised Fe_3O_4 nanoparticles clearly showed more selective placement within the block copolymer compared to neat nanoparticles.

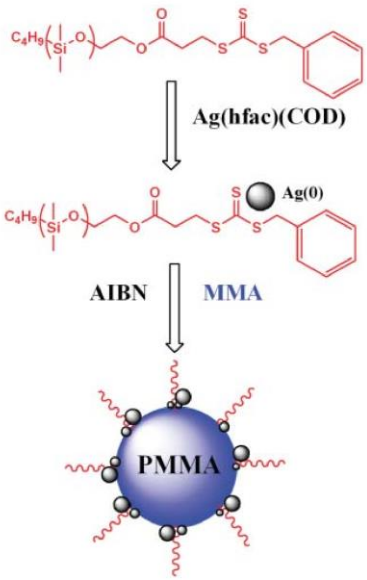
Alternatively, an *in situ* synthesis is conducted by introducing a metal nanoparticle precursor, either a metal salt or an organometallic complex, either before or after polymerisation. The precursor is subsequently reduced or decomposed thermally,[5,24] chemically,[7] ultrasonically,[25] or by UV irradiation[26,27] to form metallic nanoparticles. If the precursor is loaded before the polymerisation, nanoparticles and polymer chains should grow in tandem. This facilitates encapsulation of nanoparticles within a polymer, which is much easier than diffusion into bulk polymer due to its higher viscosity.[26] The *in situ* approach has been reported by Saito,[28] for instance, who selectively incorporated a silver nanocluster into the poly(2-vinyl pyridine) (P2VP) domains of PS-*b*-P2VP. It was performed by casting the block copolymer - 1,2-dioxane - water mixture with silver nitrate on a Teflon sheet and drying slowly at ambient temperature. The silver nitrate was converted to silver iodide, which was then reduced to zerovalent silver by reaction with hydroquinone. Transmission Electron Microscopy (TEM) and Wide Angle X-ray Scattering (WAXS) measurements were used to characterise the formed silver nanoclusters.

In other work, a poly(2-(methacryloyloxy)ethyl phosphorylcholine)-*b*-poly(2-(dimethyl amino)ethyl methacrylate (PMPC-*b*-PDMAEMA) block

copolymer was evaluated for the *in situ* synthesis of AuNPs.[29] The PDMAEMA block with its tertiary amine group acted both as a reducing agent for the acidic gold precursor and as an anchor for the formed AuNPs. Meanwhile, the PMPC block acted as a steric stabiliser and was responsible for the narrower size distribution of the AuNPs in the block copolymer. Another example of an *in situ* synthesis of AuNP formation was also conducted by exploiting the PDMAEMA block of a poly[oligo(ethylene glycol) methacrylate]-*b*-poly(2-dimethylaminoethyl methacrylate)-*b*-poly(styrene) (POEGMA-*b*-PDMAEMA-*b*-PS) triblock copolymer.[30] In this case, chloroauric acid was complexed with the PDMAEMA block and then subsequently reduced using $NaBH_4$.

Howdle and co-workers reported a single step *in situ* synthesis of polymer/silver nanoparticles (AgNPs) in $scCO_2$ through the RAFT dispersion polymerisation of MMA in $scCO_2$ in the presence of a silver precursor.[5] The precursor was (1,5-cyclooctadiene)(hexafluoroacetylacetonate)silver(I) [Ag(hfac)(COD)] which was soluble in $scCO_2$ and can be thermally decomposed during the polymerisation. Thus, polymerisation and formation of AgNPs take place in parallel. The RAFT agent used in these studies was a combination of a $scCO_2$-soluble substance, polydimethylsiloxane (PDMS) and benzylsulfanylthiocarbonylsulfanylpropionic (BSTSP) RAFT agent (Figure 5.1). The PDMS moiety stabilised the growing polymer particles and additionally located the RAFT agent on the surface of the particles to provide surface functionalisation. This result was a PMMA/AgNPs nanocomposite where the AgNPs were located on the surface of the PMMA microparticles (Figure 5.1).

a)



PDMS-BSTSP RAFT agent

b)

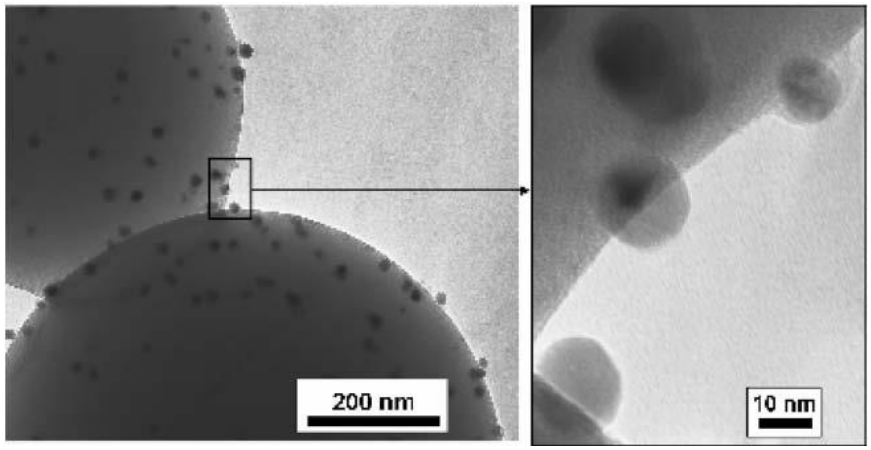


Figure 5.1. (a) Schematic diagram of the synthesis of AgNPs-decorated PMMA (PMMA/AgNPs) by using a combination of polydimethylsiloxane (PDMS) surfactant and benzylsulfanylthiocarbonylsulfanylpropionic (BSTSP) RAFT agent. (b) A bright field TEM image of the PMMA/AgNPs nanocomposite, showing location of AgNPs on the PMMA microparticles surface.[5]

Another example of an *in situ* synthesis in $scCO_2$ involved preparing Pt-loaded block copolymer micelles.[1] This synthesis utilised an ordered semifluorinated block copolymer, poly(methyl methacrylate)-*b*-poly(perfluoroalkyl methacrylate) (PMMA-*b*-PsfMA) prepared by anionic polymerisation to create patterned raspberry-like clusters of PtNPs. The

synthesis required a $scCO_2$-soluble precursor, $PtMe_2(COD)$, which was reduced by H_2 in parallel with block copolymer micelle formation under CO_2 pressure. The reduced precursor gradually lost its solubility, and hence partitioned into the inner part of the micelles (PMMA domains) that were insoluble in $scCO_2$ (Figure 5.2). This synthesis required pre-synthesised block copolymer and reducing agent to generate metal-loaded block copolymer micelles. This is different to our proposed approach, which aims to generate metal nanoparticles simultaneously during polymerisation, so that a metal-loaded block copolymer could be produced in a one-step process. Moreover, the synthesis is intended to produce a material in microparticulate form, which could lead to exciting new opportunities in sensors, catalysis, or optoelectronics.[31–33]

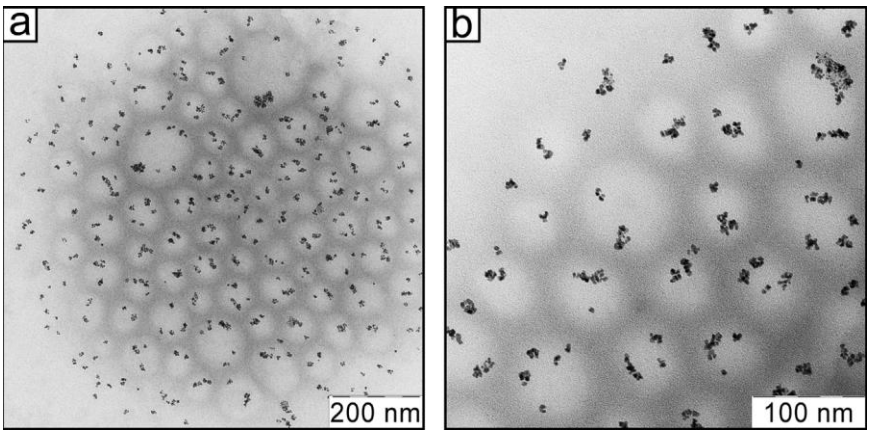


Figure 5.2. TEM images of clusters of Pt nanoparticles formed in micelles of PMMA-b-PsfMA block copolymer, with the Pt nanoparticles selectively decorating the micelle cores (PMMA domains, bright region). (a) low magnification, (b) high magnification.

Synthesis of such domain-selective nanoparticles generally requires three main steps[1]: (i) preparing the phase-separated block copolymer as micelles, thin film, or microparticles, (ii) loading a suitable nanoparticle precursor into the copolymer, and (iii) reducing or decomposing the loaded

precursor to form metal nanoparticles. Some approaches apply surface-modified nanoparticles to achieve high loading and high selectivity.[3,4,34] Such multi-step approaches are technically rather complicated so that developing simpler approaches is of great interest to many researchers in the field.

Comparing the *ex situ* and the *in situ* methods, the latter is simpler and more efficient since the polymerisation and nanoparticle formation occur in parallel. Furthermore, the formed nanoparticles are spontaneously dispersed in the polymer matrix during the polymerisation, and hence the nanoparticles are easier to homogeneously disperse within the matrix. However, the sizes and shapes of the formed nanoparticles are rather difficult to control. Supercritical fluids such as $scCO_2$ should provide an ideal medium to overcome this issue because of its high mass transfer rate and zero surface tension.[1,13] The work in this chapter explores in detail the one-step *in situ* synthesis of block copolymer/AgNPs through dispersion polymerisation in $scCO_2$ with selective localisation of the AgNPs within a particular domain. The polymerisation, nanoparticle formation, and selective localisation of the nanoparticles should all occur in parallel during the synthesis in $scCO_2$, which might lead to a simpler and 'greener' process.

5.2.3 Spatial Control of Nanoparticle Location in Phase Separated Block Copolymer

The ability of block copolymers to self-assemble into nanostructures gives rise to the possibility of controlling the location of metal nanoparticles in the host. This control allows the properties of the formed materials to be customised.[35] For example, the optical properties of block copolymer/nanocrystals are sensitive to the location of the nanocrystals within the polymer matrix.[36] Therefore, controlling the spatial distribution of

nanoparticles is crucial when preparing block copolymer/nanoparticle materials with specific targeted properties. In order to obtain good control of the nanoparticle distribution, the characteristics of both the nanoparticles and block copolymers are important.

The incorporation of inorganic nanoparticles in polymer matrices is guided by thermodynamics, i.e. enthalpy and entropy of the polymer-nanoparticle complex.[37] The enthalpy relates to the polymer-nanoparticle interface, which is controlled by the polymer-nanoparticle interaction. Meanwhile, the entropy includes a contribution from the polymer conformational entropy and the nanoparticle translational entropy, and these are controlled by polymer size (radius of gyration or polymer coil radius) and nanoparticle size, respectively. In order to incorporate nanoparticles in the polymer, the translational entropy should dominate and this can be achieved when the nanoparticle size is smaller than the polymer coil radius. If the sizes are similar, a significant enthalpy insertion must be applied, for example by functionalisation of the nanoparticle, so that the nanoparticle partitions to the polymer.

The effect of nanoparticle size on the nanoparticle distribution within block copolymer domains has been investigated.[35,38] Modelling and calculation of block copolymer nanocomposite films suggested that the metal nanoparticle distribution within a block copolymer domain depends on the nanoparticle size (d_{NP}) to block copolymer domain size (L) ratio (d_{NP}/L).[39,40] The nanoparticles will be localised around the centre of the nanoparticle-compatible domain when $d_{NP}/L \geq 0.3$. For a smaller d_{NP}/L value, the nanoparticles remain in the nanoparticle-compatible domain but tend to shift to the domain edges. As a result, the nanoparticle concentration in the centre will be lower than at the edges. An investigation of the distribution of PS coated-AuNPs within the PS

domain of a PS-*b*-P2VP block copolymer was conducted to study the effect of nanoparticle size on the nanoparticle assembly within the block copolymer domain. In this experiment, the AuNPs remain in the centre of the PS domain in all of the investigated d_{NP}/L values ranging from 0.13 to 0.44 (Figure 5.3 and Figure 5.4).[38] This result deviates from modelling studies discussed previously because the experiment used modified nanoparticles (PS coated-AuNPs) with a fair polydispersity in size, while the modelling studies only considered monodisperse, bare sphere particles.

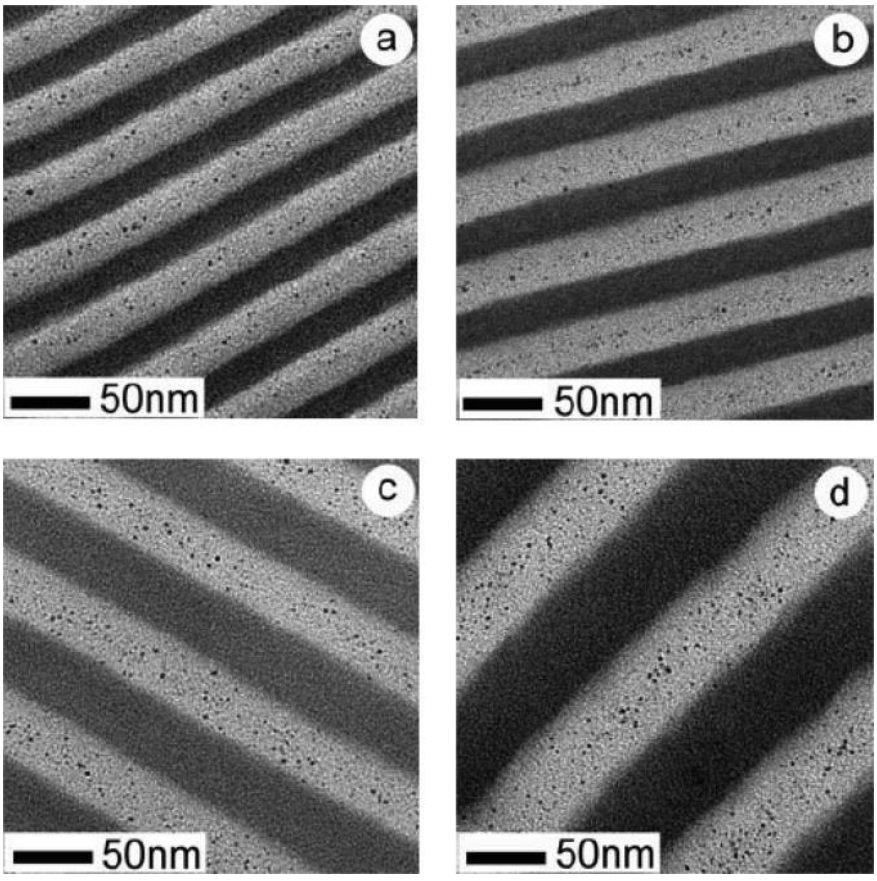


Figure 5.3. Cross-sectional TEM images of gold/block copolymer nanocomposite films of PS-*b*-P2VP with various d_{NP}/L ratios; (a) 0.44, (b) 0.31, (c) 0.18, and (d) 0.13). AuNPs are in the centre of the PS domain (bright area).[38]

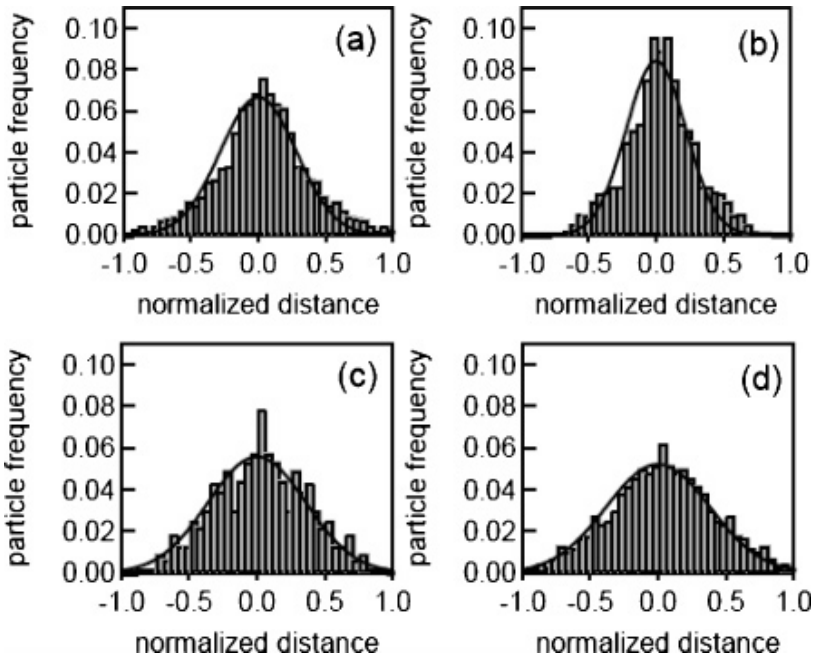


Figure 5.4. Corresponding histograms of the AuNPs distribution as a function of normalised distance from the centre of the PS domain for the samples shown in Figure 5.3.[38]

Additionally, the effect of block copolymer architecture on the spatial distribution of nanoparticles has also been reported.[41] Three different block copolymers were investigated, including a linear diblock copolymer (AB) and triblock copolymers (ABA and BAB). PS-coated AuNPs were dispersed uniformly within the PS domain of polystyrene-*b*-polyisoprene (PS-*b*-PI) and PS-*b*-PI-*b*-PS films with a lamellar structure (Figure 5.5a and b). In contrast, the AuNPs aggregated within the PS domain of a PI-*b*-PS-*b*-PI triblock copolymer film (Figure 5.5c). This is due to the different configuration of the midblock domain of the triblock copolymers in the microphase-separated state (Figure 5.6). In the latter triblock copolymer, the chains are in a bridged configuration that makes the PS chains more stretched and results in a significant reduction in their conformational entropy. As a result, AuNPs aggregated inside the PS

domain. The same results were obtained when the copolymers formed cylindrical structures.

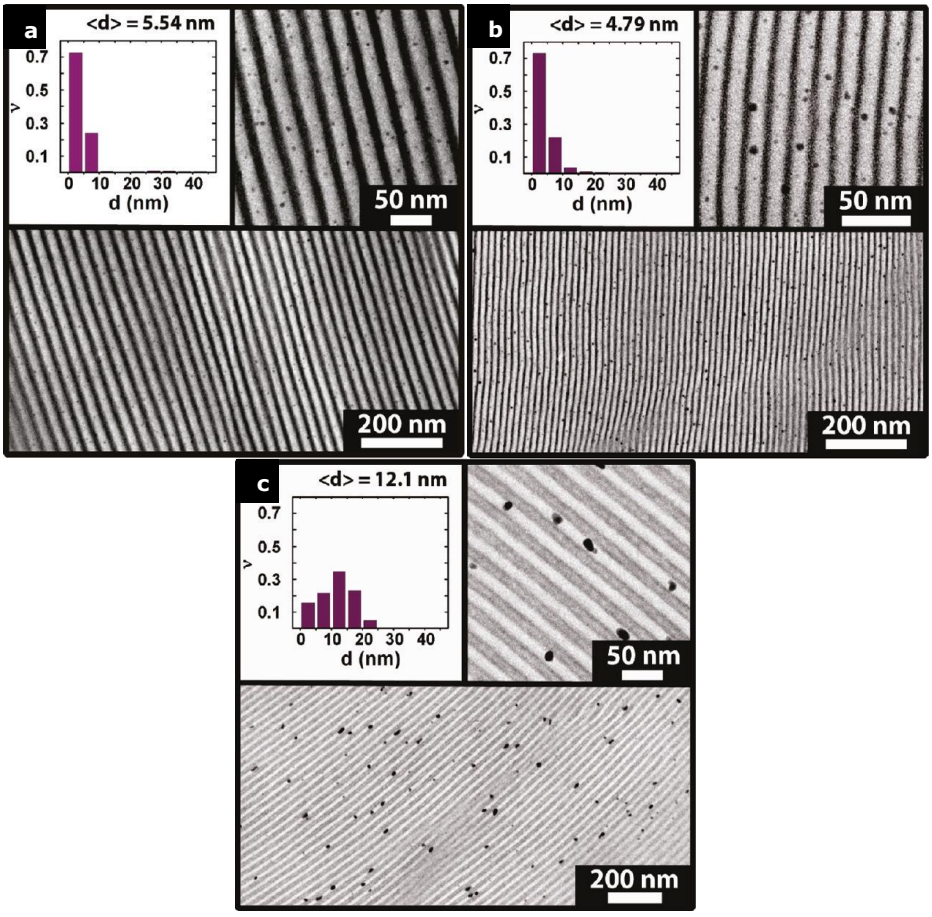


Figure 5.5. TEM images of block copolymer nanocomposite films (a) PS-*b*-PI/AuNPs and (b) PS-*b*-PI-*b*-PS/AuNPs, both have monodisperse PS-coated AuNPs within PS domain, (c) PI-*b*-PS-*b*-PI/AuNPs, PS-coated AuNPs are polydisperse and aggregated within PS domain. The left inset depicts the particle size distribution and the right inset shows a magnified image. The dark area is OsO_4-stained PI.[41]

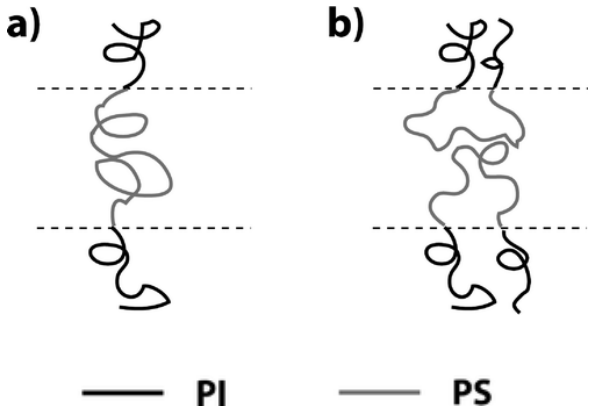


Figure 5.6. Schematic diagram of (a) bridged and (b) loop chain configurations of the midblock of triblock copolymers (PI-*b*-PS-b-PI and PS-*b*-PI-*b*-PS) films in the microphase-separated state.[41]

Furthermore, the localisation of nanoparticles can also be tuned by the addition of small molecules that may provide further control over polymer-nanoparticle interactions.[42,43] For example, two small molecules, 3-*n*-pentadecylphenol (PDP) and 4-(4'-octylphenyl)azophenol (OPAP), were applied to direct nanoparticle localisation in a PS-*b*-P4VP block copolymer.[42] The small molecules form hydrogen bonds with the P4VP block and direct the nanoparticles to the P4VP domains. This approach was shown to be applicable for a range of nanoparticles, including CdSe, PbS, and Au in different shapes and sizes.

To summarise, controlling the distribution of nanoparticles within ordered block copolymers can be achieved by considering several parameters relating to both kinetics and thermodynamics. By careful consideration of the related parameters, selective localisation can be achieved even without modifying or functionalising the nanoparticles.

5.3 Objectives

The primary aim of this chapter is to achieve a one-pot synthesis of microparticulate PMMA-*b*-PDMAEMA/AgNPs through dispersion polymerisation in $scCO_2$ with selective localisation of the AgNPs into the PDMAEMA domain. The aim is to use a $scCO_2$-soluble silver precursor to produce AgNPs *in situ* during the polymerisation. The functional groups of the PDMAEMA domain will capture and anchor the AgNPs leading to selective localisation. The hypothesis is that polymerisation, nanoparticle formation, and selective localisation of the formed nanoparticles should occur simultaneously. Electron microscopy will be used to characterise the products.

5.4 Experimental

5.4.1 Material

Methyl methacrylate (MMA, 99%, Fisher) and *N,N*-dimethylaminoethyl methacrylate (DMAEMA, 98%, Sigma Aldrich) were purified by passing through a neutral aluminium oxide column prior to use. RAFT agent, S-dodecyl-S'-(α, α'-dimethyl- α''-acetic acid)-trithiocarbonate (DATC) was synthesised following a literature procedure.[44] Poly(dimethylsiloxane monomethyl methacrylate) (PDMS-MA, 10 kDa, ABCR Gmbh), 2,2'-azobis(isobutyronitrile) (AIBN, Sigma Aldrich), silver precursor (1,5-cyclooctadiene) (hexafluoroacetylacetonato)silver(I) (Ag(hfac)(COD), Sigma Aldrich), aluminium oxide (Across Organic), HPLC grade THF (Sigma Aldrich), iodine (Fisher), and Agar 100 resin (Agar Scientific) were all used as received. Dry CO_2 (99.99%) was purchased from BOC. EPDM O-rings were acquired from Brammer. All monomers were degassed by bubbling with argon prior to use.

5.4.2 Synthesis of PMMA-*b*-PDMAEMA

To target PMMA-*b*-PDMAEMA of 75 kg mol^{-1} with a PMMA/PDMAEMA ratio of 2 : 1, pre-synthesised PMMA (presented in Chapter 3) (5,616 mg, 0.112 mmol) and PDMS-MA (280 mg, 5 %wt wrt DMAEMA) was added into a 60 mL autoclave. The autoclave was then clamped and purged with CO_2 (3 - 4 bar) for 15 minutes to remove oxygen which may otherwise inhibit the polymerisation. After sealing, the autoclave was pressurised to 55 bar by charging CO_2. The stirrer was turned on and adjusted to 300 rpm and the heater was set to 65 °C. Once 65 °C has been reached, additional CO_2 was added to reach a pressure of 205 bar and allow the system to stabilise for 1 – 2 hours. After that, degassed DMAEMA (4.6 mL, 27.86 mmol) and AIBN (18.4 mg, 0.112 mmol) were injected into the autoclave *via* an HPLC pump. Additional CO_2 was then added as required to reach a final reaction pressure of 275 bar. The reaction was allowed to proceed for 72 h.

Once the allotted time had been reached, the reaction was quenched by immersion of the autoclave in a dry ice bath. Pressure was then reduced by venting through the exit tap until atmospheric pressure (1.0 bar). The autoclave was opened and the product was collected for further analysis and characterisation.

5.4.3 Synthesis of PMMA-AgNPs

The following is a procedure for preparing PMMA-AgNPs with molecular weight of polymer 50 kg.mol^{-1}. Firstly, a silver precursor Ag(hfac)(COD) (336 mg, 2 wt% with respect to MMA) was added into the autoclave and then the autoclave was clamped and purged with CO_2 (3 - 4 bar) for 15 minutes. The degassed solution of MMA (18 mL, 168 mol), DATC (122.7 mg, 0.336 mmol), PDMS-MA (842 mg, 5 wt% w.r.t. MMA), and AIBN (55.2 mg, 0.336 mmol) was injected into the autoclave. The autoclave was sealed and CO_2 was introduced

to 50 bar. The stirrer and the heater were then switched on and set to 300 rpm and 65 °C, respectively. Once 65 °C had been reached, additional CO_2 was added gradually, as required, to reach a pressure of 275 bar. The reaction mixture was then left for 18 hours.

After the reaction had finished, the heater and the stirrer were switched off and the autoclave was left to cool to room temperature. Once this temperature had been reached, the CO_2 was slowly released. At atmospheric pressure (1.0 bar), the autoclave was opened and the product was collected. The polymer product could then be characterised as required.

5.4.4 Synthesis of PMMA-*b*-PDMAEMA/AgNPs

Pre-synthesised PMMA (5,616 mg, 0.112 mmol), PDMS-MA (140 mg, 5 wt% w.r.t. DMAEMA), and Ag(hfac)(COD) (219 mg, 5 wt% w.r.t. DMAEMA) were charged into a 60 mL autoclave. The autoclave was then clamped and purged with CO_2 (3 - 4 bar) for 15 minutes. After sealing, the autoclave was pressurised to 55 bar by charging CO_2. The stirrer was turned on and adjusted to 300 rpm. The heater was then set to 65 °C. Once 65 °C had been reached, additional CO_2 was added to reach a pressure of 205 bar and the system was allowed to equilibrate for 1 – 2 hours. After that, degassed DMAEMA (4.7 mL, 27.86 mmol) and AIBN (18.4 mg, 0.112 mmol) were added into the autoclave *via* an HPLC pump. Additional CO_2 was then added as required to reach a final reaction pressure of 275 bar. The reaction mixture was left for 72 h.

Once the allotted time had been reached, the reaction was quenched by immersion of the autoclave in a dry ice bath. Pressure was then reduced by venting through the exit tap until atmospheric pressure (1.0 bar). The autoclave was opened and the product was collected for analysis and characterisation.

5.5 Results and Discussion

5.5.1 Initial Studies

5.5.1.1 Synthesis of PMMA-b-PDMAEMA

For the preparation of a block copolymer hybrid material, synthesis of PMMA-*b*-PDMAEMA block copolymers was achieved using the two-stage synthesis method presented in Chapter 3. PDMAEMA was selected as the second block because it has tertiary amine groups that could anchor metal nanoparticles, selectively locating them within the PDMAEMA domain. It has been reported that the tertiary amine group of the PDMAEMA block can act both as a reductant and stabiliser in the formation of AuNPs[29] and AgNPs[7] in aqueous solution. However, PDMAEMA has very different properties to the previous polymers synthesised by the two-stage method. It is a relatively soft polymer with a T_g just below room temperature (19 °C). Therefore, an initial synthesis should be performed to evaluate whether the block copolymer can be prepared by the intended method.

The synthesis is a RAFT dispersion polymerisation of DMAEMA using a PMMA-DATC macro-RAFT agent (Figure 5.7). AIBN and PDMS-MA were applied as an initiator and a stabiliser, respectively. The initial synthesis prepared PMMA-*b*-PDMAEMA with a 33% mass fraction of PDMAEMA. Unfortunately, this afforded a tacky solid polymer and agglomerated particles (Table 5.1 entry 1, Figure 5.8). Indeed, this result is similar to the previous studies on such copolymers with more than 25% of PDMAEMA content.[45,46] The copolymer products tend to agglomerate as a consequence of the low T_g of PDMAEMA. The morphology of the dispersion polymerisation product depends on the T_g of the copolymer. A polymer with a low T_g tends to agglomerate, and the presence of stabiliser cannot significantly improve the morphology.[45] Moreover, the use

of $scCO_2$ as a polymerisation medium dramatically enhances plasticisation of the polymer and leads to significant agglomeration by further lowering the Tg.

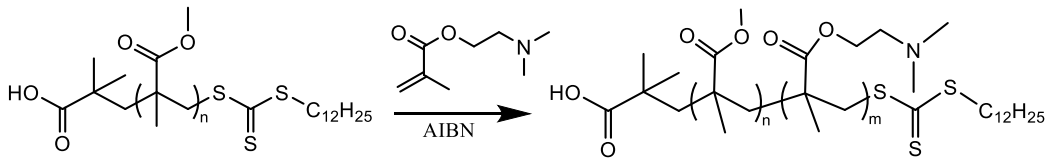


Figure 5.7. RAFT synthesis of PMMA-b-PDMAEMA in $scCO_2$ (65°C, 275 bar) using PMMA-DATC as the macro-RAFT agent.

We reasoned that the agglomeration most likely occurs at the end of the reaction when the CO_2 pressure is released: the steric stabilisation of the particles is lost and the soft tacky particles are allowed to agglomerate. To overcome this problem, we tried a new approach. An identical block copolymer was prepared, but to minimise agglomeration the product was frozen by placing the autoclave in a dry ice bath once the reaction had finished (Table 5.1, entry 2). This approach provided rapid cooling and ensured that the PDMAEMA was below its T_g and became glassy, thus the possibility of particle agglomeration was minimised. The new approach worked: a dry powder of polymer was collected upon opening the autoclave with less agglomerated particles, even with a higher content of PDMAEMA (50%) (Table 5.1 entry 3, Figure 5.8). Low dispersities ($M_w/M_n<1.4$) were obtained for all block copolymers, indicating good control over the polymerisation.

Table 5.1. Characteristics of PMMA-b-PDMAEMA deblock copolymer synthesised by two-stage RAFT dispersion polymerisation with normal cooling (entry 1) and rapid cooling (entry 2 and 3) procedure.

Entry	PMMA		Block copolymer				Morphology[d]	Conv (%)[e]
	M_n^{GPC} (kg mol^{-1})[a]	Đ[a]	PDMAEMA mass fraction[b]	M_n^{th} (kg mol^{-1})[c]	M_n^{GPC} (kg mol^{-1})[a]	Đ[a]		
1	46	1.20	33%	63	59	1.36	Tacky solid	73
2	47	1.22	33%	67	58	1.11	Dry Powder	87
3	31	1.16	50%	62	41	1.02	Dry powder	99

The reactions were conducted at 65 °C and 275 bar for 72 hrs with a molar ratio CTA : I of 1 : 1 and 5% stabiliser w.r.t. monomer. DMAEMA was added in high pressure (~200 bar) *via* a HPLC pump. PMMA was dispersed in $scCO_2$ for 2 hrs prior to DMAEMA addition.

a. Measured by GPC in THF with LS detector
b. Based on molar ratio of monomer feed
c. Calculated from: $M_n^{PMMA}+([M2]/[CTA])*MW_{M2}*conversion$
d. Initial appearance upon opening the vessel
e. Calculated gravimetrically

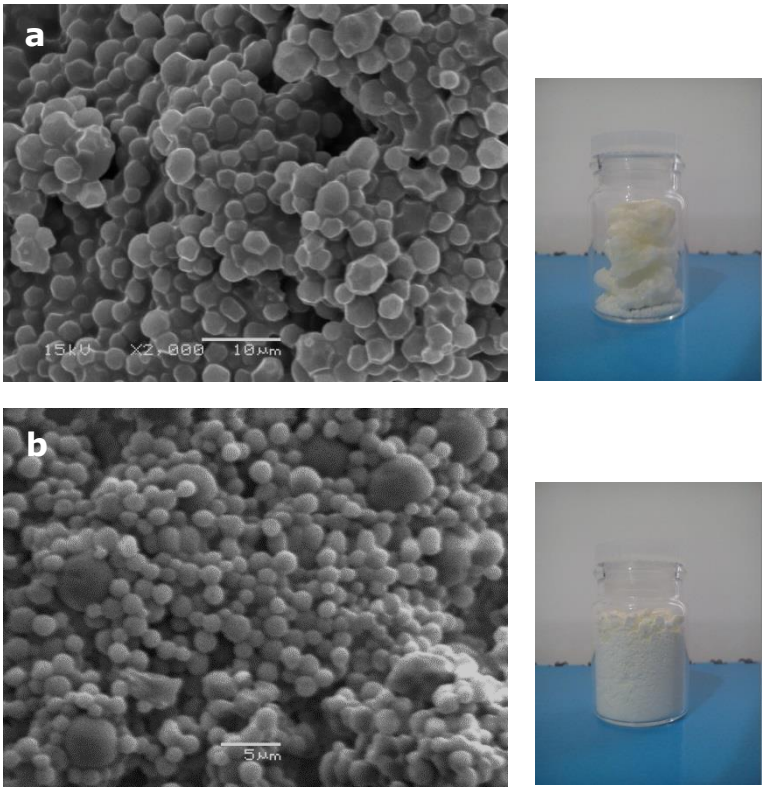


Figure 5.8. SEM images of PMMA-*b*-PDMAEMA produced with different mass fractions of PDMAEMA (Table 5.1), (a) 33% with normal cooling procedure (entry 1) produces monolith and agglomerated morphology, (b) 50% (entry 3), with the rapid cooling procedure produces fine powder and spherical morphology.

A discrepancy between M_n^{GPC} and M_n^{th} is observed (Table 5.1). Similar discrepanciesfor PDMAEMA-containing block copolymers have been previously reported and ascribed to the interaction of the PDMAEMA block with the GPC column.[47,48] PDMAEMA can adsorb onto GPC columns when residual carboxylic functionalities are present on the surface of the column, as reported by Baines *et al.*[47] This interaction will produce peak broadening and longer retention time (lower molecular weights).

GPC traces show an overlap between the initial homopolymer (PMMA-RAFT) and the block copolymer peaks that indicate incomplete chain extension (Figure 5.9). This might be attributed to the presence of dead PMMA chains

generated by radical-radical termination during the preparation of the PMMA RAFT agent. However, a shift towards higher molecular weight without any broadening of the molecular weight distribution already suggests some living character. PDMAEMA homopolymer could also be initiated during the synthesis, but according to the previous report from our research group, the blocking impurities in $scCO_2$ dispersion system are mostly attributed to dead PMMA homopolymer.[49]

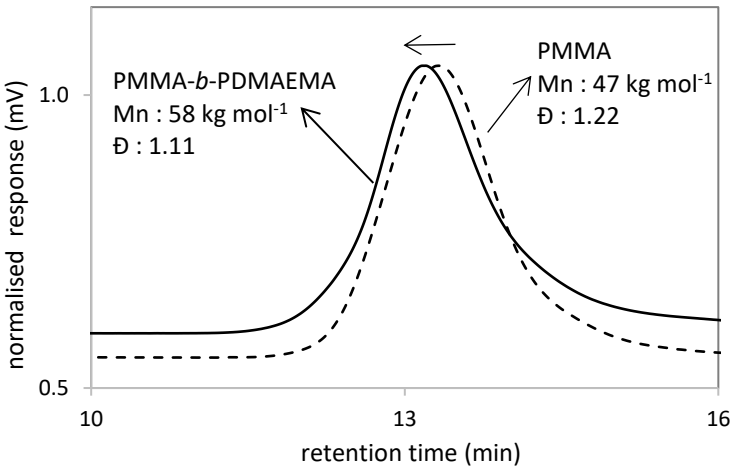


Figure 5.9. GPC traces showing the increasing molecular weight (dashed line) on addition of DMAEMA to form PMMA-b-PDMAEMA block copolymer (solid line).

The PMMA-*b*-PDMAEMA samples were then analysed in terms of their internal morphology using TEM. Spherical domains of PDMAEMA embedded in PMMA matrix were observed when the mass fraction of PDMAEMA was 33% (Figure 5.10). This morphology agreed with the typical phase behaviour for linear block copolymer with such compositions.[50] PMMA-*b*-PDMAEMA is an all-methacylate block copolymer, thus like PMMA-*b*-PBzMA, there is no $scCO_2$-selective solvent effect on the phase behaviour. For PMMA-*b*-PDMAEMA with a higher PDMAEMA mass fraction (50%), there is no internal morphology.

However, such copolymer formed core-shell microparticles. The shell is proposed to be due to dead polymer (PMMA homopolymer), as confirmed by the lighter colour under bright field TEM after staining by iodine vapour, while the core is the block copolymer with homogeneous morphology. The PMMA homopolymer tends to locate on the outer side because it has higher CO_2-philicity.

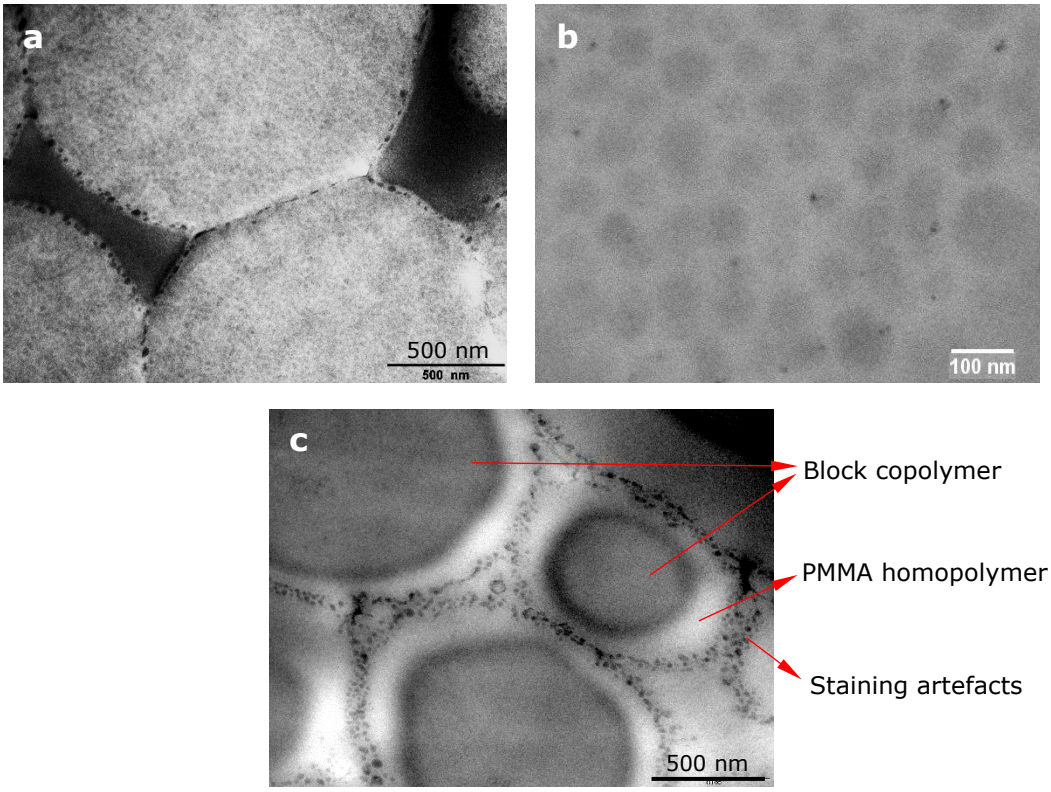


Figure 5.10. Cross-sectional TEM images of PMMA-b-PDMAEMA with (a) 33 wt% of PDMAEMA showing spherical structure, the dark domains are from the iodine-stained PDMAEMA. (b) 33 wt% of PDMAEMA at higher magnification. (c) 50 wt% of PDMAEMA showing a homogeneous central structure and additional shell.

5.5.1.2 Formation of AgNPs

In this work, AgNPs were intended to be synthesised in parallel with the dispersion polymerisation in $scCO_2$. Therefore, an ideal silver precursor should be soluble in $scCO_2$ and stable under high-pressure conditions, but must also

degrade readily when required. In the case of dispersion polymerisation, the solubility of the precursor is an important parameter for successful dissolution and to preserve the stability of the dispersion. This stability is crucial for maintaining the integrity of the block copolymer morphology. The selected precursor was Ag(hfac)COD (Figure 5.11) since it has been previously used in $scCO_2$ and has been shown to meet the above requirements.[5,6]

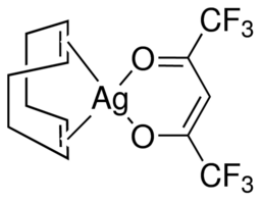


Figure 5.11. Chemical structure of Ag(hfac)COD, (1,5-cyclooctadiene) (hexafluoroacetylacetonato) silver(I), the organosilver complex used for the production of silver nanoparticles.

Synthesis of AgNPs in $scCO_2$ from the selected precursor was first investigated to ensure the decomposition worked successfully in the required system. According to the previous reports, the precursor decomposes between of 60 and 180 °C.[5,6,24,51] The higher the temperature, the faster decomposition should occur, and just 10 s is enough to decompose the precursor to zerovalent silver at 180 °C.[24] This precursor has good solubility in $scCO_2$ at 275 bar, although it is still soluble even at lower pressures (~100 bar).[51]

For initial studies, a typical RAFT dispersion polymerisation of MMA was conducted in the presence of 2 wt% (w.r.t. MMA monomer) of the silver precursor in $scCO_2$. Polymerisation of MMA was selected since this reaction is well known in our research group with a high degree of success. The reaction proceeds for 18 hours at 65 °C and 275 bar; a temperature that induces decomposition of the soluble silver precursor. This same temperature and

pressure are also required for preparation of the targeted block copolymer, PMMA-*b*-PDMAEMA.

In a control experiment, the polymerisation of MMA in the presence of Ag(hfac)(COD) resulted in a brown powder. This is an indication of the surface plasmon resonance of silver nanoparticles. Morphological analysis of the product showed that pherical PMMA microparticles were obtained (Figure 5.12a). This indicates that the presence of silver precursor has no significant negative effect on the dispersion process. Moreover, the AgNPs were clearly formed as shown by the tiny black dots in the TEM image (Figure 5.12b). Most importantly, the AgNPs do not appear within polymer particles since there are neither binding groups on the polymer particles nor pores that allow the AgNPs to diffuse into the PMMA particles. For these reasons, the AgNPs were deposited on the polymer surface when the precursor dissociated and decomposed.

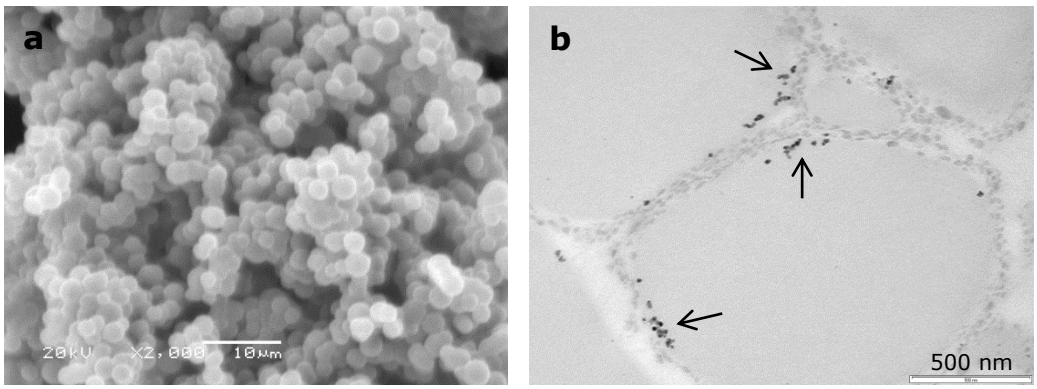


Figure 5.12. PMMA-AgNPs synthesised by dispersion polymerisation in $scCO_2$ (a) SEM image showing spherical microparticles. Scale bar is 10 µm, (b) Cross-sectional TEM image of the microparticles showing that the formed AgNPs (arrows) are located outside the PMMA microparticles and no AgNPs are found inside the microparticles. Scale bar is 500 nm.

5.5.2 Synthesis of PMMA-*b*-PDMAEMA/AgNPs

It has been demonstrated that PMMA-*b*-PDMAEMA microparticles with an ordered internal nanostructure can be successfully synthesised by the two-stage method and that the selected soluble silver precursor forms AgNPs during dispersion polymerisation in $scCO_2$. Now, the two processes are combined to introduce AgNPs into the nanostructured block copolymer. A number of reports have shown that PDMAEMA can act as a reducing agent in the formation of metal nanoparticle-loaded polymers.[7,29] However, these synthetic routes required complex steps, involving the synthesis of the polymer and nanoparticle formation independently. Here, synthesis of PMMA-*b*-PDMAEMA/AgNPs is proposed in a simple one-pot reaction. Moreover, the absence of organic solvents and a reducing agent should provide a process that is simple and environmentally benign.

The synthesis of PMMA-*b*-PDMAEMA was conducted under identical conditions (section 5.5.1), except with the addition of the silver precursor (2 wt% w.r.t. both PMMA and DMAEMA) along with the PMMA-macro RAFT to obtain PMMA-*b*-PDMAEMA/AgNPs (Figure 5.13). The PDMAEMA block was targeted at 33 wt% (w.r.t. PMMA) in order to obtain a spherical morphology.

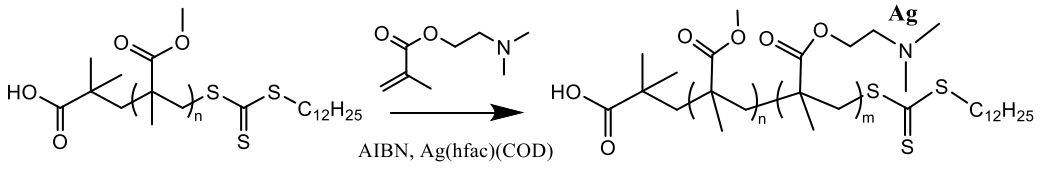


Figure 5.13. Synthetic route to PMMA-*b*-PDMAEMA/AgNPs by RAFT dispersion polymerisation of DMAEMA in $scCO_2$.

The reaction resulted in a brown powder. SEM investigation showed microparticles with some agglomeration (Figure 5.14a) that was attributed to

the formation of AgNPs. This will be discussed in the next section. The internal morphology was also observed by examining the cross-sectional images of the copolymer microparticles by TEM. The image clearly shows AgNPs located inside the block copolymer microparticles (Figure 5.14b) as tiny black dots, since only AgNPs have high enough electron density to be observed as dark areas by bright field TEM imaging.

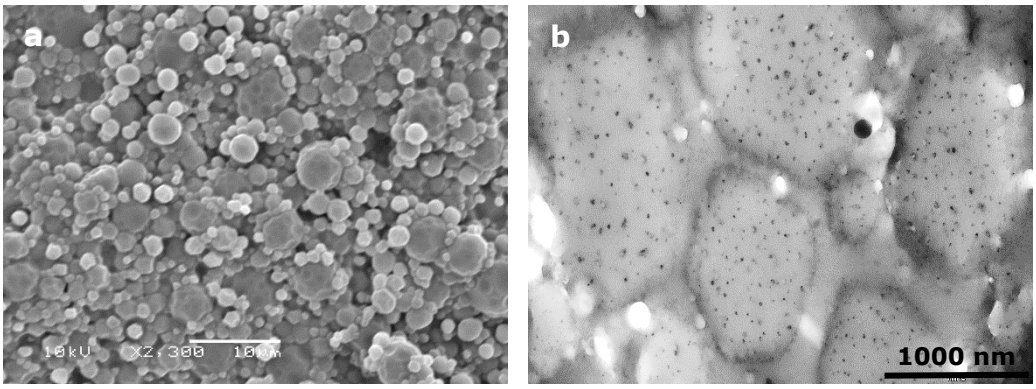


Figure 5.14. Morphological analysis of PMMA-b-PDMAEMA/AgNPs (Table 5.1, entry 2), (a) SEM image showing microparticles of the block copolymer hybrid, (b) cross-sectional TEM image showing the AgNPs (black dots) located inside the polymer particles. The TEM image was obtained without staining.

The AgNPs have been successfully introduced into the interior of the polymer particles. A direct comparison with the PMMA-AgNPs demonstrates that the presence of the PDMAEMA block has ensured the AgNPs deposit within the polymer particles. After the organocomplex precursor is dissociated by heat, the electron-rich tertiary amine groups of PDMAEMA block withdraw and reduce the electron-deficient silver ions. Moreover, the simultaneous polymerisation and AgNP formation facilitates diffusion of the silver within the polymer particles. During polymerisation, the silver diffuses into the growing polymer, which is much easier than diffusion into the highly viscous bulk polymer.[26] In addition, the high diffusivity of $scCO_2$ considerably increases the

kinetics of silver diffusion.[14] All of these factors allow efficient incorporation of AgNPs inside block copolymer particles.

Four processes occur in parallel during the synthesis; (i) dissolution of the silver precursor in $scCO_2$, (ii) thermal dissociation of the precursor to generate silver ions, (iii) polymerisation of DMAEMA and diffusion of silver ions into the growing polymer particles, and (iv) capturing silver ions by growing PDMAEMA chains and subsequently reducing silver ions to zerovalent silver. This synthesis produces a clean material as the solvent is readily removed on depressurisation and there was no additional reducing agent. Meanwhile, the dissociated ligand can be extracted at the end of the reaction by purging the autoclave with $scCO_2$.[16,52] This is necessary if a high purity product is required.

5.5.3 Selectivity of AgNPs within the polymer particles

It was obvious that the formed AgNPs decorate the interior of the block copolymer particles. However, their spatial distribution is not clear yet. Are they selective for one domain of the block copolymer or distributed randomly inside the particles? In this section, the spatial distribution and selectivity of the AgNPs within the block copolymer domains will be discussed. The spatial distribution was studied using TEM at high magnification. Some samples were treated with iodine vapour prior to imaging to increase the contrast between the PMMA and PDMAEMA domains.

TEM images of PMMA-b-PDMAEMA/AgNPs with 33% PDMAEMA content prepared by addition of 2% silver precursor were analysed. Spherical domains of PDMAEMA (dark area) within a PMMA matrix were observed (Figure 5.15a). Some of the PDMAEMA domains contained AgNPs (tiny black dots) and others were empty. It is clear that no AgNPs are located in the PMMA domains. Accordingly, the AgNPs were incorporated selectively in the PDMAEMA

domains, as hypothesised. As discussed in the previous section, during DMAEMA polymerisation, the electron-deficient silver ions diffuse into the growing polymer particles and are then captured by the electron-rich amine groups of the PDMAEMA block. The PDMAEMA block subsequently reduces the silver ions to zerovalent silver (AgNPs). In this way, the AgNPs were selectively located in the PDMAEMA domains. This also prevents AgNPs from agglomerating, without requiring the use of a stabiliser. Therefore, the $scCO_2$ synthesis enables domain selective placement of metal nanoparticles.

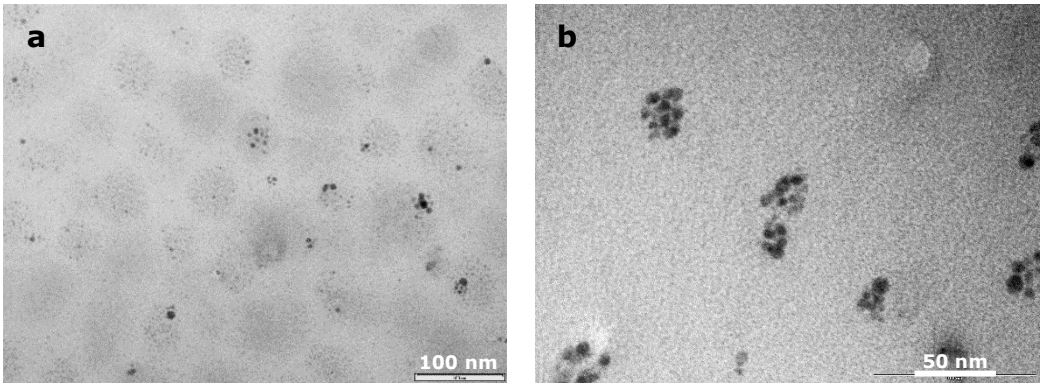


Figure 5.15. Cross-sectional TEM images (a) showing AgNPs located on the PDMAEMA domains (dark area), although not all of the PDMAEMA domains are filled by AgNPs, (b) showing clusters of AgNPs on PDMAEMA domains. The block copolymer was prepared with 2% of the soluble silver precursor.

The AgNPs also form nanoclusters to fill the PDMAEMA domains (Figure 5.15b). The clusters have a size of ~30 nm on average with an individual size of AgNP ~7 nm (Figure 5.15). The cluster size is approximately in agreement with the average size of the PDMAEMA spherical domains. In future, it may be possible to control the cluster size by varying the molecular weight or structure of the block copolymer. Close inspection reveals that the introduction of 2% silver precursor resulted in a number of empty PDMAEMA domains. This was

possibly caused by the AgNP loading, which was not sufficient to fill all available PDMAEMA domains. Therefore, synthesis with a higher concentration of silver precursor might be needed to fill more of the PDMAEMA domains.

5.5.4 The effect of precursor concentration

The concentration of silver precursor in the reaction was investigated to determine how this affected the AgNP content and size within the hybrid material as well as the thermal stability and morphology of the material. This was achieved by increasing the amount of silver precursor while keeping all other reagents and conditions constant.

5.5.4.1 Silver content within the polymer

Generally, increasing metal precursor concentration results in a higher metal content. However, TEM images (Figure 5.16) do not show an increase in the presence of AgNPs in the block copolymer clearly, especially for 2-5% of precursor loading. It should of course be appreciated that the TEM image represents local information, rather than for the whole sample. Therefore, the bulk silver content was determined further using thermogravimetric analysis (TGA).

Thermal analysis was conducted under a nitrogen atmosphere at a constant heating rate of 10 °C/min, in the range of 30-800 °C. The silver amount was predicted by assuming the TGA weight loss as the weight fraction of the block copolymer and dissociated ligand, and thus the remaining weight is approximately equal to the silver content in the sample (melting point of Ag, 961.8 °C). The analysis shows that the remaining weight increases linearly with the increase of silver precursor concentration (Figure 5.17 inset). Thus, it was clear that using the higher concentration of precursor resulted in a higher amount of silver.

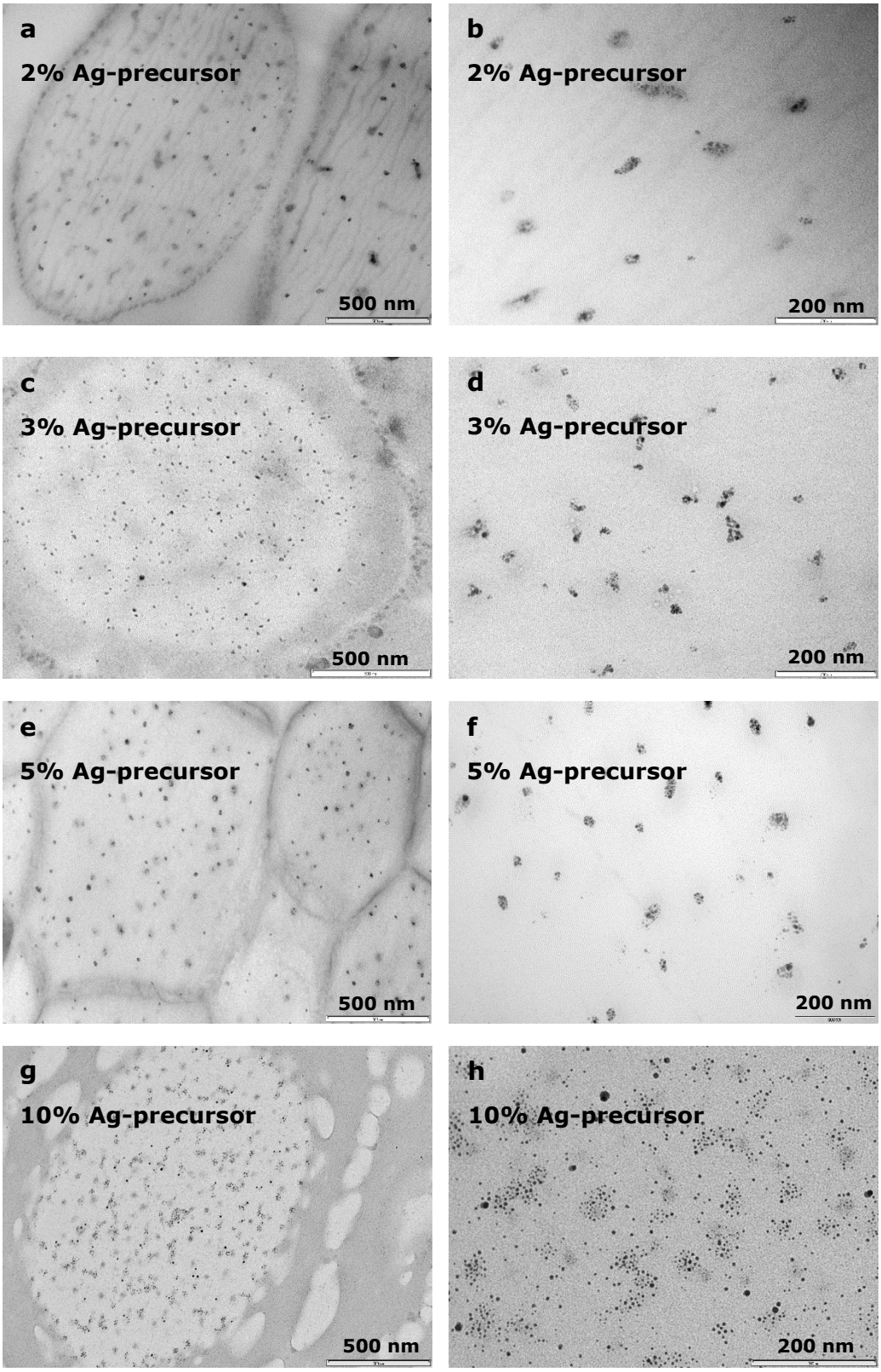


Figure 5.16. Cross-sectional TEM images of PMMA-*b*-PDMAEMA/AgNPs prepared with different soluble silver precursor concentrations (a) and (b) 2%, (c) and (d) 3%, (e) and (f) 5%, (g) and (h) 10%, showing AgNPs within copolymer particles at different magnifications.

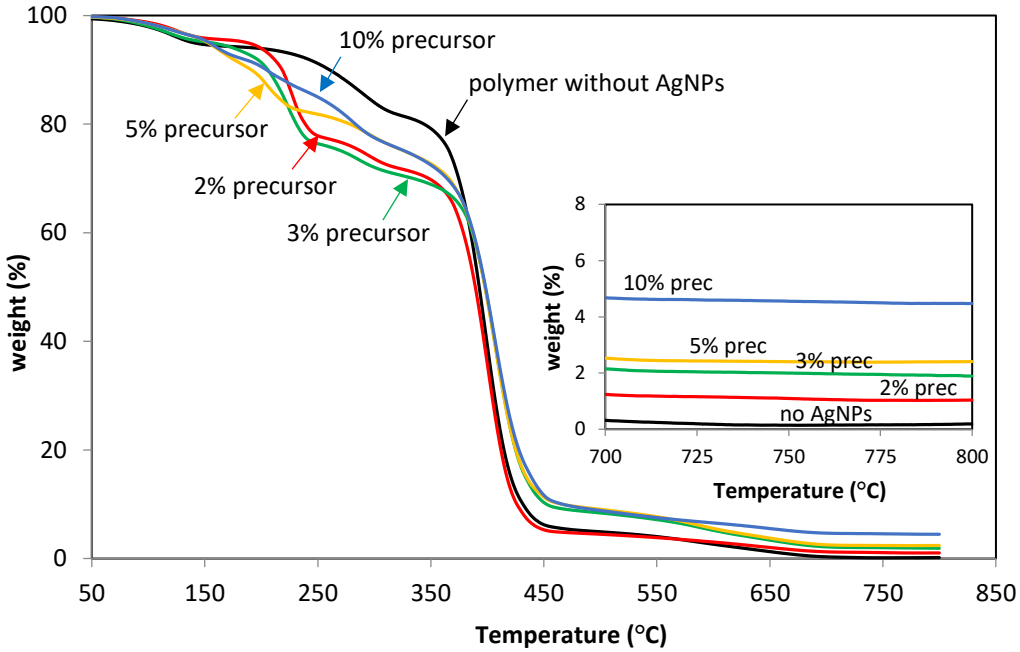


Figure 5.17. TGA curve of PMMA-*b*-PDMAEMA and PMMA-*b*-PDMAEMA/AgNPs with increasing silver precursor concentration. The inset image shows that the residual weight increases with increase of the precursor concentration and represent an increase loading of silver.

The presence of elemental silver in the microparticles was observed further in SEM images. These were taken on the resin block from which microtome thin sections were cut. This elemental analysis involves using X-rays produced *in situ* during SEM imaging to determine which elements are present in the area under observation. X-rays emitted by electron interaction with the samples produced spectra indicating the presence of silver (Figure 5.18). Other elements detected were carbon, oxigen, and sulfur is from the copolymer and its RAFT end group, while fluorine is suggested from dissociated ligand.

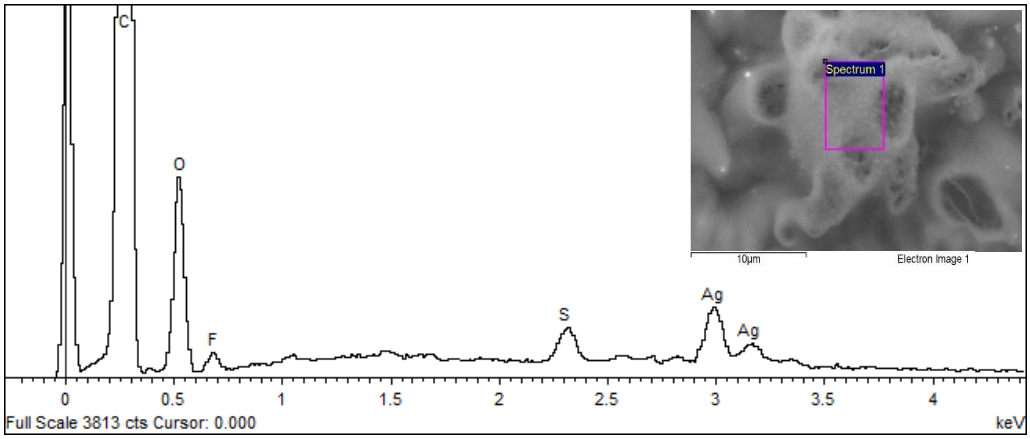


Figure 5.18. Energy dispersive X-ray (EDX) spectra of PMMA-*b*-PDMAEMA/AgNPs microparticles observed with SEM. Elements detected are carbon, oxygen, fluorine, sulfur, and silver. Inset is an SEM image of resin-embedded microparticles, the squared area is where the elemental analysis is measured.

5.5.4.2 Thermal stability of the hybrid material

TGA studies also revealed that all the samples showed a small and gradual weight loss (~3-5%) up to 150 °C. This was attributed to decomposition of the unreacted monomer and the remaining ligand. As reported, the 1,5-cyclooctadiene (COD) ligand decomposes at 110 °C.[24] Some residual ligand, may be extracted along with CO_2 release during depressurisation. Within a range of 240 – 350 °C, dissociation of saturated/unsaturated end-groups may occur.[53] Meanwhile, an abrupt weight loss attributed to the breakdown of the polymer chains begins at ~400 °C for neat PMMA-*b*-PDMAEMA. The onset of an abrupt weight loss of PMMA-*b*-PDMAEMA/AgNPs hybrid material is slightly higher at ~410 °C (Figure 5.19). This could reflect a higher thermal stability of the material because of the incorporation of AgNPs. Above 650 °C, the weight remains constant and an increase in residual content with an increase of the soluble precursor can be clearly observed (Figure 5.17).

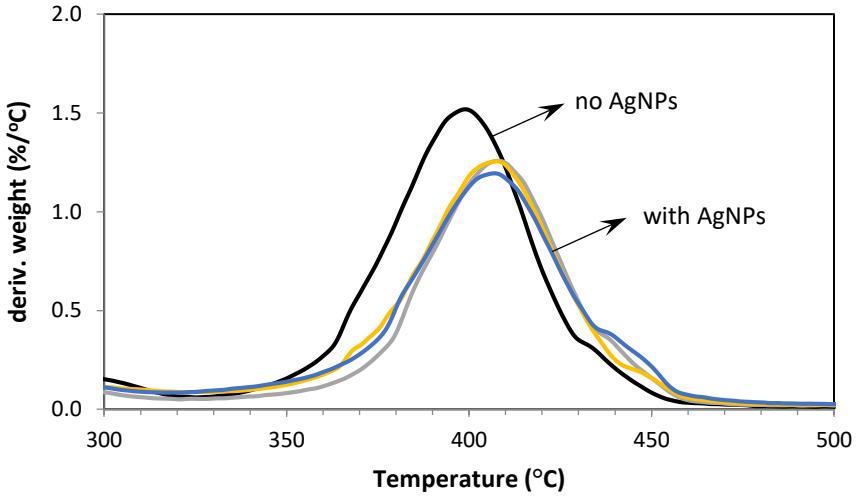


Figure 5.19. Derivative of mass loss (DTG) of PMMA-*b*-PDMAEMA and PMMA-*b*-PDMAEMA/AgNPs, showing the marginal improvement of thermal stability of the material because of the incorporation of AgNPs.

5.5.4.3 Size and Distribution of AgNPs

Further investigation of the TEM images (Figure 5.16) shows that up to 5% of precursor resulted in larger AgNPs (Table 5.2). This agrees with previous reports,[13,51] which suggest that a higher precursor concentration results in faster particle growth rate and hence yields larger particles. In this concentration range (2-5%), the AgNPs are packed in the PDMAEMA domain as a cluster morphology since the PDMAEMA domains can accommodate all of the formed AgNPs. By contrast, introducing 10% silver precursor resulted in a significantly different AgNP size and cluster morphology. A much smaller size of AgNPs is obtained (Table 5.2) and their spatial distribution within the PDMAEMA domain is more uniform (Figure 5.16 g and h) with some AgNPs now located in the PMMA phase.

Table 5.2. Particle size distribution of AgNPs with increasing silver precursor concentration

[Ag-Precursor]	AgNP diameter (nm)	C_v*
2%	7.65 ± 0.24	19%
3%	8.32 ± 0.29	19%
5%	9.14 ± 0.40	25%
10%	3.87 ± 0.08	11%

*Coefficient of variation (C_v), representing particle size distribution, calculated by Equation 2.3

In addition to the increasing particle growth rate, a high concentration of precursor can also promote faster particle nucleation.[51] This results in a higher density of nanoparticles in each PDMAEMA domain so there may not be enough space for the nanoparticles to continue growing, hence leading to smaller particle sizes. With a 10% precursor loading, AgNPs fill all PDMAEMA domains, and even exceed the capacity of the domains to accommodate all of them. As a result, some AgNPs are located in the PMMA domain.

The TEM images also revealed a rather broad size distribution of the nanoparticles for all investigated samples (Table 5.2) with the exception of the 10% precursor. This is likely due to the low reduction rate and hence slow Ag nuclei formation. In some cases, an additional reducing agent is added to initiate the reduction process and overcome the slow rate.[54]

5.5.4.4 Morphology of the polymer microparticles

As presented in the previous section, the AgNP-loaded block copolymer microparticles have a more agglomerated morphology than the pristine microparticles. This difference is clearly observed by examining the morphology of the block copolymer hybrids produced by increasing silver

precursor loading (Figure 5.20). This is intended to determine how the presence of the soluble silver precursor affected the morphology of the microparticles.

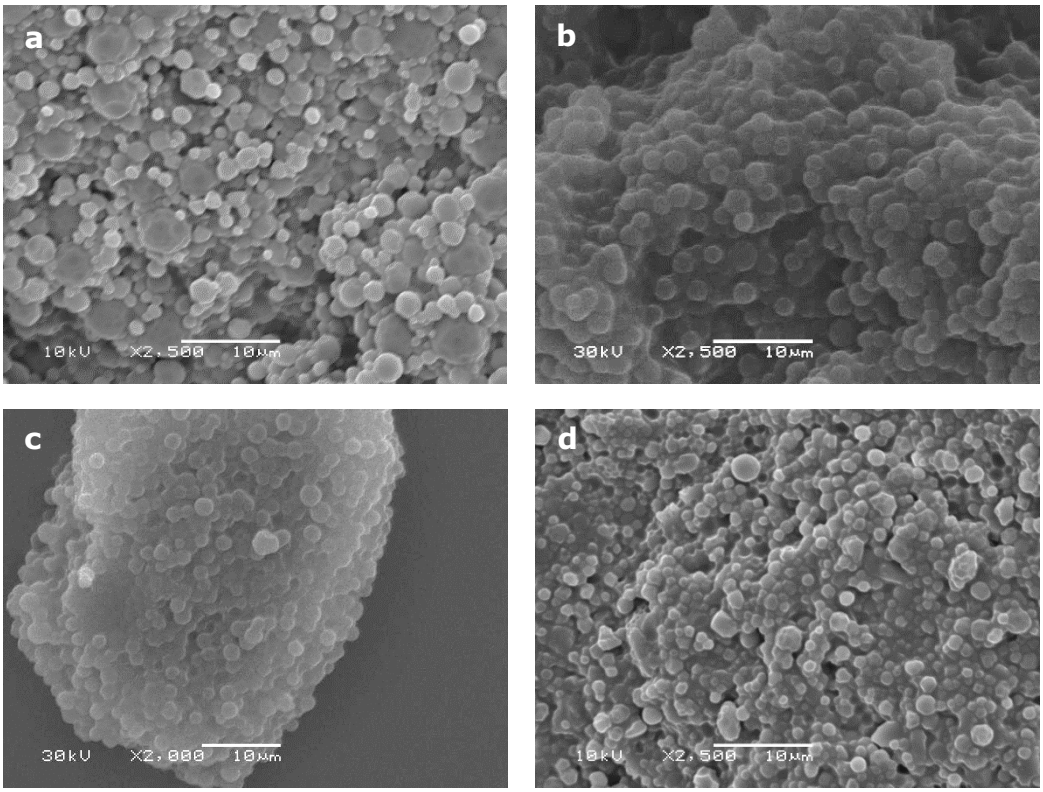


Figure 5.20. SEM images of PMMA-b-PDMAEMA/AgNPs produced by increasing the silver precursor loading to (a) 2%, (b) 3%, (c) 5%, and (d) 10%. The images illustrate that the microparticles tend to agglomerate and lead to deformed morphology as the silver precursor loading increases.

SEM investigations revealed that increasing the silver precursor concentration resulted in an ill-defined morphology (Figure 5.20). The polymer microparticles tended to agglomerate, which led to a deformed morphology. In addition to the low T_g of PDMAEMA, this is likely to be a result of the dissociated ligand, which is a fluorinated compound that acts as a co-solvent for the PMMA microparticles (the first block). The fraction of co-solvent in dispersion rises as the amount of the precursor increases, and hence results in a more

agglomerated morphology. It is often found that a small amount of co-solvent can enhance the solubility of a solute in $scCO_2$.[55]

5.6 Conclusions

The one-pot synthesis of PMMA-*b*-PDMAEMA/AgNPs hybrid material has been achieved. The synthesis combines the formation of AgNPs and DMAEMA polymerisation in one pot, simplifying the complex process that is normally applied for preparing such metal-loaded polymers. The products of the synthesis have been extensively characterised by electron microscopy.

The synthesis has successfully formed and introduced AgNPs into block copolymer microparticles, specifically incorporating the AgNPs selectively within the PDMAEMA domain without requiring surface modification of either the silver or the polymer chains as has been necessary in the literatures until now. The synthesis involves four steps; (i) dissolution of the silver precursor in $scCO_2$, (ii) thermal dissociation of the precursor to generate silver ions, (iii) diffusion of the silver ions into the growing polymer microparticles, and (iv) binding of the silver ions to the growing PDMAEMA chains and subsequently reducing the silver ions to the metallic form.

The size of the AgNPs and their loading within the block copolymer can be controlled by adjusting the silver precursor concentration. Increasing the precursor concentration up to 5% leads to larger AgNPs. By contrast, introducing 10% of the precursor results in much smaller AgNPs. The AgNPs occupy all the PDMAEMA domains, even exceeding the availability of the PDMAEMA domains (and hence some of them are found in the PMMA phase). Meanwhile, the AgNPs content linearly increases with the silver precursor concentration. However, a high concentration of the precursor results in an ill-

defined morphology for the block copolymer hybrid. The block polymer microparticles tend to agglomerate and this leads to a deformed morphology.

This synthesis results in a clean material. The solvent is readily removed on depressurisation, no additional reducing agents and no surface modification of the silver particles are required. For an industrial process, this could avoid the extra costs normally required for solvent waste removal. This synthesis route could be used not only with silver but also with other noble metals.

The results presented suggest that block copolymer microparticles can be a useful template for metallic nanostructure fabrication, although further work is required. The next target would be to improve the polymer microparticle morphology by using different precursors, for example to reduce the possibility of a co-solvent effect. The metal nanostructure could be obtained by degrading the PMMA block selectively, typically using solvent etching or UV light.[56]

5.7 References

1. Kolomytkin, D.O. et al. *Eur. Polym. J.* **71**, 73–84 (2015).
2. Zhang, K., Gao, L., Chen, Y. & Yang, Z. *Chem. Mater.* **20**, 23–25 (2008).
3. Kanahara, M., Shimomura, M. & Yabu, H. *Soft Matter* **10**, 275–280 (2014).
4. Posocco, P. et al. *J. Phys. Chem. C* **120**, 7403–7411 (2016).
5. Hasell, T., Thurecht, K.J., Jones, R.D.W., Brown, P.D. & Howdle, S.M. *Chem. Commun.* **38**, 3933–3935 (2007).
6. Hasell, T. et al. *Adv. Funct. Mater.* **18**, 1265–1271 (2008).
7. Huang, X., Xiao, Y., Zhang, W. & Lang, M. *Appl. Surf. Sci.* **258**, 2655–2660 (2012).
8. Soliveri, G. et al. *J. Phys. Chem. C* **120**, 1237–1244 (2016).
9. Palomba, M. et al. *J. Nanomater.* **2012**, 117–123 (2012).
10. Dong, X.-Y., Gao, Z.-W., Yang, K.-F., Zhang, W.-Q. & Xu, L.-W. *Catal. Sci. Technol.* **5**, 2554–2574 (2015).
11. Jennings, J. et al. *J. Am. Chem. Soc.* **134**, 4772–4781 (2012).

12. Zhang, Y. & Erkey, C. *J. Supercrit. Fluids* **38**, 252–267 (2006).
13. Erkey, C. *J. Supercrit. Fluids* **47**, 517–522 (2009).
14. Yang, J., Hasell, T., Smith, D.C. & Howdle, S.M. *J. Mater. Chem.* **19**, 8560–8570 (2009).
15. Watkins, J.J. & McCarthy, T.J. *Chem. Mater.* **7**, 1991–1994 (1995).
16. Morley, K.S. et al. *J. Mater. Chem.* **12**, 1898–1905 (2002).
17. Morley, K.S. et al. *J. Mater. Chem.* **14**, 1212–1217 (2004).
18. Saquing, C.D., Kang, D., Aindow, M. & Erkey, C. *Microporous Mesoporous Mater.* **80**, 11–23 (2005).
19. Morère, J., Sánchez-Miguel, E., Tenorio, M.J., Pando, C. & Cabañas, A. *J. Supercrit. Fluids* **120**, 7–17 (2017).
20. Lee, J.-M., Kim, D.-W., Lee, Y.-H. & Oh, S.-G. *Chem. Lett.* **34**, 928–929 (2005).
21. Haryono, A. & Binder, W.H. *Small* **2**, 600–611 (2006).
22. Kanahara, M., Shimomura, M. & Yabu, H. *Macromol. Mater. Eng.* **299**, 478–484 (2014).
23. Barandiaran, I. & Kortaberria, G. *Eur. Polym. J.* **68**, 57–67 (2015).
24. Carotenuto, G., Palomba, M. & Nicolais, L. *Sci. Eng. Compos. Mater.* **19**, 195–197 (2012).
25. Xing, H.L., Gao, S.T., Xu, G.C. & Sun, L.Q. *J. Thermoplast. Compos. Mater.* **29**, 260–269 (2014).
26. Zhang, Z., Zhang, L., Wang, S., Chen, W. & Lei, Y. *Polymer.* **42**, 8315–8318 (2001).
27. Tamai, T. et al. *Langmuir* **24**, 14203–14208 (2008).
28. Saito, R. & Ishizu, K. *Polymer.* **36**, 4119–4124 (1995).
29. Yuan, J.-J., Schmid, A., Armes, S.P. & Lewis, A.L. *Langmuir* **22**, 11022–11027 (2006).
30. Bleach, R., Karagoz, B., Prakash, S.M., Davis, T.P. & Boyer, C. *ACS Macro Lett.* **3**, 591–596 (2014).
31. Bagratashvili, V.N. et al. *Inorg. Mater. Appl. Res.* **1**, 297–302 (2010).
32. Ku, K.H. et al. *J. Am. Chem. Soc.* **136**, 9982–9989 (2014).
33. Choi, S.-J., Ku, K.H., Kim, B.J. & Kim, I.-D. *ACS Sensors* **1**, 1124–1131 (2016).
34. Yao, L., Lin, Y. & Watkins, J.J. *Macromolecules* **47**, 1844–1849 (2014).
35. Balazs, A.C., Emrick, T. & Russell, T.P. *Science.* **314**, 1107–1110 (2006).
36. Bockstaller, M.R. & Thomas, E.L. *Phys. Rev. Lett.* **93**, 1–4 (2004).
37. Sarkar, B. & Alexandridis, P. *Prog. Polym. Sci.* **40**, 33–62 (2014).
38. Chiu, J.J. et al. *Macromolecules* **40**, 3361–3365 (2007).
39. Thompson, R.B., Ginzburg, V. V, Matsen, M.W. & Balazs, A.C. *Science* **292**, 2469–2472 (2001).
40. Thompson, R.B., Ginzburg, V. V, Matsen, M.W. & Balazs, A.C.

Macromolecules **35**, 1060–1071 (2002).

41. Listak, J. et al. *Macromolecules* **42**, 5766–5773 (2009).
42. Zhao, Y. et al. *Nat. Mater.* **8**, 979–985 (2009).
43. Kao, J. et al. *Nano Lett.* **12**, 2610–2618 (2012).
44. Lai, J.T., Filla, D. & Shea, R.Y. *Macromolecules* **35**, 6754–6756 (2002).
45. Wang, W. et al. *Polymer.* **44**, 3803–3809 (2003).
46. Jennings, J. Synthesis and Self-Assembly of Block Copolymers in Supercritical CO_2. *Thesis.* The University of Nottingham (2013).
47. Baines, F.L., Billingham, N.C. & Armes, S.P. *Macromolecules* **29**, 3416–3420 (1996).
48. Zhang, X. & Matyjaszewski, K. *Macromolecules* **32**, 1763–1766 (1999).
49. Jennings, J. et al. *Macromolecules* **46**, 6843–6851 (2013).
50. Bates, F.S. *Science.* **251**, 898–905 (1991).
51. Casciato, M.J., Levitin, G., Hess, D.W. & Grover, M.A. *J. Nanoparticle Res.* **14**, (2012).
52. Wong, B., Yoda, S. & Howdle, S.M. *J. Supercrit. Fluids* **42**, 282–287 (2007).
53. Ferriol, M., Gentilhomme, A., Cochez, M., Oget, N. & Mieloszynski, J.L. *Polym. Degrad. Stab.* **79**, 271–281 (2003).
54. Jiang, X., Zeng, Q. & Yu, A. *Nanotechnology* **17**, 4929–4935 (2006).
55. Zhang, X. et al. *Chem. Eur. J.* **8**, 5107–5111 (2002).
56. Olson, D.A., Chen, L. & Hillmyer, M.A. *Chem. Mater.* **20**, 869–890 (2008).

Chapter 6 Conclusion and Future Work

6.1 Overview

This final chapter outlines the general conclusions achieved from the research presented and proposes some potential future work that could be undertaken to improve and develop further the recent results. To summarise, the objective of this Thesis has been to synthesise nanostructured block copolymers and study their microphase separation behaviour during the polymerisation in $scCO_2$. In addition, the developed synthesis method was exploited further to prepare block copolymer/metal nanoparticle hybrid materials using a simpler and greener technique.

6.2 Conclusion

In Chapter 3, a new and versatile method to prepare nanostructured block copolymer microparticles was presented, namely a two-stage method. This approach has shown that it is possible to extend the pre-synthesised PMMA RAFT powder to form block copolymers. The method was successfully applied to a range of monomers including methacrylate, styrene and dialkyl acrylamides to produce block copolymer microparticles. Importantly, the resulting block copolymers were found to phase-separate to form internal nanostructures due to enthalpic incompatibility between the polymer blocks. Different internal morphologies were observed, including body-centred cubic packing of spheres, hexagonally-packed cylinders, a bicontinuous gyroid phase, and lamellae. These morphologies were obtained by changing either the block copolymer pairs or the block volume fractions. The two-stage

synthesis method also appears to affect the particle morphology when a high concentration of the second monomer was added in the second stage. This led to large particles (>5 μm) with rough surfaces. In addition, the large particles with high dispersity have more than one internal nanostructure in each single microparticle when the blocks have large differences in CO_2-philicity.

To understand the kinetics and mechanism of the microphase separation behaviour during the block copolymer synthesis, an investigation was conducted using SAXS and presented in Chapter 4. The investigation involved *in situ* SAXS monitoring using synchrotron radiation to acquire time-resolved SAXS data during polymerisations. A new high pressure X-ray autoclave was designed to conduct these investigations. It was developed from the standard autoclave usually used for polymerisation in $scCO_2$. This new high pressure autoclave was able to produce comparable products to those obtained with the standard autoclave. More importantly, a series of *in situ* SAXS measurements of the block copolymer phase separation was successfully conducted using the new autoclave, allowing the phase separation process to be observed.

The time resolved-SAXS data in combination with TEM highlighted the development of the morphology. The development can be observed from the scattering peaks which become sharper and move to lower *q* values with reaction time. This indicates an ordering and increase in domain spacing of the microphase separation of the block copolymer chains. The structural development showed that the nanostructured morphologies remain constant after their initial formation. However, ordering of the nanostructures become more pronounced as the polymerisations proceed. The morphology is formed initially with a lower order structure. As the polymerisation proceeds, the second block segments grow to higher molecular weight and hence their

domains expand within the matrix of the first block. The neighbouring expanded domains approach each other until they interconnect and transform into a higher structure. This process seems to be facilitated by CO_2, which aids the mobility and rearrangement of the polymer chains.

Chapter 5 discussed the possibility of introducing additional components into just one of the phases of a block copolymer using the two-stage synthesis method. This strategy has successfully formed and introduced AgNPs into the PMMA-*b*-PDMAEMA block copolymer microparticles, particularly incorporating the AgNPs only in the PDMAEMA domains without requiring any surface modification of either the silver or the copolymer chains as has been necessary in the literature until now. The size of the AgNPs and their loading within the block copolymer can be controlled by adjusting the silver precursor concentration. At low concentration of silver precursor, a less aggregated block copolymer morphology with selective attachment of the AgNPs can be achieved. This developed synthesis route is clean; the solvent is readily removed on depressurisation, no additional reducing agents and no surface modification of the silver particles are required. However, further work would be necessary in order to produce a microparticle hybrid with better defined-morphology and with less aggregation.

6.3 Future work

Significant results have been described in this Thesis regarding the synthesis and phase behaviour of nanostructured block copolymer microparticles produced in $scCO_2$. However, there are a few areas where further work is desirable, including: (1) further exploration of the synthesis method for targeting wider morphologies, (2) greater control over the

microphase separation behaviour, and (3) exploration of the potential application of produced materials.

In principle, a range of morphologies such as double bicontinuous gyroid, knitting pattern, and tricontinuous double diamond[1] could be obtained by preparing a wider range of block copolymer formulations or introducing additional components such as small molecules or inorganic species.[2,3] Another strategy could be to produce ABC or ABA triblock copolymers or other complex architectures.

It has been shown in Chapter 3 that the PMMA RAFT precursor has good livingness and can be extended to produce block copolymers even after storage for weeks. However, precise characterisation of the degree of livingness and the stability of the materials is still needed to fully understand this new approach. The results could be useful to quantify the degree of livingness and investigate how it affects the block copolymer morphology because of the presence of either dead homopolymer or tapered block copolymer.

Analysis of the time-resolved SAXS data in combination with offline TEM has allowed us to propose a possible mechanism for the microphase separation of the block copolymers during their synthesis in $scCO_2$. However, these details need to be studied further to reveal the critical degree of polymerisation and volume fraction required for the corresponding morphologies during the reaction. These details could reveal comprehensive kinetics of the microphase separation process and allow construction of a precise experimental phase diagram.

The results presented in Chapter 5 hint at the potential of block copolymer microparticles as a colloidal template for metallic nanostructure

fabrication. However, further work is required, including improving the morphology. The metal nanostructures could be obtained by degrading the PMMA block selectively, typically using solvent etching or UV light.[4] This selective block degradation could also be applied to fabricate porous polymeric materials.[5] These porous materials have the potential to be useful in applications where both a high surface area and selectivity are required such as for separations, sensor, catalysis, and biomedical applications.[6–8] In microphase separation studies of block copolymers, the domain selectivity of the metal nanoparticles might allow us to greatly enhance the electron contrast between the blocks, this would be useful in SAXS analysis.

6.4 References

1. Castelletto, V. & Hamley, I.W. *Curr. Opin. Solid State Mater. Sci.* **8**, 426–438 (2004).
2. Kim, S.-M.P. and O.-H.P. and J.Y.C. and C.T.R. and H.-C. *Nanotechnology* **19**, 455304 (2008).
3. Vukovic, I. et al. *Macromolecules* **45**, 3503–3512 (2012).
4. Olson, D.A., Chen, L. & Hillmyer, M.A. *Chem. Mater.* **20**, 869–890 (2008).
5. Saba, S.A., Mousavi, M.P.S., Bühlmann, P. & Hillmyer, M.A. *J. Am. Chem. Soc.* **137**, 8896–8899 (2015).
6. Zhang, M. et al. *ACS Appl. Mater. Interfaces* **7**, 13758–13767 (2015).
7. Jiang, K. et al. *ACS Appl. Mater. Interfaces* **8**, 25529–25534 (2016).
8. Yu, H., Qiu, X., Nunes, S.P. & Peinemann, K.V. *Nat. Commun.* **5**, 4110 (2014).